View metadata, citation and similar papers at core.ac.uk

brought to you by CORE

provided by Edinburgh Research Archive

THE UNIVERSITY *of* EDINBURGH

This thesis has been submitted in fulfilment of the requirements for a postgraduate degree (e.g. PhD, MPhil, DClinPsychol) at the University of Edinburgh. Please note the following terms and conditions of use:

This work is protected by copyright and other intellectual property rights, which are retained by the thesis author, unless otherwise stated.

A copy can be downloaded for personal non-commercial research or study, without prior permission or charge.

This thesis cannot be reproduced or quoted extensively from without first obtaining permission in writing from the author.

The content must not be changed in any way or sold commercially in any format or medium without the formal permission of the author.

When referring to this work, full bibliographic details including the author, title, awarding institution and date of the thesis must be given.

Self-organisation processes in (magneto)hydrodynamic turbulence

Moritz Frederik Linkmann

Doctor of Philosophy
The University of Edinburgh
February 2016

Abstract

Self-organising processes occurring in isotropic turbulence and homogeneous magnetohydrodynamic (MHD) turbulence are investigated in relation to the stability of helical flow structures. A stability analysis of helical triad interactions shows that compared to hydrodynamics, equilibria of the triadic evolution equations have more instabilities with respect to perturbations on scales larger than the characteristic scale of the system. Some of these instabilities can be mapped to Stretch-Twist-Fold dynamo action and others to the inverse cascade of magnetic helicity. High levels of cross-helicity are found to constrain small-scale instabilities more than large scale instabilities and are thus expected to have an asymmetric damping effect on forward and inverse energy transfer. Results from a numerical investigation into the influence of helicity on energy transfer and dissipation are consistent with this observation. The numerical work also confirms the predictions of an approximate method describing the Reynolds number dependence of the dimensionless dissipation coefficient for MHD turbulence. These predictions are complemented by the derivation of mathematically rigorous upper bounds on the dissipation rates of total energy and cross-helicity in terms of applied external forces.

Large-scale helical flows are also found to emerge in relaminarisation events in direct numerical simulations of isotropic hydrodynamic turbulence at low Reynolds number, where the turbulent fluctuations suddenly collapse in favour of a large-scale helical flow, which was identified as a phase-shifted ABC-flow. A statistical investigation shows similarities to relaminarisation of localised turbulence in wall-bounded parallel shear flows. The turbulent states have an exponential survival probability indicating a memoryless process with a characteristic lifetime, which is found to depend super-exponentially on Reynolds number akin to well-established results for pipe and plane Couette flow. These and further similarites suggest that the phase space dynamics of isotropic

turbulence and wall-bounded shear flows are qualitatively similar and that the relaminarisation of isotropic turbulence can also be explained by the escape from a chaotic saddle.

Lay summary

Chaotic flows of liquids or gases far away from any boundary, like many atmospheric and oceanic flows, are often viewed by scientists as real-life realisations of isotropic turbulence - a classical idealised description of turbulent motion that dates back to the beginning of the 20th century. This picture can be extended to so-called magnetofluids, which are electrically conducting fluids such as liquid metals or plasmas, in order to facilitate the study of their turbulent dynamics, and is believed to give a good approximation of the behaviour of space plasmas.

This thesis is concerned with self-organisation events occurring within the framework of this description of turbulence. A self-organisation event can be the sudden collapse of turbulence or the emergence of a large-scale magnetic field out of a sea of small-scale chaos. Magnetic self-organisation processes are important in many areas of geo- and astrophysics, for example the Sun's magnetic field is generated by such a self-ordering process. The aim of this project was to further understand why turbulent magnetofluids are more likely to self-organise compared to fluids which do not interact with a magnetic field. By analysing the elementary mechanisms that are the building blocks of the system, it was found that flows and magnetic fields with a spiral geometry are unstable and feed disturbances at larger scales if these have a similar orientation. These special spiral structures are thus mainly responsible for the emergence of large-scale order, and they occur more frequently and are more unstable in turbulent magnetofluids than in ordinary fluids.

The investigations also showed that isotropic turbulence can suddenly disappear and that this process is very similar to turbulence in flows between boundaries, like flow in a pipe. Surprisingly, the non-turbulent, organised flow which appeared out of the turbulence has the same structure as the flow structures which were identified as the main culprits for self-ordering in magnetofluids. This suggests that these special flows have a more general connection to self-organisation.

Declaration

I declare that this thesis was composed by myself, that the work contained herein is my own except where explicitly stated otherwise in the text, and that this work has not been submitted for any other degree or professional qualification except as specified.

Parts of this work have been published in [12, 112–114, 122].

(*Moritz Frederik Linkmann, February 2016*)

Acknowledgements

I thank my supervisor Prof. Arjun Berera for scientific guidance, his creative thinking and continuous pursuit of knowledge which led to many new ideas. I also thank him for his exemplary scientific integrity and his encouragement to pursue independent research.

I thank Dr Alexander Morozov for general scientific guidance, for his help with many questions about the dynamical systems approach to the transition to turbulence and of course for the collaboration which led to the results presented in chapter 6.

Many thanks to the PhD and undergraduate students who I worked with: Mairi McKay, Bernardas Jankauskas, Erin Goldstraw, Julia Jäger and Richard Ho. Special thanks go to Mairi and Richard for proofreading this thesis. I thank Dr Samuel Yoffe for writing his hydrodynamic code well-commented and well-structured, which was of enormous advantage for the further development of it. I also thank him for help in the initial stages of my PhD, for many good discussions and collaboration on projects which are mostly outwith the scope of this thesis. I thank Prof. W. D. McComb for initial guidance and supervision of projects which are mostly outwith the scope of this thesis. Special thanks go to Dr Vassilios Dallas for many interesting and helpful discussions, especially those that lead to improvements to chapter 4, and to Dr Christopher Deans for sharing an office and his impressive knowledge of statistics. I thank Dr Jorge Morales for providing me with a dataset for testing purposes. Many thanks to Dr Kenton D'Mellow and EDCF staff for allocation and management of HPC resources.

I thank my family for their continuous support.

The numerical work has made use of the resources provided by ARCHER (`http://www.archer.ac.uk`), made available through the Edinburgh Compute and Data Facility (ECDF, `http://www.ecdf.ed.ac.uk`) and of local resources provided by ECDF. Financial support was given by the UK Engineering and Physical Sciences Research Council (EP/K503034/1).

Contents

List of Figures

List of Tables

Chapter 1

Introduction

Turbulence is a multidisciplinary problem of remarkable complexity. It is of interest to pure and applied mathematicians, physicists and engineers due to the many theoretical and practical problems that are connected to (or perhaps inherent in) turbulence. Since Leray's proof of the existence of weak solutions[1] in 1934, pure mathematicians are generally concerned with the problem of finding smooth and globally defined (strong) solutions of the Navier-Stokes equations with finite energy per unit volume, given smooth initial conditions. Since both turbulent and laminar flow is believed to be described by the Navier-Stokes equations, finding a (unique) smooth, physically reasonable solution of these equations would imply that both laminar and turbulent behaviour in a given fluid would become predictable. This problem is of such importance that it is included in the list of Millenium Prize Problems of the Clay Mathematics Institute[2]. From a physicist's point of view, the phenomenon of turbulence in fluids has not been solved in the sense of a 'theory of turbulence' or a model that adequately describes all its features.

Turbulence is of practical importance as it occurs in many situations. Sometimes it is desired because it facilitates mixing of two different fluids, in other situations it should be avoided e.g. because it leads to increased drag compared to laminar flow and thus lower mean flow speed, which is problematic in situations such as

[1] A weak solution is a solution of the corresponding integral equation, where the spatial derivatives act on test functions.

[2] The problem is also considered solved if it can be proven that for sufficiently smooth initial conditions and forces no smooth and physically reasonable solution of the Navier-Stokes equation exists.

heat conduction in cooling applications. The transition to turbulence deserves special attention due to its detrimental effects in engineering applications, where a sudden spike in pressure due to the onset of turbulence can lead to material failure. Turbulence control is therefore of interest for many real-world situations, and a further understanding of turbulence may lead to steps forward to achieve turbulence control.

In many situations a flow is coupled to a magnetic field, for example in a magnetised plasma or a liquid metal flow. Liquid metal flows occur in liquid planetary cores such as the Earth's liquid iron core, they are also used in the cooling blankets of Fast Breeder Reactors (FBR) and tokamak-type fusion reactors. In the latter two applications, turbulence in the liquid metal flow is problematic as turbulent flow results in less efficient cooling. Furthermore, in a tokamak reactor the hot plasma is confined by a magnetic field which influences the liquid metal flow in the cooling blanket. Magnetohydrodynamic (MHD) flows also occur in industrial applications such as in steel processing. In summary, turbulence in conducting and non-conducting flows is a complex problem with many important applications and poses interesting theoretical and even formal mathematical questions.

One of these questions concerns the emergence of large-scale structures out of a turbulent flow, which in turn poses immediate further questions connected with turbulence control. Examples of these *self-organisation* events are the formation of large-scale magnetic fields in certain types of MHD flows and the sudden collapse of localised turbulence in wall-bounded parallel shear flows.

Self-organisation is not specific to fluid dynamics. It occurs in many systems described by nonlinear partial differential equations in physics, mathematics, chemistry, biology, economics, etc., such as bird flocking or the behaviour of pedestrians in a crowded shopping mall. As such, self-organisation is a broadly defined term and the dynamics leading to self-ordering events will differ between different systems. In this thesis self-organisation is defined as the collective disappearance of small-scale motion and/or the amplification of large-scale motion by small-scale motion. As such, both aforementioned examples of the emergence of large-scale structure will be treated in this thesis as aspects of self-organisation in turbulent flows.

1.1 Non-conducting fluids

The dynamics of the flow of a non-conducting Newtonian fluid is governed by the Navier-Stokes equations here written in component form

$$\partial_t(\rho u_i) = -\partial_i P - u_j \partial_j(\rho u_i) + \partial_j\big(\mu[\partial_j u_i + \partial_i u_j] + \lambda \partial_k u_k \delta_{ij}\big) + f_{u,i} \ , \qquad (1.1)$$

where a summation over repeated indices is implied, and where $\boldsymbol{u} = (u_1, u_2, u_3)$ denotes the velocity field, μ and λ the shear and bulk viscosities, P the thermodynamic pressure, $\boldsymbol{f}_u$ an external force which may be present, and ρ the density. Together with the appropriate initial and boundary conditions, the Navier-Stokes equations describe fluid flow in both laminar and turbulent regimes. The Navier-Stokes equations are usually derived by considering a test volume of fluid using conservation of mass and Newton's second law. Alternatively, they can be derived in the kinetic theory of gases by taking moments of the Boltzmann equation, where the probability density function for the individual particles is considered close to Maxwellian. That is, a perturbation expansion around a Maxwellian distribution for the individual particles is considered using the Chapman-Enskog method[3].

If the flow is incompressible, the velocity field is solenoidal and obeys

$$\nabla \cdot \boldsymbol{u} = 0 \ , \qquad (1.2)$$

since the density is constant. In this case eq. (1.1) reduces to

$$\partial_t \boldsymbol{u} = -\frac{1}{\rho}\nabla P - (\boldsymbol{u} \cdot \nabla)\boldsymbol{u} + \nu \Delta \boldsymbol{u} + \boldsymbol{f}_u \ , \qquad (1.3)$$

where $\nu = \mu/\rho$ is the kinematic viscosity. The nonlinear term $(\boldsymbol{u} \cdot \nabla)\boldsymbol{u}$ on the right-hand side of the Navier-Stokes equations is responsible for mixing and energy transfer across different scales, while the viscous term $\nu\Delta\boldsymbol{u}$ represents dissipation, that is, conversion of kinetic energy into heat due to friction. Very different behaviour of a fluid is thus expected depending on which of these two terms dominates. Fluid flows are usually described by a dimensionless parameter, the Reynolds number

$$Re = \frac{UL}{\nu} \ , \qquad (1.4)$$

[3]The Navier-Stokes equations which are derived by this procedure formally apply to dilute gases only.

where U and L are velocity and length scales characteristic of the flow. For flow through e.g. a straight pipe, U may be the rms flow velocity and L the diameter of the pipe. If the Navier-Stokes equations are made dimensionless by rescaling all variables with the appropriate powers of U and L, the inverse of the Reynolds number appears in front of the Laplace operator Δ on the right-hand side (RHS) of eq. (1.3) replacing the viscosity ν. The Reynolds number thus quantifies the relative importance of inertial compared to viscous effects. For $\nu = 0$ the dissipative term in the Navier-Stokes equation (without forcing) is absent and the resulting equation is called the *Euler equation*. Since this reduces the order of the differential equation, the limit $Re \to \infty$ is singular.

The pipe flow experiments by Osborne Reynolds [152] showed that fluid flow in a straight pipe is laminar at low flow speeds and turbulent at high flow speeds. Since the fluid and the pipe were the same in the experiments and only the flow speed was varied, the statement can be expressed in terms of the Reynolds number: at low Reynolds number the flow is laminar and it is turbulent at high Reynolds number. The Reynolds number is thus the universal control parameter for (isothermal) fluid flows. Increasing the Reynolds number should lead to a transition from laminar to turbulent flow, and it is of interest how this transition proceeds. In certain types of flows the transition to turbulence is due to a linear instability of the laminar profile. However, there are flows (such as pipe flow) where the laminar profile is linearly stable. In these cases the transition to sustained turbulence occurs through a more complicated process, where relaminarisation and proliferation of localised turbulence, in other words self-organisation and increasing disorder, compete [7]. The study of self-organisation processes may therefore be of interest for the general study of turbulence in fluids.

1.2 Magnetohydrodynamics

Self-organisation processes are known to occur in magnetohydrodynamic flows, where the flow of a conducting fluid interacts with a magnetic field. In order to describe an MHD flow, Maxwell's equations are coupled with the Navier-Stokes equations [21]. The MHD equations can be derived in the kinetic theory of gases/plasmas from the Boltzmann equation by the Chapman-Enskog procedure. In plasma physics the MHD approximation is only valid for strongly collisional plasmas, however, most astrophysical and laboratory plasmas are weakly collisional. In these cases MHD gives a good approximation to plasma

dynamics on time scales larger than the characteristic time for a collision. Similarly, the MHD approximation breaks down for the description of dynamics of the very small scales. The equations describing an incompressible MHD flow are

$$\partial_t \boldsymbol{u} = -\frac{1}{\rho}\nabla P - (\boldsymbol{u}\cdot\nabla)\boldsymbol{u} + \frac{1}{\rho}(\nabla\times\boldsymbol{b})\times\boldsymbol{b} + \nu\Delta\boldsymbol{u} + \boldsymbol{f}_u \ , \tag{1.5}$$

$$\partial_t \boldsymbol{b} = (\boldsymbol{b}\cdot\nabla)\boldsymbol{u} - (\boldsymbol{u}\cdot\nabla)\boldsymbol{b} + \eta\Delta\boldsymbol{b} + \boldsymbol{f}_b \ , \tag{1.6}$$

$$\nabla\cdot\boldsymbol{u} = 0 \ \text{ and } \ \nabla\cdot\boldsymbol{b} = 0 \ , \tag{1.7}$$

where $\boldsymbol{u}$ denotes the velocity field, $\boldsymbol{b}$ the magnetic induction[4] expressed in units of velocity, ν the kinematic viscosity, η the magnetic resistivity, P the thermodynamic pressure, $\boldsymbol{f}_u$ and $\boldsymbol{f}_b$ are external mechanical and electromagnetic forces, which may be present, and ρ denotes the density which is set to unity for convenience.

The MHD equations describe the action of the Lorentz force $(\nabla\times\boldsymbol{b})\times\boldsymbol{b}$ on the fluid as well as the dynamics of the magnetic field due to interaction with the fluid flow. It can be seen from eq. (1.5) and eq. (1.6) that a magnetic field can cause a fluid to flow through the action of the Lorentz force, but (not surprisingly) the flow cannot generate a magnetic field by itself. The action of the fluid on the magnetic field has two contributions corresponding to the two interaction terms on the right-hand side of the induction equation. The term $(\boldsymbol{u}\cdot\nabla)\boldsymbol{b}$ describes advection of magnetic field lines by the flow while the term $(\boldsymbol{b}\cdot\nabla)\boldsymbol{u}$ corresponds to magnetic field line stretching by the fluid flow, it is this term that is responsible for the conversion of kinetic to magnetic energy.

The MHD equations can be formulated more symmetrically using Elsässer variables $\boldsymbol{z}^{\pm} = \boldsymbol{u} \pm \boldsymbol{b}$ [68]

$$\partial_t \boldsymbol{z}^{\pm} = -\frac{1}{\rho}\nabla\tilde{P} - (\boldsymbol{z}^{\mp}\cdot\nabla)\boldsymbol{z}^{\pm} + (\nu+\eta)\Delta\boldsymbol{z}^{\pm} + (\nu-\eta)\Delta\boldsymbol{z}^{\mp} + \boldsymbol{f}^{\pm} \ , \tag{1.8}$$

$$\nabla\cdot\boldsymbol{z}^{\pm} = 0 \ , \tag{1.9}$$

where $\boldsymbol{f}^{\pm} = \boldsymbol{f}_u \pm \boldsymbol{f}_b$ and the pressure $\tilde{P}$ consists of the sum of the thermodynamic pressure P and the magnetic pressure $0.5\rho|\boldsymbol{b}|^2$. Which formulation of the MHD equations is chosen often depends on the physical problem, for some problems the Elsässer formalism is technically convenient, while the formulation using the

[4]The magnetic induction $\boldsymbol{b}$ is often referred to as the magnetic field, although the magnetic field is $\boldsymbol{h} = \boldsymbol{b}/\mu_0$, where μ_0 is the permeability of free space.

primary fields $\boldsymbol{u}$ and $\boldsymbol{b}$ facilitates physical understanding.

1.2.1 Alfvén waves

In the presence of a strong uniform background magnetic field the MHD equations admit wave solutions. In order to obtain these solutions let $\boldsymbol{b}_0$ be the background magnetic field subject to perturbations $\boldsymbol{u}'$ and $\boldsymbol{b}'$. The MHD equations can then be linearised about $\boldsymbol{b}_0$, and one obtains

$$\partial_t \boldsymbol{u}'(\boldsymbol{x},t) = (\boldsymbol{b}_0 \cdot \nabla)\boldsymbol{b}'(\boldsymbol{x},t) + \nu\Delta\boldsymbol{u}'(\boldsymbol{x},t) \ , \tag{1.10}$$

$$\partial_t \boldsymbol{b}'(\boldsymbol{x},t) = (\boldsymbol{b}_0 \cdot \nabla)\boldsymbol{u}'(\boldsymbol{x},t) + \eta\Delta\boldsymbol{b}'(\boldsymbol{x},t) \ . \tag{1.11}$$

These equations can be solved by making a plane-wave ansatz for $\boldsymbol{u}'$ and $\boldsymbol{b}'$ leading to *Alfvén waves*[5]. Alfvén waves are transverse waves propagating at the *Alfvén speed*

$$v_A = |\boldsymbol{b}_0| \cos\varphi \tag{1.12}$$

where φ is the angle between the the direction of propagation and the background field. Since $v_A \to 0$ for $\varphi \to \pi/2$, Alfvén waves cannot propagate perpendicular to $\boldsymbol{b}_0$. Alfvén waves are central to the Iroshnikov-Kraichnan cascade picture of MHD turbulence, where turbulence is generated by collisions of counter-propagating Alfvén wave packets as further explained in sec. 1.3.2.

1.2.2 Dimensionless parameters describing MHD flows

For non-conducting fluids the Reynolds number parametrises the relative importance of inertial compared to viscous effects. Similarly, a magnetic Reynolds number can be defined

$$Rm = \frac{UL}{\eta} \ , \tag{1.13}$$

which parametrises the relative importance of inductive effects compared to Ohmic dissipation. A third parameter which is often used to characterise MHD flows is the magnetic Prandtl number

$$Pm = \frac{Rm}{Re} = \frac{\nu}{\eta} \ , \tag{1.14}$$

[5]Hannes Alfvén received the 1970 Nobel prize in physics for his work on MHD.

Situation	Re	Rm	Pm
turbulent pipe flow [7]	> 2040	n/a	n/a
laminar pipe flow [7]	< 2040	n/a	n/a
liquid metal experiments [144]	10^7	10	10^{-6}
liquid sodium coolant (FBR) [144]	10^8	100	10^{-6}
earth's core [144]	10^9	1000	10^{-6}
convection zone (sun) [144]	10^{13}	10^8	10^{-5}
possible DNS	$1 - 1000$	$1 - 1000$	$10^{-3} - 10^3$
most DNS	1000	1000	1
interstellar medium [144]	10^3	10^{15}	10^{12}

Table 1.1 *Magnetic and inertial Reynolds numbers Rm and Re, and magnetic Prandtl numbers Pm = Rm/Re for different flows occurring in nature, experiments and in numerical simulations. DNS stands for Direct Numerical Simulation and FBR for Fast Breeder Reactor.*

which is a measure of the ratio of viscous to Ohmic dissipation. For magnetised plasmas the Lundquist number

$$S = \frac{BL}{\eta} \ , \tag{1.15}$$

is often used as an alternative to Rm [21], where the B is the rms magnetic field (in units of velocity). The Lundquist number is thus mainly a measure of resistive effects in configurations dominated by the behaviour of the magnetic field such as in studies of magnetic reconnection events. Typical Lundquist numbers in laboratory plasmas range from $10^2 - 10^8$, for astrophysical plasmas the Lundquist number can exceed 10^{20} [151]. In MHD flows where the coupling between the turbulent flow and the magnetic field becomes important, in other words, in nonlinear MHD problems, Rm is usually regarded as the more important quantity [21].

A list of typical magnetic Prandtl and Reynolds numbers for different physical systems and numerical simulations is given in table 1.1. As can be seen from the table, in most physical situations Pm is either very large, such as for a plasma in the fluid approximation, or very small, such as in a liquid metal flow. However, in most numerical simulations $Pm = 1$. This is due to limited computational power. Even using the latest HPC architectures small-scale Reynolds numbers of over 1000 are hard to attain. If the aim is to study the interaction of a magnetic field with a turbulent flow, compromises thus have to be made with respect to the attainable magnetic Prandtl number.

Location	liquid metal	flow types
Perm, Russia	sodium	high rotation shear dynamo
Riga, Latvia	sodium	driven constrained counter-current helical dynamo
Karlsruhe, Germany	sodium	driven constrained counter-current helical dynamo
Princeton, USA	gallium	Ekman layer driven turbulence, Couette flow, MRI
Cadarache, France	sodium/ gallium	Von Kármán flow, unconstrained, DJ dynamo
Univ. Maryland, USA	sodium	unconstrained, DJ dynamo, thermal convection driven turbulence, MRI
Univ. Wisconsin, USA	sodium	unconstrained, DJ dynamo, MRI
Swarthmore, USA	sodium	Couette flow, turbulence-induced enhanced resistivity
Los Alamos, USA	sodium	Couette flow, helicity induced by driven plumes, MRI

Table 1.2 *Liquid metal MHD experiments (adapted from Ref. [43]). MRI stands for magneto-rotational instability and DJ refers to Dudley-James two-vortex flow.*

1.2.3 Experimental situation

Experiments in MHD flows are fraught with considerable difficulties. Liquid metals are chemically very aggressive and thus the containing vessels must be made of adequate materials. Hot wire anemometry measurements for turbulent flows are even more problematic as the probe must resolve the smallest scales generated by the turbulence, therefore a very thin wire must be used. The chemical aggressiveness of the liquid metal then precludes measurements at high Reynolds number as the necessarily thin wires do not withstand the chemical deterioration caused by contact with the liquid metal.

A possibly non-exhaustive list of liquid metal experiments is given in the review article by Colgate [43]. For convenience this list is reproduced here in tbl. 1.2. Several of these experiments are concerned with the so-called *dynamo*, which in this context refers to the amplification of a magnetic field by the fluid flow. This is of particular interest especially in geo- and astrophysical applications. Some aspects of dynamo action will be discussed in sec. 1.3.3.

For magnetised plasmas, the experimental situation is even more difficult, as

prolonged confinement of a turbulent plasma must be achieved. Therefore, researchers often use spacecraft measurements of turbulence in the solar wind. This is expensive and effects such as expansion of the solar wind may make observations difficult in certain parameter ranges [42]. The alternative is then Direct Numerical Simulations (DNSs), which are carried out by many researchers in order to gain insight into the fundamental properties of turbulent dynamics in MHD flows. However, as mentioned above, the achievable Reynolds and magnetic Prandtl numbers are constrained by computational resources. As can be seen in tbl. 1.1, typical DNSs fall short of simulating real-world flows, especially in terms of achievable values of Pm.

MHD flows are particularly interesting to study in view of self-organisation processes. More linear instabilities occur due to the interaction of the fluid flow with the magnetic field, however, turbulent MHD flows show a tendency to self-organise depending on certain topological constraints, which will be introduced in sec. 1.3.3.

1.3 Theoretical approaches to turbulence

Unless the external force is explicitly stochastic, the Navier-Stokes equations (1.3) are deterministic differential equations. However, even without any stochastic input, they give rise to ever more complex and irregular behaviour such that at some point the deterministic dynamical system given by the Navier-Stokes equations appears to be of stochastic nature[6]. This motivated the use of statistical methods to characterise turbulent flows, however, the statistical approach cannot explain how this complexity comes about, that is, it cannot describe the transition to turbulence.

As mentioned in the introduction, fluid flows are laminar at low Reynolds number and turbulent at high Reynolds number. As the Reynolds number is varied the dynamics of the system change, in other words, a *bifurcation* should occur. The nature of this change in behaviour, that is, the nature of the transition to turbulence is an active area of research in the dynamical systems approach to turbulence. Depending on the type of laminar profile, the transition to turbulence

[6]This means despite being a deterministic system it is so complex that a statistical approach is justified in the sense that not enough precise knowledge about the system can be obtained to predict its behaviour.

is well described by either linear instabilities or, in cases where the transition to turbulence occurs before linear instabilities set in or where the laminar flow is linearly stable, by a more complex process explained in further detail in the following section. As such the transition to turbulence falls naturally into the realm of dynamical systems theory.

Another area of research into turbulent flows makes use of topological constraints on the flow evolution due to inviscidly conserved quantities, which have a topological interpretation. As outlined earlier on, the Navier-Stokes equations also remain an active area of research in pure mathematics. In summary, the theoretical study of turbulent flows has developed into different branches, which are pursued sometimes without significant interaction between the subfields. Perhaps the variety of approaches somewhat reflects complexity of the problem.

1.3.1 Turbulence and dynamical systems

The dynamical systems approach to turbulence seeks to describe the properties of a fluid-dynamical system given by the Navier-Stokes equations with the appropriate boundary conditions by mapping out the phase (or state) space of that system. The starting point is often a linear stability analysis of the laminar profile depending on the Reynolds number, leading to a bifurcation analysis.

A continuous dynamical system is given by a manifold M (the state space), a semigroup X and a smooth family of functions ϕ_t such that

$$\begin{aligned} \phi : M \times X &\longrightarrow M \\ (\boldsymbol{v}, t) &\longmapsto \phi(\boldsymbol{v}, t) = \phi_t(\boldsymbol{v}). \end{aligned} \tag{1.16}$$

If $X = \mathbb{R}$ and ϕ is differentiable, the system is called a *flow* with flow map ϕ_t, which describes the time evolution of a state in the system starting from an initial state $\boldsymbol{v}_0$

$$\begin{aligned} \phi_t : \mathbb{R} &\longrightarrow M \\ t &\longmapsto \phi_t(\boldsymbol{v}_0) = \boldsymbol{v}(t), \end{aligned} \tag{1.17}$$

where $\phi_0(\boldsymbol{v}_0) = \boldsymbol{v}(0) = \boldsymbol{v}_0$. A flow with an infinite dimensional state space can be associated with a partial differential equation, where $\phi_t(\boldsymbol{v})$ is a solution of $\partial_t \boldsymbol{v} = \boldsymbol{F}(\boldsymbol{v})$ for the vector field $\boldsymbol{F}$ defined by $\boldsymbol{F}(\boldsymbol{v}) = \dot{\phi}_t(\boldsymbol{v}_0)$. If the evolution

depends on an additional (bifurcation) parameter, then the states of the system will change when this parameter is varied. A *stationary point* or *equilibrium* is given by a solution of the equation $\partial_t \boldsymbol{v} = 0$ and much information about the behaviour of a dynamical system can be gained by studying the stability of the equilibria under variation of the bifurcation parameter(s).

A *bifurcation* occurs if the topological properties of the system change suddenly under a small and smooth variation of the bifurcation parameter(s). Bifurcations can be local or global, where a local bifurcation is found by linearising about an equilibrium point of the dynamical system and occurs if the real part of at least one of eigenvalues of the Jacobian matrix of $\boldsymbol{F}$ vanishes at this point. The nature of the bifurcation depends on the value of the imaginary part of this eigenvalue [5, 141].

Local bifurcations thus describe how the stability of an equilibrium point changes under variations of the bifurcation parameter, since the real part of the eigenvalues of the Jacobian describe the growth rate of infinitesimal perturbations about the equilibrium point. If the real part of at least one eigenvalue is positive, the perturbations grow exponentially and the equilibrium point is linearly unstable. If none of the eigenvalues has a positive real part and at least one has a vanishing real part, then the stability of the equilibrium point cannot be assessed by this method and nonlinear terms have to be taken into account [5, 141]. The localness is inherent in this definition, since due to the linearisation only a small neighbourhood around the equilibrium point is considered. Global bifurcations are defined as changes in the topological structure of phase-space trajectories which do not only affect a small neighbourhood around an equilibrium point. They occur if invariant sets intersect with each other or with an equilibrium point in phase space [5, 141, 188], as such they cannot be captured by a linear stability analysis of equilibrium points.

In fluid dynamics, the state space M of a system consists of all possible flow states given by exact solutions of the evolution equations under consideration, and the properties of these flow states may change with variations in the Reynolds number. The stability of a given flow state is thus investigated with respect to the Reynolds number as the bifurcation parameter [59], and the linear stability of a given laminar profile is of interest to transition to turbulence. Many systems exhibit linear instabilities above a critical Reynolds number, such as plane Poiseuille flow, Rayleigh-Bénard convection or Taylor-Couette flow [59]. The occurrence of a linear instability is often connected to inflection points in the

laminar profile. For a flow with a linear instability of the laminar profile, above the critical Reynolds number the laminar profile disappears and gives rise to other flow states with their own stability properties. For these flows the transition to turbulence occurs through a series of bifurcations starting with the linearly unstable laminar profile. This scenario is called a *supercritical transition*.

There are also many flows where the laminar profile is linearly stable at all (finite) Reynolds numbers and nevertheless the flows become turbulent with increasing Reynolds number, such as in pipe and plane Couette flow, or the flow becomes turbulent at Reynolds numbers below the critical threshold, such as for plane Poiseuille flow. In this case other stationary flow states in the state space exist alongside the laminar profile below the critical Reynolds number for linear instability. These additional states are usually created in saddle-node bifurcations and as such have stable and unstable directions. A finite-amplitude perturbation can destabilise the laminar state by pushing it in the vicinity of one of these (saddle) states. Since this occurs at Reynolds numbers below the critical threshold for a linear instability, the transition has been named *subcritical*. It also occurs if the base flow is linearly stable at all Reynolds numbers, in which case the scenario is also referred to as a *bifurcation from infinity* [138, 156].

The prime examples of a subcritical transition to turbulence are pipe and plane Couette flow. In pipe flow these coexisting unstable flow states have been identified as travelling waves with different symmetries [69, 184, 185]. In both cases, a finite-amplitude perturbation develops into a localised turbulent patch (a *puff* in pipe flow or a *spot* in plane Couette flow) which exists as an independent entity [8, 52, 61, 62, 85, 124, 139, 162]. Experiments [7, 86] and numerical simulations [9, 70, 161] have shown that the localised patches of turbulence can spontaneously disappear (relaminarise), that is, turbulent dynamics can suddenly collapse to a much simpler, typically linearly stable, laminar state like the Hagen-Poiseuille profile in pipe flow [59] for example.

Relaminarisation events show that laminar and turbulent states coexist in the state space of the system and that a sudden escape from the turbulent region of the state space is possible. In other words, the boundary between the turbulent and laminar regions of the state space must be somewhat permeable. This has been explained with a pinball-type state space dynamics of the turbulent state, by which the flow state is attracted and repelled by the many exact stationary saddle states, until it eventually escapes into the laminar region of the state space [66, 82]. That is, the turbulent region of phase space is a *non-attracting chaotic*

set [141] and the probability to escape from this region does not depend on the amount of time the system has spent in the turbulent region of the state space. This implies that the probability of escape after time t, $P(t)$, is exponential

$$P(t) \sim \exp\left(t/\tau\right) , \tag{1.18}$$

where τ is the mean time spent in the turbulent state. This exponential law for the survival probability of localised turbulence has been confirmed in many experiments and numerical simulations of pipe [7, 9, 66, 84, 86] and plane Couette flow [24, 161, 164]. The characteristic timescale τ depends on the Reynolds number and this dependence is connected to the transition to sustained turbulence in wall-bounded shear flows. This will be discussed in further detail in chapter 6.

The dynamical systems approach to turbulence is not only concerned with transitional flows. An active area of research consists of investigations of the structure of *attractors* of the system, and this includes high Reynolds number flows. Since the dynamical system under consideration is dissipative, it has attractors [141], which are bounded volumes in phase-space populated by the asymptotes of a subset of possible initial conditions. These phase-space structures may be of multifractal nature in high Reynolds number turbulent flows [72].

1.3.2 The statistical approach to turbulence

In the statistical approach to turbulence the velocity field is taken to be a random function $\boldsymbol{u}$ of space and time and the aim is to extract information about the statistical properties of $\boldsymbol{u}$ by studying a large ensemble of realisations of the random variable $\boldsymbol{u}$. A realisation of $\boldsymbol{u}$ is then given by the instantaneous velocity field $\boldsymbol{u}(\boldsymbol{x}, t)$ at a specific space-time point $(\boldsymbol{x}, t)$. In the statistical approach to MHD turbulence both the magnetic and the velocity field are interpreted in a statistical sense.

The ensemble average of any quantity $F(\boldsymbol{u}_1, \ldots, \boldsymbol{u}_n, t)$ which depends on the instantaneous velocity fields is then given by

$$\langle F \rangle = \int_{\mathbb{R}^3} d\boldsymbol{x}_1 \ldots d\boldsymbol{x}_n F(\boldsymbol{u}_1, \ldots, \boldsymbol{u}_n, \boldsymbol{x}_1, \ldots \boldsymbol{x}_n, t) p(\boldsymbol{u}_1, \ldots, \boldsymbol{u}_n, \boldsymbol{x}_1, \ldots \boldsymbol{x}_n, t) , \tag{1.19}$$

where $p(\boldsymbol{u}_1, \ldots, \boldsymbol{u}_n, \boldsymbol{x}_1, \ldots \boldsymbol{x}_n, t)$ is the joint probability density function describing the probability that $\boldsymbol{u}(\boldsymbol{x}_i, t)$ takes a value in the infinitesimal range $\boldsymbol{u}_i + d\boldsymbol{u}_i$.

In order to calculate the ensemble average p must be known, which is a main difficulty in the statistical theory of turbulence. Furthermore, this method of averaging does not correspond to most measurement techniques where a probe (e.g. a hot wire) is located at a particular point in space and measurements are taken at different times. To circumvent this problem, the ergodic hypothesis is often invoked, by which space, time and ensemble averages are regarded as equivalent. However, this is not applicable to decaying turbulence and furthermore there is no proof of whether even sustained turbulence satisfies all necessary requirements for ergodicity. A further discussion of ergodicity in the context of the statistical approach to turbulence can be found in the book by Frisch [72]. In this thesis all averages are ensemble averages unless otherwise stated.

Statistical symmetries

The concept of homogeneous isotropic turbulence was introduced in 1935 by Taylor [174] as a simplified concept facilitating the theoretical study of turbulent flows in the framework of a statistical theory of turbulence as initiated by Osborne Reynolds. Reynolds split the velocity field into a mean and a randomly fluctuating part,

$$\boldsymbol{U} = \langle \boldsymbol{U} \rangle + \boldsymbol{u} \ , \tag{1.20}$$

where the lower case letter refer to the fluctuations about the mean, hence $\langle \boldsymbol{u} \rangle = 0$. An analogous decomposition can be written down for the magnetic field

$$\boldsymbol{B} = \langle \boldsymbol{B} \rangle + \boldsymbol{b} \ , \tag{1.21}$$

with $\langle \boldsymbol{b} \rangle = 0$. In this statistical framework homogeneous isotropic turbulence is defined by requiring the probability density function of the (turbulent) fluctuations $\boldsymbol{u}$ and $\boldsymbol{b}$ to be independent of position (homogeneity) and direction (isotropy) [11, 72, 135]. In other words, the probability density function shall be invariant under translations and rotations:

- **Homogeneity**: Invariance of the probability density function under spatial translations.

- **Isotropy**: Invariance of the probability density function under rotations and reflections. In mathematical terms, invariance under $O(3)$-transformations. With this definition, statistically isotropic turbulence is also mirror-symmetric.

- **Isotropy without mirror-symmetry**: Invariance of the probability density function under rotations but not under reflections, that is, invariance under $SO(3)$-transformations.

The notion of isotropy in this thesis refers to the latter definition, the reason for this is discussed in connection with topological invariants in sec. 1.3.3.

Real-world flows do not satisfy these properties, since the presence of boundaries precludes homogeneity while a mean flow direction violates isotropy. However, chaotic flows of liquids or gases far away from any boundary, like many atmospheric and oceanic flows, are often viewed by scientists as real-life realisations of homogeneous isotropic turbulence. This leads to the concept of local homogeneity and local isotropy [97, 135], implying that the concept of homogeneous isotropic turbulence is relevant to turbulent dynamics in high Reynolds number real-world flows at scales small enough compared to the system size [119]. Homogeneous isotropic turbulence can therefore be viewed as an attempt to reduce the external complexity of the problem in order to study the fundamental properties of turbulent flows.

Isotropic turbulence has been realised to a good approximation in the laboratory by wind tunnel experiments, where the anisotropy connected to the existence of a mean flow is circumvented by the use of coordinates moving with the mean flow [78, 179]. That is, the streamwise distance is translated into a timescale and the experiments are able to test predictions on decaying isotropic turbulence. An overview is given in the book by Sagaut [157] on p. 52, table 3.1.

The simplest case to study analytically is statistically stationary isotropic turbulence, however, no consensus has been reached on the experimental realisation of sustained isotropic turbulence. A globally decaying flow may locally be approximately stationary, but this restricts the observation times significantly and may introduce additional errors in the measurements [135]. Sustained isotropic turbulence is therefore mainly studied by DNS in order to refine the phenomenology and to test theoretical models and predictions (for a non-exhaustive list see Ref. [157], p. 52, table 3.2), where the emphasis is on

achieving high Reynolds numbers.

For the velocity field the presence of a mean flow does not pose serious problems, as $\langle \boldsymbol{U} \rangle = \boldsymbol{0}$ can be achieved by a Galilean transformation into coordinates that move with the mean flow. This is not possible for the magnetic field, therefore in MHD turbulence it must be distinguished whether a non-zero mean background field $\boldsymbol{B}_0 = \langle \boldsymbol{B} \rangle$ is present. In most physical situations (such as in solar physics) this is the case. However, again, in order to treat the simpler problem first many theoretical efforts in MHD turbulence start with case $\boldsymbol{B}_0 = 0$. In the remainder of this thesis $\boldsymbol{B}_0 = 0$ unless otherwise stated.

Correlation tensors

As in any statistical theory, correlations of the random variables are of paramount importance. In MHD turbulence, the two-point second-order correlation tensors are defined as

$$C_{ij}^{uu}(\boldsymbol{x}, \boldsymbol{x}', t) = \langle u_i(\boldsymbol{x}, t) u_j(\boldsymbol{x}', t) \rangle \ , \tag{1.22}$$

$$C_{ij}^{bb}(\boldsymbol{x}, \boldsymbol{x}', t) = \langle b_i(\boldsymbol{x}, t) b_j(\boldsymbol{x}', t) \rangle \ , \tag{1.23}$$

$$C_{ij}^{ub}(\boldsymbol{x}, \boldsymbol{x}', t) = \langle u_i(\boldsymbol{x}, t) b_j(\boldsymbol{x}', t) \rangle \ . \tag{1.24}$$

The two-point third-order correlation tensors are defined similarly

$$C_{ij,k}^{uuu}(\boldsymbol{x}, \boldsymbol{x}', t) = \langle u_i(\boldsymbol{x}, t) u_j(\boldsymbol{x}), t) u_k(\boldsymbol{x}', t) \rangle \ , \tag{1.25}$$

$$C_{ij,k}^{bbu}(\boldsymbol{x}, \boldsymbol{x}', t) = \langle b_i(\boldsymbol{x}, t) b_j(\boldsymbol{x}), t) u_k(\boldsymbol{x}', t) \rangle \ , \tag{1.26}$$

$$C_{ij,k}^{bub}(\boldsymbol{x}, \boldsymbol{x}', t) = \langle [u_i(\boldsymbol{x}, t) b_j(\boldsymbol{x}, t) - b_i(\boldsymbol{x}, t) u_j(\boldsymbol{x}, t)] b_k(\boldsymbol{x}', t) \rangle \ . \tag{1.27}$$

For homogeneous random vector fields their joint probability density function is invariant under spatial translations, and this carries over to the correlators. Therefore, the two-point correlators only depend on the displacement $\boldsymbol{r} = \boldsymbol{x} - \boldsymbol{x}'$ and not on the individual points $\boldsymbol{x}$ and $\boldsymbol{x}'$.

Statistical isotropy and solenoidality of the vector fields further restrict the form of the two-point correlation tensors [11, 31, 154], which can be expressed through

the longitudinal correlation functions

$$C_{LL}^{bb}(r,t) = \langle b_L(\boldsymbol{x},t) b_L(\boldsymbol{x}+\boldsymbol{r},t)\rangle, \tag{1.28}$$

$$C_{LL}^{uu}(r,t) = \langle b_L(\boldsymbol{x}), t b_L(\boldsymbol{x}+\boldsymbol{r},t)\rangle, \tag{1.29}$$

$$C_{LLL}^{uuu}(r,t) = \langle u_L(\boldsymbol{x},t) u_L(\boldsymbol{x},t) u_L(\boldsymbol{x}+\boldsymbol{r},t)\rangle \ , \tag{1.30}$$

$$C_{LLL}^{bbu}(r,t) = \langle u_L(\boldsymbol{x},t) b_L(\boldsymbol{x},t) b_L(\boldsymbol{x}+\boldsymbol{r},t)\rangle \ , \tag{1.31}$$

where $r = |\boldsymbol{r}|$ and $v_L = \boldsymbol{v}\cdot\boldsymbol{r}/r$ denotes the longitudinal component of a vector field $\boldsymbol{v}$, that is its component parallel to the displacement vector $\boldsymbol{r}$, and

$$\delta_L v(r) = [\boldsymbol{v}(\boldsymbol{x}+\boldsymbol{r}) - \boldsymbol{v}(\boldsymbol{x})]\cdot\frac{\boldsymbol{r}}{r} \ , \tag{1.32}$$

its longitudinal increment. In terms of the longitudinal correlators, the second order correlation tensors are given by

$$C_{ij}^{uu}(\boldsymbol{r},t) = \left(C_{LL}^{uu}(r,t) - \frac{\partial_r}{2r}\big(C_{LL}^{uu}(r,t)\big)\right)\frac{r_i r_j}{r^2} + -\frac{\partial_r}{2r}\big(C_{LL}^{uu}(r,t)\big)\delta_{ij} \ , \tag{1.33}$$

$$C_{ij}^{bb}(\boldsymbol{r},t) = \left(C_{LL}^{bb}(r,t) - \frac{\partial_r}{2r}\big(C_{LL}^{bb}(r,t)\big)\right)\frac{r_i r_j}{r^2} + -\frac{\partial_r}{2r}\big(C_{LL}^{bb}(r,t)\big)\delta_{ij} \ , \tag{1.34}$$

$$C_{ij}^{ub}(\boldsymbol{r},t) = C^{ub}(r,t)\epsilon_{ijk}\frac{r_k}{r} \ , \tag{1.35}$$

where δ_{ij} denotes the Kronecker delta and ϵ_{ijk} the totally antisymmetric Levi-Civita tensor. For the third-order tensors one obtains

$$\begin{aligned} C_{ij,k}^{uuu}(\boldsymbol{r},t) = {} & \frac{\partial_r}{4r^2}\left(r^2 C_{LLL}^{uuu}(r,t)\right)\left(\delta_{jk}\frac{r_i}{r} + \delta_{ik}\frac{r_j}{r}\right) - r^2\partial_r\left(\frac{C_{LLL}^{uuu}(r,t)}{2r}\right)\frac{r_i r_j r_k}{r^3} \\ & - C_{LLL}^{uuu}(r,t)\delta_{ij}\frac{r_k}{2r} \ , \end{aligned} \tag{1.36}$$

$$\begin{aligned} C_{ij,k}^{bbu}(\boldsymbol{r},t) = {} & \frac{\partial_r}{4r^2}\left(r^2 C_{LLL}^{bbu}(r,t)\right)\left(\delta_{jk}\frac{r_i}{r} + \delta_{ik}\frac{r_j}{r}\right) - r^2\partial_r\left(\frac{C_{LLL}^{bbu}(r,t)}{2r}\right)\frac{r_i r_j r_k}{r^3} \\ & - C_{LLL}^{bbu}(r,t)\delta_{ij}\frac{r_k}{2r} \ , \end{aligned} \tag{1.37}$$

$$C_{ij,k}^{bub}(\boldsymbol{r},t) = C^{bub}(r,t)\left(\frac{r_j}{r}\delta_{ik} - \frac{r_i}{r}\delta_{jk}\right). \tag{1.38}$$

Since the time evolution of the correlation tensors is determined by the longitudinal correlation functions and the correlation functions $C^{ub}(r,t)$ and $C^{bub}(r,t)$, the statistical information about the turbulent dynamics is encoded in these functions. The second and third-order correlation functions are related to each other through the so-called von Kármán-Howarth equation (vKHE), which is derived by writing the momentum equation (1.5) and the induction equation

(1.6) in component form, multiplying by the appropriate field components and averaging. This results in the following energy balance equation, here stated for MHD[7] in the case of free decay [31]

$$-\partial_t E(t) = -\partial_t (B_{LL}^{uu} + B_{LL}^{bb}) + \frac{3}{2r^4}\partial_r \left(\frac{r^4}{6} B_{LLL}^{uuu} + r^4 C_{LLL}^{bbu} \right) + \frac{6}{r} C^{bub} + \frac{1}{r^4}\partial_r \left(r^4 \partial_r (\nu B_{LL}^{uu} + \eta B_{LL}^{bb}) \right) \ , \tag{1.39}$$

where $E(t)$ denotes the total energy per unit volume. The terms B_{LL}^{uu}, B_{LL}^{bb} and B_{LLL}^{uuu} are the second and third-order longitudinal *structure functions*, defined as

$$B_{LL}^{uu}(r,t) = \langle (\delta u_L(\boldsymbol{r},t))^2 \rangle = \frac{2}{3} E_{kin}(t) - 2C_{LL}^{uu}(r,t) \ , \tag{1.40}$$

$$B_{LL}^{bb}(r,t) = \langle (\delta b_L(\boldsymbol{r},t))^2 \rangle = \frac{2}{3} E_{mag}(t) - 2C_{LL}^{bb}(r,t) \ , \tag{1.41}$$

$$B_{LLL}^{uuu}(r,t) = \langle (\delta u_L(\boldsymbol{r},t))^3 \rangle = 6C_{LLL}^{uuu}(r,t) \ , \tag{1.42}$$

where homogeneity and isotropy have been used to determine their relations to the longitudinal correlation functions.

Equation (1.39) and its equivalent for non-conducting fluids are some of the rare exact equations in the statistical approach to turbulence. However, the vKHE is not a closed equation. The time-evolution of the second-order moments depends on the third-order moments, and by a similar argument an equation can be derived relating the time-evolution of the third-order moment to the fourth-order moment and so forth. Again, the main problem in the statistical approach arises, that is the lack of information about the probability density function (pdf) and as such about its moments. If there were a closure to the hierarchy of moment equations, then the pdf could be determined. Much effort has therefore been made in the past in order to derive a statistical theory of turbulence which solves the closure problem, such as Kraichnan's Direct Interaction Approximation (DIA) [99, 100], the Eddy-Damped Quasi-Normal Markovian closure (EDQNM) [110] and McComb's Local Energy Transfer (LET) [120]. However, the problem is still unsolved despite the advances which these approaches represent. Furthermore, there are features of turbulent flows that escape closure theory, such as the description of regions with weak nonlinearity. A critical discussion of this point can be found in the book by Frisch [72].

The second-order longitudinal correlation functions can be used to define

[7]The corresponding equation for a turbulent non-conducting fluid follows by setting $\boldsymbol{b} = 0$.

characteristic length scales of the system. The *integral scales* are defined as

$$L_u(t) = \frac{1}{U^2} \int_0^\infty C_{LL}^{uu}(r,t)dr \ , \tag{1.43}$$

$$L_b(t) = \frac{1}{B^2} \int_0^\infty C_{LL}^{bb}(r,t)dr \ , \tag{1.44}$$

and describe the correlation of fluctuations at the large scales. A second characteristic length scale is the *Taylor microscale* [174], which is defined by the limit $r \to 0$ of the second-order spatial derivative of the second-order longitudinal correlation function. This definition can be shown [11] to simplify to

$$\lambda_u = \sqrt{\frac{15\nu U(t)^2}{\varepsilon_{kin}(t)}} \ , \tag{1.45}$$

where $\varepsilon_{kin}(t)$ is the rate of dissipation of kinetic energy. The Taylor microscale λ_b for the magnetic field is defined analogously.

Fourier representation

The requirement of statistical homogeneity permits the random fields to be viewed *at any given instant in time* as stationary random processes in space. That is, results from the theory of stationary random processes can be carried over to homogeneous turbulence, such as the Wiener-Khintchine theorem. This theorem asserts that the autocorrelation function of a stationary random process has a spectral decomposition. In other words, it is given as the Fourier transform of a monotone function, and the important point is that this is true without the stationary random process itself having a Fourier transfrom. In general, stationary random processes do not satisfy the requirements for the existence of a Fourier transform, that is they are not absolutely integrable or square-integrable. This can be understood by considering homogeneous turbulence on the infinite domain $\mathbb{R}^3$. For the random fields $\boldsymbol{u}(\boldsymbol{x},t)$ and $\boldsymbol{b}(\boldsymbol{x},t)$ to be square-integrable (i.e. $L^2(\mathbb{R})^3$) or absolutely integrable (i.e. $L^1(\mathbb{R})^3$), at any time they must decrease sufficiently rapidly for $|\boldsymbol{x}| \to \infty$, thus violating homogeneity.

Generalising the Wiener-Khintchine theorem to multidimensional stationary random processes, Cramér [46] and independently Kolmogorov [96] showed that the correlation tensor $C_{jl}(\boldsymbol{r})$ of a multidimensional stationary random process can

be expressed as the Fourier transform of a tensor in wavenumber space, namely

$$C_{jl}(\boldsymbol{r},t) = \int_{\mathbb{R}^3} dF_{jl}(\boldsymbol{k},t)\ e^{i\boldsymbol{k}\cdot\boldsymbol{r}}\ , \tag{1.46}$$

where $F_{jl}(\boldsymbol{k},t)$ is a complex tensor of finite total variation and the integral a Fourier-Stieltjes integral. If $F_{jl}(\boldsymbol{k},t)$ is differentiable or in other words if a continuous tensor $\hat{C}_{jl}(\boldsymbol{k},t)$ exists such that

$$dF_{jl}(\boldsymbol{k},t) = \hat{C}_{jl}(\boldsymbol{k},t)\ d\boldsymbol{k}\ , \tag{1.47}$$

then the above integral is a Lebesgue (or Riemann) integral. According to Batchelor [11] (footnote on p. 25) the continuity of $\hat{C}_{jl}(\boldsymbol{k},t)$ can be safely assumed as the nonlinear process would smooth out any discontinuity very quickly. From a purely mathematical point of view there is no proof of the continuity of $\hat{C}_{jl}(\boldsymbol{k},t)$. However, conforming with practice in the field it is assumed throughout the following work that the spectral correlation tensors are continuous. That is, there are continuous tensors $\hat{C}^{uu}_{ij}(\boldsymbol{k},t)$ and $\hat{C}^{bb}_{ij}(\boldsymbol{k},t)$ such that

$$C^{uu}_{ij}(\boldsymbol{r},t) = \int_{\mathbb{R}^3} d\boldsymbol{k}\ \hat{C}^{uu}_{ij}(\boldsymbol{k},t)e^{i\boldsymbol{k}\cdot\boldsymbol{r}}\ , \tag{1.48}$$

$$C^{bb}_{ij}(\boldsymbol{r},t) = \int_{\mathbb{R}^3} d\boldsymbol{k}\ \hat{C}^{bb}_{ij}(\boldsymbol{k},t)e^{i\boldsymbol{k}\cdot\boldsymbol{r}}\ . \tag{1.49}$$

The use of the Fourier representation of the magnetic and velocity fields is justified if the random fields are considered on a periodic domain $\Omega = [0,L]^3 \subset \mathbb{R}^3$ such that

$$\boldsymbol{u}(\boldsymbol{x},t) = \sum_{\boldsymbol{k}} \hat{\boldsymbol{u}}(\boldsymbol{k},t)e^{i\boldsymbol{k}\cdot\boldsymbol{x}} \ \text{ with } \ \hat{\boldsymbol{u}}(\boldsymbol{k},t) = \frac{1}{L^3}\int_{\Omega} d\boldsymbol{x}\ \boldsymbol{u}(\boldsymbol{x},t)e^{-i\boldsymbol{k}\cdot\boldsymbol{x}}\ , \tag{1.50}$$

and similarly for the magnetic field. Since the magnetic and velocity fields are real functions, their Fourier transforms must obey Hermitian symmetry

$$\hat{\boldsymbol{u}}(-\boldsymbol{k},t) = \hat{\boldsymbol{u}}^*(\boldsymbol{k},t) \ \text{ and } \ \hat{\boldsymbol{b}}(-\boldsymbol{k},t) = \hat{\boldsymbol{b}}^*(\boldsymbol{k},t)\ , \tag{1.51}$$

where $*$ denotes the complex conjugate. Now the correlators of the discrete Fourier-transformed homogeneous random fields can be calculated. For this purpose, let $\boldsymbol{A}$ and $\boldsymbol{C}$ be general homogeneous random vector fields defined on the periodic domain Ω, which can represent $\boldsymbol{b}$ and $\boldsymbol{u}$ as appropriate. The

second-order correlation tensor is

$$\begin{aligned}\langle \hat{A}_i(\boldsymbol{k},t)\hat{C}_j(\boldsymbol{k}',t)\rangle &= \frac{1}{L^6}\int_\Omega d\boldsymbol{x}\int_\Omega d\boldsymbol{x}'\ \langle A_i(\boldsymbol{x},t)C_j(\boldsymbol{x}',t)\rangle e^{-i(\boldsymbol{k}\cdot\boldsymbol{x}+\boldsymbol{k}'\cdot\boldsymbol{x}')}\\ &= \frac{1}{L^6}\int_\Omega d\boldsymbol{x}\int_\Omega d\boldsymbol{r}\ C_{ij}^{AC}(\boldsymbol{r},t)e^{-i(\boldsymbol{k}+\boldsymbol{k}')\cdot\boldsymbol{x}}e^{-i\boldsymbol{k}'\cdot\boldsymbol{r}}\\ &= \delta(\boldsymbol{k}+\boldsymbol{k}')\frac{1}{L^3}\int_\Omega d\boldsymbol{r}\ C_{ij}^{AC}(\boldsymbol{r},t)e^{-i\boldsymbol{k}'\cdot\boldsymbol{r}}\\ &= \delta(\boldsymbol{k}+\boldsymbol{k}')\hat{C}_{ij}^{AC}(\boldsymbol{k},\boldsymbol{k}',t) = \hat{C}_{ij}^{AC}(\boldsymbol{k},t)\ , \end{aligned} \tag{1.52}$$

that is, homogeneity induces unimodal coupling between the different Fourier modes for the second-order correlator [119]. The Fourier transform of the third-order correlator for three homogeneous random vector fields $\boldsymbol{A}$, $\boldsymbol{C}$ and $\boldsymbol{D}$ is

$$\langle \hat{A}_i(\boldsymbol{k})\hat{C}_j(\boldsymbol{p})\hat{D}_k(\boldsymbol{q})\rangle = \left(\frac{1}{L}\right)^9\int_\Omega\int_\Omega\int_\Omega d\boldsymbol{x}\ d\boldsymbol{x}'\ d\boldsymbol{x}''\langle A_i(\boldsymbol{x})C_j(\boldsymbol{x}')D_k(\boldsymbol{x}'')\rangle \tag{1.53}$$

$$\times\, e^{-i(\boldsymbol{k}\cdot\boldsymbol{x}+\boldsymbol{p}\cdot\boldsymbol{x}'+\boldsymbol{q}\cdot\boldsymbol{x}'')}\ , \tag{1.54}$$

where the term in the angled brackets on the right-hand side is the real-space correlation tensor C_{ijk} of the three fields. Since the fields are homogeneous, the real-space correlator only depends on the displacements $\boldsymbol{r} = \boldsymbol{x}-\boldsymbol{x}'$ and $\boldsymbol{r}' = \boldsymbol{x}-\boldsymbol{x}''$ and as such is independent of $\boldsymbol{x}$

$$\langle A_i(\boldsymbol{x})C_j(\boldsymbol{x}')D_k(\boldsymbol{x}'')\rangle = C_{ijk}(\boldsymbol{r},\boldsymbol{r}')\ . \tag{1.55}$$

The integration over $\boldsymbol{x}$ then results in a three-dimensional δ-distribution imposing the condition that the triple correlation in Fourier space is nonzero only when the wavevectors form a triad, i.e.

$$\langle \hat{A}_i(\boldsymbol{k})\hat{C}_j(\boldsymbol{p})\hat{D}_k(\boldsymbol{q})\rangle = \delta^3(\boldsymbol{k}+\boldsymbol{p}+\boldsymbol{q})\left(\frac{1}{L}\right)^6\int_\Omega\int_\Omega d\boldsymbol{r}\ d\boldsymbol{r}'\ C_{ijk}(\boldsymbol{r},\boldsymbol{r}')e^{-i(\boldsymbol{p}\cdot\boldsymbol{r}+\boldsymbol{q}\cdot\boldsymbol{r}')}\ . \tag{1.56}$$

Since the fields $\boldsymbol{A}$, $\boldsymbol{C}$ and $\boldsymbol{D}$ were arbitrary homogeneous random fields (defined on the periodic domain Ω), this result holds for any combination of triple correlations of the magnetic and velocity fields in homogeneous MHD turbulence. That is, homogeneity induces triadic coupling between the different Fourier modes for the third-order correlator [119].

In order to obtain the continuous Fourier transforms of the random variable $\boldsymbol{u}$ and $\boldsymbol{b}$ usually the limit $L\to\infty$ is taken [72, 119]. However, this limit

procedure is problematic [177] due to exchanges in the order of two limits which may not be well defined[8]. In short, the use of Fourier transforms for the individual fields in homogeneous turbulence on the infinite domain $\mathbb{R}^3$ is mathematically not rigorous. This problem may be circumvented by considering the continuous Fourier-representation only for the correlation tensors for which it can be rigorously established[9]. This is the view taken here, and any occurrence of a continuous Fourier-representation of $\boldsymbol{u}$ and $\boldsymbol{b}$ should be viewed as a purely formal expression, written down in order to facilitate a more direct access to the relation of certain spectral quantities with the random fields $\boldsymbol{u}$ and $\boldsymbol{b}$.

The angle-integrated traces of the spectral autocorrelators are the kinetic and magnetic *energy spectra*

$$E_{kin}(k,t) = \frac{1}{2}\int_{|\boldsymbol{k}|=k} d\boldsymbol{k}\ \hat{C}_{ii}^{uu}(\boldsymbol{k},t) = \frac{1}{2}\int_{|\boldsymbol{k}|=k} d\boldsymbol{k}\ \langle|\hat{\boldsymbol{u}}(\boldsymbol{k},t)|^2\rangle\ , \tag{1.57}$$

$$E_{mag}(k,t) = \frac{1}{2}\int_{|\boldsymbol{k}|=k} d\boldsymbol{k}\ \hat{C}_{ii}^{bb}(\boldsymbol{k},t) = \frac{1}{2}\int_{|\boldsymbol{k}|=k} d\boldsymbol{k}\ \langle|\hat{\boldsymbol{b}}(\boldsymbol{k},t)|^2\rangle\ , \tag{1.58}$$

where a sum over repeated indices is implied. The kinetic energy (per unit volume) is then given by

$$\begin{aligned} E_{kin}(t) &= \int_0^\infty dk\ E_{kin}(k,t) = \frac{1}{2}\int_0^\infty dk \int_{|\boldsymbol{k}|=k} d\boldsymbol{k}\ \langle|\hat{\boldsymbol{u}}(\boldsymbol{k},t)|^2\rangle \\ &= \frac{1}{2}\int_{\mathbb{R}^3} d\boldsymbol{k}\ \langle|\hat{\boldsymbol{u}}(\boldsymbol{k},t)|^2\rangle\ , \qquad (1.59) \\ &= \langle|\boldsymbol{u}(\boldsymbol{x},t)|^2\rangle\ . \qquad (1.60) \end{aligned}$$

The analogous equation holds for the magnetic energy (per unit volume)

$$E_{mag}(t) = \int_0^\infty dk\ E_{mag}(k,t) = \frac{1}{2}\int_{\mathbb{R}^3} d\boldsymbol{k}\ \langle|\hat{\boldsymbol{b}}(\boldsymbol{k},t)|^2\rangle = \langle|\boldsymbol{b}(\boldsymbol{x},t)|^2\rangle\ . \tag{1.61}$$

Spectral energy transfer and turbulent cascades

The energy balance as expressed through the vKHE (1.39) can also be stated in the Fourier representation. By taking the inner product of the MHD equations in the Fourier representation with the appropriate fields and ensemble averaging,

[8] For a discussion of this point, see Ref. [177], p. 433.
[9] Except for the continuity of the spectral tensor.

one obtains evolution equations for the magnetic and kinetic energy spectra

$$\partial_t E_{mag}(k,t) = T_{mag}(k,t) - 2\eta k^2 E_{mag}(k,t) + W_{mag}(k,t) \ , \tag{1.62}$$

$$\partial_t E_{kin}(k,t) = T_{kin}(k,t) + T_{LF}(k,t) - 2\nu k^2 E_{kin}(k,t) + W_{kin}(k,t) \ , \tag{1.63}$$

where $W_{mag}(k,t)$ and $W_{kin}(k,t)$ denote the contributions from the external forces

$$W_{mag}(k,t) = \int_{|\boldsymbol{k}|=k} d\boldsymbol{k} \ \langle \hat{\boldsymbol{b}}(\boldsymbol{k},t) \cdot \hat{\boldsymbol{f}}_b(-\boldsymbol{k},t) \rangle \ , \tag{1.64}$$

$$W_{kin}(k,t) = \int_{|\boldsymbol{k}|=k} d\boldsymbol{k} \ \langle \hat{\boldsymbol{u}}(\boldsymbol{k},t) \cdot \hat{\boldsymbol{f}}_u(-\boldsymbol{k},t) \rangle \ , \tag{1.65}$$

and the transfer terms, which originate from the inertial, Lorentz force and induction terms in the MHD equations, are given by

$$T_{HD}(k,t) = \int_{|\boldsymbol{k}|=k} d\boldsymbol{k} \int_{\mathbb{R}^3} d\boldsymbol{p} \\ \times \langle \hat{\boldsymbol{u}}(-\boldsymbol{k},t) \cdot [\hat{\boldsymbol{u}}(\boldsymbol{p},t) \times (i(\boldsymbol{k}-\boldsymbol{p}) \times \hat{\boldsymbol{u}}(\boldsymbol{k}-\boldsymbol{p},t))] \rangle \ , \tag{1.66}$$

$$T_{LF}(k,t) = -\int_{|\boldsymbol{k}|=k} d\boldsymbol{k} \int_{\mathbb{R}^3} d\boldsymbol{p} \\ \times \langle \hat{\boldsymbol{u}}(-\boldsymbol{k},t) \cdot [\hat{\boldsymbol{b}}(\boldsymbol{p},t) \times (i(\boldsymbol{k}-\boldsymbol{p}) \times \hat{\boldsymbol{b}}(\boldsymbol{k}-\boldsymbol{p},t))] \rangle \ , \tag{1.67}$$

and

$$T_{mag}(k,t) = \int_{|\boldsymbol{k}|=k} d\boldsymbol{k} \ \int_{\mathbb{R}^3} d\boldsymbol{p} \ \langle \hat{\boldsymbol{b}}(-\boldsymbol{k},t) \cdot [i\boldsymbol{k} \times (\hat{\boldsymbol{u}}(\boldsymbol{p},t) \times \hat{\boldsymbol{b}}(\boldsymbol{k}-\boldsymbol{p},t))] \rangle \ . \tag{1.68}$$

The term $T_{HD}(k,t)$ distributes kinetic energy between the Fourier modes due to the coupling of the velocity field to itself, $T_{LF}(k,t)$ converts magnetic to kinetic energy due to the Lorentz force acting on the fluid, while the redistribution of energy due to advection of the magnetic field by the flow and conversion of kinetic to magnetic energy, that is, due to dynamo action, are contained in $T_{mag}(k,t)$. The splitting of $\nabla \times (\boldsymbol{u} \times \boldsymbol{b})$ into an advective term $(\boldsymbol{u} \cdot \nabla)\boldsymbol{b}$ and a dynamo term $(\boldsymbol{b} \cdot \nabla)\boldsymbol{u}$, is somewhat obscured in Fourier space.

The evolution equation of the total energy spectrum $E(k,t) = E_{mag}(k,t) + E_{kin}(k,t)$ is given as the sum of eqs. (1.62) and (1.63)

$$\partial_t E(k,t) = T(k,t) - 2k^2(\eta E_{mag}(k,t) + \nu E_{kin}(k,t)) + W(k,t) \ , \tag{1.69}$$

where $W(k,t) = W_{mag}(k,t) + W_{kin}(k,t)$ is the total energy input per Fourier mode. Since the sum $T(k,t)$ of the individual transfer terms only redistributes the total energy between the different Fourier modes its integral over all wavenumbers must vanish and the rate of change of the total energy per unit volume, $E(t)$, is given by the difference of energy input and dissipation

$$\partial_t E(t) = -\varepsilon(t) + \varepsilon_W(t) \ , \tag{1.70}$$

where $\varepsilon(t) = \varepsilon_{mag}(t) + \varepsilon_{kin}(t)$ denotes the total dissipation rate given by the sum of Ohmic and viscous dissipation

$$\varepsilon_{mag}(t) = 2\eta \int_0^\infty dk \ k^2 E_{mag}(k,t) \ , \tag{1.71}$$

$$\varepsilon_{kin}(t) = 2\nu \int_0^\infty dk \ k^2 E_{kin}(k,t) \ , \tag{1.72}$$

and $\varepsilon_W(t) = \varepsilon_{mag,W}(t) + \varepsilon_{kin,W}(t)$ the total energy input where

$$\varepsilon_{mag,W}(t) = \int_0^\infty dk \ W_{mag}(k,t) \ , \tag{1.73}$$

$$\varepsilon_{kin,W}(t) = \int_0^\infty dk \ W_{kin}(k,t) \ . \tag{1.74}$$

As can be seen from the spectral energy balance equations (1.62), (1.63) and (1.69), the dissipative terms are higher weighted at the large wavenumbers, leading to an energy sink at the small scales and an average transfer of energy from the small wavenumbers to the large wavenumbers. That is, kinetic and magnetic energy injected by some physical process into the magnetofluid at small wavenumbers (large scales) will excite Fourier modes at higher wavenumbers before it is dissipated by Joule and viscous heating. If the magnetic and kinetic Reynolds numbers are high, that is the dissipation coefficients small, dissipative effects are pushed to very large wavenumbers, or equivalently, very small scales. That is, there is a separation between the scales (or wavenumbers) where dissipation becomes important and where energy is injected into the system. In the intermediate, so-called *inertial*, range of wavenumbers which is approximately unaffected by direct energy input and dissipation, energy 'cascades' from lower to higher wavenumbers. In hydrodynamic turbulence this concept of an inertial-range *energy cascade* was introduced by Richardson [153], it implies that in the inertial range the flux of energy through a given wavenumber k, $\Pi(k,t)$, does not depend on k.

Kolmogorov's theory

The perhaps most famous results in the statistical approach to turbulence are Kolmogorov's 1941 phenomenological theory [95, 97] and its refinement in 1962 [98]. Kolmogorov's 1941 theory was based on two hypotheses (or universality assumptions, here paraphrased from Ref. [72]):

1. "At high Reynolds numbers the statistical properties of the small scales are universal. They are only determined by the mean energy dissipation rate ε, the viscosity ν and the length scale l" [72].

2. "In the limit of infinite Reynolds number, the statistical properties of the small scales are universal and only determined by ε and l" [72].

The small scales referred to in these two assumptions are called the *universal equilibrium range*. The two hypotheses imply that the small scales are statistically independent from the large scales where the turbulence is generated. Therefore it should be possible to estimate the characteristic size of the small scales from the parameters they depend on, that is, from the viscosity and the mean energy dissipation rate. From dimensional analysis one obtains the *Kolmogorov scale*

$$\eta_D = \left(\frac{\nu^3}{\varepsilon}\right)^{\frac{1}{4}} \ . \tag{1.75}$$

Similarly, a characteristic velocity scale for the small scales can be derived by dimensional analysis

$$u_D = (\nu\varepsilon)^{\frac{1}{4}} \ , \tag{1.76}$$

and for the associated small-scale Reynolds number one obtains

$$Re_D = \frac{u_D \eta_D}{\nu} = \frac{\left(\frac{\nu^3}{\varepsilon}\nu\varepsilon\right)^{\frac{1}{4}}}{\nu} = 1 \ . \tag{1.77}$$

Since the Reynolds number is viewed as measure of the relative importance of nonlinear interactions to viscous dissipation, $Re_D = 1$ implies that the Kolmogorov microscale gives an estimation of the size of the small scales where nonlinear mixing is balanced by dissipation, that is, of the smallest scales generated by the turbulence before kinetic energy is converted by viscous friction into heat. In MHD there is an additional Kolmogorov scale associated with the smallest magnetic scales generated before magnetic energy is dissipated by Joule

heating. In experiments and numerical simulations it is therefore important that all scales at least down to the Kolmogorov microscale are resolved in order to obtain measurements which accurately represent turbulent dynamics. That is, for experiments using hot wire anemometry the size of the wire must be smaller than the Kolmogorov microscale, while in numerical simulations the grid spacing must be smaller than the Kolmogorov microscale.

Kolmogorov's theory is most known for the prediction of the functional form for the kinetic energy spectrum in the inertial range

$$E_{kin}(k) \sim \varepsilon^{\frac{2}{3}} k^{-\frac{5}{3}} \ , \tag{1.78}$$

which is known as *Kolmogorov's five-thirds law*. The inertial (sub)range is the subrange of scales l of the universal equilibrium range where dissipation is yet unimportant and the dynamics are governed by nonlinear mixing. Therefore, the second hypothesis can be applied to the inertial range and thus the dynamics in this range of scales should be determined only by ε and the length scale $l = 1/k$. It may appear contradictory that the mean energy dissipation should determine the dynamics in the inertial range, which was defined as the range of scales dominated by nonlinear transfer and not by dissipation. However, the amount of energy dissipated at the small scales must equal the amount of energy transferred across the inertial range from the large, energy containing, scales. In this way the dynamics of the inertial range depends on the mean energy transfer rate which must equal the mean energy dissipation rate.

The five-thirds law (eq. (1.78)) is derived by dimensional analysis invoking Kolmogorov's two hypotheses. According to the first hypothesis, the dynamics of the universal equilibrium range only depends on ε, ν and $l = 1/k$, that is, on dimensional grounds the kinetic energy spectrum[10] should be given by

$$E_{kin}(k) \sim \varepsilon^{\frac{1}{4}} \nu^{\frac{5}{4}} f(k\eta_D) \ , \tag{1.79}$$

where $f(k\eta_D)$ is a dimensionless function. For the inertial subrange, this expression must be made independent of the viscosity ν. Assuming power-law form for the dimensionless function $f(k\eta_D) = (k\eta_D)^\alpha$ one obtains

$$E_{kin}(k) \sim \varepsilon^{\frac{1}{4}} \nu^{\frac{5}{4}} k^\alpha \left(\frac{\nu^3}{\varepsilon}\right)^{\frac{\alpha}{4}} = \varepsilon^{\frac{(1-\alpha)}{4}} \nu^{\frac{(5+3\alpha)}{4}} k^\alpha \ , \tag{1.80}$$

[10]Note that $[E(k)] = [U^2][L] = [L^3][T^{-2}]$.

which only becomes independent of ν for $\alpha = -5/3$. Kolmogorov's form of the kinetic energy spectrum has been confirmed in many experiments and numerical simulations (see e.g. [72, 135]) of turbulent flows at high Reynolds number.

MHD cascades

The situation in MHD with respect to inertial-range scaling is more complicated due to the additional degrees of freedom and the possibility of wave solutions of the MHD equations. This led to several different approaches predicting different values for the spectral exponent in the inertial range. The Iroshnikov-Kraichnan (IK) theory is based on the assumption that the small scales are dominated by the Alfvén-effect, that is, the small-scale magnetic fluctations are well approximated as Alfvén wave packets travelling along the field lines of the large(r) scale magnetic field [87, 101]. The characteristic velocity is therefore the Alfvén speed v_A leading to a characteristic timescale, the *Alfvén time*

$$\tau_A = \frac{L}{v_A} \ , \tag{1.81}$$

where L is a characteristic length scale of the system. This leads to a power-law form for the energy spectrum

$$E(k) \sim \varepsilon^{1/2} v_A^{1/2} k^{-3/2} \ . \tag{1.82}$$

The Kolmogorov theory and the IK theory thus predict different scaling laws for the energy spectra in the inertial wavenumber range depending on the chosen interaction timescale, where IK results in a spectral exponent of -1.5, while Kolmogorov scaling predicts the value of $-5/3 \simeq -1.667$.

Although the IK scaling exponent for the energy spectrum is derived from the assumption that MHD turbulence is mainly governed by (many) interactions of Alfvén wave packets, it was originally derived for isotropic turbulence and does not imply the presence of a mean magnetic field. Iroshnikov and Kraichnan argued that the magnetic field fluctuations at larger scale act as guide fields for the smaller scales. For MHD turbulence in the presence of a mean magnetic field Kolmogorov scaling has been predicted by Goldreich and Sridhar [77] for wavenumbers perpendicular to the direction of the background magnetic field.

The different predicted values of the spectral exponent are not only numerically

close and thus difficult to distinguish in measurements, the predictions are model-dependent. To complicate things further, they also depend on the strength of the external field, which highlights one of the difficult aspects of MHD as a multi-parameter problem.

1.3.3 Topological invariants in fluid flows

Supposing dissipation is absent from the system, the first question that may come to mind then concerns possible conserved quantities. For non-conducting fluids the total energy is conserved, as the nonlinear term in the Euler equation only redistributes energy between different scales of motion. In MHD, similarly the total energy is conserved, while kinetic and magnetic energies are not individually conserved, because energy conversion from kinetic to magnetic (dynamo action) and magnetic to kinetic (through the Lorentz force acting on the fluid) takes place.

However, there are more conserved quantities, which are related to the topology of the flow and these conserved quantities have important effects even in dissipative systems. In the case of Euler evolution, this is the *kinetic helicity* [131] of the flow, while in ideal MHD there are two additional ideal invariants, the *magnetic helicity* and the *cross-helicity*. The kinetic helicity is no longer conserved in MHD.

The kinetic helicity $H_{kin}(t)$, the magnetic helicity $H_{mag}(t)$ and the cross-helicity $H_c(t)$ are defined as

$$H_{kin}(t) \equiv \int_\Omega d\boldsymbol{x}\ \boldsymbol{u}(\boldsymbol{x},t)\cdot\boldsymbol{\omega}(\boldsymbol{x},t) = \int_\Omega d\boldsymbol{k}\ \hat{\boldsymbol{u}}(\boldsymbol{k},t)\cdot\hat{\boldsymbol{\omega}}(-\boldsymbol{k},t)\ , \tag{1.83}$$

$$H_{mag}(t) \equiv \int_\Omega d\boldsymbol{x}\ \boldsymbol{a}(\boldsymbol{x},t)\cdot\boldsymbol{b}(\boldsymbol{x},t) = \int_\Omega d\boldsymbol{k}\ \hat{\boldsymbol{a}}(\boldsymbol{k},t)\cdot\hat{\boldsymbol{b}}(-\boldsymbol{k},t)\ , \tag{1.84}$$

$$H_c(t) \equiv \int_\Omega d\boldsymbol{x}\ \boldsymbol{u}(\boldsymbol{x},t)\cdot\boldsymbol{b}(\boldsymbol{x},t) = \int_\Omega d\boldsymbol{k}\ \hat{\boldsymbol{u}}(\boldsymbol{k},t)\cdot\hat{\boldsymbol{b}}(-\boldsymbol{k},t)\ , \tag{1.85}$$

where $\boldsymbol{\omega}(\boldsymbol{x},t) = \nabla\times\boldsymbol{u}(\boldsymbol{x},t)$ is the vorticity of the flow and $\boldsymbol{a}(\boldsymbol{x},t)$ the magnetic vector potential. Topologically speaking, the kinetic helicity is a measure of the linkage and twist of infinitesimal vortex tubes, the magnetic helicity a measure of the linkage and twist of magnetic field lines, and the cross-helicity a measure of the linkage of vortex lines with magnetic field lines [16, 131]. The topological interpretation of helicity conservation is that the linking number of infinitesimal flux tubes remains constant, leading to a topological constraint.

The magnetic helicity is gauge-independent on simply-connected volumes Ω with perfectly conducting boundaries and for periodic domains provided no mean field is present [14]. If the magnetic field does not vanish at the boundary of a simply connected volume, the magnetic field lines have endpoints on the boundary and the linking number becomes ill-defined [15]. In this case a generalised helicity can be defined by splitting the magnetic field into a closed internal field and an irrotational field with vanishing helicity, which circumvents this problem [16]. This construction does not solve the problem for periodic systems with a mean field [14], however, in this thesis no background magnetic field is present, as such the aforementioned complications do not arise.

In the statistical approach to MHD turbulence the helicities are of course defined in the statistical sense. As for the energy, one can straightforwardly define helicity spectra

$$H_{kin}(k,t) = \int_{|\boldsymbol{k}|=k} d\boldsymbol{k}\ \langle \hat{\boldsymbol{u}}(\boldsymbol{k},t)\cdot\hat{\boldsymbol{\omega}}(-\boldsymbol{k},t)\rangle\ , \tag{1.86}$$

$$H_{mag}(k,t) = \int_{|\boldsymbol{k}|=k} d\boldsymbol{k}\ \langle \hat{\boldsymbol{a}}(\boldsymbol{k},t)\cdot\hat{\boldsymbol{b}}(-\boldsymbol{k},t)\rangle\ , \tag{1.87}$$

$$H_{c}(k,t) = \int_{|\boldsymbol{k}|=k} d\boldsymbol{k}\ \langle \hat{\boldsymbol{u}}(\boldsymbol{k},t)\cdot\hat{\boldsymbol{b}}(-\boldsymbol{k},t)\rangle\ , \tag{1.88}$$

whose Fourier transforms give the correlations of the respective vector fields at different points in real space. The helicities therefore yield information about the correlations of different vector fields. Statistically isotropic turbulence defined with respect to $O(3)$-invariance of the pdf excludes helical flows by definition, as a helical flow breaks reflectional symmetry. The distiction between $O(3)$ and $SO(3)$ invariance of the pdf in the definition of isotropy has been highlighted in sec. 1.3.2 for this reason.

From the topological constraint of helicity conservation it is expected that the level of helicity (helicities) influences the nonlinear interactions taking place in the system. This can be illustrated as follows. Let $\Omega' \subset \Omega$ be a subvolume where, say, $|H_{kin}(t)|$ is maximal, leading to alignment of velocity and vorticity in this subvolume. That is, the velocity field in the subvolume Ω' is a so-called *Beltrami field* as it obeys the differential equation

$$\nabla\times\boldsymbol{u}(\boldsymbol{x}) = \boldsymbol{\omega}(\boldsymbol{x}) = \alpha\boldsymbol{u}(\boldsymbol{x})\ , \tag{1.89}$$

for a coefficient α (which must have dimensions of inverse length). The alignment

of $\boldsymbol{\omega}_{|\Omega'}$ and $\boldsymbol{v}_{|\Omega'}$ forces the nonlinear term in the Navier-Stokes equation to vanish which can be seen from writing it in rotational form

$$(\boldsymbol{u}\cdot\nabla)\boldsymbol{u} = (\nabla\times\boldsymbol{u})\times\boldsymbol{u} + \frac{1}{2}\nabla|\boldsymbol{u}|^2 \ . \tag{1.90}$$

Since the gradient term can be absorbed into the pressure term, the inertial dynamics are given by the term $(\nabla\times\boldsymbol{u})\times\boldsymbol{u}$ which vanishes for a Beltrami field. Beltrami fields and their connection to self-organisation in homogeneous turbulence will play a major role in this thesis.

Magnetic and kinetic helicities have known self-organising effects in MHD flows through their connection to large-scale dynamo action and the so-called inverse cascade of magnetic helicity. These concepts are briefly introduced in the following sections.

Dynamo action and helicity

Kinetic helicity has received much attention in astrophysics due to its connection to dynamo action, in particular to the Stretch-Twist-Fold (STF) mechanism [36, 125, 178]. In this picture a closed magnetic flux tube is first stretched and then twisted by a necessarily helical flow before folding enables reconnection of magnetic field lines which results in more large-scale magnetic flux, i.e. a stronger large-scale magnetic field[11]. This process creates small and large-scale magnetic helicity of opposite sign, with the small-scale magnetic helicity being of the same sign as the kinetic helicity responsible for the twisting of the magnetic flux tube. This process has a mean-field description, the so-called α-*effect* [104, 132]. It is also an example of large-scale dynamo action, where a magnetic field on scales larger than the characteristic scale of the flow is amplified. This implies that kinetic energy on a smaller scale is converted into magnetic energy on a larger scale, that is, in spectral space energy is transferred from larger to smaller wavenumbers.

Inverse cascade of magnetic helicity

The magnetic helicity has peculiar dynamics. Using arguments borrowed from equilibrium statistical mechanics, Frisch *et al.* [73] predicted the magnetic helicity

[11] This is similar to a rubber band becoming stronger by twisting and folding it back on itself.

to have an *inverse cascade*. That is, it should be transferred from the large wavenumbers to the small wavenumbers, which is the opposite of the established Kolmogorov-Richardson (forwards) cascade picture of turbulence. Alongside magnetic helicity, some magnetic energy must also be transferred to the large scales due to the *realisability condition*

$$|H_{mag}(k,t)| \leqslant \frac{2E_{mag}(k,t)}{k} \ , \tag{1.91}$$

leading to the emergence of large-scale magnetic fields. Over the years the predictions of Frisch *et al.* have been numerically verified by many groups [4, 10, 12, 25, 27, 137, 149, 150].

Helical decomposition

The connection of magnetic and kinetic helicity with the emergence of large-scale magnetic fields and the brief discussion of the relation between helicity and Beltrami fields in view of weaked nonlinear interactions already hint at Beltrami fields being of some relevance to self-organisation in turbulent flows. Furthermore, Beltrami fields have an intricate connection to homogeneous turbulence, as they can be viewed as the 'building blocks' of solenoidal (square-integrable) vector fields. As first proposed by Constantin and Majda [45], the Fourier transform of a solenoidal vector field can be decomposed into circularly polarised waves, which themselves are nothing other than Beltrami fields.

The action of the curl operator on a square-integrable real vector field $\boldsymbol{v}(\boldsymbol{x})$ can be viewed in spectral space as the action of a linear operator on the Fourier transform $\hat{\boldsymbol{v}}(\boldsymbol{k})$ of $\boldsymbol{v}(\boldsymbol{x})$,

$$\begin{aligned} I_k : \mathbb{C}^3 &\longrightarrow \mathbb{C}^3 \\ \hat{\boldsymbol{v}}(\boldsymbol{k}) &\longmapsto i\boldsymbol{k} \times \hat{\boldsymbol{v}}(\boldsymbol{k}) \ . \end{aligned}$$

The linear operator $I_k(\cdot) = i\boldsymbol{k} \times (\cdot)$ commutes with its adjoint $I_k^\dagger = I_k$, hence it is diagonalisable and has a set of mutually orthogonal complex eigenvectors defining a basis of $\mathbb{C}^3$. As such, $\hat{\boldsymbol{v}}(\boldsymbol{k})$ can be expressed as a linear combination of

eigenvectors $i\boldsymbol{k}$, $\boldsymbol{h}_+(\boldsymbol{k})$ and $\boldsymbol{h}_-(\boldsymbol{k})$ of the curl operator I_k, where

$$i\boldsymbol{k} \times \boldsymbol{h}_{s_k} = s_k k \boldsymbol{h}_{s_k} \ , \tag{1.92}$$

$$-i\boldsymbol{k} \times \boldsymbol{h}^*_{s_k} = s_k k \boldsymbol{h}^*_{s_k} \ , \tag{1.93}$$

$s_k = \pm 1$ and $s_k k = \pm k$ being the nonzero eigenvalues of the curl operator in spectral space[12]. The complex eigenvectors are fully helical, since

$$|\boldsymbol{h}_{s_k} \cdot (-i\boldsymbol{k} \times \boldsymbol{h}^*_{s_k})| = |\boldsymbol{h}_{s_k} \cdot s_k k \boldsymbol{h}^*_{s_k}| = k|\boldsymbol{h}_{s_k}|^2 \ , \tag{1.94}$$

that is, the realisability condition (1.91) is saturated.

Since the velocity field $\hat{\boldsymbol{u}}(\boldsymbol{k})$ and the magnetic induction $\hat{\boldsymbol{b}}(\boldsymbol{k})$ are solenoidal, they can be expressed in terms of $\boldsymbol{h}_-$, $\boldsymbol{h}_+$ only

$$\hat{\boldsymbol{u}}(\boldsymbol{k},t) = u_-(\boldsymbol{k},t)\boldsymbol{h}_-(\boldsymbol{k}) + u_+(\boldsymbol{k},t)\boldsymbol{h}_+(\boldsymbol{k}) = \sum_{s_k} u_{s_k}(\boldsymbol{k},t)\boldsymbol{h}_{s_k}(\boldsymbol{k}) \ , \tag{1.95}$$

$$\hat{\boldsymbol{b}}(\boldsymbol{k},t) = b_-(\boldsymbol{k},t)\boldsymbol{h}_-(\boldsymbol{k}) + b_+(\boldsymbol{k},t)\boldsymbol{h}_+(\boldsymbol{k}) = \sum_{s_k} b_{s_k}(\boldsymbol{k},t)\boldsymbol{h}_{s_k}(\boldsymbol{k}) \ , \tag{1.96}$$

where u_{s_k} and b_{s_k} are complex coefficients. The subscript $s_k = \pm 1$ denoting the sign of the respective eigenvalues of I_k describes now the positive or negative helicity modes for the velocity and magnetic modes respectively. The coefficients u_{s_k} and b_{s_k} can be calculated by taking the inner product of the basis vectors with the appropriate fields

$$u_{s_k}(\boldsymbol{k},t) = \frac{\boldsymbol{h}^*_{s_k}(\boldsymbol{k}) \cdot \boldsymbol{u}(\boldsymbol{k},t)}{\boldsymbol{h}_{s_k}(\boldsymbol{k}) \cdot \boldsymbol{h}^*_{s_k}(\boldsymbol{k})} \ , \tag{1.97}$$

and

$$b_{s_k}(\boldsymbol{k},t) = \frac{\boldsymbol{h}^*_{s_k}(\boldsymbol{k}) \cdot \boldsymbol{b}(\boldsymbol{k},t)}{\boldsymbol{h}_{s_k}(\boldsymbol{k}) \cdot \boldsymbol{h}^*_{s_k}(\boldsymbol{k})} \ . \tag{1.98}$$

The helical basis vectors are normalised to unit vectors for the remainder of this thesis.

In summary, any square-integrable solenoidal vector field is given as a superposition of Beltrami fields, which are fully helical, and helicity appears to play a

[12]The curl operator can have eigenvectors with nonzero eigenvalues, as it involves the cross product of two *complex* vectors. This is not necessarily orthogonal to the plane spanned by the two complex vectors, instead it is orthogonal to the plane spanned by the *complex conjugates* of the two vectors.

central role in self-organising processes occurring in homogeneous turbulent flows. Beltrami fields are known to appear locally in turbulent flows [134].

1.4 Self-organisation

Since the contributions by Richardson and Kolmogorov it is well established that the average transfer of kinetic energy occurring in isotropic non-conducting turbulent fluids in three dimensions proceeds from the large scales to the small scales, or, in the Fourier representation, from small to large wavenumbers. However, as we have seen, electrically conducting turbulent flows deviate from this behaviour, showing a variety of phenomena resulting in a transfer of energy from the small scales to the large scales, such as large-scale dynamo action or the inverse cascade of magnetic helicity. Furthermore, self-ordering effects in the form of an inverse cascade of kinetic energy have been predicted [181] and indeed observed in numerical simulations [18] of the Navier-Stokes equation projected onto the eigenspace of the operator I_k corresponding to positively helical Fourier modes. In all these examples of self-organisation in homogeneous turbulence, energy is transferred in spectral space from large to small wavenumbers, and a lack of mirror symmetry (i.e. the presence of kinetic and/or magnetic helicity) facilitates these types of energy transfer.

Many turbulent flows occurring in nature and/or in industrial applications also show self-organising behaviour, such as rotating flows [127], two-dimensional flows [22, 102, 128] and flows carrying polymeric additives [60]. Self-organisation also occurs in wall-bounded parallel shear flows. In these flows self-organisation is connected to the transition to turbulence and major advances in the understanding of this process from a dynamical systems perspective have been made in recent years. That is, self-organisation in wall-bounded shear flows is much better understood than the self-organising behaviour observed in homogeneous MHD turbulence.

The general picture which emerges for wall-bounded parallel shear flows is that the state space of the system consists of a complicated collection of unstable flow states and the linearly stable laminar profile. Turbulence is then characterised as the system revolving around these unstable flow states, which are exact solutions or periodic orbits of the Navier-Stokes equations (so-called 'exact coherent structures') [47, 69], and the important point is that the laminar profile and the turbulent states remain dynamically connected such that a sudden 'escape'

from the turbulent region of state space can occur. In other words, the flow can self-organise.

In summary, self-organisation in turbulent flows is not uncommon, and in this thesis an attempt is made to further understand self-organising behaviour in homogeneous (magneto)hydrodynamic flows and its connection to Beltrami flows. One of the rather surprising outcomes is that isotropic turbulence can also spontaneously relaminarise and the resulting large-scale flow is a Beltrami field. Furthermore, the statistical signature of this process is very similar to relaminarisation events in wall-bounded parallel shear flows, suggesting a state-space picture of self-organisation similar to the established results in wall-bounded parallel shear flows also for this dynamical system.

1.5 Thesis outline

The study of self-organisation of turbulent flows and the connection to Beltrami fields is the main theme of this thesis, which consists of several analytical and numerical results on this topic. Before presenting the results, the code developed for the numerical simulations is described in chapter 2 alongside a presentation of tests carried out to ensure correctness of results produced by the code.

Chapter 3 contains the main analytical results on the influence of helicity on the dynamics of MHD flows. The helical decomposition of solenoidal vector fields is used to derive a dynamical system which describes triad interactions of fully helical magnetic and velocity field modes, and a linear stability analysis of steady solutions of this dynamical system is carried out. The interpretation of the results from the stability analysis is that unstable solutions lead to energy transfer between the interacting modes, and a dependence of possible interscale energy and helicity transfers on the helicities of the interacting modes is derived.

Chapter 4 presents analytical and numerical results on the scaling of the total dissipation rate with Reynolds number. An approximate equation predicting the behaviour of the dimensionless dissipation rate at large Reynolds number is derived. The predictions of the equation are successfully compared against results from DNSs of decaying MHD turbulence with different levels of magnetic and cross-helicities, as well as against DNS results from mechanically forced stationary MHD turbulence using different forcing routines. The results from the DNSs of

decaying MHD turbulence are further discussed in view of the analytical results presented in chapter 3.

The analytical results of chapter 4 were obtained by asymptotic analysis. However, a more rigorous approach can be taken using the existence of weak solutions of the MHD equations. This leads to upper bounds for the total dissipation rates and Reynolds number scalings consistent with the approximate equation derived in chapter 4. This material is presented in chapter 5.

Chapter 6 consists of a numerical investigation of the collapse of isotropic turbulence onto a large-scale Beltrami flow. It is shown that the statistical signature of this process is analogous to relaminarisation of localised turbulence in wall-bounded shear flows, which raises further questions about the connection of Beltrami fields (and therefore helicity) with the suppression/collapse of homogeneous turbulence.

A summarising discussion of the individual results contained in chapters 3-6 is provided in chapter 7 with an emphasis on open problems and further work.

Chapter 2

The MHD code

A fully functional and extensively tested parallelised hydrodynamic code [187] was extended from hydrodynamics to MHD, where tasks specific to MHD calculations were implemented using pre-processor directives, in order to avoid the evaluation of conditional statements at runtime specifying whether an MHD or a purely hydrodynamic simulation is carried out. The main features of the code and its MHD extension are described in this chapter, along side a series of tests.

2.1 Description of the code

The extended MHD-capable version of the code numerically solves a system of two coupled nonlinear partial differential equations on a 3D regular mesh. It steps the MHD equations (1.5) - (1.7) forward in time using Heun's method [83], which is a 2nd-order predictor-corrector scheme. The viscous and resistive terms are treated exactly by integrating factors. The nonlinear term is calculated using the pseudospectral method, that is, all spatial derivatives become algebraic vector operations coupling the wavevectors with the respective Fourier-transformed fields. Since the nonlinear terms are convolutions in Fourier-space which translate to multiplications in real space, the fields are Fourier-transformed back to real space after the derivatives are taken[1]. This procedure requires several Fast Fourier Transforms (FFTs) to be performed at each timestep, which are the main source of computational workload of this program. The FFTs are carried

[1]A detailed explanation of the pseudospectral method can be found in the thesis by Dr Samuel Yoffe [187], who developed the original hydrodynamic version of the code.

out in parallel using the `FFTW3.3` library, whose parallel (MPI[2]) option allows only 1D decomposition of the 3D computational domain. Apart from the parallel FFTs the code requires very little communication between MPI-tasks as can be seen from the basic profiling analysis presented in sec. 2.3.

The input is either specified by an input file which lists all the necessary parameters of the simulation or, in case of a restart, by snapshots of the magnetic and velocity fields, which have been saved to disk by a previous run. Snapshots of both fields can also be saved at user-defined intervals, which allows visualisation of the flow and the magnetic field using visualisation tools such as `Paraview` [1]. Aside from the snapshots, the code saves several quantities of interest at user-defined intervals, such as kinetic and magnetic energy spectra, all helicities and all transfer terms. The data is post-processed separately in order to calculate all derived quantities, and since this requires much less computational resource, post-processing is usually carried out on local Linux workstations.

2.1.1 Forcing routines

The hydrodynamic version of the code could be used for decaying and statistically stationary simulations of isotropic turbulence. For the stationary simulations, the energy input was achieved by feeding the rescaled velocity field back into the system at the large scales. More precisely, the corresponding force $\boldsymbol{f}_1$ is given by

$$\begin{aligned} \hat{\boldsymbol{f}}_1(\boldsymbol{k},t) &= (\varepsilon_W/2E_f)\hat{\boldsymbol{u}}(\boldsymbol{k},t) \quad \text{for} \quad 0 < |\boldsymbol{k}| \leqslant k_f; \\ &= 0 \quad \text{otherwise} , \end{aligned} \tag{2.1}$$

where $\hat{\boldsymbol{f}}_1(\boldsymbol{k},t)$ is the Fourier transform of the forcing, $\hat{\boldsymbol{u}}(\boldsymbol{k},t)$ is the Fourier transform of the velocity field, and E_f is the total energy contained in the forcing band. The parameter k_f is the largest wavenumber at which the forcing is applied and can be set in the input file. The advantage of this method is that the energy input rate ε_W is known at the start of the simulation. However, it does not allow direct control over kinetic helicity injection. Therefore an additional type of forcing has been implemented which allows the injection of fixed amounts of kinetic, magnetic and cross-helicity. This allows more direct control over the evolution of the ideal invariants. Furthermore, specific types of numerical simulations requiring helical forcing (such as dynamo simulations) can now be

[2]Message Passing Interface

carried out. The forcing function is defined as

$$\hat{\boldsymbol{f}}_2(\boldsymbol{k},t) = A(\boldsymbol{k},t)\boldsymbol{e}_1(\boldsymbol{k}) + B(\boldsymbol{k},t)\boldsymbol{e}_2(\boldsymbol{k}) \ , \tag{2.2}$$

where $A \in \mathbb{C}$ and $B \in \mathbb{C}$, $\boldsymbol{e}_i(\boldsymbol{k}) \perp \boldsymbol{k}$ for $i = 1, 2$ and $\boldsymbol{e}_1(\boldsymbol{k}) \cdot \boldsymbol{e}_2(\boldsymbol{k})^* = 0$. The complex numbers A and B are given by

$$A = (F(k))^{\frac{1}{2}}\, g_A e^{i\alpha(\boldsymbol{k})} \ , \tag{2.3}$$

$$B = (F(k))^{\frac{1}{2}}\, g_B e^{i\alpha(\boldsymbol{k})} \ , \tag{2.4}$$

where $g_A^2 + g_B^2 = 1$, $e^{i\alpha(\boldsymbol{k})}$ a uniformly distributed random phase chosen at each time-step and $F(k)$ a normalisation factor. The basis vectors $\boldsymbol{e}_i(\boldsymbol{k})$ $(i = 1, 2)$ correspond to the helical basis vectors introduced in chapter 1.3.3, that is, the Fourier transform $\hat{\boldsymbol{f}}_2(\boldsymbol{k},t)$ of the force $\boldsymbol{f}_2(\boldsymbol{x},t)$ is expanded into helical modes. More precisely, at the initial instant a unit vector $\boldsymbol{e}$ is randomly chosen and the helical basis vectors are given by

$$\boldsymbol{e}_1(\boldsymbol{k}) = \frac{\boldsymbol{k} \times (\boldsymbol{k} \times \boldsymbol{e}) - ik(\boldsymbol{k} \times \boldsymbol{e})}{\sqrt{2[k^4 - k^2(\boldsymbol{k} \cdot \boldsymbol{e})]}} \ , \tag{2.5}$$

$$\boldsymbol{e}_2(\boldsymbol{k}) = \frac{\boldsymbol{k} \times (\boldsymbol{k} \times \boldsymbol{e}) + ik(\boldsymbol{k} \times \boldsymbol{e})}{\sqrt{2[k^4 - k^2(\boldsymbol{k} \cdot \boldsymbol{e})]}} \ , \tag{2.6}$$

as in Ref. [25], such that

$$i\boldsymbol{k} \times \boldsymbol{e}_1(\boldsymbol{k}) = k\boldsymbol{e}_1(\boldsymbol{k}) \ , \quad i\boldsymbol{k} \times \boldsymbol{e}_2(\boldsymbol{k}) = -k\boldsymbol{e}_2(\boldsymbol{k}) \ , \quad \boldsymbol{e}_1(\boldsymbol{k}) \cdot \boldsymbol{e}_2^*(\boldsymbol{k}) = 0 \ . \tag{2.7}$$

The helicity $H_{f_2}(k)$ of the forcing can then be adjusted through the coefficients g_A and g_B, since the relative helicity input is given by

$$\rho = \frac{H_{f_2}(k)}{k|\hat{\boldsymbol{f}}_2(\boldsymbol{k},t)|^2} = \frac{g_A^2 - g_B^2}{g_A^2 + g_B^2} = g_A^2 - g_B^2 \ , \tag{2.8}$$

which is then adjusted using $g_A = \sin\phi$ and $g_B = \cos\phi$ for a fixed angle ϕ.

This forcing mechanism has been implemented for the magnetic and the velocity field, that is, fixed levels of kinetic and magnetic helicity can be injected into the system. In order to inject a set amount of cross-helicity, the helical basis vectors for the mechanical force are rotated by an adjustable angle. The resulting helical basis vectors are then used to generate the electromagnetic force. A very similar method has been used in the numerical simulations of helical MHD turbulence

carried out by Müller *et al.* [137] and Malapaka *et al.* [116]. The forcing routine can also be used as a static (i.e. deterministic) force by omitting the random phases.

2.1.2 Initial conditions

The initial conditions for the velocity and the magnetic field with prescribed magnetic and kinetic energy spectra are constructed by assigning a Gaussian random vector to each point in space for both fields. The resulting fields are subsequently Fourier-transformed and expanded into helical modes in order to set the initial kinetic, magnetic and cross-helicities to the levels appropriate for the problem under consideration. Finally both Fourier-transformed fields are rescaled according to the desired energy spectra in the form

$$E_{mag,kin}(k) = Ak^4 \exp(-k^2/(2k_0)^2) \ , \tag{2.9}$$

where $A \geqslant 0$ is a real number which can be adjusted according to the desired amount of initial energy. The wavenumber k_0 which locates the peak of the initial spectrum can be adjusted freely and is mostly taken to be $k_0 = 5$, unless otherwise stated. No background magnetic field is imposed.

2.2 Tests and verification

Since the hydrodynamic version of the code had already been extensively tested [187], only tests specific to the newly developed MHD functions have been carried out. Since all new functions specific to MHD have been implemented using pre-processor directives, the hydrodynamic base version of the code has been left untouched.

2.2.1 Conserved quantities

A first important test for correctness of a given code is whether any conserved quantities are indeed conserved. As outlined in chapter 1, there are three ideal invariants in MHD, the total energy and the cross- and magnetic helicities. Instead of carrying out simulations of the ideal MHD equations the conservation

of the ideal invariants can be tested in dissipative simulations by tracking the time evolution of the nonlinear terms corresponding to the ideal invariants. Since the nonlinear terms do no work on the system and only redistribute energy and cross- and magnetic helicities, respectively, between the Fourier modes, the spatial integrals of these terms should vanish

$$\Pi_E(0,t) = \int_0^\infty dk\ T_{kin}(k,t) + T_{mag}(k,t) = 0\ , \tag{2.10}$$

$$\Pi_{H_{mag}}(0,t) = \int_0^\infty dk\ T_{H_{mag}}(k,t) = 0\ , \tag{2.11}$$

$$\Pi_{H_c}(0,t) = \int_0^\infty dk\ T_{H_c}(k,t) = 0\ . \tag{2.12}$$

This is indeed the case to a good approximation, as can be seen in fig. 2.1, where the time evolution of the spatially integrated transfer terms is shown for a statistically steady simulation on 512^3 collocation points using the forcing routine $\boldsymbol{f}_2$ for both magnetic and velocity fields. The time averages are $\langle \Pi_E(0,t) \rangle_t = 0$ to machine accuracy, $\langle \Pi_{H_{mag}}(0,t) \rangle_t = 5.85684 \times 10^{-10}$ and $\langle \Pi_{H_c}(0,t) \rangle_t = 2.27055 \times 10^{-10}$. Lower resolved stationary simulations and simulations of decaying MHD turbulence behave similarly.

2.2.2 Tests against results in the literature

The 3D Orszag-Tang vortex was used for comparison against results by Mininni *et al.* [130] and Morales *et al.* [136]. The initial conditions are

$$\begin{aligned} \boldsymbol{u} &= (-2\sin y,\ 2\sin x,\ 0)\ , \\ \boldsymbol{b} &= \beta(-2\sin 2y + \sin z,\ 2\sin x + \sin z,\ \sin x + \sin y)\ , \end{aligned} \tag{2.13}$$

where $\beta = 0.8$ has been chosen according to [130, 136]. The comparison is carried out with respect to the the time evolution of the total dissipation $\varepsilon(t)$ and the maximum of the current density in real space $\max|\boldsymbol{j}|$. The same number of grid points and dissipation coefficients as in Ref. [136] was used, that is $\nu = \eta = 0.01$ on 64^3 grid points (OT1), $\nu = \eta = 0.005$ on 128^3 grid points (OT2) and $\nu = \eta = 0.001$ on 256^3 grid points (OT3).

The results obtained are in agreement with both aforementioned sources. By comparison of the top panel of fig. 2.2 with the corresponding fig. 11 in Ref. [136] for the evolution of the total dissipation, the same delay in the peak of the

dissipation rate as the Reynolds number increases is observed. The maximum of the current density shows Reynolds number independent exponential growth until $t = 0.4$, in agreement with Morales *et al.* , while Mininni *et al.* observe exponential growth up to $t = 0.6$. This is most likely due to a slightly different definition of the initial condition in Ref. [130]. After the initial period, algebraic growth $\sim t^3$ in agreement with both sources is observed. With increasing Reynolds number the temporal maxima of $\max|\mathbf{j}|$ are achieved at later times, also in agreement with both sources. Furthermore, the data shows very good agreement in direct comparison to a dataset obtained from Morales *et al.* [136] as shown in fig. 2.2.

Results from simulations of decaying MHD turbulence with random initial data were also compared against results in the literature. Figure 2.3 shows magnetic helicity, magnetic energy and kinetic energy spectra shortly after the onset of power-law decay for a simulation of decaying MHD turbulence[3] with maximal initial magnetic helicity at an initial Taylor-scale Reynolds number $R_\lambda(0) = 645.47$ carried out on 1032^3 grid points. The magnetic helicity spectra have been multiplied by the wavenumber k for dimensional reasons, and have been shifted downwards in the figure to facilitate visual analysis. The inset shows constancy of helicity flux $\Pi_H(k)$ for the wavenumber interval $21 \leqslant k \leqslant 33$, indicating an inertial range for the magnetic helicity in the direct cascade region. It can be seen in the figure that power-law scaling of $H_{mag}(k)$ extends over a larger interval, showing the scaling $H_{mag}(k) \sim k^{-3.6}$, which is in agreement with recent results on decaying 3D MHD turbulence [137]. The flux is k-dependent in the reverse spectral transfer region, as shown in the inset of fig. 2.3. This is also in agreement with Müller *et al.* [137], who report the same behaviour. The present simulations support Kolmogorov scaling for the magnetic field as indicated by the bar parallel to $E_{mag}(k)$.

2.3 Scaling and performance of the code

A basic profiling and scaling analysis of the MHD version of the code has been carried out for two problem sizes, that is DNSs of MHD turbulence using 1032^3 and 2064^3 collocation points. For the smaller problem size (1032^3 grid points) the code shows linear scaling up to 516 cores. At 1032 cores the amount of data per core becomes small and communication costs begin to matter, this can be

[3]This simulation was carried out for a different project [12], which is outwith the scope of this thesis. It is the largest Reynolds number run of Ref. [12].

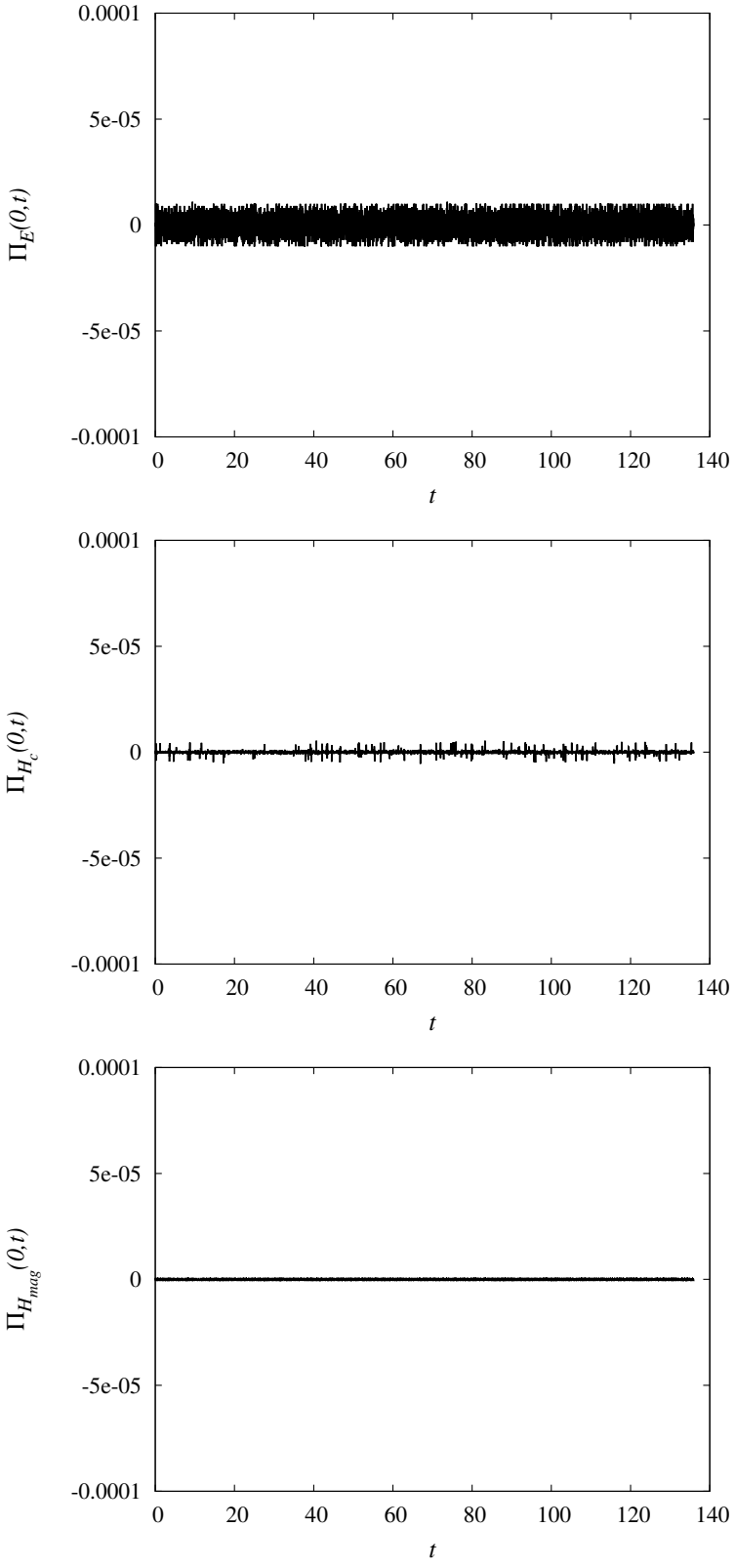

Figure 2.1 *Time evolution of integrated transfer terms of total energy (top), cross-helicity (middle) and magnetic helicity (bottom) for a statistically steady simulation on* 512^3 *collocation points using the forcing routine* $\boldsymbol{f}_2$ *for both magnetic and velocity fields.*

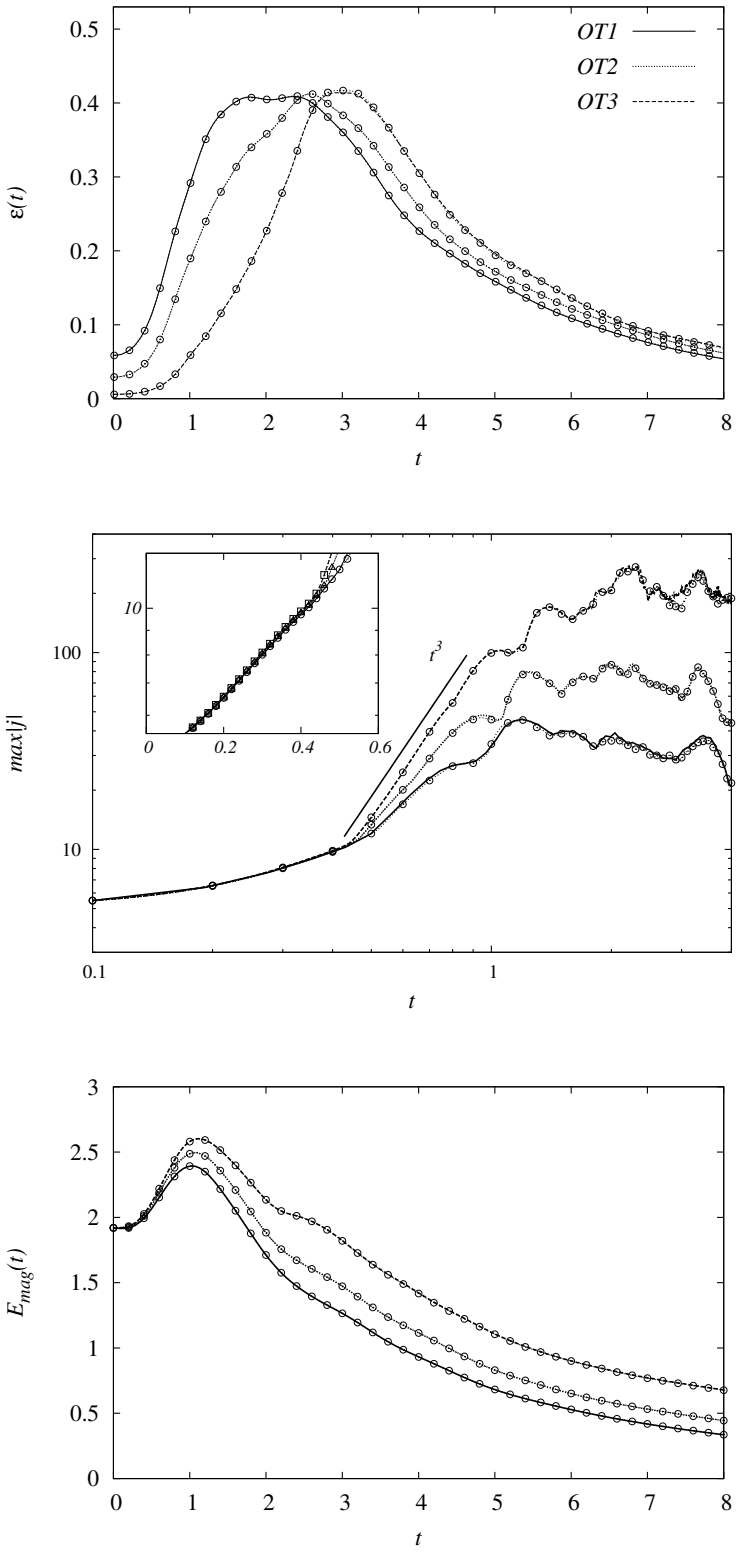

Figure 2.2 *Comparison to a dataset obtained from Morales et al. [136]. The symbols refer to the present DNS, the lines to DNS by Morales et al.*

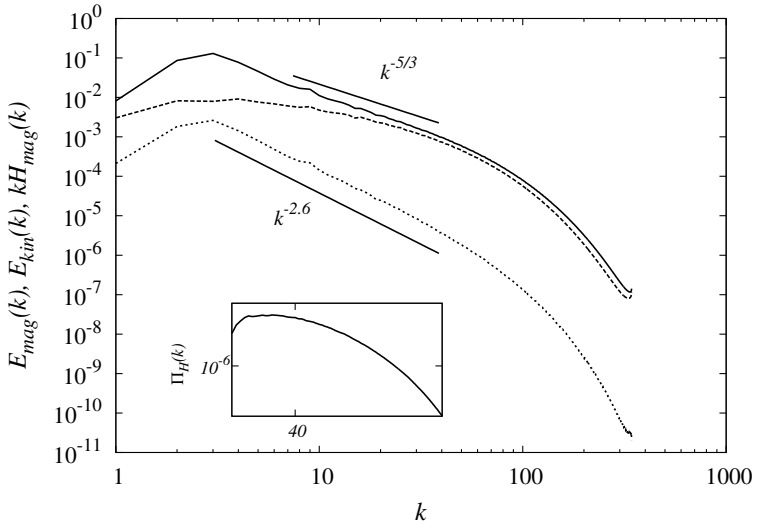

Figure 2.3 *Energy and magnetic helicity spectra. The solid line shows $E_{mag}(k)$, the middle dashed line shows $E_{kin}(k)$ and the bottom dotted line shows $kH_{mag}(k)$, which has been shifted for easier comparison. The inset shows the flux of $H_{mag}(k)$, which is constant in the higher k region, indicating an inertial range. The straight lines indicate scaling regions for $E_{mag}(k) \sim k^{-5/3}$ and $kH_{mag}(k) \sim k^{-2.6}$, which results in $H_{mag}(k) \sim k^{-3.6}$.*

seen in fig. 2.4. This data point shows the largest core count possible for the studied problem size, where the restriction is due to the one-dimensional domain decomposition, which restricts the number of MPI-tasks that can be used for a given problem size. For a grid using N^3 collocation points the maximal number of MPI-tasks is N. The larger problem size (2064 grid points) extends the linear scaling up to 2064 cores, which can also be seen in fig. 2.4, where the data of the larger problem has been rescaled by problem size in order to facilitate visual comparison between the two data sets. The scaling analysis in fig. 2.4 shows that the code has a parallel efficiency of 87% for the largest problem sizes, as given by the slope of the dashed line in fig. 2.4. In summary, the code scales well up to thousands of processing elements (PEs) for the largest currently viable problem sizes. Larger simulations would require further parallelisation of the code.

Results from a basic profiling analysis using the CrayPAT profiling tool are shown in tbl. 2.1. The percentage of execution time spent is split into library functions (ETC), which includes MPI-functions called from the FFT library, user-implemented functions (USER), communication due to user-defined functions (MPI) and I/O. The analysis clearly shows that most of the time is spent in the FFT routines, however, this included MPI-communication within the FFT

library calls. This basic analysis shows that code optimisation of user-defined functions would have little effect as most time is spent in FFTW-calls, thus any further optimisation work should concentrate on the FFTs.

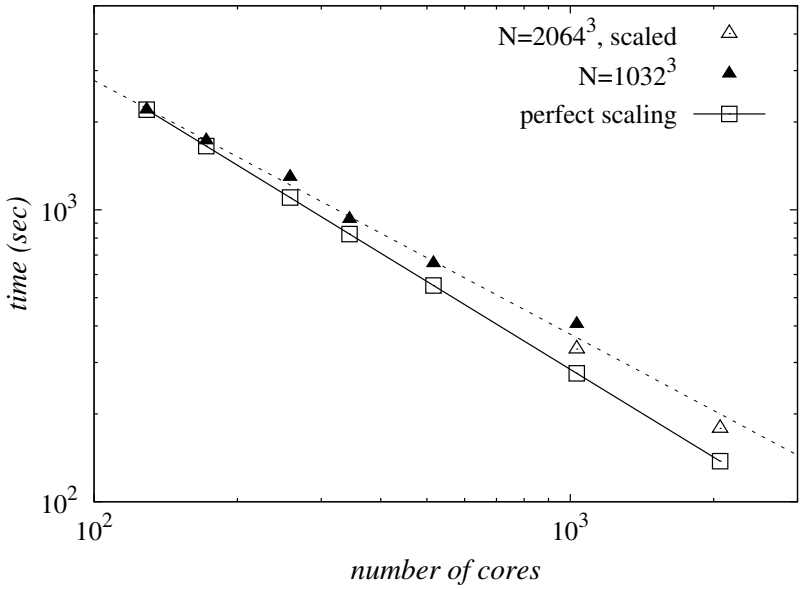

Figure 2.4 *Strong scaling results for two problem sizes. The times measured for the larger problem size have been scaled according to the difference in problem size (divided by a factor of 8) in order to facilitate comparison to the smaller runs.*

N^3	# of PEs	ETC	USER	MPI	I/O
1032^3	129	90.7%	8.4%	0.2%	< 0.5 %
1032^3	172	91.0%	8.1%	0.2%	< 0.5 %
1032^3	344	91.2%	7.7%	0.1%	< 0.5 %
1032^3	512	90.9%	7.7%	0.2%	< 0.5 %
1032^3	1032	93.6%	4.1%	0.4%	1.2 %

Table 2.1 *Profiling data corresponding to the runs on* 1032^3 *collocation points as shown in percentage of time spent in computation, communication and I/O. The percentage of time spent in computation is split between library functions (ETC), which includes MPI-functions called from the FFT library. USER refers to user implemented functions, while values in the column labelled MPI shows the percentage of time spent in communication due to user-defined functions.*

Chapter 3

Helical mode interactions and self-organisation in MHD turbulence

In this chapter spectral transfer processes in homogeneous MHD turbulence are investigated analytically in order to gain information on the deeper connection between helicity and self-organisation in homogeneous MHD turbulence. The decomposition of the velocity and magnetic fields into helical Fourier modes as explained in chapter 1 leads to a dynamical system describing the evolution of the helical coefficients, and a stability analysis of steady solutions of this system is carried out. The interpretation of the analysis is that instabilities lead to energy transfer between the interacting modes. From this, a dependence of possible interscale energy and helicity transfers on the helicities of the interacting modes is derived and the direction of the inertial-range fluxes are calculated.

As expected from the inverse cascade of magnetic helicity in 3D MHD turbulence, mode interactions with like helicities lead to transfer of energy and magnetic helicity to smaller wavenumbers, that is, systems mainly containing modes of like helicities should tend to self-organise into large-scale structures. Furthermore, it is found that high values of the cross-helicity may have an asymmetric effect on forward and reverse transfer of energy, where forward transfer is more quenched in regions of high cross-helicity than reverse transfer.

Some specific helical interactions can be mapped to large- and small-scale kinematic dynamo action such as the STF-scenario mentioned in chapter 1, in these cases the analysis is much simpler. The results are discussed in the context of numerical simulations of MHD turbulence and observations of MHD turbulence

in the solar wind.

3.1 Introduction

The effect of helicity on energy transfer and evolution in non-conducting turbulent fluids has received considerable attention in the literature [6, 18–20, 32, 33, 131, 142, 145, 146, 181]. It has been studied in a variety of ways, e.g. using analytical methods, closure calculations, conventional DNSs and novel approaches in DNS. Waleffe [181] decomposed the Fourier transform of the velocity field into eigenfunctions of the curl operator and derived evolution equations for these eigenfunctions by substitution of the decomposed field into the Navier-Stokes equations for incompressible flow. Since the nonzero eigenvalues of the corresponding eigenfunctions are related to the helicity of a given velocity field mode, the evolution equations were further analysed in order to derive the dependence of the possible energy transfers on the helicities of the interacting modes. If the largest two wavenumbers of a given wavevector triad had helicities of opposite sign energy was transferred forward in wavenumber space, while a reverse transfer of energy became possible if the helicities were of the same sign. The analysis also showed that the triads responsible for an inverse energy cascade contribute to a direct cascade of kinetic helicity. The possibility of an inverse cascade of kinetic energy and a forward cascade of kinetic helicity had previously been predicted by Brissaud *et al.* [28].

Biferale *et al.* [18] investigated numerically whether this reverse spectral transfer caused by interactions of helical modes of the same sign occurs. By defining a projection operation on the nonlinear term the authors altered the Navier-Stokes equations so to ensure that only modes of, say, positive helicity were present in the system. That is, the dynamics were restricted to one eigenspace of the operator I_k introduced in chapter 1. The altered Navier-Stokes equations were subsequently solved numerically using the standard pseudospectral method in conjunction with small-scale forcing. As predicted by Waleffe's analysis, kinetic energy was indeed transferred downwards in wavenumber space. This was the first observation of an inverse energy cascade in three-dimensional isotropic turbulence.

In a subsequent paper [19], the same authors forced the system at the large scales in order to study the predicted forward cascade of kinetic helicity, which was indeed observed in the simulations. Since the subset of positively helical

modes does not transfer energy to the small scales, it was expected that the resulting dynamical system would not show finite dissipation in the limit of infinite Reynolds number. Hence the projected Navier-Stokes equation which governs the evolution should be globally regular, which was subsequently proven by Biferale and Titi [20].

Thus, in summary, the decomposition of the Fourier transform of the turbulent velocity field fluctuations into helical modes has been proven to be very useful in terms of understanding some fundamental features of turbulent flows, which go beyond the established Kolmogorov-Richardson (direct) cascade of kinetic energy. In view of the effects of kinetic and magnetic helicities on the direction of energy transfer in MHD turbulence, and inspired by the successes of the helical decomposition used in hydrodynamics, in this chapter the decomposition of both the magnetic and velocity fields into helical modes is used in order to perhaps shed some more light on why MHD turbulence shows much more transfer from the small scales to the large scales than turbulence in non-conducting fluids. In other words, this approach is an attempt at finding out why self-ordering processes occur more frequently in MHD than in hydrodynamic turbulence.

Before embarking on the derivation of the main equations and the subsequent stability analysis, some terminology is briefly discussed. As the precise meaning of the term varies in the literature, it is not always evident what is meant by an inverse cascade. In the astrophysical literature, transfer of energy and helicity from higher to lower wavenumbers is often described as an inverse cascade [38, 39, 168], while the fluid dynamics literature requires any cascade process to possess a wavenumber-independent flux [4, 18, 20, 27, 120, 137]. It is thus of interest to not only classify the different types of reverse transfer that can occur in MHD turbulence, but also to perhaps clarify the terminology. Therefore the umbrella term reverse (or inverse) spectral transfer is proposed here, which includes all the phenomena described above as subcategories according to their properties. It is defined as any process that produces an increase in a spectral quantity (total energy, magnetic helicity, etc.) at low wavenumbers due to transfer of that quantity away from higher wavenumbers into smaller wavenumbers. In this framework an inverse cascade is a reverse spectral transfer showing constant flux of the cascading quantity over a certain wavenumber range. Concerns have been raised in MHD over the use of the term 'cascade' [137], as it may be understood to imply energy (or magnetic helicity) transfer mainly due to local interactions, which might not be the case in MHD turbulence [3, 37, 53, 137]. This point will

be addressed in the discussion section of this chapter.

3.2 The evolution of the helical modes

For simplicity at first consider periodic boundary conditions on a domain $\Omega = [0, L]^3 \subset \mathbb{R}^3$, thus working with the discrete Fourier transformed MHD equations

$$(\partial_t + \nu k^2)\hat{\boldsymbol{u}}(\boldsymbol{k}) = -FT\left[\nabla\left(P + \frac{|\boldsymbol{u}|^2}{2}\right)\right] + \sum_{\boldsymbol{k}+\boldsymbol{p}+\boldsymbol{q}=0}\left[-(i\boldsymbol{p}\times\hat{\boldsymbol{u}}(\boldsymbol{p}))^*\times\hat{\boldsymbol{u}}(\boldsymbol{q})^* + (i\boldsymbol{p}\times\hat{\boldsymbol{b}}(\boldsymbol{p}))^*\times\hat{\boldsymbol{b}}(\boldsymbol{q})^*\right] , \tag{3.1}$$

$$(\partial_t + \eta k^2)\hat{\boldsymbol{b}}(\boldsymbol{k}) = i\boldsymbol{k}\times\sum_{\boldsymbol{k}+\boldsymbol{p}+\boldsymbol{q}=0}\hat{\boldsymbol{u}}(\boldsymbol{p})^*\times\hat{\boldsymbol{b}}(\boldsymbol{q})^* , \tag{3.2}$$

where FT denotes the three-dimensional Fourier transform as a linear operator acting on $L^2(\Omega)^3$ functions. In order to determine the contribution of specific interactions to the fluxes of magnetic helicity and magnetic energy, eventually the formal limit $L \to \infty$ will be taken in sec. 3.6, necessarily assuming that the relevant functions are then well-behaved at infinity to ensure the convergence of the respective Fourier integrals, as discussed in chapter 1.

The decomposition of the Fourier transform of a solenoidal vector field in circularly polarised waves as introduced in chapter 1 has been used in several investigations of hydrodynamic turbulence [18, 20, 181] in order to establish the properties of energy transfer depending on the kinetic helicity. It was first applied to incompressible MHD flows by Lessinnes *et al.* [111], who derived a dynamical system in Fourier space describing helical triadic interactions in MHD. This system was subsequently used to construct a helical shell model of MHD turbulence.

The equations describing the evolution of the helical coefficients u_{s_k} and b_{s_k} are derived by substituting the decompositions (1.95) and (1.96) into the MHD equations for incompressible flow and then taking the inner product with $\boldsymbol{h}_{s_k}$ on both sides of the respective equations [111, 181]. The resulting evolution equation

for the helical coefficient u_{s_k} is

$$
\begin{aligned}
(\partial_t + \nu k^2) u_{s_k} &= \boldsymbol{h}^*_{s_k} \cdot \left(-FT \left[\nabla \left(P + \frac{|\boldsymbol{u}|^2}{2} \right) \right] \right) \\
&\quad + \boldsymbol{h}^*_{s_k} \cdot \sum_{\boldsymbol{k}+\boldsymbol{p}+\boldsymbol{q}=0} \left[-(i\boldsymbol{p} \times \hat{\boldsymbol{u}}(\boldsymbol{p}))^* \times \hat{\boldsymbol{u}}(\boldsymbol{q})^* + (i\boldsymbol{p} \times \hat{\boldsymbol{b}}(\boldsymbol{p}))^* \times \hat{\boldsymbol{b}}(\boldsymbol{q})^* \right] \\
&= -\frac{1}{2} \sum_{s_p, s_q} \sum_{\boldsymbol{k}+\boldsymbol{p}+\boldsymbol{q}=0} (s_p p - s_q q) \left[\boldsymbol{h}^*_{s_p} \times \boldsymbol{h}^*_{s_q} \cdot \boldsymbol{h}^*_{s_k} \right] (u^*_{s_p} u^*_{s_q} - b^*_{s_p} b^*_{s_q}) \ ,
\end{aligned}
\tag{3.3}
$$

where the dummy variables $\boldsymbol{p}$ and $\boldsymbol{q}$ were exchanged in order to symmetrise the momentum equation with respect to $\boldsymbol{p}$ and $\boldsymbol{q}$ and thus to obtain the factor $(s_p p - s_q q)/2$. Following an analogous procedure [111] for the helical coefficient b_{s_k} of the magnetic field leads to

$$
\begin{aligned}
(\partial_t + \eta k^2) b_{s_k} &= \boldsymbol{h}^*_{s_k} \cdot \left[i\boldsymbol{k} \times \sum_{\boldsymbol{k}+\boldsymbol{p}+\boldsymbol{q}=0} \hat{\boldsymbol{u}}(\boldsymbol{p})^* \times \hat{\boldsymbol{b}}(\boldsymbol{q})^* \right] \\
&= \frac{s_k k}{2} \sum_{s_p, s_q} \sum_{\boldsymbol{k}+\boldsymbol{p}+\boldsymbol{q}=0} \left[\boldsymbol{h}^*_{s_p} \times \boldsymbol{h}^*_{s_q} \cdot \boldsymbol{h}^*_{s_k} \right] (u^*_{s_p} b^*_{s_q} - b^*_{s_p} u^*_{s_q}) \ .
\end{aligned}
\tag{3.4}
$$

In order to study the interaction of helical modes, that is the evolution of the helical coefficients due to the mode coupling only, the dissipation coefficients are from now on omitted. For a given triad $\boldsymbol{k}, \boldsymbol{p}, \boldsymbol{q}$ of wavevectors, expressions for the first time-derivatives of each helical coefficient are obtained from (3.3) and (3.4) and from the corresponding equations for b_{s_p}, b_{s_q}, u_{s_p} and u_{s_q}. This leads to the following system of coupled ordinary differential equations (ODEs) describing the evolution of the helical coefficients in a single triad interaction

$$
\begin{aligned}
\partial_t u_{s_k} &= (s_p p - s_q q)\, g_{kpq}\, (u^*_{s_p} u^*_{s_q} - b^*_{s_p} b^*_{s_q}) \ , \\
\partial_t u_{s_p} &= (s_q q - s_k k)\, g_{kpq}\, (u^*_{s_q} u^*_{s_k} - b^*_{s_q} b^*_{s_k}) \ , \\
\partial_t u_{s_q} &= (s_k k - s_p p)\, g_{kpq}\, (u^*_{s_k} u^*_{s_p} - b^*_{s_k} b^*_{s_p}) \ ,
\end{aligned}
\tag{3.5}
$$

$$
\begin{aligned}
\partial_t b_{s_k} &= -s_k k\, g_{kpq}\, (u^*_{s_p} b^*_{s_q} - b^*_{s_p} u^*_{s_q}) \ , \\
\partial_t b_{s_p} &= -s_p p\, g_{kpq}\, (u^*_{s_q} b^*_{s_k} - b^*_{s_q} u^*_{s_k}) \ , \\
\partial_t b_{s_q} &= -s_q q\, g_{kpq}\, (u^*_{s_k} b^*_{s_p} - b^*_{s_k} u^*_{s_p}) \ ,
\end{aligned}
\tag{3.6}
$$

where the geometric factor

$$
g_{kpq} = -\frac{1}{2} \boldsymbol{h}^*_{s_p} \times \boldsymbol{h}^*_{s_q} \cdot \boldsymbol{h}^*_{s_k} \ ,
\tag{3.7}
$$

is introduced for conciseness [111, 181]. It can also be written as

$$g_{kpq} = \frac{s_k s_p s_q}{2} e^{i\alpha(k,p,q)} \frac{N}{2kpq}(s_k k + s_p p + s_q q) \ , \tag{3.8}$$

where α is a wavenumber-dependent real number determined by the orientation of the triad and N a factor depending on the shape of the triad. Further details and a derivation of (3.8) can be found in Ref. [181].

The total energy, the magnetic helicity and the cross-helicity can be expressed in terms of the helical coeffients

$$E = \frac{1}{2}\sum_{\boldsymbol{k}} \langle |\hat{\boldsymbol{u}}(\boldsymbol{k})|^2 + |\hat{\boldsymbol{b}}(\boldsymbol{k})|^2 \rangle = \frac{1}{2}\sum_{\boldsymbol{k},s_k} \left(\langle |u_{s_k}|^2 \rangle + \langle |b_{s_k}|^2 \rangle \right) \ , \tag{3.9}$$

$$H_{mag} = \sum_{\boldsymbol{k}} \langle \hat{\boldsymbol{a}}(\boldsymbol{k}) \hat{\boldsymbol{b}}(-\boldsymbol{k}) \rangle = \sum_{\boldsymbol{k},s_k} \frac{s_k}{k} \langle |b_{s_k}|^2 \rangle \ , \tag{3.10}$$

$$H_c = \sum_{\boldsymbol{k}} \langle \hat{\boldsymbol{u}}(\boldsymbol{k}) \hat{\boldsymbol{b}}(-\boldsymbol{k}) \rangle = \sum_{\boldsymbol{k},s_k} \Re \left(\langle u_{s_k} b^*_{s_k} \rangle \right) \ , \tag{3.11}$$

where $\Re$ denotes the real part of a complex number. All three ideal invariants are conserved per triad interaction [111].

3.3 Stability of steady solutions

Examining the linear stability of steady solutions of the system (3.5)-(3.6) can reveal the influence which the helicities of the interacting modes have on the interscale transfer of a given quantity of interest. The system (3.5) without a magnetic field (that is for $b_s = 0$) was analysed by Waleffe [181] with respect to the linear stability of its steady solutions. Linearly unstable solutions were found depending on the helicities of the interacting modes. This result was then interpreted following the *instability assumption* inspired by the formal analogy to rigid-body rotation, where rotation around the axis of middle inertia is unstable. The existence of a linearly unstable solution involving a velocity field mode $\hat{\boldsymbol{u}}$ is interpreted as the $\hat{\boldsymbol{u}}$-mode losing energy to the other two modes it interacts with[1]. A similar approach is taken here, that is, the linear stability of steady solutions of the system (3.5)-(3.6) is investigated in view of possible applications to spectral transfer processes in MHD with particular emphasis on self-ordering processes

[1] An equivalent assumption had already been used by Kraichnan [102] for two-dimensional hydrodynamic turbulence.

such as inverse transfers of total energy and magnetic helicity. In principle, a similar analysis could be carried out for the remaining ideal invariant, the cross-helicity.

3.3.1 The steady solutions

The system (3.5)-(3.6) of six coupled ODEs has several equilibria one can linearise about. To simplify the notation, a (formal) solution of the system (3.5)-(3.6) consisting of helical $\hat{\boldsymbol{u}}$- and $\hat{\boldsymbol{b}}$-field modes interacting in a given triad $\boldsymbol{k}, \boldsymbol{p}, \boldsymbol{q}$ is written as:

$$(u_{s_k}, u_{s_p}, u_{s_q}; b_{s_k}, b_{s_p}, b_{s_q}) \ . \tag{3.12}$$

In order to find the steady solutions of the system (3.5)-(3.6), it is assumed (without loss of generality) that the middle components $b_{s_p} = B_{s_p}$ and $u_{s_p} = U_{s_p}$ are constant in time. Then (3.5) and (3.6) require the other four components to vanish by the following argument. A steady solution requires $\partial_t u_{s_k} = 0$, and the only way that this can happen nontrivially is if both products $u^*_{s_p} u^*_{s_q}$ and $b^*_{s_p} b^*_{s_q}$ vanish[2]. Since $u_{s_p} = U_{s_p}$ is constant in time, $u_{s_q} = 0$ and similarly $b_{s_q} = 0$. Applying the same argument to $\partial_t u_{s_q}$, it follows that u_{s_k} and b_{s_k} must also vanish. Therefore a steady solution of the system (3.5)-(3.6) has the form

$$(0, U_{s_p}, 0; 0, B_{s_p}, 0) \ .$$

It can now be checked for consistency that $\partial_t b_s = 0$ for k, p and q as well. Therefore the solution is steady for the magnetic field and for the velocity field alike. Aside from the just explained example, steady solutions of the form $(U_{s_k}, 0, 0; B_{s_k}, 0, 0)$ and $(0, 0, U_{s_q}; 0, 0, B_{s_q})$ are obtained in the same way.

Thus the steady solutions of (3.5)-(3.6) are of the same form as for the hydrodynamic case [181], where at least two of the three interacting modes vanish. However, there are two special cases: one where the magnetic field component B_s also vanishes, while $U_s \neq 0$ and the other, where the velocity field component U_s vanishes, while $B_s \neq 0$. The former case may perhaps be connected to a dynamo process. For the kinematic dynamo, where the back-reaction of the magnetic field on the velocity field can be neglected, the (linear) stability of the velocity field

[2]This requires assuming that no cancellations occur. However, the occurrence of cancellations would require the system to be in a specific state, which is unlikely to happen frequently in a chaotic system.

coefficients u_s is only determined by hydrodynamic interactions. This point will be further discussed in sec. 3.7.

3.3.2 Linear stability analysis

In order to assess whether a given steady solution is linearly unstable in this particular setting, it is assumed without loss of generality that the coefficients u_{s_p} and b_{s_p} corresponding to wavevector $\boldsymbol{p}$ are nonzero and constant in time, that is, the linear stability of the solution $(0, U_{s_p}, 0; 0, B_{s_p}, 0)$ is studied with respect to infinitesimal perturbations of the four modes that had been set to zero. As the first-order equations (3.5)-(3.6) involve the coupling of all three modes of a given triad, little information can be obtained from them at first sight. Taking time-derivatives on both sides of eqs. (3.5)-(3.6) and subsequently substituting any occurrence of a first-order time-derivative on the RHS by the appropriate evolution equation, one obtains

$$\begin{aligned}
\partial_t^2 u_{s_k} &= |g_{kpq}|^2 (s_p p - s_q q)\Big((s_k k - s_p p)|U_{s_p}|^2 + s_q q\,|B_{s_p}|^2\Big) u_{s_k} \\
&\quad - |g_{kpq}|^2 (s_p p - s_q q)\Big((s_k k - s_p p) U_{s_p}^* B_{s_p} + s_q q\, U_{s_p} B_{s_p}^*\Big) b_{s_k} \ , \qquad (3.13) \\
\partial_t^2 b_{s_k} &= |g_{kpq}|^2 s_k k\Big(s_q q\, U_{s_p}^* B_{s_p} + (s_k k - s_p p) U_{s_p} B_{s_p}^*\Big) u_{s_k} \\
&\quad - |g_{kpq}|^2 s_k k\Big(s_q q\,|U_{s_p}|^2 + (s_k k - s_p p)|B_{s_p}|^2\Big) b_{s_k} \ . \qquad (3.14)
\end{aligned}$$

These equations do not depend on modes at wavenumber q. The evolution equations of the helical coefficients u_{s_q} and b_{s_q} can be obtained similarly and show no dependence on k, therefore attention is restricted to the evolution of u_{s_k} and b_{s_k}.

The system (3.13) and (3.14) can be written as a matrix ODE

$$\ddot{\boldsymbol{x}} = \begin{pmatrix} \alpha & \beta \\ \gamma & \delta \end{pmatrix} \boldsymbol{x} \ , \qquad (3.15)$$

where $\boldsymbol{x} \equiv (u_{s_k}, b_{s_k})$ and the matrix elements are

$$\alpha = |g_{kpq}|^2(s_p p - s_q q)\left[(s_k k - s_p p)|U_{s_p}|^2 + s_q q\,|B_{s_p}|^2\right] , \tag{3.16}$$

$$\beta = -|g_{kpq}|^2(s_p p - s_q q)\left[(s_k k - s_p p)U^*_{s_p}B_{s_p} + s_q q\,U_{s_p}B^*_{s_p}\right] , \tag{3.17}$$

$$\gamma = |g_{kpq}|^2 s_k k\left[s_q q\,U^*_{s_p}B_{s_p} + (s_k k - s_p p)U_{s_p}B^*_{s_p}\right] , \tag{3.18}$$

$$\delta = -|g_{kpq}|^2 s_k k\left[s_q q\,|U_{s_p}|^2 + (s_k k - s_p p)|B_{s_p}|^2\right] . \tag{3.19}$$

The linear stability of this system can be determined from the eigenvalues λ_1 and λ_2 of the matrix in (3.15). These eigenvalues depend not only on the helicities of the interacting modes and on the magnitudes of U_{s_p} and B_{s_p} relative to each other, but also on the alignment between the magnetic and velocity field modes at wavevector $\boldsymbol{p}$, that is, on the cross-helicity. For a given steady solution to be unstable the perturbations have to be exponentially growing, and so at least for one of the eigenvalues, $\sqrt{\lambda_i}$ (for $i = 1, 2$) must have a positive real part. The next step is to assess under which conditions this is possible.

The eigenvalues λ_i $(i = 1, 2)$ are given by

$$\lambda_{1,2} = \frac{\alpha + \delta}{2} \pm \sqrt{\frac{(\alpha + \delta)^2}{4} - \alpha\delta + \beta\gamma} . \tag{3.20}$$

For convenience define

$$x \equiv \frac{\alpha + \delta}{2} \quad \text{and} \quad Q \equiv \alpha\delta - \beta\gamma , \tag{3.21}$$

such that

$$\begin{aligned} x = & -\frac{|g_{kpq}|^2}{2}|U_{s_p}|^2[s_k k s_q q + (s_k k - s_p p)(s_q q - s_p p)] \\ & -\frac{|g_{kpq}|^2}{2}|B_{s_p}|^2[s_k k(s_k k - s_p p) + s_q q(s_q q - s_p p)] , \end{aligned} \tag{3.22}$$

and

$$Q = |g_{kpq}|^4 s_k k s_q q(s_k k - s_p p)(s_q q - s_p p)\left((|U_{s_p}|^2 + |B_{s_p}|^2)^2 - 4H_c(p)^2\right) , \tag{3.23}$$

hence the cross-helicity $H_c(p)$ enters the dynamics through the parameter Q. The derivation of (3.23) can be found in appendix A. The term $|U_{s_p}|^4 + |B_{s_p}|^4 + 2|U_{s_p}|^2|B_{s_p}|^2 - 4H_c(p)^2$ is always positive, regardless of the value of H_c since $|H_c(p)| \leqslant |U_{s_p}||B_{s_p}|$, thus the sign of Q is determined by the helicities of the interacting modes and the wavenumber ordering.

The eigenvalues λ_i can now be written more concisely as

$$\lambda_{1,2} = x \pm \sqrt{x^2 - Q} \ , \tag{3.24}$$

therefore the possibility of finding exponential solutions of the system (3.15) depends on the values of x and Q. Apart from the trivial case, where $x = 0$ and $Q = 0$, there is only one case for which no linear instability occurs: this is if $x < 0$ and $|x| > |\sqrt{x^2 - Q}|$, since then $\sqrt{\lambda_1}$ and $\sqrt{\lambda_2}$ are imaginary numbers allowing only oscillatory solutions of the matrix ODE (3.15). All other cases lead to exponentially growing as well as exponentially decaying solutions.

As can be seen from the structure of the terms x and Q, the relative magnitudes and the ordering of the wavenumbers in a given triad will influence the linear stability of the equilibria of the system (3.5)-(3.6). In view of the continuous interest in nonlocality of interactions in MHD turbulence [3, 25, 37, 53, 137], specific results for local and nonlocal interactions will be discussed where appropriate. Following Ref. [181], for wavenumbers ordered $k < p < q$, the nonlocal limit is defined as $k << p \simeq q$, while local interactions are characterised by $k \simeq p \simeq q$.

3.4 Instability and helical interactions

Since $s = \pm 1$, interactions between helical modes which all have helicities of opposite signs are not possible, and at least two modes will always have helicities of the same sign. Therefore, four classes of possible helicity combinations appear

$$s_k = s_p \neq s_q \ , \quad s_k = s_q \neq s_p \ , \quad s_k \neq s_q = s_p \quad \text{and} \quad s_k = s_q = s_p \ ,$$

each of which occurs twice as s can take the values ± 1. These four possible (classes of) combinations are now studied on a case-by-case approach in order to determine when a certain combination of helicities leads to exponentially growing solutions of the system (3.15).

3.4.1 The case $s_k = s_q \neq s_p$

Since the expressions in square brackets of (3.22) become

$$kq + (k+p)(q+p) > 0 \quad \text{and } k(k+p) + q(q+p) > 0 \ , \tag{3.25}$$

one obtains $x = (\alpha + \delta)/2 < 0$. For an unstable equilibrium $|x| < |\sqrt{x^2 - Q}|$ is required, however, $Q > 0$ since

$$Q \sim s_k s_q kq(s_k k - s_p p)(s_q q - s_p p) \ , \tag{3.26}$$

which is positive for $s_k = s_q \neq s_p$. Furthermore $Q < x^2$ (see appendix B.1) and thus $|x| > |\sqrt{x^2 - Q}|$, which results in negative eigenvalues of the matrix in eq. (3.15). Therefore there are no exponentially growing solutions of eq. (3.15) for the case $s_k = s_q \neq s_p$, and this is independent of the ordering of the wavenumbers k, p and q. This implies that exponentially growing solutions of eq. (3.15) are impossible if the perturbations u_{s_k}, u_{s_q}, b_{s_k} and b_{s_q} have helicities opposite to the helicities of the modes U_{s_p} and B_{s_p} constituting the equilibrium point.

For the remaining helicity combinations, which do result in instabilities, the ordering of wavenumbers matters. The arguments used to decide whether or not an exponentially growing solution becomes possible are similar to the procedure used for the case $s_k = s_q \neq s_p$ described above.

3.4.2 The case $s_k \neq s_p = s_q$

In this case

$$Q \sim kq(k+p)(q-p) \ , \tag{3.27}$$

and

$$x = -\frac{|g_{kpq}|^2}{2}|U_{s_p}|^2[-kq-(k+p)(q-p)] - \frac{|g_{kpq}|^2}{2}|B_{s_p}|^2[k(k+p)+q(q-p)] \ . \tag{3.28}$$

The linear stability of a steady solution depends on the signs of these terms which in turn depend on wavenumber ordering, cross-helicity and the ratio $|U_{s_p}|/|B_{s_p}|$.

- For $k < p < q$ instabilities occur if $|U_{s_p}| \gtrapprox |B_{s_p}|$, since then $x > 0$. For $|B_{s_p}| > |U_{s_p}|$ instabilities are still possible, provided $H_c(p)$ is small and $|B_{s_p}|$ not much larger than $|U_{s_p}|$. Thus in regions of large cross-helicity

instabilities only occur for weak magnetic fields. The method by which these results are obtained is explained in appendix B.2.

For nonlocal interactions ($k << p \simeq q$) the term Q vanishes, hence the sign of x determines whether instabilities occur. The term x is now of the form

$$x \simeq \frac{|g_{kpq}|^2}{2} kq(|U_{s_p}|^2 - |B_{s_p}|^2) \ , \tag{3.29}$$

hence nonlocal interactions lead to instabilities if $|B_{s_p}| < |U_{s_p}|$.

- For $k < q < p$, Q will become negative, leading to unstable solutions regardless of the ratio $|U_{s_p}|/|B_{s_p}|$ and the value of $H_c(p)$.

- For $p < k < q$, again instabilities are possible if $|U_{s_p}| \gtrapprox |B_{s_p}|$, since then $x > 0$. For $|B_{s_p}| > |U_{s_p}|$ instabilities are still possible, provided $H_c(p)$ is small and $|B_{s_p}|/|U_{s_p}|$ not $>> 1$ (see appendix B.2). Nonlocal interactions ($p << k \simeq q$) lead to instabilities if $|U_{s_p}| > |B_{s_p}|$, because then

$$x \simeq |g_{kpq}|^2 k^2 (|U_{s_p}|^2 - |B_{s_p}|^2) > 0 \ . \tag{3.30}$$

In summary, a given steady solution in this case is less likely to be unstable if the nonzero mode is at medium or low wavenumbers in regions of high cross-helicity.

3.4.3 The case $s_k = s_p = s_q$

In this case

$$Q \sim kq(k-p)(q-p) \ , \tag{3.31}$$

and

$$x = -\frac{|g_{kpq}|^2}{2}|U_{s_p}|^2[kq+(k-p)(q-p)] - \frac{|g_{kpq}|^2}{2}|B_{s_p}|^2[k(k-p)+q(q-p)] \ . \tag{3.32}$$

- For $k < p < q$ we obtain $Q < 0$ and thus $x + \sqrt{x^2 - Q} \geqslant 0$, leading to exponentially growing solutions independent of $H_c(p)$ and the ratio $|U_{s_p}|/|B_{s_p}|$. In the present case both velocity and magnetic field modes have positive and negative contributions to the sign of x. For both local ($k \simeq p \simeq q$) and nonlocal ($k << p \simeq q$) interactions $Q = 0$ and the sign of x determines whether unstable solutions occur. For the nonlocal case only

the magnetic field term is positive, and x has the form

$$x \simeq \frac{|g_{kpq}|^2}{2} kq(|B_{s_p}|^2 - |U_{s_p}|^2) \ . \tag{3.33}$$

leading to unstable solutions if $|B_{s_p}| > |U_{s_p}|$, while for local interactions no instability occurs as the only term in x that does not vanish is $-|g_{kpq}|^2 |U_{s_p}|^2 kq < 0$.

- For $k < q < p$, the possibility of exponentially growing solutions depends on the ratio $|U_{s_p}|/|B_{s_p}|$ and on the relative magnitudes of the wavenumbers k,p and q, as now $Q > 0$. Since the magnetic field term in x is now positive, instabilities occur for $|U_{s_p}|/|B_{s_p}| < 1$. If $|U_{s_p}|/|B_{s_p}| > 1$ it depends also on the cross-helicity whether instabilities occur. For maximal $H_c(p)$ one obtains $x^2 - Q > 0$, hence the perturbations cannot grow exponentially. If $H_c(p) = 0$ and $|U_{s_p}|/|B_{s_p}|$ is not too small, instabilities will occur, depending also on the shape of the triad (see appendix B.2 for further details). In general, the smaller $|U_{s_p}|/|B_{s_p}|$ the more unstable is the solution.

- For $p < k < q$ we obtain $x < 0$ and $Q > 0$, furthermore $x^2 - Q > 0$ independent of $|U_{s_p}|/|B_{s_p}|$ and $H_c(p)$ (see appendix B.1), thus no linear instabilities occur. Nonlocal interactions ($p << k \simeq q$) do not lead to instabilities, since

$$x \simeq -|g_{kpq}|^2 [k^2 - kp](|U_{s_p}|^2 + |B_{s_p}|^2) < 0 \ . \tag{3.34}$$

3.4.4 The case $s_k = s_p \neq s_q$

The terms determining the stability in this case are

$$Q \sim kq(k-p)(q+p) \ , \tag{3.35}$$

and

$$x = -\frac{|g_{kpq}|^2}{2} |U_{s_p}|^2 [-kq - (k-p)(q+p)] - \frac{|g_{kpq}|^2}{2} |B_{s_p}|^2 [k(k-p) + q(q+p)] \ . \tag{3.36}$$

- For $k < p < q$ instabilities occur independent of the ratio $|U_{s_p}|/|B_{s_p}|$, and since both magnetic and velocity field terms have positive and negative contributions to the sign of x, the situation is similar to the previous case. However, in the present case $Q \simeq 0$ only for local ($k \simeq p \simeq q$) interactions.

Helicities	H_c	constraint	stability
$s_k \neq s_q = s_p$	n/a	$\lvert U_{s_p}\rvert/\lvert B_{s_p}\rvert \gtrapprox 1$	unstable
	max	$\lvert B_{s_p}\rvert > \lvert U_{s_p}\rvert$	not unstable
	0	$\lvert B_{s_p}\rvert/\lvert U_{s_p}\rvert$ not $>> 1$	unstable
$s_k = s_p \neq s_q$	n/a	n/a	unstable
$s_k = s_q = s_p$	n/a	n/a	unstable

Table 3.1 *Summary of possible instabilities for the middle wavenumber modes $k < p < q$.*

It is now the velocity field term $|g_{kpq}|^2|U_{s_p}|^2 kq > 0$ which ensures that exponentially growing solutions of eq. (3.15) exist for local interactions provided $|U_{s_p}| > 2|B_{s_p}|$.

- For $k < q < p$ the result is the same, since reversing the relative ordering of p and q does not change the sign of Q. That is, exponentially growing solutions occur.

- For $p < k < q$ the term Q is positive and the term proportional to $|U_{s_p}|^2$ is positive while the term proportional to $|B_{s_p}|^2$ is negative. Thus instabilities occur if $|U_{s_p}|/|B_{s_p}| \gtrapprox 1$. For $|U_{s_p}|/|B_{s_p}| < 1$ the occurrence of instabilities depends on the value of $H_c(p)$. If $H_c(p)$ is maximal and the magnetic and velocity field are fully aligned, exponential growth of the perturbations does not occur. For zero cross-helicity and $|B_{s_p}|$ being not much larger than $|U_{s_p}|$, the equilibria are linearly unstable (see appendix B.2).

  This type of helicity combination is another possibility for nonlocal interactions of the type $p << k \simeq q$ leading to exponentially growing solutions if $|U_{s_p}| > |B_{s_p}|$, since then

$$x \simeq |g_{kpq}|^2 k^2 (|U_{s_p}|^2 - |B_{s_p}|^2) > 0 \ . \tag{3.37}$$

The results of the dependence of the occurrence of instabilities on combinations of helicities, wavenumber ordering, relative magnitudes of the $\boldsymbol{u}$ and $\boldsymbol{b}$ modes and cross-helicities at wavenumber p are summarised in tables 3.1-3.3.

Helicities	H_c	constraint	stability
$s_k \neq s_q = s_p$	n/a	n/a	unstable
$s_k = s_p \neq s_q$	n/a	n/a	unstable
$s_k = s_q = s_p$	n/a	$\|B_{s_p}\| > \|U_{s_p}\|$	unstable
	max	$\|U_{s_p}\| > \|B_{s_p}\|$	not unstable
	0	$\|U_{s_p}\|/\|B_{s_p}\|$ not $>> 1$	unstable

Table 3.2 *Summary of possible instabilities for the largest wavenumber modes $k < q < p$.*

Helicities	H_c	constraint	stability
$s_k \neq s_q = s_p$	n/a	$\|U_{s_p}\|/\|B_{s_p}\| \gtrapprox 1$	unstable
	max	$\|B_{s_p}\| > \|U_{s_p}\|$	not unstable
	0	$\|B_{s_p}\|/\|U_{s_p}\|$ not $>> 1$	unstable
$s_k = s_p \neq s_q$	n/a	$\|U_{s_p}\|/\|B_{s_p}\| \gtrapprox 1$	unstable
	max	$\|B_{s_p}\| > \|U_{s_p}\|$	not unstable
	0	$\|B_{s_p}\|/\|U_{s_p}\|$ not $>> 1$	unstable
$s_k = s_q = s_p$	n/a	n/a	not unstable

Table 3.3 *Summary of possible instabilities for the smallest wavenumber modes $p < k < q$.*

3.5 Energy transfers and the instability assumption

In order to use the results of the previous section to derive results for the transfers of the ideal invariants total energy E and magnetic helicity H_{mag}, the *instability assumption* [181] is invoked. This assumption asserts that energy is transferred away from the mode at an unstable equilibrium into the other two modes it is coupled to by a triad interaction given through the system (3.5)-(3.6).

Therefore the results of the stability analysis determine whether a given helicity combination mainly contributes to forward or reverse transfer of energy. That is, if a steady solution at wavenumber p is unstable and energy is transferred away from B_{s_p} and U_{s_p} into the modes they interact with (note that B_{s_p} and U_{s_p} do not interact with each other directly), then the wavenumber ordering $k < q < p$ results in reverse transfer of energy, while $p < k < q$ results in forward transfer and $k < p < q$ in a split transfer with contributions to forward and reverse directions of energy transfer.

Several immediate results can be deduced from the summary of the stability analysis for the different helicity combinations presented in tables 3.1-3.3. First,

unlike in non-conducting fluids modes corresponding to the largest wavenumber in a given triad can be unstable, leading to more possibilities for reverse spectral energy transfer in MHD compared to hydrodynamics, thus *MHD flows should be more likely to self-organise*. Second, all three helicities influence the direction of energy transfers, and reverse transfers are also possible for cases of unlike helicities. Third, forward transfers appear to be more quenched in regions of high cross-helicity than reverse transfers. Fourth, very nonlocal triads contribute mainly to reverse transfers in magnetically dominated systems through interactions of modes with like helicity. They only contribute to forward transfers through interactions of modes with unlike helicity and mostly if the kinetic energy is larger than the magnetic energy. Therefore, reverse spectral transfer becomes much more likely in MHD turbulence than in turbulence of non-conducting fluids, which reflects the predictions from absolute equilibrium spectra [73, 189] and the well-established numerical results on inverse cascades, and more generally reverse transfer, in MHD turbulence [4, 10, 12, 25, 27, 137, 149, 150].

The transfer directions deduced so far may or may not contribute to forward and inverse cascades of energy and magnetic helicity, as no information on the constancy, or otherwise, of the fluxes of these quantities through a given wavenumber is available at this point. The aim of the next section is to determine the contribution of the individual transfers to energy and magnetic helicity *cascades*.

3.6 Transfer and cascades of total energy and magnetic helicity

In order to determine the contribution of a given interaction of helical modes to energy and magnetic helicity cascades, the fluxes of these quantities need to be calculated and studied in the respective inertial ranges where they are wavenumber-independent. However, several technical details need to be discussed before proceeding to this calculation.

In the discrete Fourier representation the evolution equations of the kinetic and magnetic energy spectra $E_{kin}(k)$ and $E_{mag}(k)$ are obtained by multiplying the relevant equations in the system (3.5) by $u^*_{s_k}$ and $b^*_{s_k}$, respectively, then summing over all triads and helicity combinations and finally carrying out shell- and

ensemble averages. For the kinetic energy spectrum this leads to

$$\partial_t E_{kin}(k) = \frac{1}{2} \sum_{p,q}^{\Delta} \sum_{i=1}^{8} (t_{HD}^{(i)}(k,p,q) + t_{LF}^{(i)}(k,p,q)) \ , \tag{3.38}$$

where $\sum_{p,q}^{\Delta}$ denotes a sum over all wavenumbers p and q whose wavevectors $\boldsymbol{p}$ and $\boldsymbol{q}$ form a triad with $\boldsymbol{k}$ such that $\boldsymbol{k}+\boldsymbol{p}+\boldsymbol{q}=0$ and the superscript (i) labels the eight possible helicity combinations. The transfer terms in this equation are given by

$$t_{HD}^{(i)}(k,p,q) = (s_p p - s_q q) \sum_{S(k,p,q)} g_{kpq} \langle u_{s_k} U_{s_p} u_{s_q} \rangle + \text{c.c.} \ , \tag{3.39}$$

and

$$t_{LF}^{(i)}(k,p,q) = -(s_p p - s_q q) \sum_{S(k,p,q)} g_{kpq} \langle u_{s_k} B_{s_p} b_{s_q} \rangle + \text{c.c.} \ , \tag{3.40}$$

where $S(k,p,q)$ indicates a summation over all wavevectors in shells of radius k, p and q and c.c. denotes the complex conjugate. Homogeneity allows the summation over the shells without explicitly restricting the sum to wavevectors satisfying $\boldsymbol{k}+\boldsymbol{p}+\boldsymbol{q}=0$, since triple correlations with $\boldsymbol{k}+\boldsymbol{p}+\boldsymbol{q} \neq 0$ vanish for homogeneous MHD as shown in chapter 1.3.2. For the magnetic energy spectrum one obtains

$$\partial_t E_{mag}(k) = \frac{1}{2} \sum_{p,q}^{\Delta} \sum_{i=1}^{8} t_{mag}^{(i)}(k,p,q) \ , \tag{3.41}$$

where

$$t_{mag}^{(i)}(k,p,q) = -s_k k \sum_{S(k,p,q)} g_{kpq} \langle b_{s_k} B_{s_p} u_{s_q} - b_{s_k} U_{s_p} b_{s_q} \rangle + \text{c.c.} \ . \tag{3.42}$$

The evolution equation for the total energy spectrum $E(k) = E_{kin}(k) + E_{mag}(k)$ is given by the sum of the respective evolution equations for $E_{kin}(k)$ and $E_{mag}(k)$

$$\partial_t E(k) = \frac{1}{2} \sum_{p,q}^{\Delta} \sum_{i=1}^{8} t^{(i)}(k,p,q) \ , \tag{3.43}$$

and the total energy transfer term $t^{(i)}(k,p,q)$ consists of the sum of the three transfer terms $t_{HD}^{(i)}(k,p,q)$, $t_{LF}^{(i)}(k,p,q)$ and $t_{mag}^{(i)}(k,p,q)$.

These terms are still written in the discrete Fourier representation of the magnetic and velocity fields. However, the calculation of the energy and magnetic helicity

fluxes requires a continuous Fourier representation. The continuous transfer terms are given in terms of Fourier integrals and can formally be obtained by taking the period L to infinity, assuming that the respective integrals are well-defined. The sums then become integrals and the continuous counterpart of e.g. the hydrodynamic transfer term $t_{HD}^{(i)}$ becomes

$$\begin{aligned} T_{HD}^{(i)}(k,p,q)dk\ dp\ dq &= \lim_{L\to\infty} t_{HD}^{(i)}(k,p,q) \\ &= (s_p p - s_q q) \int_{|\boldsymbol{k}|=k} d\boldsymbol{k} \int_{|\boldsymbol{p}|=p} d\boldsymbol{p} \int_{|\boldsymbol{q}|=q} d\boldsymbol{q}\ g_{kpq} \langle u_{s_k} U_{s_p} u_{s_q} \rangle + \text{c.c.}\ . \end{aligned} \tag{3.44}$$

The transfer terms $T_{LF}^{(i)}$ and $T_{mag}^{(i)}$ are obtained analogously.

3.6.1 Total energy transfer

In the absence of dissipation the total energy is conserved and the transfer term $T(k,p,q)$ in the spectral evolution equation of the total energy redistributes energy between the Fourier modes and vanishes if integrated over all space. Therefore the flux of total energy through wavenumber k due to a given interaction (i),

$$\Pi^{(i)}(k) = -\int_0^k dk' \int_k^\infty \int_k^\infty T^{(i)}(k',p,q) dp dq\ , \tag{3.45}$$

can be written as the sum of two contributions: the flux of total energy into all modes at wavenumber k' due to triads with $p,q < k < k'$ minus the flux of total energy into all modes at k' due to triads with $k' < k < p,q$

$$\Pi^{(i)}(k) = \frac{1}{2}\int_k^\infty dk' \int_0^k \int_0^k T^{(i)}(k',p,q) dp\ dq - \frac{1}{2}\int_0^k dk' \int_k^\infty \int_k^\infty T^{(i)}(k',p,q) dp\ dq\ . \tag{3.46}$$

The next step consists of a procedure introduced by Waleffe [181] which renders the two integrals in eq. (3.46) independent of k. This is achieved using a scaling argument, where the two integrals are treated separately. For conciseness the procedure is outlined briefly for the first integral on the RHS of (3.46), the full derivation can be found in appendix C. The aim is to express the transfer function

in the first integral on the RHS of (3.46) in terms of new variables

$$v = \frac{q}{p}, \quad w = \frac{k'}{p}, \quad u = \frac{k}{p} \ , \tag{3.47}$$

in order to remove k from the integration limits. Since $T^{(i)}_{HD}(k', p, q)$ may scale differently compared to $T^{(i)}_{LF}(k', p, q)$ and $T^{(i)}_{mag}(k', p, q)$, the term $T^{(i)}(k', p, q)$ in (3.46) must be replaced by the individual transfer terms. The transfer terms are now expressed individually in terms of the new variables u, v and w

$$T^{(i)}_{HD}(k', p, q) = p^{-\beta} T^{(i)}_{HD}(w, 1, v) = \left(\frac{k}{u}\right)^{-\beta} T^{(i)}_{HD}(w, 1, v) \ , \tag{3.48}$$

$$T^{(i)}_{LF}(k', p, q) = p^{-\beta'} T^{(i)}_{LF}(w, 1, v) = \left(\frac{k}{u}\right)^{-\beta'} T^{(i)}_{LF}(w, 1, v) \ , \tag{3.49}$$

and

$$T^{(i)}_{mag}(k', p, q) = p^{-\beta'} T^{(i)}_{mag}(w, 1, v) = \left(\frac{k}{u}\right)^{-\beta'} T^{(i)}_{mag}(w, 1, v) \ , \tag{3.50}$$

where β is related to the exponent of the kinetic energy spectrum provided it has a power-law dependence on k, while the exponent β' is related to the exponents of the kinetic *and* magnetic energy spectra as explained in further detail in appendix C. In order to write down (3.48)-(3.50) it is assumed that both the magnetic energy spectrum and the kinetic energy spectrum display power law scaling in the inertial range. This assumption is made solely to allow estimates of the direction of the flux. The first term on the RHS of (3.46) then becomes

$$\begin{aligned}
&\frac{1}{2} \int_k^\infty dk' \int_0^k \int_0^k T^{(i)}(k', p, q) \; dp \; dq \\
&\quad = k^{3-\beta} \int_0^1 dv \int_1^{1+v} dw \int_1^w du \left(\frac{1}{u}\right)^{4-\beta} T^{(i)}_{HD}(w, 1, v) \\
&\qquad + k^{3-\beta'} \int_0^1 dv \int_1^{1+v} dw \int_1^w du \left(\frac{1}{u}\right)^{4-\beta'} \left[T^{(i)}_{LF}(w, 1, v) + T^{(i)}_{mag}(w, 1, v)\right] \ .
\end{aligned} \tag{3.51}$$

The second term on the RHS of (3.46) can be treated similarly [181], leading to

$$\begin{aligned}
&\frac{1}{2}\int_0^k dk' \int_k^\infty \int_k^\infty T^{(i)}(k',p,q)\; dp\; dq \\
&\quad = k^{3-\beta}\int_0^1 dv \int_1^{1+v} dw \int_v^1 du \left(\frac{1}{u}\right)^{4-\beta} T^{(i)}_{HD}(v,1,w) \\
&\qquad + k^{3-\beta'}\int_0^1 dv \int_1^{1+v} dw \int_v^1 du \left(\frac{1}{u}\right)^{4-\beta'} \left[T^{(i)}_{LF}(v,1,w) + T^{(i)}_{mag}(v,1,w)\right] .
\end{aligned} \tag{3.52}$$

The detailed derivations leading to eqs. (3.51) and (3.52) are contained in appendix C.

Combining the two results and integrating over u yields the following expression for the total energy transfer flux

$$\begin{aligned}
\Pi^{(i)}(k) =& k^{3-\beta}\int_0^1 dv \int_1^{1+v} dw \left(T^{(i)}_{HD}(w,1,v)\left[\frac{w^{\beta-3}-1}{\beta-3}\right] + T^{(i)}_{HD}(v,1,w)\left[\frac{v^{\beta-3}-1}{\beta-3}\right]\right) \\
&+ k^{3-\beta'}\int_0^1 dv \int_1^{1+v} dw \left(T^{(i)}_{LF}(w,1,v) + T^{(i)}_{mag}(w,1,v)\right)\left[\frac{w^{\beta'-3}-1}{\beta'-3}\right] \\
&+ k^{3-\beta'}\int_0^1 dv \int_1^{1+v} dw \left(T^{(i)}_{LF}(v,1,w) + T^{(i)}_{mag}(v,1,w)\right)\left[\frac{v^{\beta'-3}-1}{\beta'-3}\right] ,
\end{aligned} \tag{3.53}$$

where $0 \leqslant v \leqslant 1 \leqslant w \leqslant 1+v$ due to the triad geometry. This now enables the study of the contribution to the total energy transfer from a given interaction (i), where the scaling of the magnetic and kinetic energy spectra will influence the transfer through the exponents β and β'. In the inertial range of total energy the energy transfer flux through a given wavenumber k does not depend on that wavenumber, which leads to the characteristic values of the scaling exponents $\beta' = \beta = 3$, making the split of the total energy transfer term into its individual components redundant in this wavenumber range. In sec. 3.6.3 the contributions of the different interactions to transfers in the inertial range of total energy are calculated. This requires $\beta = 3$, necessarily taking into account only the region in wavenumber space where this scaling is established. Since the values of β and β' may influence the direction of energy transfer, a similar approach may be useful to calculate energy and helicity transfer at the very low wavenumbers. However, this awaits consensus on the low-wavenumber scaling of the magnetic and kinetic energy spectra. Furthermore, the integrals must be cut off at some wavenumber such that a single scaling exponent for the wavenumber range of interest can be

studied. As the extent of the inertial range will grow with increasing Reynolds number, contributions from the production and dissipation ranges can safely be neglected, as they will become very small compared to the extent of the inertial range. However, in the low wavenumber region, this argument is not applicable and further work is necessary in order to establish if very nonlocal interactions contribute significantly to the transfers of magnetic energy and helicity in the low wavenumber range or not.

3.6.2 Magnetic helicity transfer

Using the decomposition into helical modes, the transfer term in the evolution equation of the magnetic helicity can be expressed through the transfer term in the evolution equation of the magnetic energy, that is

$$T_H^{(i)}(k,p,q) = \frac{s_k}{k} T_{mag}^{(i)}(k,p,q) \ , \tag{3.54}$$

and only the transfer term which originates from the induction equation is present. Since H_{mag} is a purely magnetic quantity, it depends only implicitly on the evolution of the velocity field.

Since the magnetic helicity is an ideal invariant, the transfer term in the spectral evolution equation of the magnetic helicity vanishes if integrated over all space, therefore similar to the flux of total energy, the flux of magnetic helicity through wavenumber k due to a given interaction (i),

$$\Pi_H^{(i)}(k) = -\int_0^k \frac{s_{k'}}{k'} dk' \int_k^\infty \int_k^\infty T_{mag}^{(i)}(k',p,q) dp dq \ , \tag{3.55}$$

can be written as the sum of two contributions

$$\begin{aligned} \Pi_H^{(i)}(k) =& \frac{1}{2} \int_k^\infty \frac{s_{k'}}{k'} dk' \int_0^k \int_0^k T_{mag}^{(i)}(k',p,q) dp \ dq \\ & - \frac{1}{2} \int_0^k \frac{s_{k'}}{k'} dk' \int_k^\infty \int_k^\infty T_{mag}^{(i)}(k',p,q) dp \ dq \ . \end{aligned} \tag{3.56}$$

Following the approach explained in sec. 3.6.1 the integral becomes independent of k and one obtains the following expression for the flux of magnetic helicity

through k

$$\Pi_H(k) = k^{2-\beta'} \int_0^1 dv \int_1^{1+v} \frac{dw}{w} \times \left(s_w T^{(i)}_{mag}(w,1,v) \left[\frac{w^{\beta'-2}-1}{\beta'-2} \right] + s_v T^{(i)}_{mag}(v,1,w) \left[\frac{v^{\beta'-2}-1}{\beta'-2} \right] \right) . \tag{3.57}$$

3.6.3 Cascades and wavenumber-dependent transfers of total energy and magnetic helicity

From the expressions (3.53) and (3.57) for the fluxes of total energy and magnetic helicity, respectively, it is now possible to determine the sign of the fluxes and hence the direction of energy and magnetic helicity transfers using the results from the stability analysis. If the total energy flux is positive, energy is transferred from smaller to larger wavenumbers and if it is negative, energy is transferred from larger to smaller wavenumbers. As the magnetic helicity is not positive definite, the situation is slightly different. For positive magnetic helicity a positive flux indicates forward transfer just as for the total energy. For negative magnetic helicity a negative flux indicates forward transfer while a positive flux indicates inverse transfer. However, as this situation is symmetric, positive helicity is assumed throughout the analysis.

In sec. 3.5 unstable solutions of (3.5) and (3.6) were interpreted as leading to energy transfer out of the unstable mode into the two modes it interacts with for a given helical mode interaction (i). If U_{s_p} and B_{s_p} are the unstable modes, this interpretation leads to

$$\partial_t |B_{s_p}|^2 = T^{(i)}_{mag}(p,k,q) < 0 , \tag{3.58}$$

and

$$\partial_t |U_{s_p}|^2 = T^{(i)}_{HD}(p,k,q) + T^{(i)}_{LF}(p,k,q) < 0 . \tag{3.59}$$

The instability assumption therefore attributes signs to the transfer terms, which will determine their respective contributions to the overall energy (and magnetic helicity) transfer. Note that $\partial_t |U_{s_p}|^2$ and $\partial_t |B_{s_p}|^2$ cannot have different signs, as both signs are determined from the existence of exponentially growing solutions of the system (3.15).

The helicity combinations are now treated separately assuming $s_p = 1$ without loss of generality. Having determined the signs of the transfer terms within this framework, these results can now be used to calculate the contributions of the individual transfer terms to the fluxes of total energy and magnetic helicity though a given wavenumber.

Total energy cascades

For the (inertial range) energy cascade the flux is wavenumber-independent leading to $\beta = 3$ in (3.53). Hence the integrand in (3.53), which determines the sign of the total energy flux, becomes

$$I_E = T^{(i)}(w, 1, v) \ln w + T^{(i)}(v, 1, w) \ln v \ , \tag{3.60}$$

where the triad geometry imposes the wavenumber ordering $v \leqslant 1 \leqslant w \leqslant 1 + v$. That is, the term $T^{(i)}(w, 1, v)$ describes energy transfer in and out of the largest wavenumber modes while $T^{(i)}(v, 1, w)$ describes energy transfer in and out of the smallest wavenumber modes.

Using the signs of the transfer terms determined for the three helicity combinations depending on wavenumber ordering, helicity combinations contributing to forward or inverse cascades of total energy can now be identified.

- $s_v = s_1 = s_w$
  For this case the results of the stability analysis summarised in tables 3.1-3.3 imply $T^{(i)}(1, v, w) < 0$, as modes corresponding to the middle wavenumber are unstable, while $T^{(i)}(v, 1, w) > 0$, as modes corresponding to the smallest wavenumber are stable and hence these modes can only receive energy from the modes at higher wavenumbers. The sign of $T^{(i)}(w, 1, v)$ depends on the values of cross-helicity and the ratio of magnetic to kinetic energy. For a magnetically dominated system $T^{(i)}(w, 1, v) < 0$ and this case results in an inverse cascade of total energy, as

  $$I_E = T^{(i)}(w, 1, v) \ln w + T^{(i)}(v, 1, w) \ln v < 0 \ . \tag{3.61}$$

  If the kinetic energy is much larger than the magnetic energy, cancellations between the two terms in I_E occur. The term $T^{(i)}(w, 1, v) \ln w$ is now positive, since the modes at the largest wavenumber can only receive energy,

thus contributing to a forward cascade. For intermediate cases the value of the cross-helicity becomes decisive as high cross-helicity quenches the inverse transfer in this case. In summary, inverse cascade contributions from this combination of helicities are expected if the magnetic energy dominates, while for larger kinetic energy high values of cross-helicity quench the inverse transfer contribution to some extent.

- $s_v \neq s_1 = s_w$
  From tables 3.1-3.3 the instability assumption imposes $T^{(i)}(w,1,v) < 0$ and $T^{(i)}(v,1,w) > 0$ as modes corresponding to the largest wavenumbers are unstable, while modes corresponding to the smallest wavenumber are stable. This implies

$$I_E = T^{(i)}(w,1,v)\ln w + T^{(i)}(v,1,w)\ln v < 0 \ , \tag{3.62}$$

  hence this combination of helicities leads to an inverse energy cascade as $I_E < 0$, and this case behaves differently to its hydrodynamic analogue, where it led to an inverse cascade of kinetic energy [181] for nonlocal interactions and a direct cascade for local interactions. Furthermore, this inverse cascade should always be present, as it is not subject to constraints from $H_c(p)$ and $|U_{s_p}|/|B_{s_p}|$.

- $s_v = s_1 \neq s_w$
  Analogously, one obtains $T^{(i)}(1,v,w) < 0$ and $T^{(i)}(w,1,v) > 0$, since the modes corresponding to the middle wavenumber are unstable while modes corresponding to the largest wavenumber are stable. As the stability of the remaining transfer term $T^{(i)}(v,1,w)$ depends on several constraints, no clear assessment is possible. If the lowest wavenumber modes are assumed to be unstable, that is $T^{(i)}(v,1,w) < 0$, this case contributes towards a direct cascade. However, if they are stable, contributions to inverse and direct cascades are possible. The instability leading to forward transfer in this case is damped by high values of $H_c(p)$.

- $s_1 \neq s_w = s_v$
  In this case the stability analysis leads to $T^{(i)}(1,v,w) > 0$ and $T^{(i)}(w,1,v) < 0$, since the modes corresponding to the middle wavenumber are stable while modes corresponding to the largest wavenumber are unstable. Again the sign of the remaining transfer term $T^{(i)}(v,1,w)$ depends on several constraints. If the lowest wavenumber modes are assumed to be receiving

energy, that is $T^{(i)}(v,1,w) > 0$, a contribution towards an inverse cascade is obtained. However, they are unstable and thus losing energy, contributions to inverse and direct cascades are possible. Now the instability leading to inverse transfer is damped by high values of $H_c(p)$.

Magnetic helicity transfer in the inertial range of total energy

For $\beta' = 3$, the integrand I_H in (3.57) becomes

$$I_H = T^{(i)}_{mag}(w,1,v)s_w(w-1) + T^{(i)}_{mag}(v,1,w)s_v(v-1)\ . \tag{3.63}$$

Using the signs of the transfer terms determined for the three helicity combinations, helicity combinations contributing to a forward or an inverse cascade of magnetic helicity can now be identified. As can be seen in (3.63), there is an explicit dependence of the magnetic helicity flux on the helicities of the interacting modes. In the following $s_1 = 1$ is assumed, that is, positive magnetic helicity at the intermediate wavenumber.

- $s_v = s_1 = s_w$
  The integrand I_H becomes

  $$I_H = T^{(i)}_{mag}(w,1,v)(w-1) + T^{(i)}_{mag}(v,1,w)(v-1)\ . \tag{3.64}$$

  As the signs of the magnetic energy transfer term deduced from the stability analysis are the same as for the total energy and $\ln w$ and $w-1$ are both positive while $\ln v$ and $v-1$ are both negative, the result for the helicity transfer reflects the results for the total energy cascade. Thus, for this helicity combination, total energy and magnetic helicity will be transferred in the same direction, which can be both forward and inverse in this case.

- $s_v \neq s_1 = s_w$
  The integrand I_H becomes

  $$I_H = T^{(i)}_{mag}(w,1,v)(w-1) - T^{(i)}_{mag}(v,1,w)(v-1)\ , \tag{3.65}$$

  where the contributions from the smallest wavenumber modes now enter with the opposite sign. Compared to the total energy flux, which was purely inverse in this case, now a forward helicity flux and an inverse energy flux may occur simultaneously.

- $s_v = s_1 \neq s_w$
  The integrand I_H becomes

$$I_H = -T^{(i)}_{mag}(w, 1, v)(w - 1) + T^{(i)}_{mag}(v, 1, w)(v - 1) \ , \tag{3.66}$$

  where the contributions from the largest wavenumber modes now enter with the opposite sign. Compared to the total energy cascade, again it is possible that magnetic helicity and total energy are transferred in opposite directions.

- $s_1 \neq s_w = s_v$
  The integrand I_H becomes

$$I_H = -T^{(i)}_{mag}(w, 1, v)(w - 1) - T^{(i)}_{mag}(v, 1, w)(v - 1) \ , \tag{3.67}$$

  where the contributions from both transfer terms now enter with the opposite sign. That is, magnetic helicity and total energy are transferred in opposite directions.

In this subsection we determined the direction of the magnetic helicity transfer in the inertial range of total energy for different combinations of helicities and compared the results to those for the total energy cascade. It is found that a cascade of total energy is possible in one direction while the transfer of magnetic helicity may proceed in the opposite direction. A similar result had been obtained in hydrodynamics [181].

Magnetic helicity cascades

In the inertial range of magnetic helicity the flux of magnetic helicity is wavenumber-independent resulting in $\beta' = 2$ in (3.57). Therefore the integrand I_H in (3.57) becomes

$$I_H = T^{(i)}_{mag}(w, 1, v)s_w \ln w + T^{(i)}_{mag}(v, 1, w)s_v \ln v \ . \tag{3.68}$$

For the different helicity combinations this leads to

- $s_v = s_1 = s_w$
  The integrand in this case is of the same form as the integrand I_E for the

total energy cascade (that is, if $\beta = 3$ in I_E)

$$I_H = T^{(i)}_{mag}(w, 1, v) \ln w + T^{(i)}_{mag}(v, 1, w) \ln v \ , \tag{3.69}$$

hence the results for the cascades of magnetic helicity are the same as for the cascades of total energy.

- $s_v \neq s_1 = s_w$
  The integrand in this case has a different form compared to the integrand I_E for the total energy

$$I_H = T^{(i)}_{mag}(w, 1, v) \ln w - T^{(i)}_{mag}(v, 1, w) \ln v \ , \tag{3.70}$$

  hence the results for the cascades of magnetic helicity are different from the total energy cascades. In particular, this case may lead to a nonhelical reverse energy transfer while the helicity cascade may be forwards, due to the contribution from $T^{(i)}_{mag}(v, 1, w)$ now having the opposite sign in I_H compared to I_E.

- $s_v = s_1 \neq s_w$
  Again, the integrand in this case has a different form compared to the integrand I_E for the total energy

$$I_H = -T^{(i)}_{mag}(w, 1, v) \ln w + T^{(i)}_{mag}(v, 1, w) \ln v \ , \tag{3.71}$$

  hence the results for the cascades of magnetic helicity differ from the total energy cascades. In particular, this case may lead to a forward energy transfer while the helicity cascade may be backwards, due to the contribution from $T^{(i)}_{mag}(w, 1, v)$ now having the opposite sign in I_H compared to I_E.

- $s_1 \neq s_w = s_v$
  Now I_H and I_E have opposite signs

$$I_H = -T^{(i)}_{mag}(w, 1, v) \ln w - T^{(i)}_{mag}(v, 1, w) \ln v = -I_E \ , \tag{3.72}$$

  hence this case leads to helicity transfer and energy transfer in opposite directions.

Magnetic energy transfer in the inertial range of magnetic helicity

For $\beta' = 2$, the contributions to the integrand I_E due to magnetic energy transfer are

$$I_{E_{mag}} = -T^{(i)}_{mag}(w,1,v)\left(\frac{1}{w}-1\right) - T^{(i)}_{mag}(v,1,w)\left(\frac{1}{v}-1\right) \ . \tag{3.73}$$

The signs of T_{mag} and T are the same by eqs. (3.58)-(3.59), and $\ln w$ and $w-1$ are both positive while $\ln v$ and $v-1$ are both negative. Hence, the result for the contributions of these terms to the total energy transfer in the inertial range of magnetic helicity is the same as in the inertial range of total energy for all helicity combinations. That is, magnetic energy transfer and conversion in the inertial ranges of total energy and magnetic helicity proceed in the same direction.

Discussion

This assessment of contributions to forward and inverse transfers and cascades is based on an analysis of the nonlinear terms in the MHD equations only, thus neglecting the symmetry-breaking effect of dissipation creating an energy sink at the small scales. Accounting for this effect, it is plausible that the contributions from transfer terms leading to forward transfer are weighted higher than contributions leading to inverse transfer. This is particularly relevant in interactions where forwards and reverse contributions are present and the overall transfer depends on cancellations between the two terms. It would perhaps be safest to attribute these cases to forwards rather than inverse energy cascades.

Although it is not possible to exactly determine which helical interactions are weighted higher than others, some information can be obtained from the magnitude of the geometric factor g_{kpq} defined in eq. (3.7). The magnitude of g_{kpq} depends on the helicity combinations since it involves the helicity-dependent factor $I = s_k k + s_p p + s_q q$. Therefore it parametrises the strength of a given helical interaction, and the case of all helicities being of the same sign gives the largest value of $|I|$, since in this case $|I| = |k+p+q|$.

For the reverse transfers, that is, for $k < p, q$, the factor $|I|$ takes the smallest value for the case $s_k = s_p \neq s_q$, since $|I| = |k + (p-q)|$. Note that in this case I becomes small for small k even in the nonlocal limit $k << p \simeq q$, suggesting that the nonhelical reverse transfer found in this case is less efficient in increasing

spectral power at the very low wavenumbers. The remaining class of helical interactions $s_k \neq s_p = s_q$ leads to $|I| = |k - (p + q)|$. In this case $|I|$ does not necessarily become small for small k which is due to the contribution of nonlocal interactions, where p and q are large compared to k. According to the results from the stability analysis, in the nonlocal limit instabilities occur for the case $s_k = s_p = s_q$ only if $|B_{s_p}| > |U_{s_p}|$ and for the case $s_k \neq s_p = s_q$ if $|U_{s_p}| > |B_{s_p}|$.

It is therefore possible to deduce within the framework of the instability assumption that most of the increase in energy at the very largest scales (in a magnetically dominated system) is mainly due to a breaking of mirror-symmetry, which had been established before by [73] using a different approach. That is, it is due to the presence of kinetic and magnetic helicity, since interactions of the type $s_k = s_p = s_q$, which account for most of the inverse transfer, can only occur in significant numbers for fields consisting of many modes with the same helicity. Recent numerical results in hydrodynamics showed that there is an overall reverse flux of energy only when the system mainly contains helical modes of the same sign. As soon as a small amount of oppositely polarised modes is introduced, the usual direct cascade is recovered [158].

In summary, in this section the *direction* of total energy and magnetic helicity transfers in their respective inertial ranges was determined. Not surprisingly, fully helical magnetic fields lead to inverse cascades of magnetic helicity and inverse transfer of magnetic energy, but the analysis also showed that an inverse energy cascade is possible for nonhelical magnetic fields, which is a new theoretical result. However, due to the coupling of the momentum and induction equations, within this framework it is not possible to determine the *nature* of the energy transfers resulting from an instability of a given steady solution, since the same eigenvalue controls the growth of the exponential solution of (3.15) for both the magnetic and the velocity field. Nevertheless, for some special cases the evolution equations (3.5)-(3.6) decouple and more detailed information becomes available. These cases are treated in the following section.

3.7 Special solutions and the (kinematic) dynamo

As mentioned before, special cases exist where the analysis becomes much simpler and which are relevant to specific problems in MHD such as the kinematic dynamo. In sec. 3.3.2 the stability of general equilibria of the dynamical system

(3.5)-(3.6) describing the evolution of a triad of interacting helical modes was analysed. Using the notation (3.12), the general equilibria were of the form $(0, U_{s_p}, 0; 0, B_{s_p}, 0)$. In this section cases are considered where either $U_{s_p} = 0$ or $B_{s_p} = 0$, that is this section is concerned with the stability of steady solutions of (3.5)-(3.6) which are of the form $(0, U_{s_p}, 0; 0, 0, 0)$ and $(0, 0, 0; 0, B_{s_p}, 0)$. The former case may be of particular interest due to its relation to dynamo action.

3.7.1 The kinematic dynamo

For small magnetic fields the Lorentz force is small compared to inertial forces, and can be neglected in the momentum equation. This decouples the momentum equation from the induction equation and defines the kinematic dynamo problem. In the present setting, it corresponds to $|U_{s_p}|/|B_{s_p}| >> 1$, and terms proportional to $|B_{s_p}|$ can be neglected as they are very small compared to terms proportional to $|U_{s_p}|$.

Alternatively, one could also consider the steady solution $B_{s_p} = 0$ while $U_{s_p} \neq 0$. This would correspond to a stability analysis of a flow field at a particular length scale subject to small perturbations of the magnetic and velocity fields, where the magnetic field perturbation may be viewed as the magnetic seed field to be amplified by dynamo action. In this setting it can be seen from eq. (3.5) that the term corresponding to the Lorentz force disappears while in eq. (3.14) terms involving B_{s_p} disappear, thus the system simplifies to

$$\partial_t^2 u_{s_k} = |g_{kpq}|^2 (s_p p - s_q q)(s_k k - s_p p) \, |U_{s_p}|^2 u_{s_k} \ , \tag{3.74}$$

$$\partial_t^2 b_{s_k} = -|g_{kpq}|^2 s_k k \, s_q q \, |U_{s_p}|^2 b_{s_k} \ . \tag{3.75}$$

As the only contribution to the evolution of the magnetic field now comes from the velocity field, the remaining terms in eq. (3.6) are associated with dynamo action. Equation (3.75) implies that this system has exponential solutions leading to magnetic field growth if $s_k \neq s_q$, regardless of wavenumber ordering. So for energy transfer from U_{s_p} into b_{s_k} (and b_{s_q}) to become possible, the magnetic modes at wavenumbers k and q should be of opposite helicity.

For small k, nonlocal interactions with $k << p \simeq q$ provide most of the transfer into b_{s_k}. This is because the eigenvalue determining the growth of the exponential solution of (3.75) is larger for $q >> k$ than for $q \simeq k$, thus the perturbations should grow faster in the former than in the latter case. Hence, according to the

instability assumption, U_{s_p} loses energy in favour of b_{s_k} mainly due to nonlocal interactions if b_{s_k} describes the largest scales of the system.

The α-effect

One well-known example of a large-scale dynamo is the α-effect of mean-field electrodynamics (see e.g. [132]), where α is a coefficient in the mean-field induction equation related to the kinetic helicity of the flow. The α-effect leads to a generation of large and small-scale magnetic helicities of opposite sign [25, 26]. It is a mean-field description of the STF dynamo [36, 125, 178] introduced in chapter 1, which describes how a positively helical velocity field generates magnetic field perturbations leading to the large-scale component of the magnetic field becoming negatively helical. By conservation of magnetic helicity, the small-scale component of the magnetic field then has to become positively helical (and more so if the initial magnetic field was positively helical). That is, the small-scale magnetic and kinetic helicities are of the same sign.

It is plausible that the type of interaction $(0, U_{s_p}, 0; 0, B_{s_p} = 0, 0)$ for $k < p, q$ with $s_k \neq s_p = s_q$ can be associated with an STF dynamo and hence the α-effect. First, nonzero small-scale kinetic helicity (we have $s_p = s_q$) is present. Second, the magnetic field growth at the large scales is described by (3.75), where magnetic fluctuations at k and q of opposite helicities are necessary to obtain an instability. That is, the large-scale magnetic field has opposite helicity to the small-scale one, reminiscent of the α-dynamo. This combination of helicities also produces a transfer of kinetic energy from small to large scales [181]. Thus this type of interaction feeds into the magnetic and velocity fields on scales larger than the characteristic scale $L = 1/p$ of the velocity field. The magnetic field mode which is amplified by this process has helicity opposite to the velocity field at p, which conforms to expectations in terms of STF dynamo action and the α-effect.

3.7.2 Excitation of a flow by the Lorentz force

For the other special solution $(0,0,0;0,B_{s_p}\neq 0,0)$ the system (3.13) - (3.14) simplifies to

$$\partial_t^2 u_{s_k} = |g_{kpq}|^2 (s_p p - s_q q) s_q q \, |B_{s_p}|^2 u_{s_k} \ , \tag{3.76}$$

$$\partial_t^2 b_{s_k} = -|g_{kpq}|^2 s_k k (s_k k - s_p p) \, |B_{s_p}|^2 b_{s_k} \ , \tag{3.77}$$

where the inertial term in (3.5) and the 'dynamo' term in (3.6) are now absent and the system of coupled ODEs has split into two decoupled ODEs. This case may perhaps be associated with the generation of turbulence caused by the action of the Lorentz force on the fluid (i.e. energy conversion from B_{s_p} to u_{s_k} or u_{s_q}) and interscale transfer of magnetic energy from B_{s_p} into b_{s_k} or b_{s_q}. Exponentially growing solutions of (3.77) only occur if $s_p = s_k$ and $k < p$, leading to a reverse transfer of magnetic energy. Exponentially growing solutions of (3.76) occur for $p > q$ and $s_p = s_q$ leading to forward and reverse transfers corresponding to $k > p$ and $k < p$, respectively. Interestingly, energy transfer only becomes possible if the magnetic field is helical and the helicity of the velocity field mode does not affect the analysis.

3.8 Conclusions

The four main results of the present work are: First, unlike in non-conducting fluids [181], the stability analysis shows that in MHD turbulence energy can be transferred away from the smallest scales in a triad interaction. Second, the stability analysis reveals mechanisms for reverse energy transfer for nonhelical magnetic fields, in which case it does not need to be driven by the inverse transfer of magnetic helicity. Third, forward energy transfers are more quenched in regions of high cross-helicity than reverse energy transfers. Fourth, significant cancellations are expected to occur between the contributions to forward and reverse transfers, as on several occasions they occur with opposite signs in the same equation. The theoretical analysis was conducted within the framework of the instability assumption, and it is crucial to discuss the results within the wider context of MHD turbulence research.

Interscale energy transfers between the two different vector fields as well as within the same fields have been studied by several groups for freely decaying [27, 53] and

stationary [3, 25, 30, 37] MHD turbulence as well as for the kinematic dynamo regime [126] and for magnetic helicity transfer [4], using shell-filtered transfer terms calculated from DNSs or from a helical shell model [172]. In the stationary case, it was found that transfers between the same fields are mainly local while transfers between different fields were nonlocal, and transfers from the injection scale to the largest scales in the system were observed. In the decaying case, energy transfers were generally found to be mainly local. However, transfers between different fields were more nonlocal than transfers between the same fields. Furthermore, large cancellations occurred between the contributions to forward and reverse transfers [53]. The analysis presented here also predicts cancellations between these contributions to occur, thus being consistent with the aforementioned numerical results.

In terms of locality and nonlocality of energy (and helicity) transfer, it was found that nonlocal interactions contribute to forward transfer only for interactions of helical modes with unlike helicity and mainly if the kinetic energy exceeds the magnetic energy. Interestingly, for inverse transfers less constraints on nonlocal interactions are found. In particular for magnetically dominated systems nonlocal interactions between modes of like helicity contribute to reverse energy transfer. In view of the cancellations that occur between forward and reverse transfers, the inverse cascade may thus have a significant nonlocal component which is not cancelled by forward transfers within the same triad interaction.

A numerical study of large-scale magnetic field generation in helically forced globally isotropic MHD turbulence was carried out by Brandenburg [25]. It was found that the injection of energy from the velocity field into the magnetic field occurs directly from the forcing scale into the largest resolved scale, implying that this is a nonlocal process. Due to the non-locality of the observed increase in spectral power of the magnetic field at the lowest resolved wavenumber $k = 1$ and the excellent agreement of numerical results with an α-dynamo model, the transfer of energy into the $k = 1$ mode is explained by the α-effect rather than an inverse cascade, and it is shown to occur after saturation of the small-scale dynamo. The results in sec. 3.7 suggest that one type of helical mode interaction may be mapped to the α-effect, and it was established that large-scale dynamo action is more active in the nonlocal limit than certain other types of interactions.

One of the main results of the present work is the possibility of inverse energy transfer for nonhelical magnetic fields. Such inverse transfer has recently been found in high resolution DNSs of slightly compressible [27] and relativistic [190]

MHD turbulence. An analysis of interscale transfers showed that this inverse transfer was mainly due to energy transfer away from the medium scale (see Supplemental Material of Ref. [27], last figure), while energy transfer away from the smallest scales also occurred. The analytic approach put forward here also shows that energy is transferred away from the medium and small scales for interactions of modes with unlike helicities, thus being qualitatively consistent with these numerical results. However, since no numerical work decomposing the MHD equations into helical contributions as suggested by Biferale *et al.*in Refs. [18] and [20] has been carried out so far, no direct numerical confirmation of the presented analytical results is available at this point.

Another testbed for theoretical results in MHD turbulence are measurements of energy transfer in the solar wind. Unlike in the present analysis and in the numerical results discussed so far except for the work by Cho [37], a background magnetic field is present in the solar wind. Recent measurements at 1 AU showed negative Elsässer fluxes in regions of high cross-helicity [171], giving possible evidence of inverse energy transfer in these regions. This cannot be explained by selective decay, that is the faster decay of the total energy compared to H_c and H_{mag} [21], as cross-helicity is predicted to cascade forwards [73]. The material presented in this chapter may be helpful in explaining this phenomenon as one of the results obtained here was a quenching of forward energy transfer in regions of high cross-helicity, leaving more inverse transfer to perhaps dominate the dynamics in these regions. This point will be discussed in connection to numerical results in chapter 4.

In subsequent work [42], concerns were raised on the implications of the effect of expansion in the solar wind especially in regions of high H_c. Expansion effects had been neglected in the previous analysis. In Ref. [171] the authors restricted their measurements to regions where the relative cross helicity σ_c is not too large, that is $0 \leqslant |\sigma_c| \leqslant 0.5$ and measure positive energy fluxes on average, while the instantaneous flux shows large variations including negative values. It is shown that the broad distribution of the measured instantaneous fluxes is related to intermittency of the energy cascade in terms of the variability of the energy flux [93, 147], and not caused by experimental uncertainty. The various possibilities of energy transfer in forward and reverse directions determined in the present work are consistent with these measurements, as they also would result in broader tails of the probability distribution of the energy flux, even if on average energy transfer proceeds in the forward direction. As for the concerns about the validity

of the negative fluxes measured by Stawarz *et al.* [171], the results presented here do suggest that the measured inverse fluxes may be a genuine effect due to quenching of forward energy transfers if H_c is large.

Since most of this discussion is based on statements of plausibility rather than certainty, more work clearly has to be carried out before a decisive result on energy transfer in MHD turbulence can be achieved. As suggested by Biferale *et al.* [18, 20], energy and helicity transfers could be investigated numerically by projecting out helical modes of a particular sign, similar to work done by these authors [18, 20] and Sahoo *et al.* [158] in hydrodynamic turbulence. However, numerical verification of reverse spectral transfer due to the particular nonhelical interactions found in the present work may be difficult to obtain in that framework, and a particular DNS study concentrating on inverse transfer for nonhelical magnetic fields using the full MHD equations subject to small-scale forcing may be needed in order to provide further insight. An analysis of Fourier-filtered transfer terms from DNSs of highly unbalanced MHD turbulence compared to balanced MHD turbulence could be carried out in order to verify (or otherwise) the proposed quenching of forward transfers by high values of H_c, especially as it is not possible to quantify this effect from theoretical analysis only. On the analytical side, the present work may be extended to include the effects of a background magnetic field and of compressive fluctuations, which would be included in the decomposition of the velocity field as modes parallel to the wavevector $\boldsymbol{k}$.

Chapter 4

Self-organisation and nonuniversality

MHD turbulence is present in many areas of physics, ranging from industrial applications such as liquid metal technology to nuclear fusion and plasma physics, geo-, astro- and solar physics, and even cosmology. The numerous different MHD flow types that arise in these different settings due to anisotropy, alignment, different values of the diffusivities, to name only a few, lead to the question of universality in MHD turbulence, which has been the subject of intensive research by many groups [2, 13, 23, 48, 49, 80, 81, 107, 125, 160, 163, 182]. The behaviour of the (dimensionless) dissipation rate is connected to this problem, in the sense that correlation (alignment) of the different vector fields could influence the energy transfer across the scales [21, 49, 150], and thus possibly the amount of energy that is eventually dissipated at the small scales. This includes the self-organising processes discussed in the previous chapters. More precisely, a system with a pronounced reverse transfer of energy should lead to a lower dissipation rate compared to a system where such a self-ordering process is absent.

4.1 Introduction

For neutral fluids it has been known for a long time that the dimensionless dissipation rate in forced and freely decaying homogeneous isotropic turbulence tends to a constant with increasing Reynolds number. The first evidence for this

was reported by Batchelor [11] in 1953, while the experimental results reviewed by Sreenivasan in 1984 [169], and subsequent experimental and numerical work by many groups, established the now well-known characteristic curve of the dimensionless dissipation rate against Reynolds number: see [88, 120, 121, 169, 170] and references therein. For statistically steady isotropic turbulence, the theoretical explanation of this curve was recently found to be connected to the energy balance equation for forced turbulent flows [121], where the asymptote describes the inertial transfer flux in the limit of infinite Reynolds number.

For freely decaying MHD, recent results suggest that the temporal maximum of the total dissipation tends to a constant value with increasing Reynolds number. The first evidence for this behaviour in MHD was put forward in 2009 by Mininni and Pouquet [129] using results from DNSs of homogeneous MHD turbulence without a mean magnetic field. The temporal maximum of the total dissipation rate $\varepsilon(t)$ became independent of Reynolds number at a Taylor-scale Reynolds number R_λ (measured at the peak of $\varepsilon(t)$) of about 200.

Dallas and Alexakis [50] measured the dimensionless dissipation rate C_ε from DNS data, where $\varepsilon(t)$ was non-dimensionalised with respect to the initial values of the rms velocity $U(t)$ and the integral length scale $L(t)$ (defined with respect to the total energy), for random initial fields with strong correlations between the velocity field and the current density. The authors compared data with Ref. [129], and again it was found that $C_\varepsilon \to const.$ with increasing Reynolds number. Interestingly the approach to the asymptote was slower than for the data of Ref. [129].

In this chapter an approximative equation describing the dependence of the dimensionless dissipation coefficient C_ε on a generalised Reynolds number R_- is derived from the energy balance equation in terms of Elsässer variables:

$$C_\varepsilon = C_{\varepsilon,\infty} + \frac{C}{R_-} + \frac{D}{R_-^2} + O(R_-^{-3}) \ . \tag{4.1}$$

The coefficients $C_{\varepsilon,\infty}$, C and D depend on several parameters, which themselves depend on the magnetic, cross and kinetic helicities. That is, they are related to the aforementioned self-ordering behaviour of the system. In particular, eq. (4.1) predicts nonuniversal values of the asymptotic value $C_{\varepsilon,\infty}$ of the dimensionless dissipation rate in the infinite Reynolds number limit. The most general form of this equation for nonstationary flows with large-scale external forcing is presented, which can be applied to freely decaying and stationary flows by setting the

corresponding terms to zero.

The resulting theoretical predictions for the stationary case are compared to DNS data for stationary MHD turbulence for three different types of mechanical forcing. The DNS data shows good agreement with eq. (4.1) and the different forcing schemes have no measurable effect on the values of the coefficients in eq. (4.1). For the case of freely decaying MHD turbulence, several series of DNSs have been carried out with emphasis on different initial values of the ideal invariants and resulting nonuniversal values of the asymptotic dissipation rate. Again, the DNS data agrees with the theoretical prediction and indeed nonuniversal values of $C_{\varepsilon,\infty}$ are measured depending on the initial levels of cross- and magnetic helicities.

4.2 Derivation of the equation

In hydrodynamics, the dimensionless dissipation coefficient $C_{\varepsilon,u}$ is defined in terms of the Taylor surrogate expression for the total dissipation rate, U^3/L_u, where U denotes the rms value of the velocity field and L_u the integral scale defined with respect to the velocity field, as

$$C_{\varepsilon,u} \equiv \varepsilon_{kin} \frac{L_u}{U^3} \ . \tag{4.2}$$

However, in MHD there are several quantities that may be used to define an MHD analogue to the Taylor surrogate expression, such as the rms value B of the magnetic field, one of the different length scales defined with respect to either $\boldsymbol{b}$ or $\boldsymbol{u}$, or the total energy.

Since the total dissipation in MHD turbulence should be related to the flux of total energy through different scales, one may think of defining a dimensionless dissipation coefficient for MHD in terms of the total energy. However, this would lead to a nondimensionalisation of the hydrodynamic transfer term $\boldsymbol{u} \cdot (\boldsymbol{u} \cdot \nabla)\boldsymbol{u}$ with a magnetic quantity. This can be seen by considering the energy balance equation in real space [31] introduced in chapter 1 and re-stated here for

convenience (for the case of free decay)

$$\varepsilon(t) = -\partial_t(B^{uu}_{LL}(r,t) + B^{bb}_{LL}(r,t)) + \frac{3}{2r^4}\partial_r\left(\frac{r^4}{6}B^{uuu}_{LLL}(r,t) + r^4 C^{bbu}_{LLL}(r,t)\right) + \frac{6}{r}C^{bub}(r,t) + \frac{1}{r^4}\partial_r\left(r^4\partial_r(\nu B^{uu}_{LL}(r,t) + \eta B^{bb}_{LL}(r,t))\right) \ . \tag{4.3}$$

As can be seen from their respective definitions given in chapter 1, the functions C^{bbu}_{LLL} and C^{ubb} scale with B^2U while the function B^{uuu}_{LLL} scales with U^3. If eq. (4.3) were to be nondimensionalised with respect to the total energy

$$E(t) = \frac{1}{2}\left\langle |\boldsymbol{b}(\boldsymbol{x},t)|^2 + |\boldsymbol{u}(\boldsymbol{x},t)|^2 \right\rangle \ , \tag{4.4}$$

then the purely hydrodynamic term B^{uuu}_{LLL} would be scaled partially by a magnetic quantity. This problem can be avoided by working with Elsässer fields.

4.2.1 The total dissipation in terms of Elsässer fields

As introduced in chapter 1, the total rate of energy dissipation in MHD turbulence is given by the sum of Ohmic and viscous dissipation

$$\varepsilon(t) = \varepsilon_{mag}(t) + \varepsilon_{kin}(t) \ . \tag{4.5}$$

Similarly, the total dissipation rate can be decomposed into its respective contributions from the Elsässer dissipation rates

$$\varepsilon(t) = \frac{1}{2}\big(\varepsilon_+(t) + \varepsilon_-(t)\big) \ , \tag{4.6}$$

where the Elsässer dissipation rates are defined as

$$\varepsilon^{\pm}(t) = \nu_+ \int_\Omega d\boldsymbol{k}\ k^2\langle|\hat{\boldsymbol{z}}^{\pm}(\boldsymbol{k},t)|^2\rangle + \nu_- \int_\Omega d\boldsymbol{k}\ k^2\langle\hat{\boldsymbol{z}}^{\pm}(\boldsymbol{k},t)\cdot\hat{\boldsymbol{z}}^{\mp}(-\boldsymbol{k},t)\rangle \ , \tag{4.7}$$

with $\hat{\boldsymbol{z}}^{\pm}$ denoting the (formally) Fourier-transformed Elsässer fields and $\nu_\pm = (\nu \pm \eta)$. The total dissipation rate relates to the sum of the Elsässer dissipation rates

$$\varepsilon^+(t) + \varepsilon^-(t) = \varepsilon(t) + \varepsilon_{H_c}(t) + \varepsilon(t) - \varepsilon_{H_c}(t) = 2\varepsilon(t) \ , \tag{4.8}$$

where

$$H_c(t) = \int_\Omega d\boldsymbol{k}\ \langle \hat{\boldsymbol{u}}(\boldsymbol{k},t)\cdot\hat{\boldsymbol{b}}(-\boldsymbol{k},t)\rangle = \frac{1}{2}\int_\Omega d\boldsymbol{k}\ \langle |\boldsymbol{z}^+(\boldsymbol{k},t)|^2 - |\boldsymbol{z}^-(\boldsymbol{k},t)|^2\rangle\ , \quad (4.9)$$

is the cross-helicity and the dissipation rate ε_{H_c} of the cross-helicity is given by

$$\varepsilon_{H_c}(t) = \frac{1}{2}\big(\varepsilon^+(t) - \varepsilon^-(t)\big)\ . \quad (4.10)$$

As introduced in chapter 1, the total rate of energy input, ε_W, can be split up in a similar way into kinetic and magnetic contributions

$$\varepsilon_W(t) = \varepsilon_{mag,W}(t) + \varepsilon_{kin,W}(t)\ . \quad (4.11)$$

Similarly, the Elsässer fields have energy input rates $\varepsilon_W^\pm(t)$, and the total energy input rate is given in terms of $\varepsilon_W^\pm(t)$ as

$$\varepsilon_W(t) = \frac{1}{2}\big(\varepsilon_W^+(t) + \varepsilon_W^-(t)\big)\ . \quad (4.12)$$

This equation can be rewritten as

$$\varepsilon_W^+(t) = \varepsilon_W(t) + \frac{1}{2}\left(\varepsilon_W^+(t) - \varepsilon_W^-(t)\right) = \varepsilon_W(t) + \varepsilon_{W,H_c}(t)\ , \quad (4.13)$$

where ε_{W,H_c} denotes the input rate of the cross-helicity.

Since the rate of change of the total energy is given by the difference of energy input and dissipation (see chapter 1), in the most general case the total energy dissipation rate is given by

$$\varepsilon(t) = \varepsilon_W(t) - d_tE(t)\ . \quad (4.14)$$

For the stationary case $d_tE(t) = 0$ and one obtains $\varepsilon(t) = \varepsilon_W(t)$. For the freely decaying case $\varepsilon_W(t) = 0$ and the change in total energy is due to dissipation only, that is $-d_tE(t) = \varepsilon(t)$. In terms of Elsässer variables $\varepsilon(t)$ can also be expressed as

$$\varepsilon(t) = \varepsilon_W(t) - d_tE(t) = \varepsilon_W(t) - d_tE^\pm(t)\rangle \mp d_tH_c(t)\ , \quad (4.15)$$

where $E^\pm(t)$ denote the Elsässer energies.

4.2.2 A definition for the dimensionless dissipation coefficient

Since the total dissipation rate can be expressed either in terms of the Elsässer fields or the primary fields $\boldsymbol{u}$ and $\boldsymbol{b}$, it can also be described by the energy balance equations for $\boldsymbol{z}^{\pm}$ [148], which are stated here for the most general case of homogeneous forced nonstationary MHD flows without a mean magnetic field

$$\begin{aligned} -\partial_t E^{\pm}(t) + I^{\pm}(r,t) = &-\frac{3}{4}\partial_t B_{LL}^{\pm\pm}(r,t) - \frac{\partial_r}{r^4}\left(\frac{3r^4}{2} C_{LL,L}^{\pm\mp\pm}(r,t)\right) \\ &+ \frac{3}{4r^4}\partial_r\left(r^4\partial_r(\nu+\eta)B_{LL}^{\pm}(r,t)\right) \\ &+ \frac{3}{4r^4}\partial_r\left(r^4\partial_r(\nu-\eta)B_{LL}^{\mp}(r,t)\right) \ , \end{aligned} \tag{4.16}$$

where $I^{\pm}(r,t)$ are (scale-dependent) energy input terms and

$$C_{LL,L}^{\pm\mp\mp}(r,t) = \langle z_L^{\pm}(\boldsymbol{x},t) z_L^{\mp}(\boldsymbol{x},t) z_L^{\pm}(\boldsymbol{x}+\boldsymbol{r},t)\rangle \ , \tag{4.17}$$

$$B_{LL}^{\pm\pm}(r,t) = \langle (\delta_L z^{\pm}(r,t))^2\rangle \ , \tag{4.18}$$

$$B_{LL}^{\pm\mp}(r,t) = \langle \delta_L z^{\pm}(r,t)\delta_L z^{\mp}(r,t)\rangle \ , \tag{4.19}$$

are the third-order longitudinal correlation function and the second-order structure functions of the Elsässer fields, respectively. As can be seen from the definition, the third-order correlation function scales with $(z^{\pm})^2 z^{\mp}$, where $z^{\pm}$ denote the respective rms values of the Elsässer fields. This permits a consistent nondimensionalisation of the Elsässer energy balance equations using the appropriate quantities defined in terms of Elsässer variables. As such the complication that arose if the energy balance was written in terms of $\boldsymbol{b}$ and $\boldsymbol{u}$ can be circumvented. Therefore the dimensionless Elsässer dissipation rates can be defined[1] as

$$C_{\varepsilon}^{\pm}(t) \equiv \frac{\varepsilon(t) L_{\pm}(t)}{z^{\pm}(t)^2 z^{\mp}(t)} \ , \tag{4.20}$$

where

$$L_{\pm}(t) = \frac{3\pi}{8E^{\pm}(t)} \int_{\Omega} d\boldsymbol{k}\ k^{-1} \langle |\boldsymbol{z}^{\pm}(\boldsymbol{k},t)|^2\rangle \ , \tag{4.21}$$

[1]The scaling is ill-defined for the (measure zero) cases $\boldsymbol{u} = \pm\boldsymbol{b}$, which correspond to exact solutions to the MHD equations where the nonlinear terms vanish. Thus no turbulent transfer is possible, and these cases are not amenable to an analysis which assumes nonzero energy transfer [148].

are the integral scales defined with respect to $\boldsymbol{z}^{\pm}$. For zero cross-helicity one should expect $C_{\varepsilon}^{+}(t) = C_{\varepsilon}^{-}(t)$, since

$$E^{\pm}(t) = 2E(t) \pm 2H_c(t) = 2E(t) \ . \tag{4.22}$$

Therefore all quantities defined with respect to the rms fields z^{+} and z^{-} should be the same in this case. Finally, the dimensionless dissipation rate $C_{\varepsilon}(t)$ is defined as

$$C_{\varepsilon}(t) = C_{\varepsilon}^{+}(t) + C_{\varepsilon}^{-}(t) \equiv \frac{\varepsilon(t) L_{+}(t)}{z^{+}(t)^{2} z^{-}(t)} + \frac{\varepsilon(t) L_{-}(t)}{z^{-}(t)^{2} z^{+}(t)} \ . \tag{4.23}$$

Using this definition the Elsässer energy balance equations (4.16) can now be consistently nondimensionalised. For conciseness the explicit time and spatial dependences are from now on omitted, unless there is a particular point to make.

4.2.3 Dimensionless energy balance

By introducing the nondimensional variables $\sigma_{\pm} = r/L_{\pm}$ [182] and non-dimensionalising eq. (4.16) as proposed in the definitions of $C_{\varepsilon}^{\pm}$ given in eq. (4.20) one obtains

$$\begin{aligned} -\left(d_t E^{\pm} - I^{\pm}\right) \frac{L_{\pm}}{z^{\pm 2} z^{\mp}} = & -\frac{1}{\sigma_{\pm}^{4}} \partial_{\sigma_{\pm}} \left(\frac{3\sigma_{\pm}^{4} C_{LL,L}^{\pm\mp\pm}}{2 z^{\pm 2} z^{\mp}} \right) - \frac{L_{z^{\pm}}}{z^{\pm 2} z^{\mp}} \left(\partial_t \frac{3 B_{LL}^{\pm\pm}}{4} - \varepsilon_{H_c} \right) \\ & + \frac{\eta + \nu}{L_{\pm} z^{\mp}} \frac{3}{4\sigma_{\pm}^{4}} \left(\sigma_{\pm}^{4} \partial_{\sigma_{\pm}} \frac{B_{LL}^{\pm\pm}}{z^{\pm 2}} \right) \\ & + \frac{\nu - \eta}{L_{\pm} z^{\pm}} \frac{3}{4\sigma_{\pm}^{4}} \left(\sigma_{\pm}^{4} \partial_{\sigma_{\pm}} \frac{B_{LL}^{\pm\mp}}{z^{\pm} z^{\mp}} \right) \ . \end{aligned} \tag{4.24}$$

Before proceeding further, the scale-dependent forcing term on the left-hand side of this equation needs to be analysed in some detail in order to clarify its relation to the energy input terms $\varepsilon_{W}^{\pm}$.

Scale-dependence of the energy input

The energy input $I^{\pm}$ is given by

$$I^{\pm}(r) = \frac{3}{r^{3}} \int_{0}^{r} dr' r'^{2} \langle \boldsymbol{z}^{\pm}(\boldsymbol{x} + \boldsymbol{r}') \boldsymbol{f}^{\pm}(\boldsymbol{x}) \rangle \ . \tag{4.25}$$

In the limit of infinite Reynolds number, the inertial range extends through all wavenumbers, formally implying that energy is injected at the lowest wavenumber and dissipated at infinity [67, 120]. This can be modelled using a $\delta(\boldsymbol{k})$-input term [67], such that

$$W_\infty^\pm(\boldsymbol{k}) \equiv \varepsilon_W^\pm \delta(\boldsymbol{k}) \ , \tag{4.26}$$

hence formally

$$\lim_{Re\to\infty} I^\pm = \frac{3}{r^3}\int_0^r dr' r'^2 \int_{\mathbb{R}^3} d\boldsymbol{k}\ W_\infty^\pm(k) e^{-i\boldsymbol{k}\cdot\boldsymbol{r}'} = \varepsilon_W^\pm \ . \tag{4.27}$$

Therefore it should be possible to split the term $I^\pm(r)$ into a constant, $\varepsilon_W^\pm$, and a scale-dependent term $J^\pm(r)$, which encodes the additional scale dependence introduced by realistic, finite Reynolds number forcing. For consistency, this scale-dependent term must vanish in the formal limit $Re \to \infty$, that is

$$I^\pm(r) = \varepsilon_W + J^\pm(r) \ , \tag{4.28}$$

with $\lim_{Re\to\infty} J^\pm(r) = 0$.

Formulation of the evolution equation for $C_\varepsilon^\pm$

The inverse of the coefficients in front of the dissipative terms in eq. (4.24) have the form $z^\mp L_\pm/(\nu+\eta)$ and $z^\pm L_\pm/(\nu-\eta)$, respectively, which is similar to a Reynolds number. Therefore the generalised large-scale Reynolds numbers

$$R_\mp = z^\mp L_\pm/(\nu+\eta) \ \text{ and } \ R'_\pm = z^\pm L_\pm/(\nu-\eta) \ , \tag{4.29}$$

are introduced, which leads to a dimensionless version of the Elsässer energy balance equation for homogeneous MHD turbulence in the most general case for nonstationary flows at any magnetic Prandtl number

$$\begin{aligned} C_\varepsilon^\pm = &-\frac{\partial_{\sigma_\pm}}{\sigma_\pm^4}\left(\frac{3\sigma_\pm^4 C_{LL,L}^{\pm\mp\pm}}{2z^{\pm 2}z^\mp}\right) + \frac{L_\pm}{z^{\pm 2}z^\mp}\left(d_t H_c - \partial_t \frac{3B_{LL}^{\pm\pm}}{4} - J^\pm\right) \\ &+ \frac{1}{R_\mp}\frac{3\partial_{\sigma_\pm}}{2\sigma_\pm^4}\left(\sigma_\pm^4 \partial_{\sigma_\pm}\frac{B_{LL}^{\pm\pm}}{z^{\pm 2}}\right) + \frac{1}{R'_\pm}\frac{3\partial_{\sigma_\pm}}{2\sigma_\pm^4}\left(\sigma_\pm^4\partial_{\sigma_\pm}\frac{B_{LL}^{\pm\mp}}{z^\pm x^\mp}\right) \ . \end{aligned} \tag{4.30}$$

where the splitting of the energy input term derived in the previous section has been used. For conciseness, the following dimensionless functions are defined

$$g^{\pm\mp\pm} = \frac{C^{\pm\mp\pm}_{LL,L}}{z^{\pm 2} z^{\pm}} \ , \tag{4.31}$$

$$h_2^{\pm\pm} = \frac{B^{\pm\pm}_{LL}}{z^{\pm 2}} \ , \tag{4.32}$$

$$h_2^{\pm\mp} = \frac{B^{\pm\mp}_{LL}}{z^{\pm} z^{\mp}} \ , \tag{4.33}$$

$$G^{\pm} = \frac{L_{\pm}}{z^{\pm 2} z^{\pm}} \partial_t B^{\pm\pm}_{LL} \ , \tag{4.34}$$

$$F^{\pm} = J^{\pm} \frac{L_{\pm}}{z^{\pm 2} z^{\pm}} \ , \tag{4.35}$$

such that eq. (4.30) can be written as

$$\begin{aligned} C_{\varepsilon}^{\pm} = &- \frac{\partial_{\sigma_\pm}}{\sigma_{\pm}^4} \left(\frac{3\sigma_{\pm}^4}{2} g^{\pm\mp\pm} \right) - F^{\pm} - G^{\pm} - \frac{3}{4} H_2^{\pm\pm} \\ &+ \frac{3}{R_{\mp}} \frac{\partial_{\sigma_\pm}}{\sigma_{\pm}^4} \left(\sigma_{\pm}^4 \partial_{\sigma_\pm} h_2^{\pm\pm} \right) + \frac{3}{R'_{\mp}} \frac{\partial_{\sigma_\pm}}{\sigma_{\pm}^4} \left(\sigma_{\pm}^4 \partial_{\sigma_\pm} h_2^{\pm\mp} \right) \ . \end{aligned} \tag{4.36}$$

This equation can be applied to the two simpler cases of freely decaying and stationary MHD turbulence by setting the corresponding terms to zero. For the case of free decay there are no external forces therefore $F^{\pm} = 0$, while for the stationary case the term $G^{\pm}$ vanishes. A further simplification concerns the case $Pm = 1$, that is $\nu = \eta$, where the generalised Reynolds numbers $R'_{\pm}$ tend to infinity. In this case the evolution of $C_{\varepsilon}^{\pm}$ depends only on $R_{\mp}$, and an approximate analysis using asymptotic series is possible. Most numerical results are concerned with this case due to computational constraints, hence it would be very difficult to test an approximate equation against DNS data if not only Re but also Pm needs to be varied. From now on the magnetic Prandtl number is therefore set to unity, keeping in mind that the analysis should be extended to $Pm \neq 1$ provided the approximate equation derived in the following section is consistent with DNS data.

4.2.4 Asymptotic expansions for the case $Pm = 1$

Equation (4.36) suggests a dependence of $C_{\varepsilon}^{\pm}$ on $1/R_{\mp}$, however, the structure and correlation functions also have a dependence on Reynolds number, which describes their deviation from their respective inertial-range forms. The highest

derivative in eq. (4.36) is multiplied by the small parameter $1/R_\mp$, which suggests that this equation may be viewed as singular perturbation problem amenable to asymptotic analysis [115][2]. The Elsässer energy balance equation had been rescaled by the rms values of the Elsässer fields and the corresponding integral length scales, where the integral scales are by definition the large-scale quantities, the interpretation in hydrodynamics usually being that they represent the size of the largest eddies. As such, the nondimensionalisation was carried out with respect to quantities describing the large scales, that is, with respect to 'outer' variables. As such, outer asymptotic expansions of the nondimensional structure and correlation functions are considered with respect to the inverse of the (large-scale) generalised Reynolds numbers $1/R_\mp$.

The formal asymptotic series of a generic function f (used for conciseness in place of the functions on the RHS of (4.36)) up to second order in $1/R_\mp$ reads

$$f = f_0 + \frac{1}{R_\mp} f_1 + \frac{1}{R_\mp^2} f_2 + O(R_\mp^{-3}) \ . \tag{4.37}$$

After substitution of the expansions into (4.36), collecting terms of the same order in $1/R_\mp$, one arrives at equations describing the behaviour of C_ε^+ and $C_\varepsilon-$

$$C_\varepsilon^\pm = C_{\varepsilon,\infty}^\pm + \frac{C^\pm}{R_\mp} + \frac{D^\pm}{R_\mp^2} + O(R_\mp^{-3}) \ , \tag{4.38}$$

up to third order in $1/R_\mp$, using the coefficients $C_{\varepsilon,\infty}^\pm$, $C^\pm$ and $D^\pm$ defined as

$$C_{\varepsilon,\infty}^\pm = -\frac{\partial_{\sigma_\pm}}{\sigma_\pm^4}\left(\frac{3\sigma_\pm^4}{2} g_0^{\pm\mp\pm}\right) \mp G_0^\pm \mp H_2^{\pm\pm} \ , \tag{4.39}$$

$$C^\pm = \frac{3\partial_{\sigma_\pm}}{\sigma_\pm^4}\left[\sigma_\pm^4\left(\partial_{\sigma_\pm} h_{2,0}^{\pm\pm} - \frac{g_1^{\pm\mp\pm}}{2}\right)\right] \mp F_1^\pm \mp G_1^\pm \ , \tag{4.40}$$

$$D^\pm = \frac{3\partial_{\sigma_\pm}}{\sigma_\pm^4}\left[\sigma_\pm^4\left(\partial_{\sigma_\pm} h_{2,1}^{\pm\pm} - \frac{g_2^{\pm\mp\pm}}{2}\right)\right] \mp F_2^\pm \mp G_2^\pm \ , \tag{4.41}$$

in order to write (4.36) in a more concise way. The zero-order term in the expansion of the function $F^\pm$ vanishes, since $F^\pm$ corresponds to the scale-dependent part $J^\pm$ of the energy input which vanishes in the limit $R_\mp \to \infty$. According to the definition of C_ε in eq. (4.23), the asymptote $C_{\varepsilon,\infty}$ is given by

$$C_{\varepsilon,\infty} = C_{\varepsilon,\infty}^+ + C_{\varepsilon,\infty}^- \ , \tag{4.42}$$

[2]The case $Pm \neq 1$ requires expansions in two parameters, which may not be well defined especially since $R'_\pm$ can be negative.

and using the definition of the generalised Reynolds numbers, which implies $R_+ = (L_-/L_+)(z^+/z^-)R_-$ one can define

$$C = C^+ + \frac{L_-}{L_+}\frac{z^+}{z^-}C^- \ , \tag{4.43}$$

(D is defined analogously), resulting in the following expression for the dimensionless dissipation rate

$$C_\varepsilon = C_{\varepsilon,\infty} + \frac{C}{R_-} + \frac{D}{R_-^2} + O(R_-^{-3}) \ . \tag{4.44}$$

Since the time dependence of the various quantities in this problem has been suppressed for conciseness, it has to be emphasised that eq. (4.44) is time dependent, including the Reynolds number R_-.

Nonstationary flows at the peak of dissipation

At the peak of dissipation the term $G_0^\pm$ in eq. (4.39) vanishes for constant flux of cross-helicity (that is, $d_t^2 H_c = 0$), since in the infinite Reynolds number limit the second-order structure function will have its inertial range form at all scales. By self-similarity the spatial and temporal dependences of e.g. B_{LL}^{++} should be separable in the inertial range, that is

$$B_{LL}^{++}(r,t) \sim (\varepsilon^+(t)r)^\alpha \ , \tag{4.45}$$

for some value α, and

$$\partial_t B_{LL}^{++} \sim \alpha \varepsilon^+(t)^{\alpha-1}\, d_t\varepsilon^+ r^\alpha \ . \tag{4.46}$$

At the peak of dissipation

$$d_t\varepsilon^+|_{t_{peak}} = d_t\varepsilon|_{t_{peak}} - d_t^2 H_c = d_t\varepsilon|_{t_{peak}} = 0 \ , \tag{4.47}$$

which implies $G_0^+(t_{peak}) = 0$. Equation (4.39) taken for nonstationary flows at the peak of dissipation is thus identical to eq. (4.39) for stationary flows, which implies that at this point in time a nonstationary flow may behave similarly to a stationary flow. Due to selective decay, that is the faster decay of the total energy compared to H_c and H_{mag} [21], one could perhaps expect $d_t H_c$ to be small

compared to ε in the infinite Reynolds number limit in most situations. In this case $G_0^\pm \simeq 0$ and

$$C^\pm_{\varepsilon,\infty}(t_{peak}) = -\frac{\partial_{\sigma_\pm}}{\sigma_\pm^4}\left(\frac{3\sigma_\pm^4}{2} g_0^{\pm\mp\pm}\right) \ , \tag{4.48}$$

which recovers the inertial-range scaling results of Ref. [148] and reduces to Kolmogorov's 4/5th law for $\boldsymbol{b} = 0$.

4.2.5 Relation of $C_{\varepsilon,\infty}$ to energy and cross-helicity fluxes

In analogy to hydrodynamics, the asymptotes $C^\pm_{\varepsilon,\infty}$ should describe the total energy flux, that is the contribution of the cross-helicity flux to the Elsässer flux should be cancelled by the respective terms $G_0^\pm$ in eq. (4.39). However, since this is not immediately obvious from the derivation, further details are given here for the case of free decay. The argument for the stationary case proceeds analogously.

For decaying turbulence at the peak of dissipation, eq. (4.39) for the asymptotes $C^\pm_{\varepsilon,\infty}$ reduces to

$$C^\pm_{\varepsilon,\infty} = -\frac{\partial_{\sigma_\pm}}{\sigma_\pm^4}\left(\frac{3\sigma_\pm^4}{2} g_0^{\pm\mp\pm}\right) \pm G_0^\pm \ . \tag{4.49}$$

The dimensional version of this equation is

$$\varepsilon = -\frac{\partial_r}{r^4}\left(\frac{3r^4}{2} C^{\pm\mp\pm}_{LL,L}\right) \pm d_t H_c \ , \tag{4.50}$$

where it is assumed that the function $C^{\pm\mp\pm}_{LL,L}$ has its inertial range form corresponding to $g_0^{\pm\mp\pm}$. The function $C^{\pm\mp\pm}_{LL,L}$ can also be expressed through the Elsässer increments [148]

$$C^{\pm\mp\pm}_{LL,L} = \frac{1}{4}\left(\langle(\delta_L z^\pm(\boldsymbol{r}))^2 \delta_L z^\mp(\boldsymbol{r})\rangle - 2\langle z_L^\pm(\boldsymbol{x}) z_L^\pm(\boldsymbol{x}) z_L^\mp(\boldsymbol{x}+\boldsymbol{r})\rangle\right) \ , \tag{4.51}$$

which can be written in terms of the primary fields $\boldsymbol{u}$ and $\boldsymbol{b}$ as

$$\begin{aligned} C^{\pm\mp\pm}_{LL,L} = &\frac{1}{4}\frac{2}{3}\langle(\delta_L u(\boldsymbol{r}))^3 - 6 b_L(\boldsymbol{x})^2 u_L(\boldsymbol{x}+\boldsymbol{r})\rangle \\ &\mp \frac{1}{4}\frac{2}{3}\langle(\delta_L b(\boldsymbol{r}))^3 - 6 u_L(\boldsymbol{x})^2 b_L(\boldsymbol{x}+\boldsymbol{r})\rangle \ , \end{aligned} \tag{4.52}$$

(see e.g. Ref. [148]). The two terms on the first line of eq. (4.52) are the flux terms in the evolution equation of the total energy, while the two terms on last line correspond to the flux terms in the evolution equation of the cross-helicity

[148].

Now eq. (4.50) can be expressed in terms of the primary fields

$$\begin{aligned}\varepsilon &= -\frac{\partial_r}{r^4}\left(\frac{3r^4}{2}C_{LL,L}^{\pm\mp\pm}\right) \pm d_t H_c \\ &= -\frac{\partial_r}{r^4}\left(\frac{r^4}{4}\langle(\delta_L u(\boldsymbol{r}))^3 - 6b_L(\boldsymbol{x})^2 u_L(\boldsymbol{x}+\boldsymbol{r})\rangle\right) \\ &\quad \pm \frac{\partial_r}{r^4}\left(\frac{r^4}{4}\langle(\delta_L b(\boldsymbol{r}))^3 - 6u_L(\boldsymbol{x})^2 b_L(\boldsymbol{x}+\boldsymbol{r})\rangle\right) \pm d_t H_c \\ &= \varepsilon_T \pm \varepsilon_{H_c} \pm d_t H_c = \varepsilon_T \ , \end{aligned} \tag{4.53}$$

where ε_T is the flux of total energy and ε_{H_c} the cross-helicity flux, which must equal $-d_t H_c$ for freely decaying MHD turbulence. Thus the contribution from the third-order correlator $C_{LL,L}^{\pm\mp\pm}$ resulting in ε_{H_c} is cancelled by $d_t H_c$, or, after nondimensionalisation, the cross-helicity flux $\varepsilon_{H_c} L_\pm/[(z^\pm)^2 z^-]$ is cancelled by $G_0^\pm$. In the stationary case the same reasoning applies where ε_{H_c} and the cross-helicity input rate $\varepsilon_{H_c,W}$ cancel out.

4.3 Nonuniversality and self-organisation

Since $C_{\varepsilon,\infty}$ is a measure of the flux of total energy across different scales in the inertial range, differences for the value of this asymptote should be expected for systems with different initial values for the ideal invariants H_{mag} and H_c. The flux of total energy and thus the asymptote $C_{\varepsilon,\infty}$ is an averaged quantity. This implies that cancellations between forward and reverse fluxes may take place leading on average to a positive value of the flux, that is, forward transfer from the large scales to the small scales. In case of $H_{mag} \neq 0$, the value of $C_{\varepsilon,\infty}$ should therefore be *less* than for $H_{mag} = 0$ due to a more pronounced reverse energy transfer in the helical case, the result of which is *less* average forward transfer and thus a smaller value of the (average) flux of total energy. For $H_c \neq 0$ the asymptote $C_{\varepsilon,\infty}$ is expected to be smaller than for $H_c = 0$, since alignment of $\boldsymbol{u}$ and $\boldsymbol{b}$ weakens the coupling of the two fields in the induction equation, leading to less transfer of magnetic energy across different scales and presumably also less transfer of kinetic to magnetic energy. In short, nonuniversal values of $C_{\varepsilon,\infty}$ are expected.

Furthermore, from the analysis of triad interactions carried out in chapter 3, it may be expected that high values of cross-helicity have a different effect on

the asymptote $C_{\varepsilon,\infty}$, depending on the level of magnetic helicity. The analytical results suggested that the cross-helicity may have an asymmetric effect on the nonlinear transfers in the sense that the self-ordering reverse triadic transfers are less quenched by high levels of H_c compared to the forward transfers. The triads contributing to reverse transfers were mainly those where magnetic field modes of the same sign interact, and so for simulations with maximal initial magnetic helicity the dynamics will be dominated by these triads. If the reverse fluxes are less affected by the cross-helicity than the forward fluxes, then the expectation is that for a comparison of the value of $C_{\varepsilon,\infty}$ between systems with (i) high H_{mag} and H_c, (ii) high H_{mag} and $H_c = 0$, (iii) $H_{mag} = 0$ and high H_c and finally (iv) $H_{mag} = 0$ and $H_c = 0$, the value of $C_{\varepsilon,\infty}$ should diminish more between cases (i) and (ii) compared to between cases (iii) and (iv).

4.4 Comparison to DNS data

Before comparing eq. (4.44) with DNS data and addressing this question of nonuniversality numerically, the numerical method is briefly outlined. Equations (1.5)-(1.7) are solved numerically in a periodic box of length $L_{box} = 2\pi$ using the fully de-aliased pseudospectral MHD code described in chapter 2. All simulations resolve the Kolmogorov magnetic and kinetic Kolmogorov scales η_{mag} and η_{kin}, that is $k_{max}\eta_{mag,kin} \geqslant 1$. No background magnetic field is imposed, and both the initial magnetic and velocity fields are random Gaussian with zero mean with energy spectra as described in chapter 2.

Several series of simulations have been carried out for stationary and freely decaying MHD turbulence. In the case of free decay the dependence of the asymptote on the initial level of the ideal invariants is studied while for the stationary simulations all helicities are initially negligible. Different external mechanical forces were used to maintain the system in stationary state in order to assess the influence different forcing methods may have on the system.

For the stationary simulations all helicities are initially negligible. In the simulations of freely decaying MHD turbulence the initial relative magnetic helicity was either maximal (series H and CH) or negligible (series NH and CNH), while the relative cross-helicity ρ_c was adjusted to range from $0 \leqslant \rho_c \leqslant 0.8$ for series CH and CNH as specified in tables 4.2 and 4.3.

4.4.1 Specification of different forcing schemes

Three different types of mechanical forces labelled $\boldsymbol{f}_1$, $\boldsymbol{f}_2$ and $\boldsymbol{f}_3$ have been applied at wavenumbers $k \leqslant k_f = 2.5$. The first type of mechanical force $\boldsymbol{f}_1$ has been introduced in chapter 2, eq. (2.1), and corresponds to the DNS series ND in tbl. 4.1. It essentially feeds the rescaled velocity field back into the system at the large scales and as such there is no direct control over the injected helicities.

The second type of mechanical force $\boldsymbol{f}_2$, which corresponds to the DNS series HF in tbl. 4.1 has also been introduced in chapter 2. It is based on the decomposition of the Fourier transform of the force into helical modes as explained in chapter 1 and has the advantage that the helicity of the force can be adjusted at each wavenumber [25, 116, 137], which gives optimal control over the helicity injection. For all simulations using this type of forcing the relative helicity of the force was set to zero.

The third type of mechanical force[3] corresponds to the DNS series SF in tbl. 4.1 and is given by

$$\boldsymbol{f}_3 = f_0 \sum_{k_f} \begin{pmatrix} \sin k_f z + \sin k_f y \\ \sin k_f x + \sin k_f z \\ \sin k_f y + \sin k_f x \end{pmatrix} , \tag{4.54}$$

where f_0 is an adjustable constant. This type of force is nonhelical by construction.

All three forces have been used in several simulations of stationary homogeneous MHD simulations. The scheme labelled $\boldsymbol{f}_1$ was shown by Sahoo *et al.* [159] to keep the helicities at negligible levels even though zero helicity injection cannot be guaranteed with this forcing scheme. At low Reynolds number this conservation of helicities appears to be broken and induces peculiar self-ordering effects which will be discussed in further detail in chapter 6. The adjustable helicity forcing $\boldsymbol{f}_2$ has been extensively used in the literature [25, 116, 137], mainly when nonzero levels of kinetic [25] or magnetic [116, 137] helicity injection are required. The third forcing scheme $\boldsymbol{f}_3$ has been employed in the simulations by Dallas and Alexakis [51], where it was shown that despite zero injection of all helicities, the system self-organised into large-scale fully helical states. This point will be further discussed in chapter 6 in the connection with relaminarisation events.

[3]This scheme was implemented by E. Goldstraw [79].

Run id	N^3	$k_{max}\eta_{mag}$	$k_{max}\eta_{kin}$	R_-	R_L	R_λ	η	C_ε	σ_{C_ε}	run time
ND1	128	3.22	2.53	27.93	78.68	42.65	0.01	0.280	0.0028	100
ND2	128	2.59	2.52	35.00	90.97	48.24	0.009	0.317	0.0065	100
ND3	128	2.12	2.12	45.63	119.92	59.59	0.007	0.285	0.0021	100
ND4	128	1.85	1.93	53.12	137.38	65.32	0.006	0.290	0.0057	83.56
ND5	128	1.46	1.58	66.21	173.33	75.83	0.0045	0.285	10^{-5}	50
ND6	256	2.68	3.10	81.34	209.77	87.33	0.004	0.283	0.0029	50
ND7	256	2.14	2.53	114.94	284.48	105.29	0.003	0.272	0.015	72.44
ND8	256	1.74	2.05	123.08	330.73	115.83	0.0023	0.260	0.0072	72.52
ND9	256	1.44	1.75	169.47	447.34	137.50	0.0018	0.255	0.0025	79.87
ND11	512	1.84	2.31	301.07	834.51	196.91	0.001	0.239	0.015	69.98
ND12	512	1.56	1.96	345.32	968.76	211.51	0.0008	0.238	0.0017	70.67
ND13	512	1.45	1.82	359.68	1017.72	219.99	0.00073	0.235	0.0025	53.40
ND14	528	1.37	1.72	454.79	1218.98	234.97	0.00067	0.231	0.0072	50
ND15	1024	2.18	2.74	629.44	1593.58	236.97	0.0005	0.230	0.0041	59.54
ND16	1024	1.51	1.86	919.16	2538.24	293.12	0.0003	0.226	0.0043	50
SF1	256	1.71	2.04	152.95	428.57	140.64	0.0035	0.240	0.0056	100
SF2	256	1.52	1.85	197.87	481.87	144.61	0.003	0.251	0.01	100
SF3	256	1.23	1.51	239.91	620.40	165.39	0.0023	0.245	0.0028	100
SF4	256	1.01	1.25	315.74	812.38	184.64	0.0018	0.246	0.0022	100
SF5	512	1.69	2.11	392.42	1039.16	213.55	0.0014	0.238	0.0035	60
SF6	512	1.31	1.65	528.32	1443.83	251.76	0.001	0.230	0.0006	60
HF1	256	1.52	1.75	135.81	385.19	123.22	0.0018	0.260	0.0055	63.37
HF2	256	1.04	1.29	262.66	735.98	184.03	0.0014	0.237	0.0028	79.87
HF3	512	0.96	1.17	613.83	1718.40	267.67	0.0006	0.228	0.0075	50

Table 4.1 *Specifications of stationary simulations. ND refers to an external force as defined in* (2.1)*, SF refers to an external force as defined in* (4.54)*, HF refers to an external force as defined in* (2.2)-(2.6)*, R_L denotes the integral-scale Reynolds number, R_λ the Taylor-scale Reynolds number, R_- the generalised Reynolds number given in* (4.29)*, η the magnetic resistivity, k_{max} the largest resolved wavenumber, η_{mag} the Kolmogorov microscale associated with the magnetic field, C_ε the dimensionless total dissipation rate defined in* (4.23) *and σ_{C_ε} the standard error on C_ε. All Reynolds numbers are time averages. Simulations of the series SF were carried out by E. Goldstraw [79].*

Run id	N^3	$k_{max}\eta_{mag}$	R_-	R_L	R_λ	η	k_0	#	C_ε	σ	$\rho_c(0)$
H1	128^3	1.30	33.37	25.28	14.87	0.009	5	10	0.756	0.008	0
H2	256^3	2.42	37.77	27.81	15.85	0.008	5	10	0.704	0.007	0
H3	512^3	1.38	50.81	35.08	18.55	0.002	15	10	0.608	0.001	0
H4	256^3	1.80	61.14	40.63	20.34	0.005	5	10	0.569	0.006	0
H5	256^3	1.59	76.72	48.73	23.11	0.004	5	10	0.510	0.005	0
H6	1024^3	1.38	89.32	55.51	25.76	0.00075	23	10	0.4589	0.0003	0
H7	256^3	1.29	102.53	60.65	26.91	0.003	5	10	0.450	0.004	0
H8	512^3	2.33	123.17	69.40	29.67	0.0025	5	10	0.419	0.003	0
H9	512^3	2.01	154.67	83.06	33.84	0.002	5	10	0.384	0.003	0
H10	512^3	1.45	255.89	123.97	45.21	0.0012	5	10	0.320	0.004	0
H11	528^3	1.31	308.69	143.71	50.18	0.001	5	10	0.310	0.004	0
H12	1024^3	2.03	441.25	194.38	61.39	0.0007	5	5	0.281	0.002	0
H13	1032^3	1.38	771.34	309.08	82.97	0.0004	5	5	0.268	0.001	0
H14	1024^3	1.24	885.05	358.72	88.76	0.00035	5	5	0.265	0.002	0
H15	2048^3	1.35	2042.52	724.71	136.25	0.00015	5	1	0.250	-	0
CH06H1	512^3	2.17	124.89	108.81	49.88	0.002	5	1	0.380	-	0.6
CH06H2	512^3	1.57	207.61	171.87	68.57	0.0012	5	5	0.309	0.002	0.6
CH06H3	1024^3	2.21	351.52	277.21	95.31	0.0007	5	1	0.260	-	0.6
CH06H4	1024^3	1.76	491.50	380.70	116.85	0.0005	5	1	0.236	-	0.6
CH06H5	1024^3	1.37	696.19	523.08	132.48	0.00035	5	1	0.231	-	0.6
CHH1	512^3	1.46	254.64	129.83	47.55	0.0012	5	5	0.315	0.002	0.2
CHH2	512^3	1.50	240.35	147.68	55.25	0.0012	5	5	0.311	0.003	0.4
CHH3	512^3	1.74	149.28	195.27	90.60	0.0012	5	5	0.323	0.03	0.8

Table 4.2 *Specifications of simulations with maximal initial magnetic helicity [175]. R_L denotes the integral-scale Reynolds number, R_λ the Taylor-scale Reynolds number, R_- the generalised Reynolds number, η the magnetic resistivity, k_0 the peak wavenumber of the initial energy spectra, k_{max} the largest resolved wavenumber, η_{mag} the Kolmogrov microscale associated with the magnetic field at the peak of total dissipation, # the ensemble size, C_ε the dimensionless total dissipation rate, σ the standard error on C_ε and $\rho_c(0)$ the initial relative cross helicity. All Reynolds numbers are measured at the peak of total dissipation. All C-series runs were carried out by M. McKay.*

Run id	N^3	$k_{max}\eta_{mag}$	R_-	R_L	R_λ	η	k_0	#	C_ε	σ	$\rho_c(0)$
NH1	256^3	1.51	55.57	53.89	25.57	0.004	5	10	0.587	0.005	0
NH2	256^3	1.26	71.51	68.60	30.11	0.003	5	10	0.530	0.004	0
NH3	512^3	1.86	103.41	96.69	37.68	0.002	5	10	0.468	0.004	0
NH4	512^3	1.51	133.14	122.51	43.94	0.0015	5	10	0.431	0.004	0
NH5	512^3	1.29	161.35	151.76	50.73	0.0012	5	10	0.394	0.004	0
NH6	1024^3	2.28	192.40	168.28	54.44	0.001	5	5	0.358	0.002	0
NH7	1024^3	1.76	259.58	232.10	65.42	0.0007	5	5	0.358	0.002	0
NH8	1024^3	1.40	354.30	301.71	76.73	0.0005	5	5	0.323	0.002	0
NH9	2048^3	1.15	1071.44	823.58	134.73	0.00015	5	1	0.279	-	0
CH06NH1	512^3	2.02	94.39	113.02	49.29	0.002	5	1	0.482	-	0.6
CH06NH2	512^3	1.41	148.86	174.61	65.48	0.0012	5	5	0.417	0.003	0.6
CH06NH3	1024^3	1.93	242.06	272.85	87.50	0.0007	5	1	0.365	-	0.6
CH06NH4	1024^3	1.52	325.62	365.54	104.45	0.0005	5	1	0.341	-	0.6
CH06NH5	1024^3	1.16	450.01	515.23	127.09	0.00035	5	1	0.313	-	0.6
CHNH1	512^3	1.31	168.31	152.84	51.40	0.0012	5	5	0.401	0.003	0.2
CHNH2	512^3	1.34	162.27	157.48	55.52	0.0012	5	5	0.402	0.006	0.4
CHNH3	512^3	1.58	116.71	204.78	87.52	0.0012	5	5	0.456	0.002	0.8

Table 4.3 *Specifications of simulations [175] for magnetic fields with negligible initial magnetic helicity. R_L denotes the integral-scale Reynolds number, R_λ the Taylor-scale Reynolds number, R_- the generalised Reynolds number, η the magnetic resistivity, k_0 the peak wavenumber of the initial energy spectra, k_{max} the largest resolved wavenumber, η_{mag} the Kolmogrov microscale associated with the magnetic field at the peak of total dissipation, # the ensemble size, C_ε the dimensionless total dissipation rate, σ the standard error on C_ε and $\rho_c(0)$ the initial relative cross helicity. All Reynolds numbers are measured at the peak of total dissipation. Simulations NH5-NH9 and all C-series runs were carried out by M. McKay.*

4.4.2 Decaying MHD turbulence

Figure 4.1 shows fits of eq. (4.44) to DNS data for datasets that differ in the initial value of H_{mag} and H_c. As can be seen, eq. (4.44) fits the data very well. For the series H runs and for $R_- > 70$ it is sufficient to consider terms of first order in R_-, while for the series NH the first-order approximation is valid for $R_- > 100$. The cross-helical CH06H runs gave consistently lower values of C_ε compared to the series H runs, while little difference was observed between series CH06NH and NH. The asymptotes were $C_{\varepsilon,\infty} = 0.241 \pm 0.008$ for the H series, $C_{\varepsilon,\infty} = 0.265 \pm 0.013$ for the NH series, $C_{\varepsilon,\infty} = 0.193 \pm 0.006$ for the CH06H series and $C_{\varepsilon,\infty} = 0.268 \pm 0.005$ for the CH06NH series.

As predicted by the qualitative theoretical arguments outlined previously, the measurements show that the asymptote calculated from the nonhelical runs is larger than for the helical case, as can be seen in fig. 4.1. The asymptotes of the series H and NH do not lie within one standard error of one another. Simulations carried out with $H_c \neq 0$ suggest little difference in C_ε for magnetic fields with initially zero magnetic helicity. For initially helical magnetic fields C_ε is further quenched if $H_c \neq 0$. In view of nonuniversality, an even larger variance of $C_{\varepsilon,\infty}$ can be expected once other parameters such as external forcing, plasma β, Pm, etc., are taken into account. Here attention is restricted to nonuniversality caused by different degrees of vector field correlations in view of their connection to self-ordering effects as discussed in chapter 3.

4.4.3 Stationary MHD turbulence

Figure 4.2 shows error-weighted fits of eq. (4.44) to DNS data. As can be seen, eq. (4.44) fits the data very well, provided terms of second order in R_- are included. For $R_- > 80$, it is sufficient to consider terms of first order in R_- only. The asymptote has been calculated to be $C_{\varepsilon,\infty} = 0.223 \pm 0.003$, where the error is obtained from the fit. Furthermore, the figure shows that the result is independent of the forcing scheme, as the datasets obtained from simulations using the three different forcing functions are consistent with each other. This is likely to change if the strategy of energy input is fundamentally changed, for example if an electromagnetic force is used or the system is forced at the small scales. The independence of C_ε of the forcing scheme established here only shows independence of the specific implementation of the forcing.

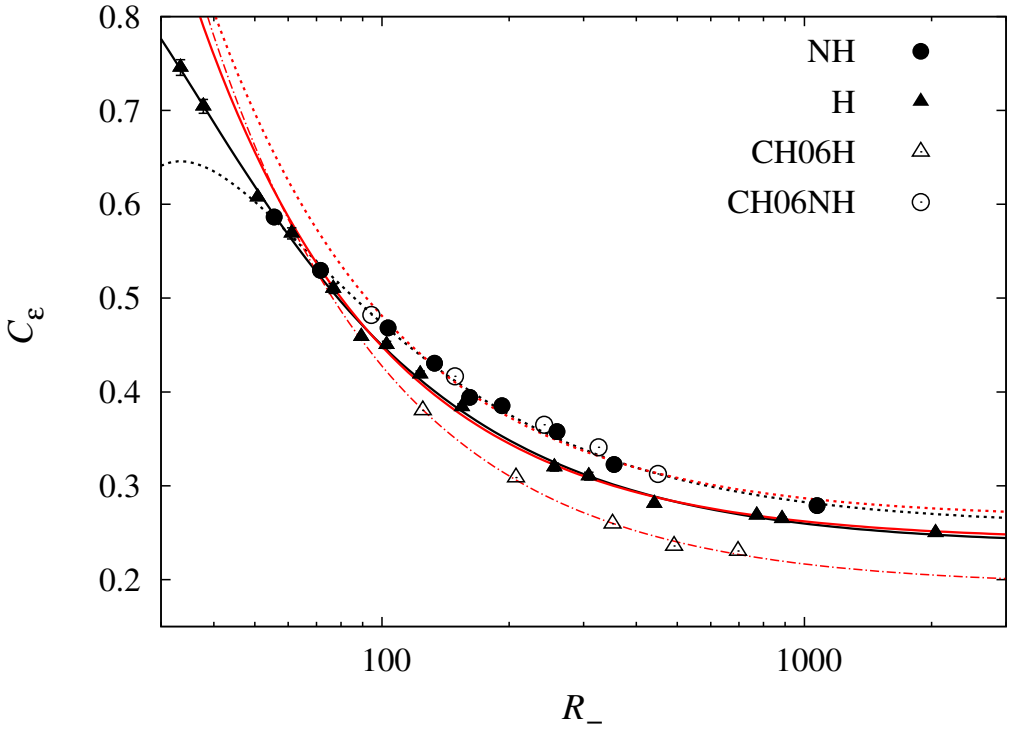

Figure 4.1 *The solid and dotted and dash-dotted lines show eq.* (4.44) *fitted to helical, non-helical and cross-helical DNS data, respectively. The red (grey) lines refer to fits using eq.* (4.44) *up to first order, while the black lines use eq.* (4.44) *up to second order in* $1/R_-$*. As can be seen, the respective asymptotes differ for the data sets.*

4.5 Discussion and conclusions

The behaviour of the dimensionless dissipation coefficient C_ε in homogeneous MHD turbulence with $Pm = 1$ and no background magnetic field is given by

$$C_\varepsilon = C_{\varepsilon,\infty} + \frac{C}{R_-} + \frac{D}{R_-^2} + O(R_-^{-3}) \; . \tag{4.55}$$

This equation was derived from the energy balance equations for $\boldsymbol{z}^\pm$ in real space by outer asymptotic expansions in powers of $1/R_\mp$, *leading necessarily to a large-scale description of the behaviour of the dimensionless dissipation rate.* The approximative equation (4.55) has been shown to agree well with data obtained from medium to high resolution DNSs of decaying and statistically steady MHD turbulence sustained by large-scale forcing.

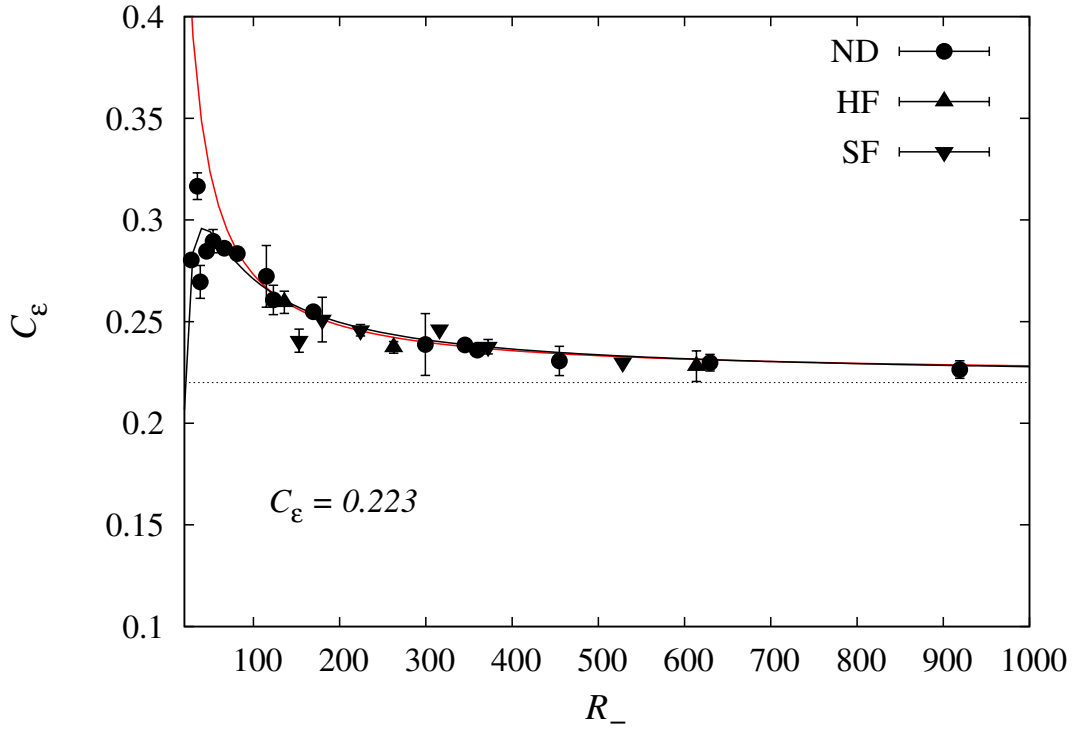

Figure 4.2 *The expression given in eq.* (4.44) *fitted to DNS data from the ND-series. The red line shows a fit to data for* $R_- > 80$ *to first order in* $1/R_-$*, the black line results from a fit using all data points and including terms up to second order in* $1/R_-$*. The error bars show one standard error.*

The asymptote in the limit $R_- \to \infty$ comes from the sum of the nonlinear terms in the momentum and induction equations, that is, it measures the total transfer flux, which is expected to depend on the values of the ideal invariants. As predicted, the values of the respective asymptotes from the datasets differ, suggesting a dependence of $C_{\varepsilon,\infty}$ on different values of the helicities, and thus a connection to the questions of universality and self-organisation in MHD turbulence. For maximally helical magnetic fields $C_{\varepsilon,\infty}$ is larger than for nonhelical fields. This is expected from the inverse cascade of magnetic helicity. The dependence of $C_{\varepsilon,\infty}$ on the remaining ideal invariant, the cross-helicity, is more complex. Since $C_{\varepsilon,\infty}$ describes the flux of total energy across the scales, this flux is expected to diminish for increasing cross-helicity. This is indeed the case for helical magnetic fields, where $C_{\varepsilon,\infty}$ depends on the cross-helicity in the expected way. Surprisingly, for nonhelical magnetic fields $C_{\varepsilon,\infty}$ does *not* depend on the cross-helicity. This is consistent with the asymmetric effect of the cross-

helicity on forward and reverse fluxes of total energy suggested by the analysis of triad interactions in chapter 3, where high levels of cross-helicity quench forward transfer more than reverse transfer.

The numerical results also showed that $C_{\varepsilon,\infty}$ is universal with respect to different forcing schemes applied to the same field in the same wavenumber range, thus confirming that the particular functional form of a large-scale force is irrelevant to the small-scale turbulent dynamics as long as the ideal invariants remain the same for the different forcing schemes. However, this may not be the case for forces applied at smaller scales. The analysis presented here relies on taking outer asymptotic expansions of all scale-dependent functions in the energy balance equation, including the energy input from the forcing. Here it was crucial to assume that the system was forced at the large scales, as the limit of infinite Reynolds number was defined as energy input at the lowest wavenumbers $k \to 0$ and removal of energy at the largest wavenumbers $k \to \infty$. This clearly precludes the application of the present analysis to situations where the system is forced at intermediate or small scales. Therefore, it can be expected that systems forced at intermediate scales deviate from the $1/R_{-}$-scaling of C_ε. For hydrodynamics, this seems to be the case.

In hydrodynamics, mathematically rigorous bounds have been derived for sufficiently smooth forcing functions from the existence of weak solutions of the Navier-Stokes equations [55, 57], where it was necessary to assume that the force function was square-integrable with square-summable Fourier coefficients [54]. The resulting bound for the dimensionless dissipation rate was

$$C_\varepsilon \leqslant C_1 + \frac{C_2}{Re} \,, \tag{4.56}$$

where C_1 and C_2 are constants depending on the shape (i.e. the wavenumber-dependence) of the forcing function [55]. This inequality is consistent with the large-scale analysis presented here when applied to hydrodynamic turbulence [121]. The constants C_1 and C_2 diverge for less well-behaved forcing functions [54], in particular, this may be the case for forces applied at the small scales for which the asymptotic analysis presented here does not apply. However, weak solutions of the Navier-Stokes equation still exist for less regular (rougher) forcing functions, leading not to an unbounded dissipation rate but to a different Reynolds number scaling. In particular, this applies to forces acting at the small scales [54]. Bounds for the energy dissipation rate have been derived for forces

which are not square-integrable [34] and indeed lead to a different prediction for the Reynolds number dependence of the dimensionless dissipation rate for hydrodynamic turbulence sustained by rough forces, which is consistent with results from numerical simulations using fractal forcing functions [17, 54, 118].

In view of the inverse cascade of magnetic helicity, there is growing interest in small-scale forcing in MHD turbulence, for which a large-scale asymptotic analysis is not directly applicable, as discussed above. Therefore it may be of interest to extend the mathematically rigorous results obtained in hydrodynamics to MHD in order to gain insight into the many interesting flow configurations making up the complex problem of MHD turbulence. Some basic results in this direction are presented in the next chapter.

The results presented here were restricted to the simplest cases of homogeneous MHD turbulence. In the general case in plasmas there will be a mean magnetic field, which leads to spectral anisotropy and the breakdown of the conservation of magnetic helicity [117]. This might introduce several difficulties to be overcome when generalising this method, as the spectral flux will then depend on the direction of the mean field [182, 183] and a more generalised description and role for the magnetic helicity would be needed. Other questions concern the generalisation of this approach to MHD flows with magnetic Prandtl numbers $Pm \neq 1$, the influence of other vector field correlations on the dissipation rate, the effect of compressive fluctuations, as well as to turbulent systems where the flow carries other quantities such as temperature, pollutants or additives.

Chapter 5

Bounds on the dissipation rates

Rigorous estimates for the dimensionless dissipation coefficient $C_{\varepsilon,u}$ in hydrodynamics have been derived using the existence of weak solutions of the Navier-Stokes equations [55, 57, 71]. In order to derive these estimates, it is assumed that the flow is maintained by an external body force $\boldsymbol{f}$, which needs to satisfy certain regularity conditions and may or may not be time-dependent. The MHD equations also have weak solutions, therefore it should be possible to derive estimates for the dissipation rate of total energy for MHD by a very similar method.

In this chapter the results obtained in hydrodynamics are extended to MHD. In order to facilitate a comparison to the results of the approximate methods put forward in chapter 4, the MHD equations are analysed in the Elsässer formulation. This also permits a straightforward extension of the results on the dissipation rate of total energy to the dissipation rate of cross-helicity. As in the rest of this thesis, it is assumed that no background magnetic field is present.

5.1 Notation and definitions

This chapter is different in nature from the rest of this thesis and requires mathematical concepts and definitions which are not used elsewhere. In order to keep the material compact and accessible, these relevant concepts are introduced here.

As in chapter 3, the MHD equations are considered on a three-dimensional domain $\Omega = [0, L]^3$ with periodic boundary conditions and sufficiently well-behaved initial conditions to allow weak solutions. A weak solution to a partial differential equation (PDE) is a solution of the corresponding integral equation where all derivatives act on test functions, which are by definition infinitely many times differentiable. That is, weak solutions solve a given PDE in the distributional sense, they may not be differentiable and are usually not unique.

Physically reasonable solutions of the Navier-Stokes equations are required to have finite kinetic energy and finite mean square vorticity, while physically reasonable solutions of the MHD equations also require finiteness of the magnetic energy and the mean square current. In mathematical terms, this can be formulated by requiring the appropriate norms

$$||\boldsymbol{u}||_2 \equiv (\boldsymbol{u}, \boldsymbol{u})^{1/2} = \left(\int_\Omega d\boldsymbol{x} \ |\boldsymbol{u}(\boldsymbol{x}, t)|^2 \right)^{1/2} , \tag{5.1}$$

$$||\boldsymbol{u}||_{H^1} \equiv (\boldsymbol{u}, \boldsymbol{u})_{H^1}^{1/2} = \left(\int_\Omega d\boldsymbol{x} \ |\nabla \boldsymbol{u}(\boldsymbol{x}, t)|^2 \right)^{1/2} , \tag{5.2}$$

to be finite, where the inner products on the respective function spaces are given by

$$(\boldsymbol{u}, \boldsymbol{v}) \equiv \int_\Omega d\boldsymbol{x} \ \boldsymbol{u}(\boldsymbol{x}, t) \cdot \boldsymbol{v}(\boldsymbol{x}, t) \ , \tag{5.3}$$

$$(\boldsymbol{u}, \boldsymbol{v})_{H^1} \equiv \int_\Omega d\boldsymbol{x} \ \partial_j u_i(\boldsymbol{x}, t) \partial_j v_i(\boldsymbol{x}, t) \ . \tag{5.4}$$

The first norm, $||\cdot||_2$, is the familiar L^2-norm, where $||\boldsymbol{u}||_2^2$ essentially describes the total kinetic (or magnetic) energy. The square of the norm on the Sobolev space H^1 describes the mean square vorticity and the mean square current, provided the vector fields have zero spatial mean which is the case here. Therefore $||\cdot||_2$ and $||\cdot||_{H^1}$ are the natural choices for the mathematical study of fluid flows. Two additional norms are required for particular steps using the Hölder inequality, these are the L^1-norm and the L^∞ norm, defined as

$$||\boldsymbol{u}||_1 \equiv \int_\Omega d\boldsymbol{x} \ |\boldsymbol{u}(\boldsymbol{x}, t)| \ , \tag{5.5}$$

$$||\boldsymbol{u}||_\infty \equiv \sup_{\boldsymbol{x} \in \Omega} |\boldsymbol{u}(\boldsymbol{x}, t)| \ . \tag{5.6}$$

In the statistical approach to turbulence, the dissipation rates are given as time

or ensemble averages. The time average can be put on rigorous mathematical grounds by considering statistical solutions to the Navier-Stokes and MHD equations [71], and a long-time average can be defined. A proper definition of a statistical solution and the corresponding time average requires the introduction of measure spaces and a reformulation of the notion of weak solutions in terms of probability measures. For reasons of clarity and conciseness this is not carried out here, the necessary mathematical details can be found in the book by Foias *et al.* [71]. The long-time average is denoted by $\langle\cdot\rangle_t$ in this chapter.

The arguments presented in the following sections use several functional inequalities in order to derive the bounds. These are Hölder's inequality, Grönwall's inequality and the Cauchy-Schwarz inequality. Hölder's inequality states that for functions $\boldsymbol{v} \in L^p(\Omega)^3$ and $\boldsymbol{w} \in L^q(\Omega)^3$ with $1/p + 1/q = 1$

$$||\boldsymbol{v} \cdot \boldsymbol{w}||_1 \leqslant ||\boldsymbol{v}||_p \; ||\boldsymbol{w}||_q \; , \tag{5.7}$$

where the p-norm for $\leqslant p < \infty$ is given by

$$||\boldsymbol{v}||_p \equiv \left(\int_\Omega d\boldsymbol{x} \; |\boldsymbol{v}|^p \right)^{1/p} \; . \tag{5.8}$$

The Hölder inequality also holds for the L^∞ norm, that is

$$||\boldsymbol{v} \cdot \boldsymbol{w}||_1 \leqslant ||\boldsymbol{v}||_\infty \; ||\boldsymbol{w}||_1 \; . \tag{5.9}$$

Grönwall's inequality asserts that for functions u, v and w the inequality $d_t u(t) \leqslant u(t)v(t) + w(t)$ implies

$$u(t) \leqslant u(0) \exp\left(\int_0^t ds \; v(s) \right) + \int_0^t ds \; w(s) \exp\left(\int_s^t ds' \; v(s') \right) \; . \tag{5.10}$$

The Cauchy-Schwarz inequality, which follows from the Hölder inequality for $p = q = 1$, states that for $\boldsymbol{v}, \boldsymbol{w} \in L^2(\Omega)^3$

$$|(\boldsymbol{v}, \boldsymbol{w})| \leqslant ||\boldsymbol{v}||_2 \; ||\boldsymbol{w}||_2 \; . \tag{5.11}$$

5.2 Weak solutions on periodic domains

In 1934 Leray established the existence of weak solutions of the Navier-Stokes equation in three spatial dimensions for square-integrable sufficiently regular initial conditions and external forces [109] (see also [44, 56, 71, 106]). These weak solutions are square-integrable and the existence result is valid for the 3D torus as well as for the whole space $\mathbb{R}^3$ with the appropriate boundary conditions. The analogous result has been obtained for the incompressible MHD equations in the primary variables [63, 75], which carries over to the Elsässer formulation.

Regarding the external force, sufficiently regular usually means that the Fourier coefficients of the force and its spatial derivatives are bounded at all times, that is, $\boldsymbol{f}_\pm \in L^2(\Omega)^3$ and

$$\sup_{t\geqslant 0} ||(-\Delta)^{-1/2}\boldsymbol{f}^\pm||_2^2 = L^3 \sup_{t\geqslant 0} \sum_{\boldsymbol{k}\neq 0} \frac{1}{|\boldsymbol{k}|^2} |\hat{\boldsymbol{f}}_\pm(\boldsymbol{k},t)|^2 < \infty \ . \tag{5.12}$$

Furthermore, the forces must be solenoidal at all times.

In summary, given sufficiently regular initial conditions $\boldsymbol{z}_0^\pm \in L^2(\Omega)^3$ and external forces $\boldsymbol{f}^\pm$ with the aforementioned properties, it is possible to find vector fields $\boldsymbol{z}^\pm \in L^2(\Omega)^3$ such that for all test functions $\varphi \in C^\infty(\Omega)$ and all solenoidal (test) vector fields $\boldsymbol{v} \in C^\infty(\Omega)^3$, which have compact support in time,

$$\begin{aligned}\int_0^\infty dt \int_\Omega d\boldsymbol{x}\ \boldsymbol{z}^\pm \cdot \partial_t \boldsymbol{v} + \boldsymbol{z}^\pm \cdot (\nabla \boldsymbol{v}) \cdot \boldsymbol{z}^\mp + (\nu_+ \boldsymbol{z}^\pm + \nu_- \boldsymbol{z}^\mp) \cdot \Delta \boldsymbol{v} \\ + \int_0^\infty dt \int_\Omega d\boldsymbol{x}\ \boldsymbol{f}^\pm \cdot \boldsymbol{v} + \int_\Omega d\boldsymbol{x}\ \boldsymbol{z}_0^\pm(\boldsymbol{x}) \cdot \boldsymbol{v}(\boldsymbol{x},0) = 0 \ ,\end{aligned} \tag{5.13}$$

and

$$\int_0^\infty dt \int_\Omega d\boldsymbol{x}\ \boldsymbol{z}^\pm \cdot \nabla \varphi = 0 \ , \tag{5.14}$$

$$\int_0^\infty dt \int_\Omega d\boldsymbol{x}\ \boldsymbol{f}^\pm \cdot \nabla \varphi = 0 \ . \tag{5.15}$$

As $\boldsymbol{z}^\pm$ are not necessarily differentiable, any occurrence of a derivative acting on $\boldsymbol{z}^\pm$ in this chapter is understood as short-hand notation for the derivatives acting in the distributional sense on test functions.

All solutions $\boldsymbol{z}^{\pm}$ of eqs. (5.13) - (5.15) satisfy the *energy inequality*

$$\begin{aligned}\frac{1}{2}d_t\Big(||\boldsymbol{z}^-||_2^2+||\boldsymbol{z}^-||_2^2\Big) \leqslant &-\nu_+(||\nabla\boldsymbol{z}^+||_2^2+||\nabla\boldsymbol{z}^-||_2^2)\\ &-\nu_-\int_\Omega d\boldsymbol{x}\Big[(\boldsymbol{z}^+\cdot\Delta\boldsymbol{z}^-)+(\boldsymbol{z}^-\cdot\Delta\boldsymbol{z}^+)\Big]\\ &+\int_\Omega d\boldsymbol{x}\,\Big((\boldsymbol{f}^+\cdot\boldsymbol{z}^+)+(\boldsymbol{f}^-\cdot\boldsymbol{z}^-)\Big)\,, \end{aligned}\tag{5.16}$$

which is an equality for strong solutions (if they exist). Physically reasonable weak solutions should saturate this inequality as otherwise the total energy would not be conserved. Weak solutions which saturate eq. (5.16) also satisfy the following equality for the cross-helicity evolution

$$\begin{aligned}\frac{1}{2}d_t\Big(||\boldsymbol{z}^+||_2^2-||\boldsymbol{z}^-||_2^2\Big) = &-\nu_+(||\nabla\boldsymbol{z}^+||_2^2-||\nabla\boldsymbol{z}^-||_2^2)\\ &-\nu_-\int_\Omega d\boldsymbol{x}\Big[(\boldsymbol{z}^+\cdot\Delta\boldsymbol{z}^-)-(\boldsymbol{z}^-\cdot\Delta\boldsymbol{z}^+)\Big]\\ &+\int_\Omega d\boldsymbol{x}\,\Big((\boldsymbol{f}^+\cdot\boldsymbol{z}^+)-(\boldsymbol{f}^-\cdot\boldsymbol{z}^-)\Big)\,. \end{aligned}\tag{5.17}$$

In the same way as for the Navier-Stokes equations, Grönwall's inequality (5.10) applied to eq. (5.16) and eq. (5.17) guarantees that the time-derivatives are uniformly bounded, therefore the long-time average $\langle\cdot\rangle_t$ of the respective time-derivative vanishes in eq. (5.16) and eq. (5.17), leading to

$$\begin{aligned}L^3\varepsilon &= \big\langle-\nu_+(||\nabla\boldsymbol{z}^+||_2^2+||\nabla\boldsymbol{z}^-||_2^2)-\nu_-(||\nabla\boldsymbol{z}^++\nabla\boldsymbol{z}^-||_2^2-||\nabla\boldsymbol{z}^--\nabla\boldsymbol{z}^+||_2^2)\big\rangle_t\\ &\leqslant\left\langle\int_\Omega d\boldsymbol{x}\,\Big((\boldsymbol{f}^+\cdot\boldsymbol{z}^+)+(\boldsymbol{f}^-\cdot\boldsymbol{z}^-)\Big)\right\rangle_t\\ &\leqslant\langle||\boldsymbol{f}^+||_2\,||\boldsymbol{z}^+||_2\rangle_t+\langle||\boldsymbol{f}^-||_2\,||\boldsymbol{z}^-||_2\rangle_t\,, \end{aligned}\tag{5.18}$$

which again would be an equality for strong solutions (if they exist). Similarly, for the cross-helicity

$$\begin{aligned}L^3|\varepsilon_{H_c}| &= \big|\big\langle\nu_+(||\nabla\boldsymbol{z}^+||_2^2-||\nabla\boldsymbol{z}^-||_2^2)+\nu_-(||\nabla\boldsymbol{z}^++\nabla\boldsymbol{z}^-||_2^2+||\nabla\boldsymbol{z}^--\nabla\boldsymbol{z}^+||_2^2)\big\rangle_t\big|\\ &\leqslant\left|\left\langle\int_\Omega d\boldsymbol{x}\,\Big((\boldsymbol{f}^+\cdot\boldsymbol{z}^+)-(\boldsymbol{f}^-\cdot\boldsymbol{z}^-)\Big)\right\rangle_t\right|\\ &\leqslant\langle||\boldsymbol{f}^+||_2\,||\boldsymbol{z}^+||_2\rangle_t+\langle||\boldsymbol{f}^-||_2\,||\boldsymbol{z}^-||_2\rangle_t\,, \end{aligned}\tag{5.19}$$

where the absolute value of ε_{H_c} needs to be considered, since the cross-helicity is not positive definite.

The aim is now to estimate the L^2-norms of the forces with a view of extracting a dependence on the characteristic quantities describing the system. These are the dissipation parameters $\nu_\pm$, characteristic length scales associated with the forces and the rms values of the Elsässer fields.

5.3 Estimating the forces

Characteristic length scales of the forces $\boldsymbol{f}^\pm$ can be defined with respect to the Laplacian acting on the forces. In order to do this while requiring as little as possible in terms of additional constraints on the forces, the length scales $L_{f,\pm}$ can be defined as

$$L_{f,\pm} = \left(\frac{\langle ||(-\Delta)^{-1/2} \boldsymbol{f}^\pm||_2 \rangle_t}{\langle ||(-\Delta)^{1/2} \boldsymbol{f}^\pm||_2 \rangle_t} \right)^{1/2} , \tag{5.20}$$

following Ref. [71]. The forces $\boldsymbol{f}^\pm$ have been assumed to lie in the domain of the operator $(-\Delta)^{-1/2}$ by eq. (5.12) and are further assumed to obey $||(-\Delta)^{1/2} \boldsymbol{f}^\pm||_2 < \infty$ at all times, such that the above definition is possible. The L^2-norm of $(-\Delta)^{-1/2} \boldsymbol{f}^\pm$ can be expressed as an inner product

$$||(-\Delta)^{-1/2} \boldsymbol{f}^\pm||_2^2 = ((-\Delta)^{-1/2} \boldsymbol{f}^\pm, (-\Delta)^{-1/2} \boldsymbol{f}^\pm) = (\boldsymbol{f}^\pm, (-\Delta)^{-1} \boldsymbol{f}^\pm) , \tag{5.21}$$

which motivates the next step, that is, to take the inner product of the MHD equations with $(-\Delta)^{-1} \boldsymbol{f}^\pm$, in order extract the length scale $L_{f,\pm}$. The resulting equation reads

$$\begin{aligned} \frac{1}{2} \Big(d_t(\boldsymbol{z}^\pm, (-\Delta)^{-1} \boldsymbol{f}^\pm) - (\boldsymbol{z}^\pm, \partial_t (-\Delta)^{-1} \boldsymbol{f}^\pm) \Big) &= -\nu_+(\boldsymbol{z}^\pm, \boldsymbol{f}^\pm) - \nu_-(\boldsymbol{z}^\mp, \boldsymbol{f}^\pm) \\ - \int_\Omega d\boldsymbol{x} \; (-\Delta)^{-1} \boldsymbol{f}^\pm \cdot (\boldsymbol{z}^\mp \cdot \nabla) \boldsymbol{z}^\pm &+ (\boldsymbol{f}^\pm, (-\Delta)^{-1} \boldsymbol{f}^\pm) , \end{aligned} \tag{5.22}$$

where in the penultimate term on the RHS a spatial derivative acts on $\boldsymbol{z}^\mp$, which introduces an unknown length scale. This can be remedied by integrating this term by parts resulting in

$$- \int_\Omega d\boldsymbol{x} \; (-\Delta)^{-1} \boldsymbol{f}^\pm \cdot (\boldsymbol{z}^\mp \cdot \nabla) \boldsymbol{z}^\pm = \int_\Omega d\boldsymbol{x} \; \boldsymbol{z}^\pm \cdot (\boldsymbol{z}^\mp \cdot \nabla) (-\Delta)^{-1} \boldsymbol{f}^\pm , \tag{5.23}$$

where all spatial derivatives now act on the forces. The surface terms which arise in the integration by parts are not present since $\boldsymbol{z}^\pm$ and $\boldsymbol{f}^\pm$ vanish at the boundary $\partial\Omega$. It is this and other integrations by parts where a background magnetic field,

which by definition does not vanish at the boundary, poses problems.

The next step consists of obtaining an estimate on the L^2-norm of the forces from eq. (5.22). The argument proceeds similarly to the derivation of eq. (5.18), where Grönwall's inequality (5.10) implied that the kinetic energy was uniformly bounded in time such that the long-time average of the time derivative vanishes. Since the force was assumed to be bounded in time, and the Elsässer fields are bounded as a consquence of the energy inequality, the long-time average of all terms involving a time-derivative must vanish, hence

$$\begin{aligned}\langle||(-\Delta)^{-1/2}\boldsymbol{f}^{\pm}||_2^2\rangle_t \leqslant \langle\nu_+(\boldsymbol{z}^{\pm},\boldsymbol{f}^{\pm})+\nu_-(\boldsymbol{z}^{\mp},\boldsymbol{f}^{\pm})\rangle_t \\ + \left\langle\int_\Omega d\boldsymbol{x}\ \boldsymbol{z}^{\pm}\cdot(\boldsymbol{z}^{\mp}\cdot\nabla)(-\Delta)^{-1}\boldsymbol{f}^{\pm}\right\rangle_t .\end{aligned} \tag{5.24}$$

The dissipative terms on the RHS can be estimated by the Cauchy-Schwarz inequality (5.11)

$$\nu_+(\boldsymbol{z}^{\pm},\boldsymbol{f}^{\pm}) \leqslant \nu_+||\boldsymbol{z}^{\pm}||_2\ ||\boldsymbol{f}^{\pm}||_2 \tag{5.25}$$

$$\nu_-(\boldsymbol{z}^{\mp},\boldsymbol{f}^{\pm}) \leqslant |\nu_-|\ ||\boldsymbol{z}^{\mp}||_2\ ||\boldsymbol{f}^{\pm}||_2\ , \tag{5.26}$$

while for the last term on the RHS the Hölder inequality (5.7) is applied twice to obtain

$$\begin{aligned}\int_\Omega d\boldsymbol{x}\ \boldsymbol{z}^{\pm}\cdot(\boldsymbol{z}^{\mp}\cdot\nabla)(-\Delta)^{-1}\boldsymbol{f}^{\pm} &\leqslant ||\nabla(-\Delta)^{-1}\boldsymbol{f}^{\pm}||_\infty\ ||\boldsymbol{z}^{\pm}\cdot\boldsymbol{z}^{\mp}||_1 \\ &\leqslant ||\nabla(-\Delta)^{-1}\boldsymbol{f}^{\pm}||_\infty\ ||\boldsymbol{z}^{\pm}||_2||\boldsymbol{z}^{\mp}||_2\ .\end{aligned} \tag{5.27}$$

Combining these results leads to

$$\begin{aligned}\langle||(-\Delta)^{-1/2}\boldsymbol{f}^{\pm}||_2^2\rangle_t \leqslant \nu_+\langle||\boldsymbol{z}^{\pm}||_2\ ||\boldsymbol{f}^{\pm}||_2\rangle_t + |\nu_-|\langle||\boldsymbol{z}^{\mp}||_2\ ||\boldsymbol{f}^{\pm}||_2\rangle_t \\ + \langle||\nabla(-\Delta)^{-1}\boldsymbol{f}^{\pm}||_\infty\ ||\boldsymbol{z}^{\pm}||_2\ ||\boldsymbol{z}^{\mp}||_2\rangle_t\ .\end{aligned} \tag{5.28}$$

Now the derivatives of the forces need to be determined with a view of making the dependence on the characteristic scale of the forces explicit. Following Doering and Foias [55], the forces $\boldsymbol{f}^{\pm}$ are decomposed into an amplitude $F_\pm$ and a shape function $\boldsymbol{\phi}_\pm$, such that

$$\boldsymbol{f}^{\pm}(\boldsymbol{x},t) = F_\pm\boldsymbol{\phi}_\pm(\boldsymbol{x}/L_{f,\pm},t)\ , \tag{5.29}$$

where most importantly the force is time-dependent but it acts at the same

characteristic length scale $L_{f,\pm}$ at all times. This mimicks practise in numerical simulations, where the forcing is applied in a fixed range of wavenumbers and may or may not be time-dependent. In most numerical work the time-dependence of the force is given by the evolution of phase factors, in other words, it is contained in the shape function and not in the amplitude $F_\pm$. Alternatively, the amplitude could be time-dependent while the shape function is constant. In order to conform with numerical simulations, here it is assumed that the amplitude $F_\pm$ is constant and that the shape function depends on time. The distinction is important since the long-time average of the $||\boldsymbol{f}^\pm||_2$ is taken, and if both $F_\pm$ and $\boldsymbol{\phi}_\pm$ are time-dependent the time average $\langle||\boldsymbol{f}^\pm||_2\rangle_t$ may not factorise in $\langle F_\pm\rangle_t\langle||\boldsymbol{\phi}_\pm||_2\rangle_t$, which is necessary in one step of the argument. The shape function is further restricted by the requirement $||\nabla(-\Delta)^{-1}\boldsymbol{\phi}_\pm||_\infty < \infty$ at all times.

Using the Fourier representation $\hat{\boldsymbol{\phi}}_\pm$ of the shape function $\boldsymbol{\phi}_\pm$, the dependence of $||(-\Delta)^{-1/2}\boldsymbol{f}^\pm||_2^2$ on $L_{f,\pm}$ can be made explicit

$$\begin{aligned} ||(-\Delta)^{-1/2}\boldsymbol{f}^\pm||_2^2 &= \int_\Omega d\boldsymbol{x}\ \boldsymbol{f}^\pm\cdot(-\Delta)^{-1}\boldsymbol{f}^\pm = F_\pm^2 L_{f,\pm}^2 L^3 \sum_{\boldsymbol{k}\neq 0}\frac{|\hat{\boldsymbol{\phi}}_\pm(\boldsymbol{k},t)|^2}{k^2} \\ &= F_\pm^2 L_{f,\pm}^2 L^3 C_{1,\pm}\ , \end{aligned} \tag{5.30}$$

where

$$C_{1,\pm} \equiv \sum_{\boldsymbol{k}\neq 0}\frac{|\hat{\boldsymbol{\phi}}_\pm(\boldsymbol{k},t)|^2}{k^2}\ , \tag{5.31}$$

which is finite, since the forces were assumed to satisfy eq. (5.12). Similarly, $L_{f,\pm}$ can be extracted from the L^∞-norm of $\nabla(-\Delta)^{-1}\boldsymbol{f}^\pm$, that is

$$\begin{aligned} ||\nabla(-\Delta)^{-1}\boldsymbol{f}^\pm||_\infty &= F_\pm||\nabla(-\Delta)^{-1}\boldsymbol{\phi}_\pm(\boldsymbol{x}/L_f^\pm,t)||_\infty = F_\pm^2 L_{f^\pm}^2 L_{f,\pm}^{-1}||\nabla(-\Delta)^{-1}\boldsymbol{\phi}_\pm||_\infty \\ &= F_\pm L_{f,\pm} D_\pm\ , \end{aligned} \tag{5.32}$$

where $D_\pm \equiv ||\nabla(-\Delta)^{-1}\boldsymbol{\phi}_\pm||_\infty$. Combining the two estimates then gives

$$\begin{aligned} F_\pm^2\langle C_{1,\pm}\rangle_t L_{f^\pm}^2 L^3 \leqslant& \nu_+ F_\pm\langle||\boldsymbol{z}^\pm||_2\ ||\boldsymbol{\phi}_\pm||_2\rangle_t + |\nu_-|F_\pm\langle||\boldsymbol{z}^\mp||_2\ ||\boldsymbol{\phi}_\pm||_2\rangle_t \\ &+ F_\pm L_{f^\pm}\langle D_\pm||\boldsymbol{z}^\pm||_2\ ||\boldsymbol{z}^\mp||_2\rangle_t\ , \end{aligned} \tag{5.33}$$

which can be rearranged to

$$F_\pm \leqslant \frac{1}{L^3}\,\nu_+\frac{\langle||\boldsymbol{z}^\pm||_2\;||\boldsymbol{\phi}_\pm||_2\rangle_t}{L_{f\pm}^2\langle C_{1,\pm}\rangle_t}+\frac{1}{L^3}\,|\nu_-|\frac{\langle||\boldsymbol{z}^\mp||_2\;||\boldsymbol{\phi}_\pm||_2\rangle_t}{L_{f\pm}^2\langle C_{1,\pm}\rangle_t} + \frac{1}{L^3}\frac{\langle D_\pm||\boldsymbol{z}^\pm||_2\;||\boldsymbol{z}^\mp||_2\rangle_t}{L_{f\pm}^2 L_{f\pm}}\;. \tag{5.34}$$

5.4 Estimating the dissipation rates

For the next step is it useful to recall the estimation of the dissipation rate from the energy inequality

$$\begin{aligned}\varepsilon &\leqslant \frac{1}{L^3}\langle||\boldsymbol{f}^+||_2\;||\boldsymbol{z}^+||_2\rangle_t+\frac{1}{L^3}\langle||\boldsymbol{f}^-||_2\;||\boldsymbol{z}^-||_2\rangle_t\\ &= \frac{1}{L^3}F_+\langle||\boldsymbol{\phi}_+||_2\;||\boldsymbol{z}^+||_2\rangle_t+\frac{1}{L^3}F_-\langle||\boldsymbol{\phi}_-||_2\;||\boldsymbol{z}^-||_2^2\rangle_t\;,\end{aligned} \tag{5.35}$$

which can be further estimated by applying the bounds on $F^\pm$ given in eq. (5.34)

$$\begin{aligned}\varepsilon \leqslant\;& \frac{1}{L^6}\,\nu_+\frac{\langle||\boldsymbol{z}^+||_2\;||\boldsymbol{\phi}_+||_2\rangle_t^2}{L_{f,+}^2\langle C_{1,+}\rangle_t}+\frac{1}{L^6}\,|\nu_-|\frac{\langle||\boldsymbol{z}^-||_2\;||\boldsymbol{\phi}_+||_2\rangle_t\;\langle||\boldsymbol{z}^+||_2\;||\boldsymbol{\phi}_+||_2\rangle_t}{L_{f,+}^2\langle C_{1,+}\rangle_t}\\ &+\frac{1}{L^6}\,\nu_+\frac{\langle||\boldsymbol{z}^-||_2\;||\boldsymbol{\phi}_-||_2\rangle_t^2}{L_{f,-}^2\langle C_{1,-}\rangle_t}+\frac{1}{L^6}\,|\nu_-|\frac{\langle||\boldsymbol{z}^+||_2\;||\boldsymbol{\phi}_-||_2\rangle_t\langle||\boldsymbol{z}^-||_2\;||\boldsymbol{\phi}_-||_2\rangle_t}{L_{f,-}^2\langle C_{1,-}\rangle_t}\\ &+\frac{1}{L^6}\frac{\langle D_+||\boldsymbol{z}^+||_2\;||\boldsymbol{z}^-||_2\rangle_t\langle||\boldsymbol{z}^+||_2\;||\boldsymbol{\phi}_+||_2\rangle_t}{L_{f,+}\langle C_{1,+}\rangle_t}\\ &+\frac{1}{L^6}\frac{\langle D_-||\boldsymbol{z}^-||_2\;||\boldsymbol{z}^+||_2\rangle_t\langle||\boldsymbol{z}^-||_2\;||\boldsymbol{\phi}_-||_2\rangle_t}{L_{f,-}\langle C_{1,-}\rangle_t}\;.\end{aligned} \tag{5.36}$$

Using the definition of the spatial rms values of the Elsässer fields

$$z^\pm \equiv \left(\frac{1}{L^3}\int_\Omega d\boldsymbol{x}\;|\boldsymbol{z}^\pm|^2\right)^{1/2}=\frac{1}{L^{3/2}}||\boldsymbol{z}^\pm||_2\;, \tag{5.37}$$

it becomes evident that the estimate of the energy dissipation rate ε does not depend on the system size, and the estimate can be written more concisely

$$\begin{aligned}\varepsilon \leqslant \nu_+ \frac{\langle (z^+)^2\ C_{0,+}\rangle_t}{L_{f,+}^2 \langle C_{1,+}\rangle_t} + |\nu_-| \frac{\langle z^- \sqrt{C_{0,+}}\rangle_t \langle z^+ \sqrt{C_{0,+}}\rangle_t}{L_{f,+}^2 \langle C_{1,+}\rangle_t} \\ + \nu_+ \frac{\langle (z^-)^2\ C_{0,-}\rangle_t}{L_{f,-}^2 \langle C_{1,-}\rangle_t} + |\nu_-| \frac{\langle z^- \sqrt{C_{0,-}}\rangle_t \langle z^+ \sqrt{C_{0,-}}\rangle_t}{L_{f,-}^2 \langle C_{1,-}\rangle_t} \\ + \frac{\langle D_+ z^+ z^-\rangle_t \langle z^+\rangle_t}{L_{f,+} \langle C_{1,+}\rangle_t} + \frac{\langle D_- z^+ z^-\rangle_t \langle z^-\rangle_t}{L_{f,-} \langle C_{1,-}\rangle_t}\ ,\end{aligned} \tag{5.38}$$

where

$$C_{0,\pm} \equiv ||\boldsymbol{\phi}_\pm||_2^2 / L^3 = \sum_{\boldsymbol{k}\neq 0} |\hat{\boldsymbol{\phi}}_\pm|^2\ . \tag{5.39}$$

All time averages of the form $\langle (z^+)^2\ C_{0,+}\rangle_t$ can be bound from above by taking the supremum of the respective coefficients $C_{0,\pm}$ and $D_\pm$, such that for example $\langle (z^+)^2\ C_{0,+}\rangle_t \leqslant \langle (z^+)^2\rangle_t \sup_{t\geqslant 0} C_{0,+}$. Equation (5.38) can thus be bounded from above and expressed more compactly by defining the coefficients

$$A_\pm \equiv \frac{\sup_{t\geqslant 0} C_{0,\pm}(t)}{\langle C_{1,\pm}\rangle_t} \quad \text{and} \quad B_\pm \equiv \frac{\sup_{t\geqslant 0} D_\pm(t)}{\langle C_{1,\pm}\rangle_t}\ , \tag{5.40}$$

which results in

$$\begin{aligned}\varepsilon \leqslant \nu_+ \frac{\langle (z^+)^2\rangle}{L_{f,+}^2}\ A_+ + |\nu_-| \frac{\langle z^-\rangle_t \langle z^+\rangle_t}{L_{f,+}^2}\ A_+ + \nu_+ \frac{\langle (z^-)^2\rangle_t}{L_{f,-}^2}\ A_- + |\nu_-| \frac{\langle z^+\rangle_t \langle z^-\rangle_t}{L_{f,-}^2}\ A_- \\ + B_+\ \frac{\langle z^+ z^-\rangle_t \langle z^+\rangle_t}{L_{f,+}} + B_-\ \frac{\langle z^+ z^-\rangle_t \langle z^-\rangle_t}{L_{f,-}}\ .\end{aligned} \tag{5.41}$$

In order to express this estimate in terms of dimensionless parameters, generalised Reynolds numbers are defined similarly to eq. (4.29)

$$R_\mp = \frac{\langle z^\mp\rangle_t L_{f,\pm}}{\nu_+} \quad \text{and} \quad R'_\pm = \frac{\langle z^\pm\rangle_t L_{f,\pm}}{|\nu_-|}\ , \tag{5.42}$$

where the only difference to the definition given in eq. (4.29) is the length scale used. The generalised Reynolds numbers relate to each other by

$$R_+ = \frac{\langle z^+\rangle_t L_{f,-}}{\langle z^-\rangle_t L_{f,+}} R_- \quad \text{and} \quad R'_- = \frac{\langle z^-\rangle_t L_{f,-}}{\langle z^+\rangle_t L_{f,+}} R'_+\ , \tag{5.43}$$

such that ε can be estimated in terms of the generalised Reynolds numbers

$$\varepsilon \leqslant \frac{\langle z^+ z^- \rangle_t \langle z^+ \rangle_t}{L_{f,+}} \left(B_+ + \frac{A'_+}{R_-} \right) + \frac{\langle z^+ z^- \rangle_t \langle z^- \rangle_t}{L_{f,-}} \left(B_- + \frac{A'_-}{R_-} \left[\frac{\langle z^- \rangle_t}{\langle z^+ \rangle_t} \frac{L_{f,+}}{L_{f,-}} \right] \right) + \frac{\langle z^- \rangle_t^2 \langle z^+ \rangle_t}{L_{f,+}} \frac{A_+}{R'_+} + \frac{\langle z^+ \rangle_t^2 \langle z^- \rangle_t}{L_{f,+}} \frac{A_-}{R'_+} \left[\frac{\langle z^- \rangle_t}{\langle z^+ \rangle_t} \frac{L_{f,-}}{L_{f,+}} \right] , \tag{5.44}$$

where $A'_\pm \equiv (A_\pm \langle z^+ \rangle_t \langle z^- \rangle_t)/(\langle z^+ z^- \rangle_t)$. This inequality is the main result of this chapter and applies to the most general case of MHD flows on the 3D-torus without any restrictions regarding the magnetic Prandtl number. In the limit $\nu \to 0$ and $\eta \to 0$, the residual dissipation rate is thus bounded by

$$\varepsilon \leqslant \frac{\langle z^+ z^- \rangle_t \langle z^+ \rangle_t}{L_{f,+}} B_+ + \frac{\langle z^+ z^- \rangle_t \langle z^- \rangle_t}{L_{f,-}} B_- \, . \tag{5.45}$$

This procedure also results in a very similar estimate for the cross-helicity dissipation rate

$$|\varepsilon_{H_c}| \leqslant \frac{\langle z^+ z^- \rangle_t \langle z^+ \rangle_t}{L_{f,+}} \left(B_+ + \frac{A'_+}{R_-} \right) + \frac{\langle z^+ z^- \rangle_t \langle z^- \rangle_t}{L_{f,-}} \left(B_- + \frac{A'_-}{R_-} \left[\frac{\langle z^- \rangle_t}{\langle z^+ \rangle_t} \frac{L_{f,+}}{L_{f,-}} \right] \right) + \frac{\langle z^- \rangle_t^2 \langle z^+ \rangle_t}{L_{f,+}} \frac{A_+}{R'_+} + \frac{\langle z^+ \rangle_t^2 \langle z^- \rangle_t}{L_{f,+}} \frac{A_-}{R'_+} \left[\frac{\langle z^- \rangle_t}{\langle z^+ \rangle_t} \frac{L_{f,-}}{L_{f,+}} \right] , \tag{5.46}$$

which is derived from eq. (5.19) using the estimates of $F_\pm$ given in eq. (5.34). Again, since the cross-helicity is not positive definite, care has to be taken with the estimates, and eq. (5.46) is only valid for weak solutions of the MHD equations which saturate the energy inequality.

5.5 Special cases

Equation (5.44) simplifies for specific cases, the most relevant are $\boldsymbol{f}^+$ and $\boldsymbol{f}^-$ acting on the same scales, while not necessarily having the same magnitude or shape function, for example in the case of mechanical forces where $\boldsymbol{f}^- = \boldsymbol{f}^+$. Another simplifying case is $Pm = 1$, for which $\nu_- = \nu - \eta = 0$.

5.5.1 Mechanical and electromagnetic forcing

For mechanical forcing $\boldsymbol{f}^- = \boldsymbol{f}^+$ while for electromagnetic forcing $\boldsymbol{f}^- = -\boldsymbol{f}^+$, as such in both cases there is a single length scale L_f and a single parameter $F_+ = F_- = F$ associated with the force. This results in the generalised Reynolds numbers relating to each other only through the ratios of the rms Elsässer fields. For the coefficients one obtains in the case $A_+ = A_- = A$, $B_+ = B_- = B$ and $A'_+ = A'_- = A'$, such that the estimate for the dissipation rate simplifies to

$$\varepsilon \leqslant \left(\frac{\langle z^+ z^- \rangle_t \langle z^+ \rangle_t}{L_f} + \frac{\langle z^+ z^- \rangle_t \langle z^- \rangle_t}{L_f} \right) B + \frac{\langle z^+ z^- \rangle_t \langle z^+ \rangle_t}{L_f} \frac{A + A'}{R_-} + \frac{\langle z^+ z^- \rangle_t \langle z^- \rangle_t}{L_f} \frac{A + A'}{R'_+} \ . \tag{5.47}$$

and in the ideal limit one obtains

$$\varepsilon \leqslant \left(\frac{\langle z^+ z^- \rangle_t \langle z^+ \rangle_t}{L_f} + \frac{\langle z^+ z^- \rangle_t \langle z^- \rangle_t}{L_f} \right) B \ . \tag{5.48}$$

5.5.2 $Pm = 1$

This case is particularly simple, since the dependence of ε on the generalised Reynolds number R'_+ disappears

$$\varepsilon \leqslant \frac{\langle z^+ z^- \rangle_t \langle z^+ \rangle_t}{L_{f,+}} \left(B_+ + \frac{A'_+}{R_-} \right) + \frac{\langle z^+ z^- \rangle_t \langle z^- \rangle_t}{L_{f,-}} \left(B_- + \frac{A'_-}{R_-} \left[\frac{\langle z^- \rangle_t}{\langle z^+ \rangle_t} \frac{L_{f,+}}{L_{f,-}} \right] \right) \ . \tag{5.49}$$

5.6 Discussion and Conclusions

Equation (5.48) is very similar in structure to the definition of the dimensionless dissipation rate C_ε given eq. (4.23) in the previous chapter. Furthermore, the dependence of C_ε in eq. (4.44) on the generalised Reynolds number R_- is the same as in eq. (5.49), taking into account that in chapter 4 R_- was defined with respect to the integral scale of $\boldsymbol{z}^+$ and not with respect to the external force.

Similar to hydrodynamics, there are thus two ways at arriving at very similar expressions for the dimensionless dissipation coefficient. The method proposed

in chapter 4 resulted in an approximate equation while the second method described here results in a rigorous bound. In that sense the two approaches are complementary. Furthermore, it is interesting to see that the coefficients $C_{\varepsilon,\infty}$ and B, which describe the asymptotes obtained by the respective methods, are given by different quantities. In the first case, $C_{\varepsilon,\infty}$ was related to the third-order longitudinal structure function in the infinite Reynolds number limit, while in the second case B is given by the ratio of the L^∞-norm to the L^2-norm of the shape function describing the spatial form of the external force. That is, the forward flux of energy across the scales is bounded from above by a quantity related to the regularity and type of the force. As such it may be possible to devise a particular type of force which minimises the forward flux of energy, thus leading to a suppression of nonlinear mixing and therefore of turbulence.

Systems only showing inverse transfer (i.e. self-organising systems) should be regular, since in these cases the asymptote of the forward flux vanishes in the infinite Reynolds number limit. As mentioned in chapter 3, this has been rigorously proven to be the case for the Navier-Stokes equation with dynamics projected onto the one of the eigenspaces corresponding to nonzero eigenvalues of the curl operator $I_k(\cdot)$, that is, projected onto one helicity eigenspace. Therefore there may be external forces which 'regularise' the system by restricting the dynamics to evolve mostly in one helicity eigenspace. For the MHD equations with electromagnetic forcing only, Dallas and Alexakis [51] showed that a fully helical electromagnetic force acting on a particular length scale led to an estimate for the dissipation rate of total energy which vanishes in the limit $\eta \to 0$. The same argument may be applicable to the Navier-Stokes equations subject to a fully helical mechanical force. Fully helical forces acting on a particular length scale are Beltrami fields, therefore another connection between Beltrami fields and the suppression of turbulence has been found, now in terms of Beltrami-type forces. This will become more apparent in the next chapter in the context of relaminarisation events.

Chapter 6

Relaminarisation of isotropic turbulence

In parallel wall-bounded shear flows such as flow in a pipe or a channel the transition to turbulence does not occur due to a linear instability of the laminar profile, which poses difficulties in understanding how the transition to turbulence proceeds in these systems. However, recent years have seen significant advances in the understanding of this transition, which turns out to be much more complex than the transition to turbulence in other flows which do have linear instabilities.

In contrast to turbulence in wall-bounded shear flows, stationary isotropic turbulence, that can be thought of as a turbulent flow far away from boundaries [135], is believed to exhibit much simpler dynamics: its motion is turbulent for all Reynolds numbers and there is no actual transition. This chapter reports evidence for an unexpected connection between isotropic turbulence and wall-bounded parallel shear flows: at low Reynolds number isotropic turbulence can suddenly collapse onto a large-scale flow (i.e. relaminarise), and the statistical signature of these relaminarisation events is very similar to established results in relaminarisation of wall-bounded parallel shear flows.

Sudden breakdowns of the turbulent dynamics in favour of a much simpler state are observed in DNSs of stationary isotropic turbulence at moderately large[1] Reynolds numbers, with the asymptotic state given by a large-scale Beltrami flow. A detailed study of the nature of this self-ordering process shows that

[1]The analysis does not concern Stokes flow, that is, although the Reynolds number may be considered low they are greater than unity.

it is analogous to the relaminarisation events in wall-bounded parallel shear flows. Forced isotropic turbulence at relatively low Reynolds numbers is therefore transient and the rate of its collapse is constant in time, resulting in exponentially distributed lifetimes of the turbulent state similar to pipe [7, 9, 66, 86] and plane Couette flow [24, 161, 164].

Before presenting results, the background material and recent developments on relaminarisation and transition to turbulence in parallel wall-bounded shear flows is summarised in order to facilitate the understanding of the presented results in this context.

6.1 Relaminarisation and transition to turbulence in wall-bounded shear flows

As outlined in chapter 1, localised turbulence in wall-bounded parallel shear flows can suddenly relaminarise. Relaminarisation events have been explained by dynamical systems theory as the escape from a chaotic saddle in state space with a constant (time independent) rate of escape [29, 64–66, 141]. More precisely, it has been found that relaminarisation is a memoryless process, that is, it does not depend on the amount of time the system has spent in the turbulent region of the state space. The characteristic timescale associated with this process increases with Reynolds number as a double exponential [84], which implies that there is always a finite probability of relaminarisation, even at high Reynolds numbers: localised turbulence in parallel wall-bounded shear flows is transient.

At first sight the transient nature of turbulence is at odds with ubiquitous observations of sustained turbulence at high Reynolds numbers. In fact, relaminarisation of localised turbulence is not the only process at work in parallel shear flows. The transition to sustained turbulence occurs due to the presence of a competing process: the splitting of a locally turbulent region into two [7]. This process also has a characteristic timescale which *decreases* with Reynolds number as a double exponential [7]. The critical Reynolds number for sustained turbulence is then defined as the point where the two timescales are equal [7], marking the point where it is equally probable for localised turbulence to relaminarise or to proliferate. In pipe flow this occurs at a Reynolds number of about 2040 [7], for other types of shear flows such as plane Couette flow or

counter-rotating Taylor-Couette flow this number will be different.

Since a critical point for the transition to sustained turbulence has been identified, immediate questions about the nature of the transition arise. Turbulence is a driven-dissipative system and as such far from equilibrium, therefore it is natural to ask whether the transition to sustained turbulence may fall into one of the known universality classes of nonequilibrium phase transitions. Recent research suggests that the transition to sustained turbulence in parallel shear flows constitutes a second-order nonequilibrium phase transition belonging to the Directed Percolation universality class [108, 164, 165, 167]. Spatio-temporal visualisations of localised turbulence show remarkable similarities to percolation models, allowing identification of spatial and temporal correlation lengths as well as the fraction of 'occupied sites'. Hence much effort is put into measurement of critical exponents close to the critical point for different parallel shear flows. Depending on the type of flow this poses considerable difficulty. For example the aspect ratio of pipes needed to resolve the dynamics near the critical Reynolds number is very large, leading to prohibitively long pipe lengths. Very recently, critical exponents have been measured in plane Couette flow which are in close agreement with the values predicted for the Directed Percolation universality class [108].

There is mounting evidence that the transition scenario that has been developed for parallel shear flows may be more generally applicable. For example, a cellular automaton model of nucleation of turbulent spots in boundary layers based on a Directed Percolation model has reproduced results from numerical simulations of the full system to remarkable accuracy [173], thus connecting boundary layer transition with the Directed Percolation picture of the transition to turbulence in wall-bounded shear flows. The results presented in this chapter suggest that certain periodic flows may show a similar type of transition to turbulence.

6.2 Observations from DNS

The dynamical system under consideration consists of the incompressible Navier-Stokes equation together with the large-scale force $\boldsymbol{f}_1$ as defined in chapter 2. Random initial conditions for the velocity field with a prescribed energy spectrum are constructed as described in chapter 2 with negligible initial kinetic helicity. This system was stepped forward in time using the standard fully de-aliased

pseudospectral method [187] on a three-dimensional periodic domain of length $L_{box} = 2\pi$ with the smallest wavenumber being $k_{min} = 2\pi/L_{box} = 1$.

The functional form of the large-scale forcing function $\boldsymbol{f}_1$ as defined eq. (2.1) is restated here for convenience

$$\begin{aligned} \hat{\boldsymbol{f}}(\boldsymbol{k},t) &= (\varepsilon_W/2E_f)\hat{\boldsymbol{u}}(\boldsymbol{k},t) \quad \text{for} \quad 0 < |\boldsymbol{k}| < k_f; \\ &= 0 \quad \text{otherwise.} \end{aligned} \tag{6.1}$$

At wavenumbers $k_{min} \leqslant k \leqslant k_f = 2.5$ the Fourier transform $\hat{\boldsymbol{u}}$ of the velocity field is normalised by the energy content E_f in this wavenumber band and subsequently rescaled by the energy input rate ε_W. This has the advantage that the energy input is known at the start of the simulation and can be held constant while other parameters such as the viscosity may be varied. Here ε_W has been set to $\varepsilon_W = 0.1$ for all simulations.

This forcing provides an energy input that does not prefer any particular direction and has a complicated, time-dependent spatial profile. The choice $k_f = 2.5$ corresponds to 80 possible wavevectors and thus 80 different velocity field modes are being forced. This type of energy input is commonly used in numerical investigations of homogeneous isotropic turbulence [90, 92, 121, 123, 186], the prime example being the series of high-resolution simulations of Kaneda *et al.* [91]. It has been studied theoretically by Doering and Petrov [57], leading to bounds on the dissipation rate similar to those presented in chapter 5.

The simulations are evolved for 1271 initial large-eddy turnover times $t_0 = L/U$, where U denotes the initial rms velocity and L is the initial integral length scale; $t_0 = 0.78$ in simulation units. The parameter that is varied in the simulations is the kinematic viscosity ν changing from 0.1 to 0.055, and the results are presented in terms of a system-scale Reynolds number $Re = L_{box}^{4/3}\varepsilon_W^{1/3}/\nu$ that ranges from 53.80 to 97.82 for different simulations; in each individual run, Re is kept constant during the whole simulation. The system-scale Reynolds number is used instead of a Reynolds number based on one of the usual length scales characteristic to turbulence, since this allowed the systematic change of only one parameter. Furthermore, as alluded to in the introduction, turbulence collapses during the simulations, that is a Reynolds number based on the the integral scale L or the Taylor microscale λ would not remain constant during the evolution of the flow. In order to facilitate comparison to other simulations of isotropic turbulence, the range of viscosities quoted above corresponds to the integral scale Reynolds

numbers $R_L = 9.3 - 17.5$ and the Taylor-Reynolds numbers $R_\lambda = 7.7 - 13.5$ during turbulent evolution. All simulations [176][2] are carried out using 32^3 collocation points where the product of the largest resolved wavenumber k_{max} and the Kolmogorov lengthscale η is in the range of $2.85 \leqslant k_{max}\eta \leqslant 1.82$.

As mentioned above, the form of the forcing term employed here, eq. (2.1), is routinely used in DNS of isotropic turbulence as its complicated spatial form would seem to guarantee that the system is turbulent at any Reynolds number larger than unity. Indeed, even at sufficiently low Reynolds numbers, the simulations reach a turbulent stationary state, where the energy injection is balanced by the average dissipation and there is motion at all length scales. However, after staying in this steady state for a long time, the system exhibits a transition to a different state, as shown, for example, in fig. 6.1 for $Re = 76.86$. The figure shows the time evolution of the total energy of the system,

$$E(t) = \int_{k_{min}}^{k_{max}} dk\ E(k,t)\ , \tag{6.2}$$

and the energy content of small scales,

$$E'(t) = \int_{k>k_{min}}^{k_{max}} dk\ E(k,t)\ , \tag{6.3}$$

as a function of time, where the largest scale in the system corresponds to $k_{min} = 2\pi/L_{box} = 1$.

As fig. 6.1 demonstrates, the turbulent dynamics persists until about $t/t_0 \approx 240$. After that, the total energy becomes constant and the small-scale fluctuations in the kinetic energy produced by the characteristic turbulent cascade process suddenly disappear. This implies that for $t/t_0 > 240$ the kinetic energy is confined to the largest scale of the system and no nonlinear transfer exciting the smaller scales takes place. The system thus transitions from a turbulent to a large-scale 'laminar'[3] state. This can also be seen in fig. 6.2, which shows streamlines of the flow for two snapshots in time, one before and one after the collapse of turbulence. The streamlines in the top image, which corresponds to the snapshot taken in the turbulent flow state, are entangled and follow quite complicated paths showing the complexity and disorder of the flow. For the snapshot taken after relaminarisation shown in the bottom image, the streamlines appear to be

[2]Some of this data was generated and post-processed by Bernardas Jankauskas [89].

[3]In this context laminar means having the same spatial structure as the force with vanishing nonlinearity.

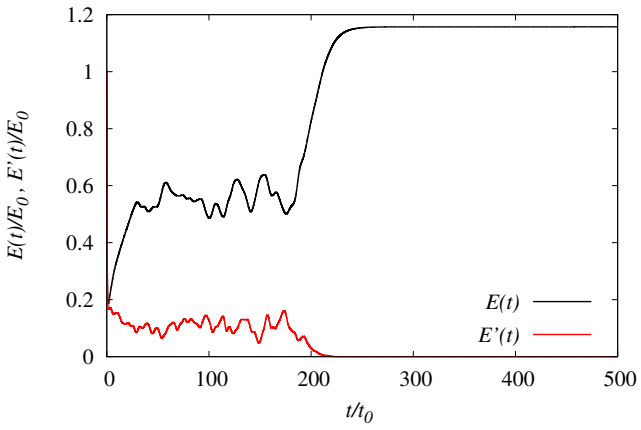

Figure 6.1 *Time evolution of the total energy $E(t)$ and the energy content of the small scales $E'(t)$ for $Re = 76.86$ normalised by the initial energy E_0. Time is given in units of initial large eddy turnover time $t_0 = L/U$, where U is the initial rms velocity and L the initial integral scale. The point around $t/t_0 \approx 240$ when $E'(t)$ vanishes and the total energy becomes constant marks the onset of the self-organised state as discussed in the main text.*

nearly parallel to each other and no entanglement is visible, the flow is now in a much simpler state.

The existence of such a large-scale state with vanishing nonlinearity can be understood by considering a model velocity field with $u_x \sim \cos(y)$ while $u_y = u_z = 0$. This flow profile is similar to a simple shear flow: it satisfies the incompressibility condition, it does not produce any pressure gradient in the system, and the non-linear term vanishes exactly for this profile. It is, therefore, an exact solution of the equations of motion, eqs. (1.3)-(1.2), with its magnitude being set by the injection rate ε_W and the kinematic viscosity ν. In general, one can construct many exact solutions of the Navier-Stokes equations with $k = 1$, similar to the model profile discussed above, for which the non-linear term vanishes. What is surprising, however, is that this self-organised large-scale state is dynamically connected to isotropic turbulence at sufficiently low Reynolds numbers.

6.2.1 Discussion

Since the observed collapse of the small-scale turbulent fluctuations is surprising, the results should be carefully tested and independently verified. Therefore a

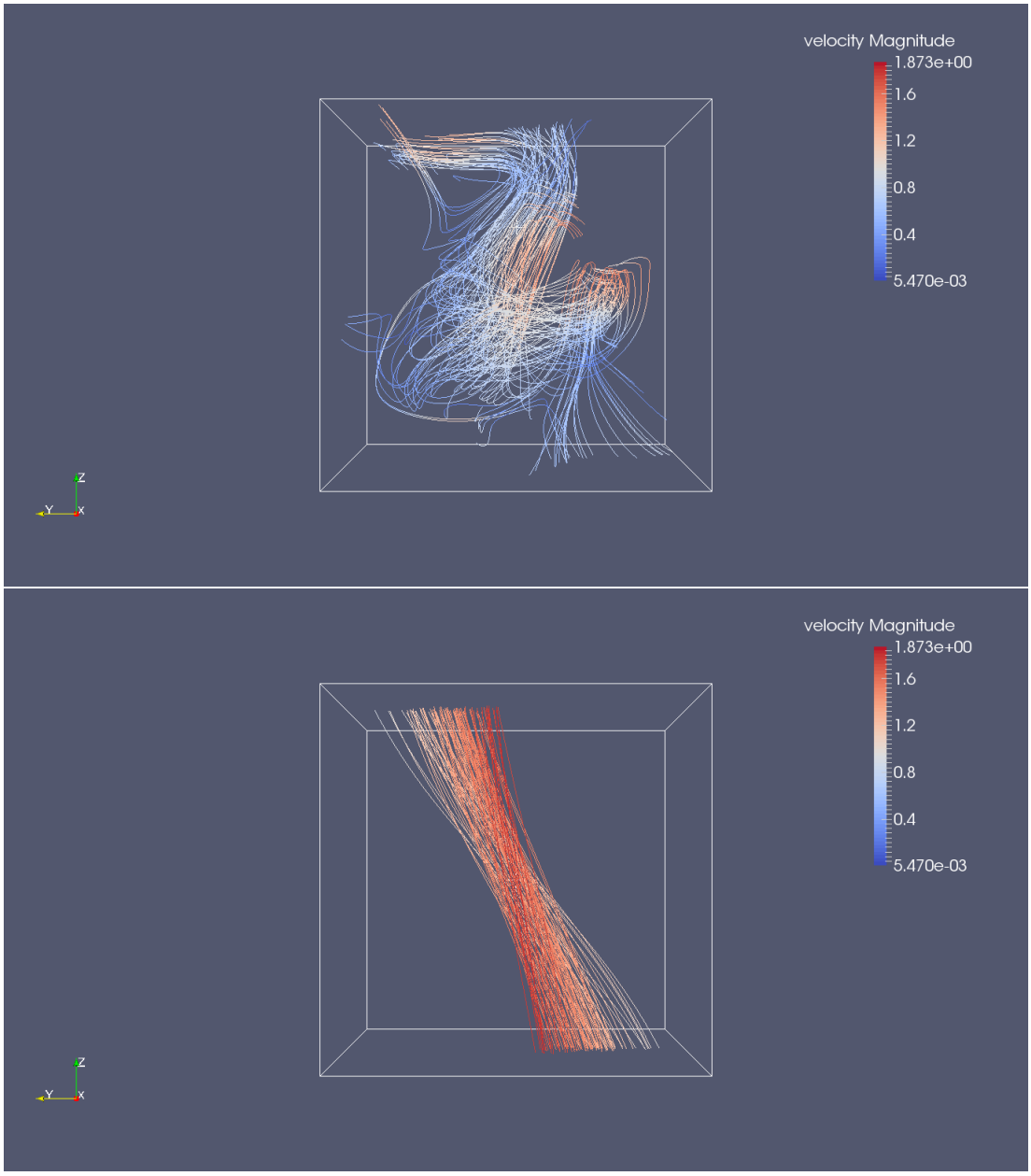

Figure 6.2 *Top: Streamlines of the flow before the collapse of turbulence showing the complexity and disorder of the flow. Bottom: Streamlines of the flow after the collapse of turbulence. Compared to the top panel the flow is now in a much simpler state.*

small number of test cases were run using the publicly available code `hit3d` [40, 41], which confirmed the self-organising behaviour of the fluid. Test simulations were also carried out using a larger box size and at higher small-scale resolution. The flow relaminarised in all test cases, further details of all test simulations are included in appendix D. In summary, the observed relaminarisation of isotropic turbulence, as modelled by the Navier-Stokes equations and the forcing $\boldsymbol{f}_1$, is robust under increasing both small-scale and large-scale resolution, and has been verified with a different code.

The results presented so far show that relaminarisation events occur in forced isotropic turbulence at low Reynolds number as modelled by the Navier-Stokes equation with the forcing as specified in eq. 2.1. One could infer that the observed self-organising behaviour may thus be an artifact of this specific type of forcing and as such of little relevance. It is certainly possible to construct external forces which should preclude the formation of the observed large-scale 'laminar' flow, as relaminarisation is only possible for forces $\boldsymbol{f}$ that actually allow a sustained laminar state, that is, for which the nonlinear term vanishes exactly while the energy input is balanced by the energy dissipation. Therefore any forcing function that does not satisfy $\boldsymbol{f} \times (\nabla \times \boldsymbol{f}) = 0$ should suppress relaminarisation events.

The type of forcing given in eq. 2.1 (here re-stated in eq. 6.1) feeds the velocity field back into the system at the large scales. If the flow is turbulent then nonlinear mixing is active and the forcing function is unlikely to satisfy $\boldsymbol{f} \times (\nabla \times \boldsymbol{f}) = 0$ because it is given by the turbulent velocity field restricted to the large(r) scales. That is, there is no obvious reason for the flow to self-organise if sustained by this type of energy input, and the numerous studies of isotropic turbulence cited above confirm that a turbulent state is generally maintained by this type of forcing.

Nevertheless, at low Reynolds number the flow relaminarises. An important consequence of the forcing function used here is that it does allow a laminar state to form. This is because once the flow has self-organised the nonlinear coupling of the different Fourier modes of the velocity field, and hence of the forcing function, is no longer active. That is, the laminar flow cannot be destabilised by the forcing. The observed relaminarisation should therefore be a consequence of the flow dynamics, allowed by a forcing which cannot destroy the laminar state.

The observed relaminarisation process can proceed in two ways, either by formation of a flow where $\nabla \times \boldsymbol{u} = 0$ as for the example profile $u_x \sim \cos(y), u_y = u_z = 0$ mentioned in the previous section, or alternatively by formation of a large-

scale Beltrami flow. This is studied in further detail in sec. 6.4, where properties of the self-ordered state are discussed.

6.3 Statistical analysis of lifetimes in isotropic turbulence and connection to wall-bounded shear flows

As discussed in the introduction, relaminarisation events occur in wall-bounded parallel shear flows and are well understood in terms of dynamical systems theory. If the collapse of isotropic turbulence observed in the present DNSs shows similar features to relaminarisation of wall-bounded parallel shear flows, the dynamical systems picture of the transition to turbulence may be more generally applicable. Furthermore, it would give further justification for the theoretical study of isotropic turbulence (modelled by the Navier-Stokes equations and the forcing $\boldsymbol{f}_1$) as a simplified system with important similarities to real-world turbulent flows.

6.3.1 Statistics of relaminarisation events

At a fixed Reynolds number, the time of self-organisation ($t/t_0 \approx 240$ in the example above) strongly depends on the initial conditions. This variability can be investigated systematically by starting 100 runs with different initial conditions for a fixed value of Re. In each simulation, the time-evolution of the total kinetic energy $E(t)$ and the dissipation rate $\varepsilon(t)$ is monitored. In order to identify the moment when the turbulent dynamics collapses onto the self-organised state, a criterion is used which is based on the observation that since the kinetic energy in the self-organised state is confined to modes with $k = k_{min} = 1$, the asymptotic value E_∞ for all individual runs in a given ensemble (at a given Re) can be calculated from the energy input rate ε_W and ν. For statistically stationary flows the energy input rate ε_W must equal the dissipation rate ε, hence the total energy of the self-organised state is given by

$$E_\infty = E(k_{min}) = \frac{\varepsilon_W}{2\nu k_{min}^2} = \frac{\varepsilon_W}{2\nu} = \text{ constant.} \tag{6.4}$$

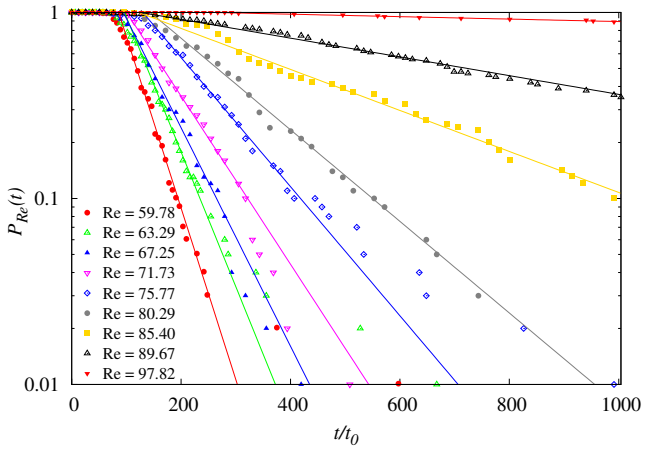

Figure 6.3 *Survival probability as a function of the dimensionless time t/t_0 from the beginning of a simulation.*

The data confirms that in every simulation, the total energy eventually reaches the asymptotic value E_∞, and the self-organisation time can be defined as the time when $E(t) = E_\infty$.

The variability of the self-organisation times is then quantified by introducing a survival probability $P_{Re}(t)$ which at a given Re gives the probability that the system is still turbulent at time t, having started in a turbulent state at time $t = 0$. For each t, this probability is estimated by dividing the number of runs that are still turbulent after time t by the total number of runs carried out at this Reynolds number. The resulting survival probabilities are shown in fig. 6.3 for a range of Re. After some initial lag time during which the system has evolved from the initial condition into the turbulent state, the survival probability follows a simple exponential law

$$P_{Re}(t) \sim \exp(-t/\tau(Re)), \tag{6.5}$$

where $\tau(Re)$ is the typical lifetime of turbulence that only depends on the Reynolds number. The exponential form of the survival probability suggests that the process is memoryless, i.e. at each time the rate of relaminarisation is constant and does not depend on the previous dynamics of the system. This behaviour is identical to what was observed in wall-bounded shear flows, such as pipe [7, 9, 66, 84, 86] or plane Couette flow [24, 161, 164]. There, it was attributed to the escape from a chaotic saddle associated with relaminarisation of localised turbulence [64, 66, 84].

The characteristic lifetime τ is obtained at each Reynolds number from fitting the survival probabilities to eq. (6.5), see the solid lines in fig. 6.3. A steep increase in τ with increasing Reynolds number is found, as shown in fig. 6.4. In order to find the functional form $\tau = \tau(Re)$, the observed lifetime is fitted to various model expressions. First, a power law with an exponent $n < 0$ in the form $\tau \sim (Re_c - Re)^n$ is considered, which would suggest a divergence of the lifetime at some critical Reynolds number Re_c. It is found that this is not compatible with the data for any value of n; fig. 6.4 shows an example with $n = -1$. The same applies to an exponential increase of τ with Re. However, a super-exponential scaling in the form

$$\frac{\tau(Re)}{t_0} = c \exp\left[\exp(a + bRe)\right] \tag{6.6}$$

is compatible with the data for a fixed amplitude $c = 15.63$ and $a = -3.48 \pm 0.51$, $b = 0.052 \pm 0.005$, see fig. 6.4. Again, this conclusion parallels the super-exponential scaling of the lifetimes in wall-bounded shear flows [64, 84, 86].

In order to further check that the statistics of relaminarisation events follow a simple exponential law with a super-exponential lifetime, the results obtained above for the survival probability can be combined, yielding

$$P(t) = \exp\left(-\frac{t - 35}{20 \exp\left[\exp(-3.48 + \frac{Re}{19.23})\right]}\right). \tag{6.7}$$

Now the collection of the relaminarisation times for various values of Re from the simulations can be used to calculate the survival probability of the system being still turbulent after a fixed time t *as a function of the Reynolds number*. In fig. 6.5 these results are compared to the prediction of eq. (6.7) for various values of the observation times t, where the constant dividing Re is held fixed while letting the additive constant $a = 3.48 \pm 0.51$ vary within its error bounds calculated from the fitting procedure specified above. As can be seen in fig. 6.5, the agreement between the two data sets is good. This provides further support to the exponential form of the survival probability with a superexponential lifetime. The characteristic S-shape of the curves shown in fig. 6.5 is very also similar to the results in wall-bounded parallel shear flows [64, 84, 86].

The super-exponential law given in eq. (6.6) is not the only possible functional form that produces an acceptable fit to the data. Another super-exponential dependence, $\tau(Re)/t_0 = \exp[-a' + (b'Re)^{5.6}])$ with $a' = -3.18 \pm 0.14$ and $b' = 0.0136 \pm 0.0003$ also gives a good agreement with the dataset, as can be seen in

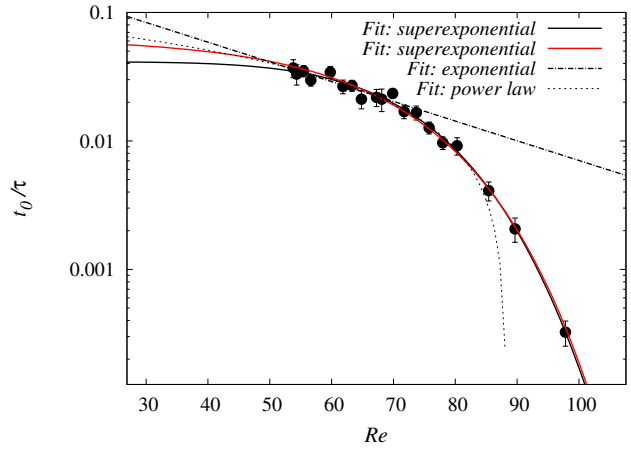

Figure 6.4 *Reynolds number dependence of the escape rate t_0/τ. The red (grey) line is a two-parameter fit of the expression $t_0/\tau(Re) = 0.064\exp(-\exp[a+bRe])$, the black line a two-parameter fit of the expression $t_0/\tau(Re) = \exp[a' - (b'Re)^{5.6}])$, the dash-dotted line a fit of an exponential and the faint dotted line a fit of a linear dependence of t_0/τ on Reynolds number.*

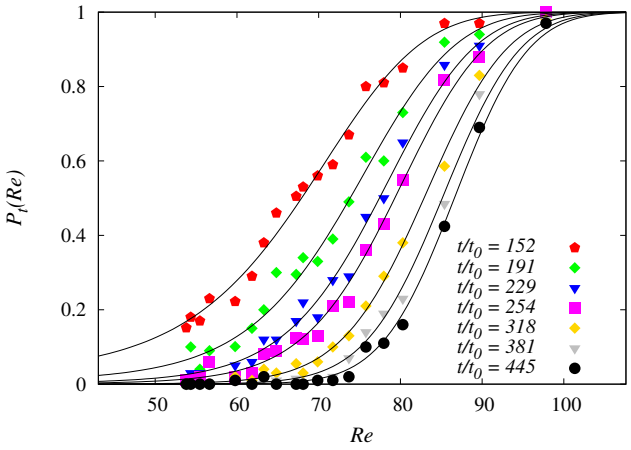

Figure 6.5 *Reynolds number dependence of the survival probabilities at different dimensionless observation times t/t_0.*

fig. 6.4. The Reynolds number range where the two superexponential forms differ from each other is not accessible for precise measurements, since at these low Reynolds numbers the turbulent lifetimes become comparable to the transient time that needs to pass before the system has evolved away from the artificial initial condition.

In order to verify that the results do not depend on the size of the simulation box, one ensemble of 100 runs was created using a larger simulation box with

$L_{box} = 4\pi$. The collapse of turbulence is also observed in these runs and leads to an exponential survival probability with the same characteristic lifetime as the reference dataset at $L_{box} = 2\pi$. Further details and results of these simulations are contained in appendix D.

6.3.2 Stability of the self-organised state

When the system selects the self-organised state, it stays there for as long as the simulations continue. Together with the fact that this state is dynamically selected by the system, it seems to imply that this state is linearly stable. In order to further probe this statement, exploratory simulations have been carried out where the self-ordered state was subjected to random perturbations with different amplitudes. For sufficiently small amplitude of the perturbations, simulations always returned to the self-organised state, while for larger perturbations the system became turbulent, as shown in fig. 6.6 for an example run at $Re = 75.78$. Simulations are started from the self-organised state obtained at the end of a long run after a relaminarisation event at the same Reynolds number. This state is perturbed by a random initial perturbation of various amplitudes. Figure 6.6 shows the time evolution of three runs, with relatively small, medium and large amplitudes. The small and medium amplitude runs return to the laminar state after some transient dynamics, while the large amplitude run becomes turbulent until its dynamics again collapses to the self-organised state. The lifetime of turbulence in the large-amplitude run is similar but not equal to the lifetime of the original run, which is shown in fig. 6.6 for comparison, as can be expected from a process with an exponential survival probability.

Therefore the simple asymptotic state has the same property as the laminar state in many wall-bounded parallel shear flows (cf. the Hagen-Poiseuille profile in pipe flow [59]): it is a linearly stable simple exact solution that can be destabilised by a finite-amplitude perturbation.

6.3.3 Phase-space dynamics

The phase space of turbulent wall-bounded shear flows is organised by exact solutions and periodic orbits of the Navier-Stokes equations [47, 69] and the relaminarisation events are associated with a sudden escape from this part of

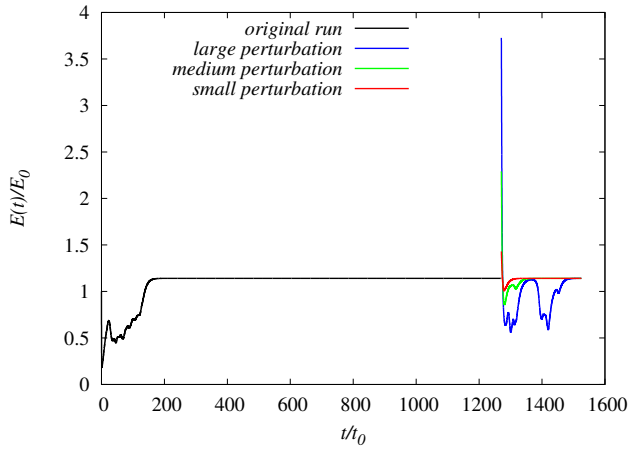

Figure 6.6 *Stability of the self-organised state for* $Re = 75.78$.

the phase space [141]. Since the same phenomenology is observed, the phase space of forced isotropic turbulence could perhaps also be organised by coherent structures (exact solutions and periodic orbits). Figure 6.7 shows the energy content of the $k = 2$ mode plotted against the energy content of the $k = 1$ mode for a run at $Re = 76.86$. Each point corresponds to a particular moment in time and the dynamics proceeds from left to right, until the system relaminarises (i.e. $E_1 = E_\infty$ and $E_2 = 0$). The dynamics revolves around several points in phase space that are very suggestive of exact unstable solutions [47].

Periodic orbits in isotropic turbulence have been found by van Veen *et al.* [180], where the period-5 solutions were shown to reproduce Kolmogorov scaling of the energy spectrum. Furthermore, the turbulent state appeared to stay close or evolve around the period-5 orbit.

6.4 Helicity dynamics and properties of the laminar attractor

There is a dynamic scenario that may lead to the observed self-organisation and that is by amplification of helicity fluctuations. The kinetic helicity was initially negligible for all simulations. However, during the evolution of the system, fluctuations in the kinetic helicity may occur. If these fluctuations happen in the forcing shell, the force will also become slightly helical, leading to an injection of helicity into the system. High kinetic helicity implies alignment between

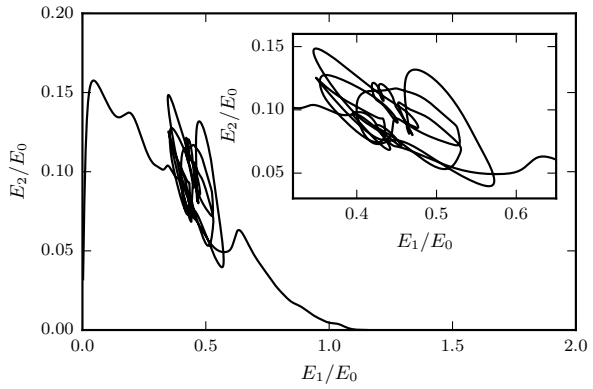

Figure 6.7 *Phase portrait E_2 vs E_1 for $Re = 76.86$. Each point corresponds to a particular moment in time. All energies are scaled with the initial total kinetic energy E_0. Inset: Zoom of the turbulent region of the main graph showing that the dynamics is organised by several points in phase space suggestive of unstable exact solutions.*

vorticity and velocity and hence a depletion of inertial transfer, consistent with the observations in sec. 6.2.

As explained in chapter 2, the kinetic helicity is invariant under Euler evolution. That is, at large Reynolds numbers an initially nonhelical velocity field will stay approximately nonhelical. This does not imply that helicity does not fluctuate, as conservation of helicity under Euler evolution is a only statement about the spatial average. Fluctuations of positive helicity at one length scale are thus possible if accompanied by fluctuations of negative helicity at another length scale. A build-up of kinetic helicity is not expected at high Reynolds number and high resolution numerical simulations confirm this picture, as shown in the right panel of fig. 6.8 for a simulation on 2048^3 grid points[4] at $Re = 48935.1$ ($R_\lambda = 435.2$). However, the kinetic helicity is not conserved at low Reynolds number and thus an increase in kinetic helicity over time is possible, and could eventually lead to relaminarisation of the flow.

The time evolution of the relative kinetic helicity

$$\rho_{kin}(t) = \frac{\int \boldsymbol{u}(\boldsymbol{x},t)\boldsymbol{\omega}(\boldsymbol{x},t)d\boldsymbol{x}}{\left(\int |\boldsymbol{u}(\boldsymbol{x},t)|^2 d\boldsymbol{x}\right)^{1/2}\left(\int |\boldsymbol{\omega}(\boldsymbol{x},t)|^2 d\boldsymbol{x}\right)^{1/2}} \ , \tag{6.8}$$

is shown in fig. 6.8 for a typical simulation at $Re = 75.78$ (left panel) and

[4]This simulation has been carried out for a different project [121], which is outwith the scope of this thesis.

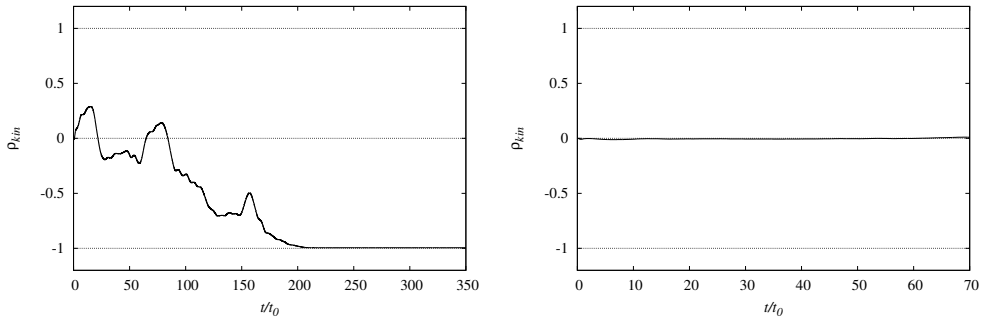

Figure 6.8 *Left: Evolution of the relative kinetic helicity $\rho_{kin}(t)$ for a typical run at $Re = 75.78$. Right: Evolution of $\rho_{kin}(t)$ for a run at $Re = 48931.5$.*

at high Reynolds number run (right panel). It is clearly visible that ρ_{kin} is initially negligible for both simulations. For $Re = 48931.5$ this remains so for the duration of the simulation, however for $Re = 75.78$ there are already much larger fluctuations in $\rho_{kin}(t)$ during the transient turbulent state. Eventually $|\rho_{kin}(t)|$ starts to increase and during self-organisation $|\rho_{kin}(t)| \to 1$. The turbulent fluctuations thus collapse in favour of a large-scale fully helical flow at $k_{min} = 1$, which necessarily satisfies eq. (1.89). That is, the asymptotic laminar state $\boldsymbol{u}_\infty$ is a Beltrami field at $k = 1$, that is

$$\nabla \times \boldsymbol{u}_\infty(\boldsymbol{x}) = \pm \boldsymbol{u}_\infty(\boldsymbol{x}) \ , \tag{6.9}$$

where

$$\boldsymbol{u}_\infty(\boldsymbol{x}) = \hat{\boldsymbol{u}}(\boldsymbol{k}_1)e^{ix_1} + \hat{\boldsymbol{u}}(\boldsymbol{k}_2)e^{ix_2} + \hat{\boldsymbol{u}}(\boldsymbol{k}_3)e^{ix_3} + \text{c.c.} \ , \tag{6.10}$$

with $\boldsymbol{k}_1 = (1,0,0)^t$, $\boldsymbol{k}_2 = (0,1,0)^t$, $\boldsymbol{k}_3 = (0,0,1)^t$ and $\boldsymbol{x} = (x_1, x_2, x_3)^t$.

The occurrence of localised Beltrami fields in fluid flows and the connection to turbulence has been explored theoretically and numerically in the 1980s, after Moffatt's [133] suggestion that high local values of $\rho_{kin}(t)$ should occur in regions of low dissipation. Pelz *et al.* [143] carried out DNSs of steady channel and Taylor-Green flow at 32^3 grid points, calculating the pdf of the relative kinetic helicity. For channel flow they found that the pdf has two distinctive peaks, one at zero and one at unity. The peak at zero was related to the viscous sublayer near the channel walls, while the peak at unity originated mainly from regions towards the middle of the channel. This implies that high localised alignment between $\boldsymbol{u}$ and $\boldsymbol{\omega}$ indeed occurs in the bulk flow. Strong relative helicities were also measured in

DNSs of decaying and stationary isotropic turbulence [103, 142, 155, 166]. The numerical study by Kerr [94], which was carried out using the same type of forcing as in the present analysis but at higher Reynolds number ($R_\lambda = 83$) and thus on a larger number of grid points (128^3), showed no particular strong alignment of velocity and vorticity. Higher levels of helicity were found in the forcing shell, but this did not appear to affect the helicity distribution at the smaller scales.

6.4.1 Relation to ABC-flows

Equation (6.9) further determines the structure of $\boldsymbol{u}_\infty$, and e.g. a positively helical solution has the form

$$\boldsymbol{u}_\infty(\boldsymbol{x}) = 2 \begin{pmatrix} \Re(u_2)\cos x_2 - \Im(u_2)\sin x_2 + \Re(u_3)\cos x_3 - \Im(u_3)\sin x_3 \\ \Re(u_1)\cos x_1 - \Im(u_1)\sin x_1 - \Re(u_3)\sin x_3 - \Im(u_3)\cos x_3 \\ -\Re(u_1)\sin x_1 - \Im(u_1)\cos x_1 + \Re(u_2)\sin x_2 + \Im(u_2)\cos x_2 \end{pmatrix} , \tag{6.11}$$

where $\Re$ and $\Im$ denote the real and imaginary parts of a complex number, respectively, while u_1, u_2 and u_3 parametrise $\hat{\boldsymbol{u}}(\boldsymbol{k}_1), \hat{\boldsymbol{u}}(\boldsymbol{k}_2)$ and $\hat{\boldsymbol{u}}(\boldsymbol{k}_3)$. Setting

$$\begin{aligned} A \equiv |u_3| \quad &\text{and} \quad \phi_3 \equiv \arccos\left(\Im(u_3)^2/|u_3|^2\right) , \\ B \equiv |u_1| \quad &\text{and} \quad \phi_1 \equiv \arccos\left(\Im(u_1)^2/|u_1|^2\right) , \\ C \equiv |u_2| \quad &\text{and} \quad \phi_2 \equiv \arccos\left(\Re(u_2)^2/|u_2|^2\right) , \end{aligned}$$

shows that the final state $\boldsymbol{u}_\infty$ can be written as a phase-shifted ABC-flow [35, 58]

$$\boldsymbol{u}_\infty(\boldsymbol{x}) = \begin{pmatrix} A\sin(x_3+\phi_3) + C\cos(x_2+\phi_2) \\ B\sin(x_1+\phi_1) + A\cos(x_3+\phi_3) \\ C\sin(x_2+\phi_2) + B\cos(x_1+\phi_1) \end{pmatrix} . \tag{6.12}$$

As shown in sec. 3.3.2, the self-ordered ABC-flow $\boldsymbol{u}_\infty$ is linearly stable. The linear stability of ABC-flows has been investigated by Galloway and Frisch [74] for specific cases where either $A = B = C$ or where one or two out of the three coefficients A, B and C vanish. ABC flows with $A = B = C$ are linearly unstable with respect to perturbations at the same wavelength of the base flow for Reynolds numbers $R_{ABC} \equiv L_{box}U_{ABC}/\nu < 15$, where U_{ABC} is the velocity magnitude of the ABC-flow. Similar results hold for the case where, say $A = 0$ and $B = C$. However, the linear stability properties are different for the specific case where two of the coefficients vanish. In this case, the base flow is linearly stable at all

Reynolds numbers. At lower Reynolds numbers in all cases the flow is unstable with respect to perturbations of larger wavelength compared to the wavelength of the base flow for $R_{ABC} > \sqrt{2}$. The simulations carried out in this study were at viscosities in the range $0.1 \leqslant \nu \leqslant 0.055$ with $1 \leqslant |\boldsymbol{u}_\infty| \leqslant 1.35$, so at Reynolds numbers $63 \leqslant R_{ABC} \leqslant 154$ well above the threshold of linear stability of the two aforementioned cases. Since the final ordered state is at $k = 1$ which corresponds to the largest scales available in the simulation box, the large-scale instabilities cannot be present.

The flow profile for the case where two out of the three coefficients A, B and C vanish, e. g. $u_{x,\infty} = 0, u_{y,\infty} \sim \sin(x)$ and $u_{z,\infty} \sim \cos(x)$ is very similar to the (generalised) Kolmogorov flow $u_x \sim \sin(y)$, $u_y = u_z = 0$ studied by van Veen and Goto [105] in the same periodic domain $[0, 2\pi]^3$ used here. The authors provide a direct proof of the stability of the laminar flow (at $k = 1$) and show that the transition to turbulence in this system is subcritical. Furthermore, they tracked a state on the boundary between the turbulent and laminar regions of the state space and found that a saddle-node bifurcation occurs at finite Reynolds number.

The results from the numerical tests presented in sec. 3.3.2 together with known results on the stability of ABC-flows suggest that the base flow found here may be a particular stable type of ABC-flow. Until the system finds this stable state, it may visit the many possible unstable ABC-states. This would result in relaminarisation attempts with a signature consistent with the behaviour of the blue curve in fig. 6.6, where the system bounced back into turbulence from a highly helical large-scale state.

As discussed earlier, the linear stability of ABC-flows is only known for specific values of A, B and C. In view of the present results, it may be interesting to construct a phase diagram showing the linear stability of ABC-flows depending on the values of the coefficients A, B and C. Such a study would require considerable effort, and may be restricted to the most relevant cases. ABC-flows are known to form six regions of high flow speed aligned in pairs with the x, y and z-axes of the simulation box [58]. The streamlines of $\boldsymbol{u}_\infty$ shown in the bottom panel of fig. 6.2 confirm the presence of only one pair of such regions (only one of which is shown), therefore at least one of the coefficients A, B or C must vanish and a systematic study of the stability properties of the case where e.g. $A = 0$ while the ratio $|B/C|$ ranges from $0 \leqslant |B/C| \leqslant 1$ may be sufficient.

Large-scale Beltrami fields with the same spatial signature as $\boldsymbol{u}_\infty$ have also

been observed in connection to symmetry-breaking in magnetohydrodynamic flows subject to large-scale static electromagnetic forcing [51]. Interestingly, relaminarisation of these flows also occurred at high Reynolds numbers.

6.5 Conclusions

The results presented here show that there is a surprising analogy between the behaviour of isotropic turbulence forced at large scales by the procedure decribed in eq. (6.1) and wall-bounded parallel shear flows at low Reynolds numbers. There is a spontaneous transition from turbulence to a spatially-simple state, which is identified here being a phase-shifted ABC-flow, and this 'laminar' state is linearly stable but can be destabilised by a finite-amplitude perturbation. The turbulent-laminar transition is abrupt and memoryless, and the associated survival probability is exponential in time, cf. [7, 9, 66, 84, 86, 141]. The turbulent lifetimes do not diverge with an increase in Re, instead they grow super-exponentially, cf. [76, 84]. This analogy implies that the phenomena of the transition to turbulence in wall-bounded shear flows and forced isotropic turbulence, typically thought of as a high-Re phenomenon away from boundaries, are dynamically similar and can be understood within the same theoretical framework.

Isotropic turbulence is thus not as featureless as previously thought. Furthermore, periodic motion is present in isotropic turbulence and appears to represent much of the statistical signatures of it [180]. Therefore extending the dynamical systems approach from shear flows to isotropic turbulence may help in understanding some of its dynamical properties which are not accessible from the statistical approach to the problem [180].

Chapter 7

Conclusions

In this thesis the dynamics of homogeneous turbulence occurring in incompressible flows of conducting and non-conducting fluids was studied in view of self-organising effects connected to the occurrence of fully helical structures. The main outcome can be summarised as:

The stability properties of helical structures are responsible for self-ordering processes in homogeneous (MHD) turbulence and are related to the transition to homogeneous turbulence occurring in MHD and non-conducting flows, because

1. Helicity influences the stability of steady solutions of the Navier-Stokes and MHD equations. Large-scale instabilities lead to self-ordering, while small-scale instabilities lead to increasing disorder. Since large-scale instabilities occur more frequently in the MHD equations compared to the Navier-Stokes equation, homogeneous turbulence occurring in MHD flows is more prone to self-organisation than turbulence in non-conducting flows.

2. Homogeneous isotropic turbulence as modelled by the Navier-Stokes equation and sustained by feeding the rescaled velocity field back into the system at the large scales can suddenly relaminarise similar to localised turbulence in wall-bounded shear flows. The 'laminar flow' onto which the system collapses is a large-scale linearly stable helical structure.

The theoretical analysis presented in chapter 3 showed that self-ordering is much more likely to occur in homogeneous MHD turbulence compared to homogeneous

turbulence in nonconducting fluids. This was due to a specific result from a stability analysis of triadic interactions, taking into account the helicities of the interacting modes. Compared to nonconducting fluids, steady unimodal solutions of the triadic evolution equations in magnetofluids have more instabilities with respect to perturbations on scales larger than the characteristic scale of the system. Furthermore, high correlation between the magnetic and velocity field was found to constrain small-scale instabilities more than large scale instabilities. Therefore it is expected that high levels of magnetic and cross-helicity damp the average forward interscale energy transfer characteristic for developed turbulence by which smaller and smaller scales are excited.

This average forward energy transfer was shown in chapter 4 to correspond to the residual dissipation in the infinite Reynolds number limit. That is, the residual dissipation can be interpreted as a proxy for the amount of turbulent activity in the system and thus dissipation rate quenching can be interpreted as a form of drag-reducing effect. The results in chapter 4 confirmed expectations that the turbulent activity is lower for MHD turbulence consisting mainly of modes with like-signed magnetic helicity. Additionally, if the magnetic and velocity field are strongly correlated, the turbulent activity was even further quenched, consistent with the theoretical analysis presented in chapter 3.

The turbulence-damping feature of helical structures became more clear due to numerical results on relaminarisation of isotropic hydrodynamic turbulence modelled by the Navier-Stokes equation plus an external force keeping the kinetic energy constant in the forcing shell. The observed relaminarisation process, where the turbulence collapes in favour of a large-scale Beltami flow, was shown to have the same statistical signature as relaminarisation of localised turbulence in wall-bounded parallel shear flows. The dynamics of stationary isotropic turbulence has been thought to be simpler than that of parallel shear flows, that is, it is not expected to show transitional behaviour and little is known about its phase space structure. The observed collapse of turbulence happens despite the continuous stirring of the flow at the large scales and has very similar features to relaminarisation events in pipe flow: it is a memoryless process with a characteristic timescale that increases with Reynolds number in much the same way as in parallel wall-bounded shear flows. Furthermore, the base flow appears to be linearly stable. That is, isotropic turbulence at low Reynolds numbers is transient and the presented results suggest that the phase space dynamics of parallel shear flows and isotropic turbulence may be very similar, with the

laminar state given by a Beltrami field. This result highlights that there may be a connection between the occurrence of (localised) Beltrami fields in homogeneous turbulence and relaminarisation events and suggests that the stability properties of locally occurring Beltrami fields are connected to the transition to turbulence.

7.1 Further work

As recent research shows, the transition to turbulence in wall-bounded parallel shear flows belongs to the directed percolation universality class [108, 164, 165, 167], and it can be argued that the same might be valid for forced isotropic turbulence as modelled by the Navier-Stokes equation plus the forcing used here. In view of this current research into the nature of the transition to turbulence, the alignment between vorticity and velocity fields may be a useful marker to determine the turbulent fraction in the present system, since the laminar state is a Beltrami field where vorticity and velocity are aligned. However, so far only relaminarisation events have been observed and there should be another process leading to sustained turbulence, which is yet to be identified.

The results presented here may help to identify or construct new potential target states for turbulence control. Since there are stable large-scale states hidden in what appears to be homogeneous turbulence, a particular choice of external force may be sufficient to push the system into the basin of attraction of one of these stable states. Furthermore, the helical decomposition implies that Beltrami states are intrinsic to fluid flows in the sense that any sufficiently well behaved[1] solenoidal vector field (and therefore any incompressible flow at least in the bulk) can be seen as a superposition of Beltrami flows, and it should be possible to identify the stable subset of these states. That is, linearly stable Beltrami states may be useful targets for turbulence control.

One immediate question then arises: how can these stable Beltrami fields be found? The combination of results from chapters 4 and 5 shows that the residual dissipation, in other words the 'turbulent activity', can be estimated either from the spatial structure of the external force or the level of magnetic, kinetic and cross-helicities. It should therefore be possible to find a connection between the two descriptions, which may help in finding a force function that perhaps minimises the turbulent activity while maximising the helicities.

[1] In this context this means having a Fourier transform.

Appendix A

The dependence of Q on the cross-helicity

In section 3.3, the parameter Q was defined as $Q = \alpha\delta - \beta\gamma$, where α, β, γ and δ were the entries of the matrix in (3.15). Using the expressions for these terms given in (3.19), we obtain

$$Q = |g_{kpq}|^4 s_k k s_q q (s_k k - s_p p)(s_q q - s_p p) \left(|U_{s_p}|^4 + |B_{s_p}|^4 - 2\mathrm{Re}([U^*_{s_p} B_{s_p}]^2) \right) . \tag{A.1}$$

In general, the helical coefficients U_{s_p} and B_{s_p} are related by a complex number $M = m + in$ such that $B_{s_p} = MU_{s_p}$. Expressions for m and n can be found by decomposing the two fields into their real and imaginary parts. Let $U_{s_p} = U_1 + iU_2$ and $B_{s_p} = B_1 + iB_2$. Then

$$m = \frac{1}{|U_{s_p}|^2}(U_1 B_1 + U_2 B_2) \text{ and} \tag{A.2}$$

$$n = \frac{1}{|U_{s_p}|^2}(U_1 B_2 - U_2 B_1), \tag{A.3}$$

where n is constrained by $n^2 = |B_{s_p}|^2/|U_{s_p}|^2 - m^2$ which follows from the definition of M. Decomposing the cross-helicity in the same way results in $H_c(p) = |U_{s_p}|^2 m$. Now the expression $\mathrm{Re}([U^*_{s_p} B_{s_p}]^2)$ can be related to the cross-helicity by rewriting

it in terms of the components of U_{s_p} and B_{s_p}:

$$\begin{aligned}\mathrm{Re}([U^*_{s_p}B_{s_p}]^2) =&(U_1B_1 + U_2B_2)^2 - (U_1B_2 - U_2B_1)^2 && \text{(A.4)}\\ =&|U_{s_p}|^4m^2 - |U_{s_p}|^4\left(\frac{|B_{s_p}|^2}{|U_{s_p}|^2} - m^2\right) && \text{(A.5)}\\ =&2H_c(p)^2 - |U_{s_p}|^2|B_{s_p}|^2 \ , && \text{(A.6)}\end{aligned}$$

and (3.23) is obtained by substitution of this expression for $\mathrm{Re}([U^*_{s_p}B_{s_p}]^2)$ into (A.1).

Since the maximum and minimum values of $|H_c(p)|$ are $|U_{s_p}||B_{s_p}|$ and 0 respectively, it is useful to define the relative cross-helicity $\rho = H_c(p)/(|U_{s_p}||B_{s_p}|)$, which takes values between -1 and 1. We obtain[1]

$$\mathrm{Re}([U^*_{s_p}B_{s_p}]^2) = |U_{s_p}|^2|B_{s_p}|^2(2\rho^2 - 1) \ , \qquad \text{(A.7)}$$

which is bounded by $-|U_{s_p}|^2|B_{s_p}|^2$ and $|U_{s_p}|^2|B_{s_p}|^2$, where the first value is the case of vanishing cross-helicity and the latter occurs when there is maximal cross-helicity. This implies that the term $(|U_{s_p}|^4 + |B_{s_p}|^4 + 2|U_{s_p}|^2|B_{s_p}|^2 - 4H_c(p)^2)$ in (3.23) cannot be negative.

[1]This particular form of the equation is due to M. McKay.

Appendix B

Determination of unstable triad interactions

B.1 $x^2 - Q > 0$ for specific cases

In section 3.4.1, the result was dependent on whether $x^2 - Q$ is positive or negative. Recall that the helicity combinations in question were $s_k = s_q \neq s_p$ and $s_k = s_p = s_q$ with the wavenumber ordering $p \leqslant k, q$ for the latter case. Therefore $x^2 - Q$ becomes[1]

$$\begin{aligned} x^2 - Q =& \frac{1}{4}[|U_{s_p}|^4(kq + (k \pm p)(q \pm p))^2 + |B_{s_p}|^4(k(k \pm p) + q(q \pm p))^2 \\ &+ 2|U_{s_p}|^2|B_{s_p}|^2[kq + (k \pm p)(q \pm p)][k(k \pm p) + q(q \pm p)]] \\ &- [kq(k \pm p)(q \pm p)](|U_{s_p}|^4 + |B_{s_p}|^4 - 2\mathrm{Re}([U^*_{s_p}B_{s_p}]^2)) \\ =& \frac{1}{4}[|U_{s_p}|^4(kq - (k \pm p)(q \pm p))^2 + |B_{s_p}|^4(k(k \pm p) - q(q \pm p))^2 \\ &+ 2|U_{s_p}|^2|B_{s_p}|^2[kq + (k \pm p)(q \pm p)][k(k \pm p) + q(q \pm p)]] \\ &+ 2\mathrm{Re}([U^*_{s_p}B_{s_p}]^2)[kq(p \pm p)(q \pm p)] \ . \end{aligned} \tag{B.1}$$

In general, $|\mathrm{Re}([U^*_{s_p}B_{s_p}]^2)| \leqslant |U_{s_p}|^2|B_{s_p}|^2$ (see appendix A), hence it is assumed that $\mathrm{Re}([U^*_{s_p}B_{s_p}]^2) = -|U_{s_p}|^2|B_{s_p}|^2$ as this would be the most negative value this term can take. It corresponds to zero cross-helicity at $\boldsymbol{p}$. Equation (B.1) is now

[1]The particular simple form of this proof for the case $s_k = s_q \neq s_p$ is due to M. McKay and the case $s_k = s_p = s_q$ with the wavenumber ordering $p \leqslant k, q$ is joint work with M. McKay.

an inequality and reads

$$\begin{aligned} x^2 - Q \geqslant & \frac{1}{4}\left[|U_{s_p}|^4(kq-(k\pm p)(q\pm p))^2 + |B_{s_p}|^4(k(k\pm p)-q(q\pm p))^2\right] \\ & + \frac{1}{2}|U_{s_p}|^2|B_{s_p}|^2[kq+(k\pm p)(q\pm p)][k(k\pm p)+q(q\pm p)] \\ & - 2|U_{s_p}|^2|B_{s_p}|^2[kq(k\pm p)(q\pm p)] \ , \end{aligned} \tag{B.2}$$

hence the result $x^2 - Q > 0$ follows immediately if one can show

$$[kq+(k\pm p)(q\pm p)][k(k\pm p)+q(q\pm p)] - 4kq(k\pm p)(q\pm p) \geqslant 0 \ . \tag{B.3}$$

For this purpose, set $a^{\pm} \equiv (k \pm p)$ and $b^{\pm} \equiv (q \pm p)$. The expression on the left-hand side of (B.3) can now be further simplified

$$\begin{aligned} & [kq + a^{\pm}b^{\pm}][ka^{\pm} + qb^{\pm}] - 4kqa^{\pm}b^{\pm} \\ & = k^2qa^{\pm} + (a^{\pm})^2kb^{\pm} + q^2kb^{\pm} + (b^{\pm})^2qa - 4kqab \\ & = qa^{\pm}(k-b^{\pm})^2 + kb^{\pm}(q-a^{\pm})^2 \geqslant 0 \ . \end{aligned} \tag{B.4}$$

The last line follows for the case $s_k = s_q \neq s_p$ since both $a^+ \geqslant 0$ and $b^+ \geqslant 0$, while for the case $s_k = s_p = s_q$ both $a^- \geqslant 0$ and $b^- \geqslant 0$ due to the wavenumber ordering $p \leqslant k, q$. Hence the inequality (B.3) is satisfied and $x^2 - Q \geqslant 0$ in both cases.

B.2 Graphical determination of contraints on stability

As explained in the main body of the text, the term Q given in (3.23) determines the stability of the system (3.15) if $x < 0$. As such, a solution is unstable if $Q < 0$ or if $x^2 - Q < 0$, where the latter case is the more difficult to determine, as the sign of $x^2 - Q$ depends on the shape of the wavenumber triad, the cross-helicity and the ratio $|U_{s_p}|/|B_{s_p}|$. Given the multitude of possibilities that can emerge for this, the simplest way of determining the constraints on the stability of a solution of (3.15) is using a graphical method. For each combination of helicities $x^2 - Q$ is plotted[2] for several set values of $|U_{s_p}|/|B_{s_p}|$ and $H_c(p)$ in order to show in which parameter range instabilities are more likely to occur.

[2] All figures were produced by M. McKay.

The dependence of $x^2 - Q$ on the triad k, p, q can be reduced to a dependence on the triad's *shape* by rescaling each wavenumber similar to the procedure in appendix B.1, which enables the use of two-dimensional plots and the triad geometry to obtain the necessary information. Figures B.1-B.4. show the function $x^2(v, w) - Q(v, w)$ for the different cases shown in tables 3.1-3.3, where v and w correspond to the smallest and largest wavenumber in a given triad, rescaled by the middle one such that the triad geometry enforces the contraint $0 < v \leqslant 1 \leqslant w < 1 + v$, hence each wavenumber pair (v, w) describes a shape of triad. Each subfigure corresponds to set values of $H_c(p)$ and $|U_{s_p}|/|B_{s_p}|$, while each point (v, w) in a particular graph corresponds to a class of triad interactions characterised by their shape. Regions in wavenumber space excluded from the analysis by the constraints of the triad geometry are shaded in grey, positive values of $x^2 - Q$ leading to stability are indicated in black and negative values of $x^2 - Q$ leading to unstable solutions are marked white. Across the main four figures, $H_c(p)$ increases towards the bottom of the figure while $|U_{s_p}|/|B_{s_p}|$ increases from left to right, leading to the constraints summarised in tables 3.1-3.3. Depending on the wavenumber ordering, the definitions of v and w are slightly different, and the procedures for each case are explained individually.

- $s_k \neq s_p = s_q$ and $k < p < q$
  In this case all wavenumbers are divided by p, such that $v \equiv k/p$ and $w \equiv q/p$. As can be seen in fig. B.1, for decreasing $|U_{s_p}|/|B_{s_p}|$ and increasing $H_c(p)$ less and less unstable solutions occur, which leads to the constraints on split transfer shown in tbl. 3.1.

- $s_k \neq s_p = s_q$ and $p < k < q$
  In this case all wavenumbers by are devided k, such that $v \equiv p/k$ and $w \equiv q/k$. As can be seen in fig. B.2, for decreasing $|U_{s_p}|/|B_{s_p}|$ and increasing $H_c(p)$ less and less unstable solutions occur which leads to the constraints on forward transfer shown in tbl. 3.3.

- $s_k = s_p \neq s_q$ and $p < k < q$
  In this case all wavenumbers are rescaled by k, such that $v \equiv p/k$ and $w \equiv q/k$. As can be seen in fig. B.3, for decreasing $|U_{s_p}|/|B_{s_p}|$ and increasing $H_c(p)$ less and less unstable solutions occur which leads to the constraints on forward transfer shown in tbl. 3.3.

- $s_k = s_p = s_q$ and $k < q < p$
  In this case all wavenumbers are rescaled by q, such that $v \equiv k/q$ and

$w \equiv p/q$. As can be seen in fig. B.4, now for *increasing* $|U_{s_p}|/|B_{s_p}|$ and increasing $H_c(p)$ less and less triads lead to unstable solutions and the constraints on reverse transfer shown in tbl. 3.2 are obtained.

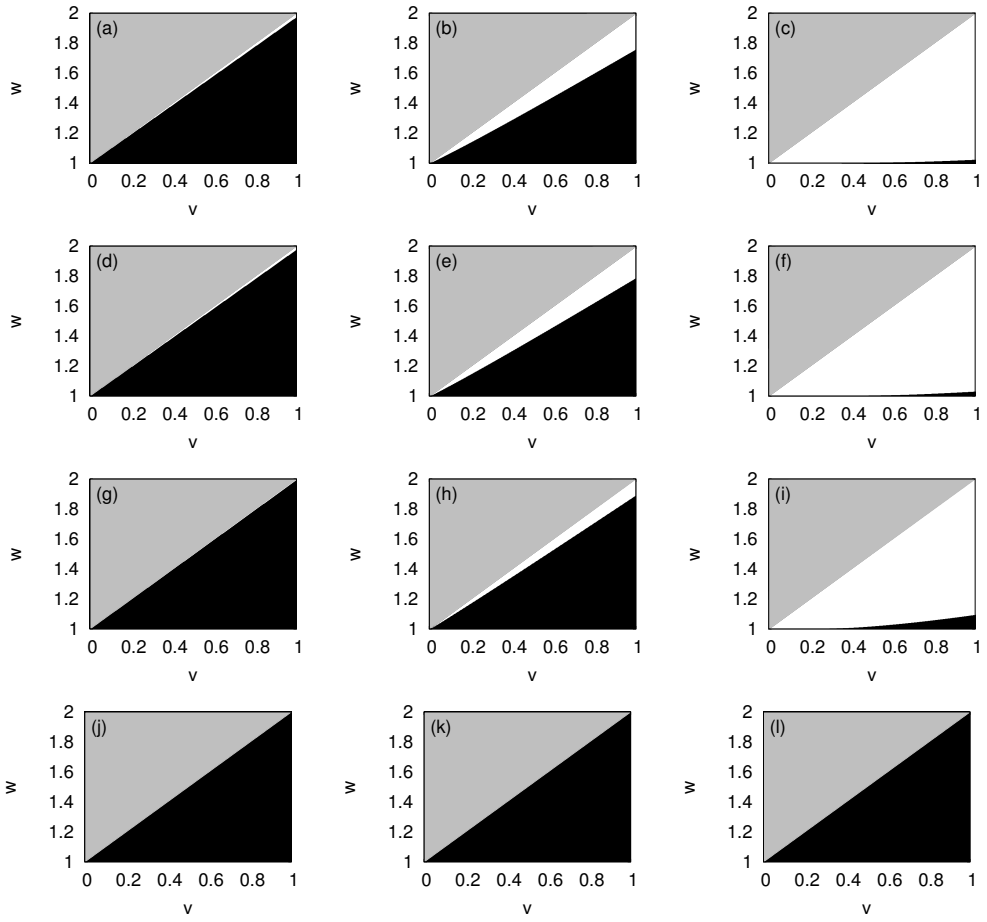

Figure B.1 *Plots of $f(v,w) = x^2 - Q$ for various values of $|U_{s_p}|/|B_{s_p}|$ and cross-helicity for case 1 in appendix B.2 ($s_k \neq s_p = s_q, k < p < q$). The upper grey triangle is ruled out by the condition $w < 1 + v$ and unstable values are shown in white. The ratio $|U_{s_p}|/|B_{s_p}|$ increases from left to right, with each column of subfigures taking the values 0.01, 0.1 and 1 respectively, while each row takes the following values of relativ cross-helicity: $H_c(p)/(|U_{s_p}||B_{s_p}|) = 0, 0.5, 0.9$ and 1. These figures were produced by M. McKay.*

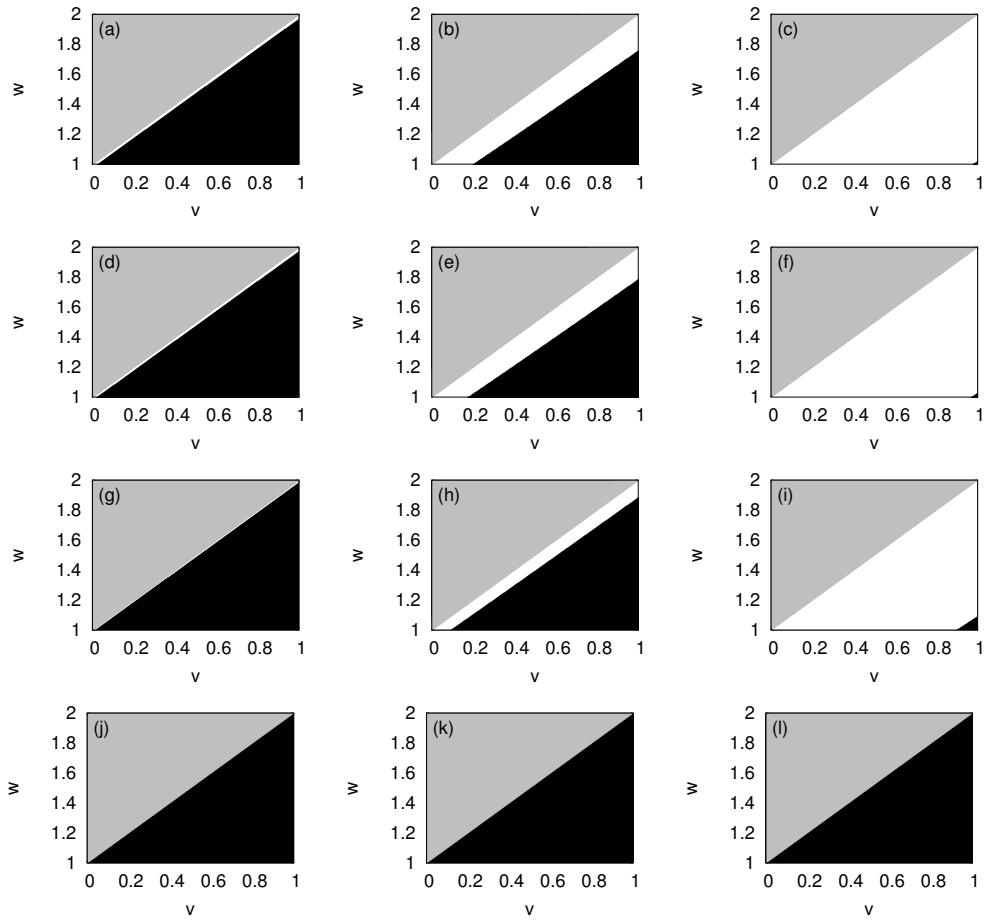

Figure B.2 *Plots of* $f(v,w) = x^2 - Q$ *for various values of* $|U_{s_p}|/|B_{s_p}|$ *and cross-helicity for case 2 in appendix B.2* ($s_k \neq s_p = s_q, p < k < q$). *The upper grey triangle is ruled out by the condition* $w < 1 + v$ *and unstable values are shown in white. The ratio* $|U_{s_p}|/|B_{s_p}|$ *increases from left to right, with each column of subfigures taking the values 0.01, 0.1 and 1 respectively, while each row takes the following values of relative cross-helicity:* $H_c(p)/(|U_{s_p}||B_{s_p}|) = 0, 0.5, 0.9$ *and* 1. *These figures were produced by M. McKay.*

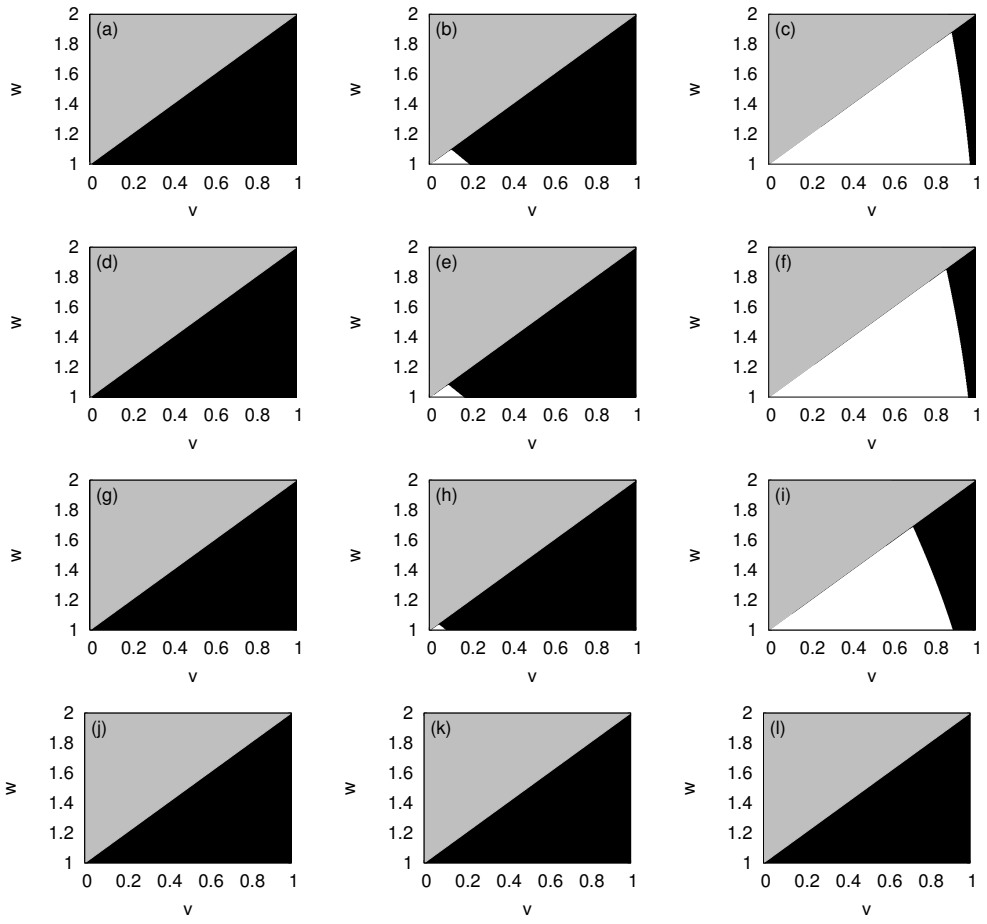

Figure B.3 *Plots of* $f(v,w) = x^2 - Q$ *for various values of* $|U_{s_p}|/|B_{s_p}|$ *and cross-helicity for case 3 in appendix B.2 (*$s_k = s_p \neq s_q, p < k < q$*). The upper grey triangle is ruled out by the condition* $w < 1 + v$ *and unstable values are shown in white. The ratio* $|U_{s_p}|/|B_{s_p}|$ *increases from left to right, with each column of subfigures taking the values 0.01, 0.1 and 1 respectively, while each row takes the following values of relative cross-helicity:* $H_c(p)/(|U_{s_p}||B_{s_p}|) = 0, 0.5, 0.9$ *and* 1*. These figures were produced by M. McKay.*

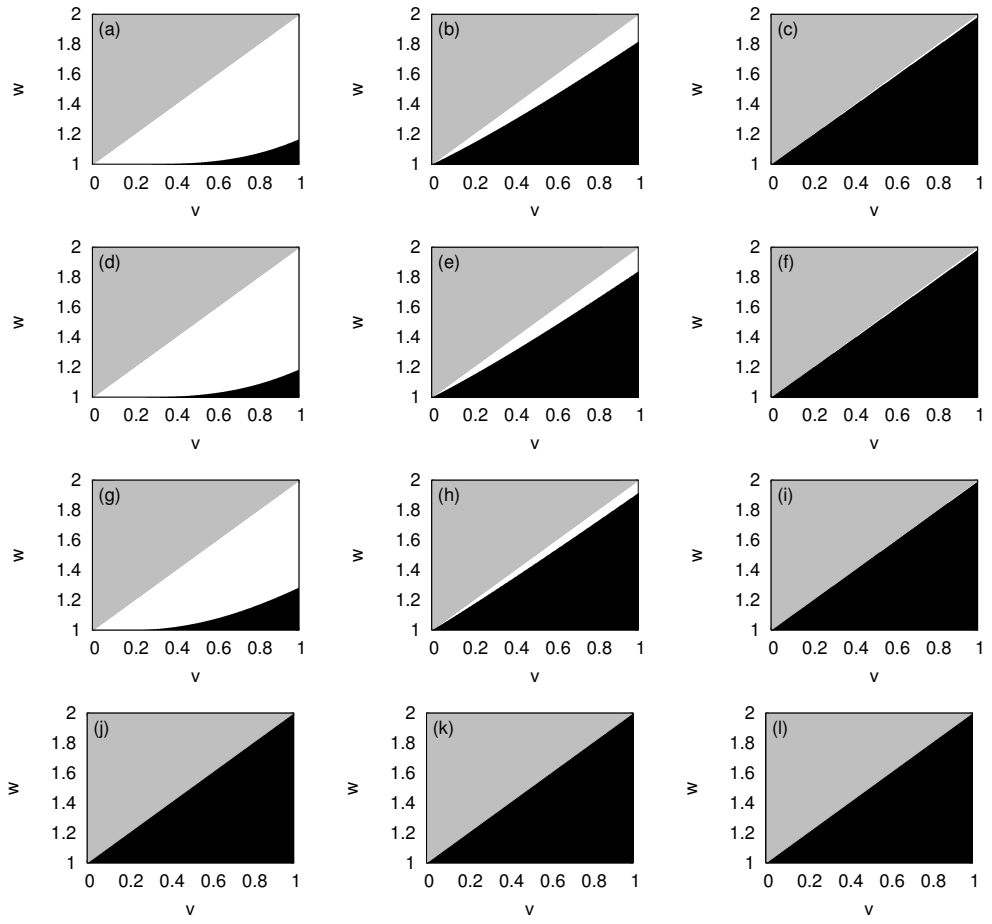

Figure B.4 *Plots of* $f(v,w) = x^2 - Q$ *for various values of* $|U_{s_p}|/|B_{s_p}|$ *and cross-helicity for case 4 in appendix B.2* ($s_k = s_p = s_q, k < q < p$). *The upper grey triangle is ruled out by the condition* $w < 1 + v$ *and unstable values are shown in white. The ratio* $|U_{s_p}|/|B_{s_p}|$ *increases from left to right, with each column of subfigures taking the values 1, 10 and 100 respectively, while each row takes the following values of relative cross-helicity:* $H_c(p)/(|U_{s_p}||B_{s_p}|) = 0, 0.5, 0.9$ *and* 1. *These figures were produced by M. McKay.*

Appendix C

Similarity scaling

For theoretical convenience it is assumed that both kinetic and magnetic energy spectra have power law scalings in the inertial range, that is

$$E_{kin}(\alpha k)/E_{kin}(k) = \alpha^{-n}, \quad E_{mag}(\alpha k)/E_{mag}(k) = \alpha^{-m} \tag{C.1}$$

where α is a real number and $n > 0$ and $m > 0$ are the spectral indices of the kinetic and magnetic energy spectra, respectively. From

$$\begin{aligned} E_{kin}(\alpha k) &= \frac{1}{2}\int_{|\alpha\boldsymbol{k}|=\alpha k} d(\alpha\boldsymbol{k}) \int_{\mathbb{R}^3} d(\alpha\boldsymbol{p})\ \langle u_+(\alpha\boldsymbol{k})u_+(\alpha\boldsymbol{p}) + u_-(\alpha\boldsymbol{k})u_-(\alpha\boldsymbol{p})\rangle \\ &= \frac{\alpha^2}{2}\int_{|\boldsymbol{k}|=k} d\boldsymbol{k}\ \alpha^3 \int_{\mathbb{R}^3} d\boldsymbol{p}\ \alpha^{2\xi}\langle u_+(\boldsymbol{k})u_+(\boldsymbol{k}) + u_-(\boldsymbol{k})u_-(\boldsymbol{p})\rangle \\ &= \alpha^{5+2\xi}E_{kin}(k)\ , \end{aligned} \tag{C.2}$$

and

$$\begin{aligned} E_{mag}(\alpha k) &= \frac{1}{2}\int_{|\alpha\boldsymbol{k}|=\alpha k} d(\alpha\boldsymbol{k}) \int_{\mathbb{R}^3} d(\alpha\boldsymbol{p})\ \langle b_+(\alpha\boldsymbol{k})b_+(\alpha\boldsymbol{p}) + b_-(\alpha\boldsymbol{k})b_-(\alpha\boldsymbol{p})\rangle \\ &= \frac{\alpha^2}{2}\int_{|\boldsymbol{k}|=k} d\boldsymbol{k}\ \alpha^3 \int_{\mathbb{R}^3} d\boldsymbol{p}\ \alpha^{2\zeta}\langle b_+(\boldsymbol{k})b_+(\boldsymbol{k}) + b_-(\boldsymbol{k})b_-(\boldsymbol{p})\rangle \\ &= \alpha^{5+2\zeta}E_{mag}(k)\ , \end{aligned} \tag{C.3}$$

where ξ and ζ are the scaling exponent of $u_\pm(\boldsymbol{k})$ and $b_\pm(\boldsymbol{k})$, respectively, one

obtains

$$u_\pm(\alpha\boldsymbol{k}) = \alpha^\xi u_\pm(\boldsymbol{k}) = \alpha^{-(5+n)/2} u_\pm(\boldsymbol{k}) \ , \tag{C.4}$$

$$b_\pm(\alpha\boldsymbol{k}) = \alpha^\zeta b_\pm(\boldsymbol{k}) = \alpha^{-(5+m)/2} b_\pm(\boldsymbol{k}) \ . \tag{C.5}$$

The scaling of $T^{(i)}_{HD}(k,p,q)$, $T^{(i)}_{LF}(k,p,q)$ and $T^{(i)}_{mag}(k,p,q)$ is then found by a similar argument, outlined here for $T^{(i)}_{LF}(k,p,q)$

$$\begin{aligned} T^{(i)}_{LF}(\alpha k,\alpha p,\alpha q) &= -\alpha(s_p p - s_q q) \int_{|\alpha\boldsymbol{k}|=\alpha k} d(\alpha\boldsymbol{k}) \int_{|\alpha\boldsymbol{p}|=\alpha p} d(\alpha\boldsymbol{p}) \int_{|\alpha\boldsymbol{q}|=\alpha q} d(\alpha\boldsymbol{q}) \\ &\qquad \times g_{kpq} \langle u_{s_k}(\alpha\boldsymbol{k}) b_{s_p}(\alpha\boldsymbol{p}) b_{s_q}(\alpha\boldsymbol{q})\rangle + \text{c.c.} \\ &= -\alpha(s_p p - s_q q)\ \alpha^6 \int_{|\boldsymbol{k}|=k} d\boldsymbol{k} \int_{|\boldsymbol{p}|=p} d\boldsymbol{p} \int_{|\boldsymbol{q}|=q} d\boldsymbol{q} \\ &\qquad \times g_{kpq} \alpha^{2\zeta+\xi} \langle u_{s_k}(\boldsymbol{k}) b_{s_p}(\boldsymbol{p}) b_{s_q}(\boldsymbol{q})\rangle + \text{c.c.} \\ &= \alpha^{7-(5+m)-(5+n)/2}\ T^{(i)}_{LF}(k,p,q) = \alpha^{-(1+n+2m)/2}\ T^{(i)}_{LF}(k,p,q) \ . \end{aligned} \tag{C.6}$$

The remaining cases proceed analogously. In summary, the transfer terms scale as

$$\frac{T^{(i)}_{HD}(\alpha k,\alpha p,\alpha q)}{T^{(i)}_{HD}(k,p,q)} = \alpha^{-(1+3n)/2} = \alpha^{-\beta} \ , \tag{C.7}$$

$$\frac{T^{(i)}_{LF}(\alpha k,\alpha p,\alpha q)}{T^{(i)}_{LF}(k,p,q)} = \alpha^{-(1+n+2m)/2} = \alpha^{-\beta'} \ , \tag{C.8}$$

$$\frac{T^{(i)}_{mag}(\alpha k,\alpha p,\alpha q)}{T^{(i)}_{mag}(k,p,q)} = \alpha^{-(1+n+2m)/2} = \alpha^{-\beta'} \ , \tag{C.9}$$

In hydrodynamics $n = 5/3$ in the inertial range, while in MHD there are different predictions for the spectral exponent, either $m = 3/2$ (Iroshnikov-Kraichnan) or $m = 5/3$ (Kolmogorov). Note that $n = m = 5/3$ implies $\beta' = \beta = 3$ while $n = 5/3$ and $m = 3/2$ implies $\beta' = 2 + 5/6$. In both cases $\beta - 2 > 0$.

Derivation of eq. (3.53)

In chapter 3, the flux of total energy was given by two contributions,

$$\Pi^{(i)}(k) = \Pi^{(i)}_+(k) - \Pi^{(i)}_-(k) \ , \tag{C.10}$$

where

$$\Pi_+^{(i)}(k) = \frac{1}{2}\int_k^\infty dk' \int_0^k \int_0^k T^{(i)}(k',p,q)dp\ dq\ , \tag{C.11}$$

describes the flux of total energy into all modes at wavenumber k' due to triads with $p, q < k < k'$ and

$$\Pi_-^{(i)}(k) = \frac{1}{2}\int_0^k dk' \int_k^\infty \int_k^\infty T^{(i)}(k',p,q)dp\ dq\ , \tag{C.12}$$

which describes the flux of total energy into all modes at k' due to triads with $k' < k < p, q$.

The integrals can be made independent of k by changing variables. Since p and q are dummy variables one can write

$$\frac{1}{2}\int_0^k \int_0^k T^{(i)}(k',p,q)dp\ dq = \int_0^k dp\ \int_0^p dq\ T^{(i)}(k',p,q)\ , \tag{C.13}$$

$$\frac{1}{2}\int_k^\infty \int_k^\infty T^{(i)}(k',p,q)dp\ dq = \int_k^\infty dp\ \int_p^\infty dq\ T^{(i)}(k',p,q)\ . \tag{C.14}$$

For eq. (C.11), define

$$v = \frac{q}{p}, \quad w = \frac{k'}{p}, \quad u = \frac{k}{p}\ , \tag{C.15}$$

where the constraint $p, q < k < k'$ enforces $v < u < w$ and $u > 1$, and the triad geometry is reflected by the inequality $w \leqslant 1 + v$. The integral over p in eq. (C.11) can now be written as

$$\int_0^k dp = -k\int_{k/u=k}^{k/u=k} du\ \frac{1}{u^2} = k\int_1^\infty du\ \frac{1}{u^2} = k\int_1^{1+v} du\ \frac{1}{u^2}\ , \tag{C.16}$$

where the last equality follows from the constraint $u < w < 1 + v$. Using $q = vp = vk/u$, the integral over q in eq. (C.11) becomes

$$\int_0^p dq = \frac{k}{u}\int_0^{vk/u=p} dv = \frac{k}{u}\int_0^1 dv\ . \tag{C.17}$$

The remaining integral over k' is rewritten using $k' = wp = wk/u$

$$\int_k^\infty dk' = \frac{k}{u}\int_0^\infty dw = \frac{k}{u}\int_u^{1+v} dw\ , \tag{C.18}$$

where the ultimate step follows from $u < w < 1 + v$. Combining these results

then gives

$$\int_k^\infty dk' \int_0^k dp \int_0^p dq = k^3 \int_0^1 dv \int_1^{1+v} du \, \frac{1}{u^4} \int_u^{1+v} dw \, ,$$
$$= k^3 \int_0^1 dv \int_1^{1+v} dw \int_1^w du \, \frac{1}{u^4} \, . \qquad \text{(C.19)}$$

For eq. (C.12), define

$$v = \frac{k'}{p}, \quad w = \frac{q}{p}, \quad u = \frac{k}{p} \, , \qquad \text{(C.20)}$$

where the constraint $k' < k < p, q$ enforces $v < u < w$ and $u < 1$, and the triad geometry is reflected by the inequality $w \leqslant u + v < 1 + v$. The integral over p in eq. (C.12) can now be written as

$$\int_k^\infty dp = -k \int_{k/u=k}^{k/u=\infty} du \, \frac{1}{u^2} = k \int_0^1 du \, \frac{1}{u^2} = k \int_v^1 du \, \frac{1}{u^2} \, , \qquad \text{(C.21)}$$

where the last equality follows from the constraint $v < u$. Using $q = wp = wk/u$, the integral over q in eq. (C.12) becomes

$$\int_p^\infty dq = \frac{k}{u} \int_{wk/u=p}^\infty dw = \frac{k}{u} \int_1^{1+v} dw \, , \qquad \text{(C.22)}$$

where the last step follows from $u < w < 1 + v$. The remaining integral over k' is rewritten using $k' = vp = vk/u$

$$\int_0^k dk' = \frac{k}{u} \int_0^{vk/u=k} dv = \frac{k}{u} \int_0^u dv \, . \qquad \text{(C.23)}$$

Combining these results then gives

$$\int_0^k dk' \int_k^\infty dp \int_p^\infty dq = k^3 \int_0^1 du \int_1^{1+v} dw \int_0^u dv \, \frac{1}{u^4} \, ,$$
$$= k^3 \int_0^1 dv \int_1^{1+v} dw \int_v^1 dv \, \frac{1}{u^4} \, . \qquad \text{(C.24)}$$

Equations (C.9), (C.19) and (C.24) together produce eq. (3.53) after integrating over u.

Appendix D

Test simulations (chapter 6)

A small number of test cases were run using the publicly available code `hit3d` [40, 41], which confirmed the self-organising behaviour of the fluid reported in chapter 6. Figure D.1 shows a comparison between a simulation using the in-house code and `hit3d` at the same Reynolds number and at a higher resolution (64^3 grid points). As can be seen from the figure, both simulations show the saturation of the total energy $E(t)$ characteristic for self-organisation of the flow. Moreover, for both codes $E(t)$ saturates at the same asymptotic value.

In order to demonstrate that the observed collapse of (transient) isotropic turbulence shown in chapter 6 is not an artefact of a too small simulation box ($L_{box} = 2\pi$ in the runs presented in chapter 6), an ensemble of 100 runs was created using a box of size $L_{box} = 4\pi$. The left panel in fig. D.2 shows the time evolution of the total energy $E(t)$ and the energy content of the small scales $E'(t)$ for one simulation belonging to this ensemble. The collapse of the small-scale fluctuations is clearly visible, and the figure looks qualitatively very similar to fig. 6.4. The survival probabilities for this ensemble and an ensemble using $L_{box} = 2\pi$ at the same Reynolds number are shown in the right panel of fig. D.2. The simulations using $L_{box} = 4\pi$ take longer to reach a (transient) turbulent stationary state compared to the simulations using $L_{box} = 2\pi$. This is the reason for the shift between the survival probabilities visible in the figure. However, the slopes of the two exponentials, and, hence, the characteristic lifetimes obtained from the two datasets are almost indistinguishable, and certainly well within the error bars obtained from eq. (6.7). Since the simulations carried out on the larger box size show very similar features to the data obtained from simulation using the

conventional box size $L_{box} = 2\pi$, it can be concluded that the results presented in chapter 6 are not induced by the size of the simulation box.

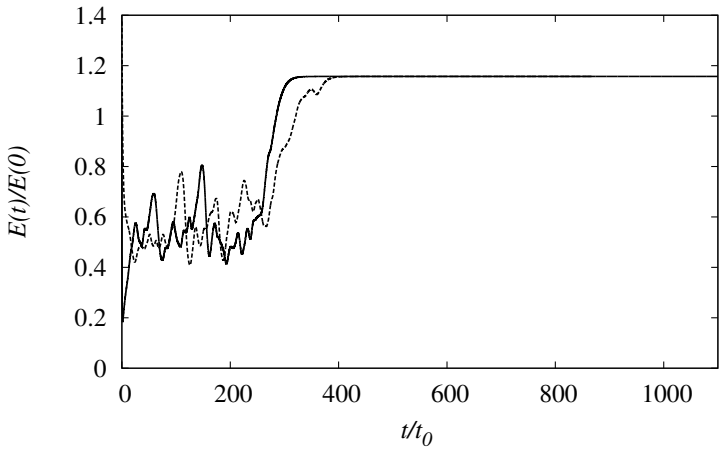

Figure D.1 *Verification of the observed self-organisation using a competitor code. The solid line shows results for $E(t)$ from the in-house code and the dashed line results from* `hit3d`*. Both simulations have been carried out using 64^3 collocation points.*

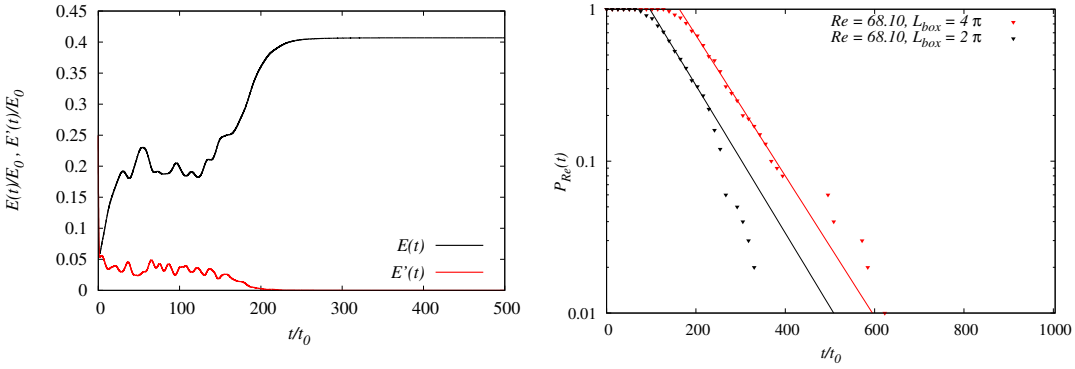

Figure D.2 *Time evolution of the total energy $E(t)$ and the energy content of the small scales $E'(t)$ for $Re = 68.10$ normalised by the initial energy E_0 for $L_{box} = 4\pi$. Time is given in units of initial large eddy turnover time $t_0 = L/U$, where U is the initial rms velocity and L the initial integral scale. Right: Survival probabilities as a function of the dimensionless time t/t_0 from the beginning of a simulation using $L_{box} = 2\pi$ (black) and $L_{box} = 4\pi$ (red) for $Re = 68.10$. The solid lines represent fits of $P(t) = \exp(-t/\tau)$ to the respective datasets.*

Bibliography

[1] `http://www.paraview.org/`.

[2] A. Pouquet and P. Mininni and D. Montgomery and A. Alexakis. Dynamics of the Small Scales in Magnetohydrodynamic Turbulence. In Y. Kaneda, editor, *IUTAM Symposium on Computational Physics and New Perspectives in Turbulence*, pages 305–312. Springer, 2008.

[3] A. Alexakis, P. D. Mininni, and A. Pouquet. Shell-to-shell energy transfer in magnetohydrodynamics. I. Steady state turbulence. *Phys. Rev. E*, 72:046301, 2005.

[4] A. Alexakis, P. D. Mininni, and A. Pouquet. On the inverse cascade of magnetic helicity. *Astrophy. J.*, 640:335–343, 2006.

[5] K. Alligood, T. D. Sauer, and J. A. Yorke. *Chaos - An Introduction to Dynamical Systems*. Springer, New York, 1997.

[6] J. C. André and M. Lesieur. Influence of helicity on the evolution of isotropic turbulence at high Reynolds number. *J. Fluid Mech.*, 81:187–207, 1977.

[7] K. Avila, D. Moxey, A. de Lozar, M. Avila, D. Barkley, and B. Hof. The Onset of Turbulence in Pipe Flow. *Science*, 333:192, 2011.

[8] M. Avila, F. Mellibovsky, N. Roland, and B. Hof. Streamwise-Localized Solutions at the Onset of Turbulence in Pipe Flow. *Phys. Rev. Lett.*, 110:224502, 2013.

[9] M. Avila, A. P. Willis, and B. Hof. On the transient nature of localized pipe flow turbulence. *J. Fluid Mech.*, 646:127–136, 2010.

[10] D. Balsara and A. Pouquet. The formation of large-scale structures in supersonic magnetohydrodynamic flows. *Phys. Plasmas*, 6:89, 1999.

[11] G. K. Batchelor. *The theory of homogeneous turbulence*. Cambridge University Press, Cambridge, 1st edition, 1953.

[12] A. Berera and M. F. Linkmann. Magnetic helicity and the evolution of decaying magnetohydrodynamic turbulence. *Phys. Rev. E*, 90:041003(R), 2014.

[13] A. Beresnyak. Spectral slope and Kolmogorov constant of MHD turbulence. *Phys. Rev. Lett.*, 106:075001, 2011.

[14] M. A. Berger. Magnetic helicity in a periodic domain. *J. Geophys. Res.*, 102:2637–2644, 1997.

[15] M. A. Berger. Introduction to magnetic helicity. *Plasma Physics and Controlled Fusion*, 41, 1999.

[16] M. A. Berger and G. B. Field. The topological properties of magnetic helicity. *J. Fluid Mech.*, 147:133–148, 1984.

[17] L. Biferale, A. S. Lanotte, and F. Toschi. Effects of forcing in three-dimensional turbulent flows. *Phys. Rev. Lett.*, 92:094503, 2004.

[18] L. Biferale, S. Musacchio, and F. Toschi. Inverse energy cascade in three-dimensional isotropic turbulence. *Phys. Rev. Lett.*, 108:164501, 2012.

[19] L. Biferale, S. Musacchio, and F. Toschi. Split Energy-Helicity cascades in three dimensional Homogeneous and Isotropic Turbulence. *J. Fluid Mech.*, 730:309–327, 2013.

[20] L. Biferale and E. S. Titi. On the global regularity of a helical-decimated version of the 3D Navier-Stokes equation. *Journ. Stat. Phys*, 151:1089, 2013.

[21] D. Biskamp. *Nonlinear Magnetohydrodynamics.* Cambridge University Press, 1st edition, 1993.

[22] G. Boffetta and S. Musacchio. Evidence for the double cascade scenario in two-dimensional turbulence. *Phys. Rev. E*, 82:016307, 2010.

[23] S. Boldyrev, J. C. Perez, J. E. Borovsky, and J. J. Podesta. Spectral scaling laws in magnetohydrodynamic turbulence simulations and in the solar wind. *Astrophys. J.*, 741:L19, 2011.

[24] S. Bottin and H. Chaté. Statistical analysis of the transition to turbulence in plane Couette flow. *Eur. Phys. J. B*, 6:143–155, 1998.

[25] A. Brandenburg. The inverse cascade and nonlinear alpha-effect in simulations of isotropic helical magnetohydrodynamic turbulence. *Astrophys. J.*, 550:824–840, 2001.

[26] A. Brandenburg. The Helicity Issue in Large Scale Dynamos. In E. Falgarone and T. Passot, editors, *Turbulence and Magnetic Fields in Astrophysics, Lecture Notes in Physics 614*, pages 402–413. Springer, Berlin Heidelberg, 2003.

[27] A. Brandenburg, T. Kahniashvili, and A. G. Tevzadze. Nonhelical inverse transfer of a decaying turbulent magnetic field. *Phys. Rev. Lett*, 114:075001, 2015.

[28] A. Brissaud, U. Frisch, J. Léorat, M. Lesieur, and A. Mazure. Helicity cascades in fully developed isotropic turbulence. *Phys. Fluids*, 16:1366, 1973.

[29] U. Brosa. Turbulence without strange attractor. *J. Stat. Phys.*, 55:1301–12, 1989.

[30] D. Carati, O. Debliquy, B. Knaepen, B. Teaca, and M. Verma. Energy transfers in forced MHD turbulence. *J. Turbulence*, 7:1–12, 2006.

[31] S. Chandrasekhar. The Invariant Theory of Isotropic Turbulence in Magneto-Hydrodynamics. *Proc. Roy. Soc. London. Series A*, 204:435–449, 1951.

[32] Q. Chen, S. Chen, and G. L. Eyink. The joint cascade of energy and helicity in three-dimensional turbulence. *Phys. Fluids*, 15:361–374, 2003.

[33] Q. Chen, S. Chen, G. L. Eyink, and D. D. Holm. Intermittency in the joint cascade of energy and helicity. *Phys. Rev. Lett.*, 90:214503, 2003.

[34] A. Cheskidov, C. R. Doering, and N. P. Petrov. Energy dissipation in fractal-forced flow. *J. Math. Phys.*, 48:065208, 2007.

[35] S. Childress. New solutions of the kinematic dynamo problem. *J. Math. Phys.*, 11:3063–3076, 1970.

[36] S. Childress and A. D. Gilbert. *Stretch, Twist, Fold: The Fast Dynamo.* Springer, Berlin, 1995.

[37] J. Cho. Non-locality of hydrodynamic and magnetohydrodynamic turbulence. *Astrophys. J.*, 725:1786–1791, 2010.

[38] J. Cho. Magnetic Helicity Conservation and Inverse Energy Cascade in Electron Magnetohydrodynamic Wave Packets. *Phys. Rev. Lett.*, 106:191104, 2011.

[39] M. Christensson, M. Hindmarsh, and A. Brandenburg. Inverse cascade in decaying 3D magnetohydrodynamic turbulence. *Phys. Rev. E*, 64:056405, 2001.

[40] S. G. Chumakov. Scaling properties of subgrid-scale energy dissipation. *Phys. Fluids*, 19:058104, 2007.

[41] S. G. Chumakov. A priori study of subgrid-scale flux of a passive scalar in turbulence. *Phys. Rev. E*, 78:15563, 2008.

[42] J. T. Coburn, C. W. Smith, B. J. Vasquez, M. A. Forman, and J. E. Stawarz. Variable cascade dynamics and intermittency in the solar wind at 1 AU. *Astrophys. J.*, 713:920–934, 2014.

[43] S. A. Colgate. Dynamo and hydromagnetic liquid metal experiments. *Astron. Nachr.*, 327:456–460, 2006.

[44] P. Constantin and C. Foias. *Navier-Stokes Equations*. University of Chicago Press, 1988.

[45] P. Constantin and A. Majda. The Beltrami spectrum for incompressible flows. *Commun. Math. Phys.*, 115:435–456, 1988.

[46] H. Cramér. On the theory of stationary random processes. *Ann. Math.*, 41:215–230, 1940.

[47] P. Cvitanović and J. F. Gibbon. Geometry of the turbulence in wall-bounded shear flows: periodic orbits. *Physica Scripta*, 142:014007, 2010.

[48] V. Dallas and A. Alexakis. Structures and dynamics of small scales in decaying magnetohydrodynamic turbulence. *Phys. Fluids*, 25:105196, 2013.

[49] V. Dallas and A. Alexakis. Symmetry breaking of decaying magnetohydrodynamic Taylor-Green flows and consequences for universality. *Phys. Rev. E*, 88:063017, 2013.

[50] V. Dallas and A. Alexakis. The signature of initial conditions on magnetohydrodynamic turbulence. *Astrophys. J.*, 788:L36, 2014.

[51] V. Dallas and A. Alexakis. Self-organisation and non-linear dynamics in driven magnetohydrodynamic turbulent flows. *Phys. Fluids*, 27:045105, 2015.

[52] A. G. Darbyshire and T. Mullin. Transition to turbulence in constant-mass-flux pipe flow. *J. Fluid Mech.*, 289:83–114, 1995.

[53] O. Debliquy, M. K. Verma, and D. Carati. Energy fluxes and shell-to-shell transfers in three-dimensional decaying magnetohydrodynamic turbulence. *Phys. Plasmas*, 12:042309, 2005.

[54] C. R. Doering. The 3D Navier-Stokes Problem. *Annu. Rev. Fl. Mech.*, 41:109–128, 2009.

[55] C. R. Doering and C. Foias. Energy dissipation in body-forced turbulence. *J. Fluid Mech.*, 467:289–306, 2002.

[56] C. R. Doering and J. D. Gibbon. *Applied Analysis of the Navier-Stokes Equations*. Cambridge University Press, 1995.

[57] C. R. Doering and N. P. Petrov. Low-wavenumber forcing and turbulent energy dissipation. In M. Oberlack, J. Peinke, A. Kittel, and S. Barth, editors, *Progress in Turbulence*, volume 101 of *Springer Proc. Physics*, pages 11–18. Springer, New York, 2005.

[58] T. Dombre, U. Frisch, J. M. Greene, M. Hénon, A. Mehr, and A. M. Soward. Chaotic streamlines in the ABC flows. *J. Fluid Mech.*, 167:353–391, 1986.

[59] P. Drazin and W. Reid. *Hydrodynamic Stability*. Cambridge University Press, Cambridge, 2004.

[60] Y. Dubief, V. E. Terrapon, and J. Soria. On the mechanism of elasto-inertial turbulence. *Phys. Fluids*, 25:110817, 2013.

[61] Y. Duguet, P. Schlatter, and D. S. Henningson. Localized edge states in plane Couette flow. *Phys. Fluids*, 21:111701, 2009.

[62] Y. Duguet, P. Schlatter, D. S. Henningson, and B. Eckhardt. Self-Sustained Localized Structures in a Boundary-Layer Flow. *Phys. Rev. Lett.*, 108:044501, 2012.

[63] G. Duvaut and J. L. Lions. Inéquations en thermoélasticité et magnétohydrodynamique. *Arch. Rational Mech. Anal.*, 46:241–279, 1972.

[64] B. Eckhardt, H. Faisst, A. Schmiegel, and T. M. Schneider. Dynamical systems and the transition to turbulence in linearly stable shear flows. *Phil. Trans. R. Soc. A*, 366:1297–1315, 2008.

[65] B. Eckhardt and T. M. Schneider. How does flow in a pipe become turbulent? *Eur. Phys. J. B*, 64:457–462, 2008.

[66] B. Eckhardt, T. M. Schneider, B. Hof, and J. Westerweel. Turbulence Transition in Pipe Flow. *Annu. Rev. Fluid Mech.*, 39:447–468, 2007.

[67] S. F. Edwards. Turbulence in hydrodynamics and plasma physics. In *Proc. Int. Conf. on Plasma Physics, Trieste*, page 595. IAEA, 1965.

[68] W. M. Elsässer. The hydromagnetic equations. *Phys. Rev.*, 79:183, 1950.

[69] H. Faisst and B. Eckhardt. Traveling waves in pipe flow. *Phys. Rev. Lett.*, 91:224502, 2003.

[70] H. Faisst and B. Eckhardt. Sensitive dependence on initial conditions in transition to turbulence in pipe flow. *J. Fluid Mech.*, 504:343–52, 2004.

[71] C. Foias, O. Manley, R. Rosa, and R. Temam. *Navier-Stokes Equations and Turbulence*, volume 83 of *Encyclopedia of Mathematics and its Applications*. Cambridge University Press, 2001.

[72] U. Frisch. *Turbulence: The Legacy of Kolmogorov*. Cambridge University Press, 1995.

[73] U. Frisch, A. Pouquet, J. Léorat, and A. Mazure. Possibility of an inverse cascade of magnetic helicity in magnetohydrodynamic turbulence. *J. Fluid Mech.*, 68:769–778, 1975.

[74] D. Galloway and U. Frisch. A note on the stability of a family of space-periodic Beltrami flows. *J. Fluid Mech.*, 180:557–564, 1987.

[75] J.-F. Gerbeau, C. Le Bris, and T. Lelièvre. *Mathematical Methods for the Magnetohydrodynamics of Liquid Metals*. Oxford University Press, 2006.

[76] N. Goldenfeld, N. Guttenberg, and G. Gioia. Extreme fluctuations and the finite lifetime of the turbulent state. *Phys. Rev. E*, 81:035304, 2010.

[77] P. Goldreich and S. Sridhar. Toward a theory of interstellar turbulence. II. Strong Alfvénic turbulence. *Astrophys. J.*, 438:763, 1995.

[78] S. Goldstein. *Modern developments in fluid dynamics*. Oxford University Press, 1938.

[79] E. E. Goldstraw. Large-scale forcing in magnetohydrodynamic turbulence. Master's thesis, University of Edinburgh, 2015.

[80] R. Grappin and W.-C. Müller. Scaling and anisotropy in magnetohydrodynamic turbulence in a strong mean magnetic field. *Phys. Rev. E*, 82:026406, 2010.

[81] R. Grappin, A. Pouquet, and J. Léorat. Dependence of MHD turbulence spectra on the velocity field-magnetic field correlation. *Astron. Astrophys.*, 126:51, 1983.

[82] S. Grossmann. The onset of shear flow turbulence. *Rev. Mod. Phys.*, 72:603–618, 2000.

[83] K. Heun. Neue Methoden zur approximativen Integration der Differentialgleichungen einer unabhängigen Veränderlichen. *Z. Math. Phys.*, 45:23–38, 1900.

[84] B. Hof, A. de Lozar, D. J. Kuik, and J. Westerweel. Repeller or attractor? selecting the dynamical model for the onset of turbulence in pipe flow. *Phys. Rev. Lett.*, 101:214501, 2008.

[85] B. Hof, C. W. H. van Doorne, J. Westerweel, F. T. M. Nieuwstadt, H. Faisst, B. Eckhardt, H. Wedin, R. R. Kerswell, and F. Waleffe. Experimental observation of nonlinear traveling waves in turbulent pipe flow. *Science*, 305:1594–1598, 2004.

[86] B. Hof, J. Westerweel, T. M. Schneider, and B. Eckhardt. Finite lifetime of turbulence in shear flows. *Nature*, 443:59–62, 2006.

[87] P. S. Iroshnikov. Turbulence of a Conducting Fluid in a Strong Magnetic Field. *Soviet Astronomy*, 7:566–571, 1964.

[88] S. Jagannathan and D. A. Donzis. Reynolds and Mach number scaling in solenoidally-forced compressible turbulence using high-resolution direct numerical simulations. *J. Fluid Mech.*, 789:669–707, 2016.

[89] B. Jankauskas. Numerical Investigation of Forced Isotropic Turbulence. Master's thesis, University of Edinburgh, 2014.

[90] J. Jiménez, A. A. Wray, P. G. Saffman, and R. S. Rogallo. The structure of intense vorticity in isotropic turbulence. *J. Fluid Mech.*, 255:65, 1993.

[91] Y. Kaneda and T. Ishihara. High-resolution direct numerical simulation of turbulence. *J. Turbulence*, 7:1–17, 2006.

[92] Y. Kaneda, T. Ishihara, M. Yokokawa, K. Itakura, and A. Uno. Energy dissipation and energy spectrum in high resolution direct numerical simulations of turbulence in a periodic box. *Phys. Fluids*, 15:L21, 2003.

[93] H. Karimabadi, V. Roytershteyn, M. Wan, W. H. Matthaeus, W. Daughton, P. Wu, M. Shay, B. Loring, J. Borovsky, E. Leonardis, S. C. Chapman, and T. K. M. Nakamura. Coherent structures, intermittent turbulence, and dissipation in high-temperature plasmas. *Phys. Plasmas*, 20:012303, 2013.

[94] R. M. Kerr. Histograms of Helicity and Strain in Numerical Turbulence. *Phys. Rev. Lett.*, 59:783, 1987.

[95] A. N. Kolmogorov. Dissipation of energy in locally isotropic turbulence. *C. R. Acad. Sci. URSS*, 32:16, 1941.

[96] A. N. Kolmogorov. Stationary sequences in Hilbert space. *Bull. Moscow Univ., Ser. Math.*, 2:1–40, 1941.

[97] A. N. Kolmogorov. The local structure of turbulence in incompressible viscous fluid for very large Reynolds numbers. *C. R. Acad. Sci. URSS*, 30:301, 1941.

[98] A. N. Kolmogorov. A refinement of previous hypotheses concerning the local structure of turbulence in a viscous incompressible fluid at high Reynolds number. *J. Fluid Mech.*, 13:82–85, 1962.

[99] R. H. Kraichnan. Decay of isotropic turbulence in the Direct-Interaction Approximation. *Phys. Fluids*, 7(7):1030–1048, 1964.

[100] R. H. Kraichnan. Direct-interaction approximation for shear and thermally driven turbulence. *Phys. Fluids*, 7(7):1048–1062, 1964.

[101] R. H. Kraichnan. Inertial Range Spectrum of Hydromagnetic Turbulence. *Phys. Fluids*, 8(7):1385–1387, 1965.

[102] R. H. Kraichnan. Inertial ranges in two-dimensional turbulence. *Phys. Fluids*, 10(10):1417, 1967.

[103] R. H. Kraichnan and R. Panda. Depression of nonlinearity in decaying isotropic turbulence. *Phys. Fluids*, 31:2395, 1988.

[104] F. Krause and K. Rädler. *Mean-Field Magnetohydrodynamics and Dynamo Theory*. Pergamon Press, Ltd., Oxford, 1980.

[105] L. van Veen and S. Goto. Subcritical transition to turbulence in three-dimensional Kolmogorov flow. `http://arxiv.org/abs/1512.02570`.

[106] O. A. Ladyshenskaya. *The Mathematical Theory of Viscous Incompressible Flow*. Gordon and Breach, New York, 2nd edition, 1969.

[107] E. Lee, M. E. Brachet, A. Pouquet, P. D. Mininni, and D. Rosenberg. Lack of universality in decaying magnetohydrodynamic turbulence. *Phys. Rev. E*, 81:016318, 2010.

[108] G. Lemoult, L. Shi, K. Avila, S. V. Jalikop, M. Avila, and B. Hof. Directed percolation phase transition to sustained turbulence in Couette flow. *Nat. Phys.*, Letter, 2016.

[109] J. Leray. Sur le mouvement d'un liquide visqueux emplissant l'espace. *Acta Mathematica*, 63:193–248, 1934.

[110] M. Lesieur. *Turbulence in fluids*. Springer-Verlag, 1st edition, 1990.

[111] T. Lessinnes, F. Plunian, and D. Carati. Helical shell models for MHD. *Theor. Comput. Fluid Dyn.*, 23:439–450, 2009.

[112] M. F. Linkmann, A. Berera, W. D. McComb, and M. E. McKay. Nonuniversality and finite dissipation in decaying magnetohydrodynamic turbulence. *Phys. Rev. Lett.*, 114:235001, 2015.

[113] M. F. Linkmann and A. Morozov. Sudden relaminarization and lifetimes in forced isotropic turbulence. *Phys. Rev. Lett.*, 114:134502, 2015.

[114] M. F. Linkmann, A. Berera, M. E. McKay and J. Jäger. Helical mode interactions and spectral energy transfer in magnetohydrodynamic turbulence. *J. Fluid Mech.*, 791:61–96, 2016.

[115] T. S. Lundgren. Kolmogorov two-thirds law by matched asymptotic expansion. *Phys. Fluids*, 14:638, 2002.

[116] S. K. Malapaka and W.-C. Müller. Large-scale magnetic structure formation in 3D-MHD turbulence. *Astrophys. J.*, 778(1), 2013.

[117] W. H. Matthaeus and M. L. Goldstein. Measurement of the Rugged Invariants of Magnetohydrodynamic Turbulence in the Solar Wind. *J. Geophys. Res.*, 87:6011–6028, 1982.

[118] B. Mazzi and J. C. Vassilicos. Fractal-generated turbulence. *J. Fluid Mech.*, 502:65, 2004.

[119] W. D. McComb. *The Physics of Fluid Turbulence*. Oxford University Press, 1990.

[120] W. D. McComb. *Homogeneous, Isotropic Turbulence: Phenomenology, Renormalization and Statistical Closures*. Oxford University Press, 2014.

[121] W. D. McComb, A. Berera, S. R. Yoffe, and M. F. Linkmann. Energy transfer and dissipation in forced isotropic turbulence. *Phys. Rev. E*, 91:043013, 2015.

[122] W. D. McComb, M. F. Linkmann, A. Berera, S. R. Yoffe, and B. Jankauskas. Self-organization and transition to turbulence in isotropic fluid motion driven by negative damping at low wavenumbers. *J. Phys. A: Math. Theor.*, 48:25FT01, 2015.

[123] W. D. McComb, S. R. Yoffe, M. F. Linkmann, and A. Berera. Spectral analysis of structure functions and their scaling exponents in forced isotropic turbulence. *Phys. Rev. E*, 90:053010, 2014.

[124] F. Mellibovsky, A. Meseguer, T. M. Schneider, and B. Eckhardt. Transition in localized pipe flow turbulence. *Phys. Rev. Lett.*, 103:054502, 2009.

[125] P. D. Mininni. Scale interactions in magnetohydrodynamic turbulence. *Annu. Rev. Fluid Mech.*, 43:377–397, 2011.

[126] P. D. Mininni, A. Alexakis, and A. Pouquet. Shell-to-shell energy transfer in magnetohydrodynamics. II. Kinematic dynamo. *Phys. Rev. E*, 72:046302, 2005.

[127] P. D. Mininni, A. Alexakis, and A. G. Pouquet. Scale interactions and scaling laws in rotating flows at moderate Rossby numbers and large Reynolds numbers. *Phys. Fluids*, 21:015108, 2009.

[128] P. D. Mininni and A. Pouquet. Inverse cascade behavior in freely decaying two-dimensional fluid turbulence. *Phys. Rev. E*, 87:033002, 2013.

[129] P. D. Mininni and A. G. Pouquet. Finite dissipation and intermittency in magnetohydrodynamics. *Phys. Rev. E.*, 80:025401, 2009.

[130] P. D. Mininni, A. G. Pouquet, and D. C. Montgomery. Small-Scale Structures in Three-Dimensional Magnetohydrodynamic Turbulence. *Phys. Rev. Lett.*, 97:244503, 2006.

[131] H. K. Moffatt. The degree of knottedness of tangled vortex lines. *J. Fluid Mech.*, 35:117–129, 1969.

[132] H. K. Moffatt. *Magnetic Field Generation in Electrically Conducting Fluids.* Cambridge University Press, 1978.

[133] H. K. Moffatt. Magnetostatic equilibria and analogous Euler flows of arbitrarily complex topology Part I, Fundamentals. *J. Fluid Mech.*, 159:359–78, 1985.

[134] H. K. Moffatt and A. Tsinober. Helicity in Laminar and Turbulent Flow. *Annu. Rev. Fluid Mech.*, 24:281–312, 1992.

[135] A. S. Monin and A. M. Yaglom. *Statistical Fluid Mechanics.* MIT Press, 2nd edition, 1975.

[136] J. A. Morales, M. Leroy, W. J. T. Bos, and K. Schneider. Simulation of confined magnetohydrodynamic flows using a pseudo-spectral method with volume penalization. *J. Comp. Phys.*, 274:64–94, 2014.

[137] W. C. Müller, S. K. Malapaka, and A. Busse. Inverse cascade of magnetic helicity in magnetohydrodynamic turbulence. *Phys. Rev. E*, 85:015302, 2012.

[138] M. Nagata. Three-dimensional finite-amplitude solutions in plane Couette flow: bifurcation from infinity. *J. Fluid Mech.*, 217:519–527, 1990.

[139] M. Nishi, B. Ünsal, F. Durst, and G. Biswas. Laminar-to-turbulent transition of pipe flows through puffs and slugs. *J. Fluid Mech.*, 614:425, 2008.

[140] E. A. Novikov. Functionals and the random-force method in turbulence theory. *Soviet Physics JETP*, 20:1290–1294, 1965.

[141] E. Ott. *Chaos in Dynamical Systems*. Cambridge University Press, Cambridge, 2nd edition, 2002.

[142] R. B. Pelz, B. Shtilman, and A. Tsinober. The helical nature of unforced turbulent flows. *Phys. Fluids*, 29:3506–3508, 1986.

[143] R. B. Pelz, V. Yakhot, and S. A. Orszag. Velocity-Vorticity Patterns in Turbulent Flow. *Phys. Rev. Lett.*, 54:2505, 1985.

[144] F. Plunian, R. Stepanov, and P. Frick. Shell models of magnetohydrodynamic turbulence. *Physics Reports*, 523:1–60, 2013.

[145] W. Polifke. Statistics of helicity fluctuations in homogeneous turbulence. *Phys. Fluids A*, 3:115, 1991.

[146] W. Polifke and L. Shtilman. The dynamics of helical decaying turbulence. *Phys. Fluids A*, 1:2025, 1989.

[147] H. Politano and A. Pouquet. Model of intermittency in magnetohydrodynamic turbulence. *Phys. Rev. E*, 52:636, 1995.

[148] H. Politano and A. Pouquet. von Kármán-Howarth equation for magnetohydrodynamics and its consequences on third-order structure and correlation functions. *Phys. Rev. E*, 57:R21, 1998.

[149] A. Pouquet, U. Frisch, and J. Léorat. Strong MHD helical turbulence and the nonlinear dynamo effect. *J. Fluid Mech.*, 77:321–354, 1976.

[150] A. Pouquet and G. S. Patterson. Numerical simulation of helical magnetohydrodynamic turbulence. *J. Fluid Mech.*, 85:305–323, 1978.

[151] E. Priest and T. Forbes. *Magnetic Reconnection: MHD theory and applications*. Cambridge University Press, 2000.

[152] O. Reynolds. An experimental investigation of the circumstances which determine whether the motion of water shall be direct or sinuous, and of the law of resistance in parallel channels. *Philos. Trans. R. Soc. London*, 174:935–982, 1883.

[153] L. F. Richardson. *Weather Prediction by Numerical Process*. Cambridge University Press, 1963.

[154] H. P. Robertson. The theory of axisymmetric turbulence. *Proc. Camb. Phil. Soc.*, 36:209, 1940.

[155] M. M. Rogers and P. Moin. Helicity in incompressible turbulent flows. *Phys. Fluids*, 30:2662, 1987.

[156] S. Rosenblat and S. H. Davis. Bifurcation From Infinity. *SIAM J. Appl. Math.*, 37:1–19, 1979.

[157] P. Sagaut and C. Cambon. *Homogeneous Turbulence Dynamics*. Cambridge University Press, Cambridge, 2008.

[158] G. Sahoo, F. Bonaccorso, and L. Biferale. On the role of helicity for large- and small-scales turbulent fluctuations. *Phys. Rev. E*, 92:051002, 2015.

[159] G. Sahoo, P. Perlekar, and R. Pandit. Systematics of the magnetic-Prandtl-number dependence of homogeneous, isotropic magnetohydrodynamic turbulence. *New Journal of Physics*, 13:013036, 2011.

[160] A. A. Schekochihin, S. C. Cowley, and T. A. Yousef. MHD Turbulence: Nonlocal, Anisotropic, Nonuniversal? In Y. Kaneda, editor, *IUTAM Symposium on Computational Physics and New Perspectives in Turbulence*, pages 347–354. Springer, Berlin, 2008.

[161] A. Schmiegel and B. Eckhardt. Fractal stability border in plane Couette flow. *Phys. Rev. Lett.*, 79:5250–5253, 1997.

[162] T. M. Schneider, D. Marinc, and B. Eckhardt. Localized edge states nucleate turbulence in extended plane Couette cells. *J. Fluid Mech.*, 646:441–451, 2010.

[163] S. Servidio, W. H. Matthaeus, and P. Dmitruk. Depression of Nonlinearity in Decaying Isotropic MHD Turbulence. *Phys. Rev. Lett.*, 100:095005, 2008.

[164] L. Shi, M. Avila, and B. Hof. Scale Invariance at the Onset of Turbulence in Couette Flow. *Phys. Rev. Lett.*, 110:204502, 2013.

[165] H.-Y. Shih, T.-L. Hsieh, and N. Goldenfeld. Ecological collapse and the emergence of travelling waves at the onset of shear turbulence. *Nat. Phys.*, Letter, 2015.

[166] L. Shtilman, R. B. Pelz, and A. Tsinober. Numerical investigation of helicity in turbulent flow. *Computers & Fluids*, 16:341–347, 1988.

[167] M. Sipos and N. Goldenfeld. Directed percolation describes lifetime and growth of turbulent puffs and slugs. *Phys. Rev. E*, 84:035304, 2011.

[168] D. T. Son. Magnetohydrodynamics of the Early Universe and the Evolution of Primordial Magnetic Fields. *Phys. Rev. D*, 59:063008, 1999.

[169] K. R. Sreenivasan. On the scaling of the turbulence dissipation rate. *Phys. Fluids*, 27:1048, 1984.

[170] K. R. Sreenivasan. An update on the energy dissipation rate in isotropic turbulence. *Phys. Fluids*, 10:528, 1998.

[171] J. E. Stawarz, C. W. Smith, B. J. Vasquez, M. A. Forman, and B. T. MacBride. The turbulent cascade for high cross-helicity states at 1 AU. *Astrophys. J.*, 713:920–934, 2010.

[172] R. Stepanov, P. Frick, and I. Mizeva. Joint inverse cascade of magnetic energy and magnetic helicity in MHD turbulence. *Astrophys. J.*, 798:L35, 2015.

[173] T. Kreilos and T. Khapko and P. Schlatter and Y. Duguet and B. Eckhardt. Bypass transition in boundary layers as an activated process. `http://www.etc15.nl/proceedings/proceedings/documents/352.pdf`.

[174] G. I. Taylor. Statistical theory of turbulence. *Proc. R. Soc., London, Ser. A*, 151:421, 1935.

[175] The data is publicly available. see `http://dx.doi.org/10.7488/ds/247`.

[176] The data is publicly available. `http://dx.doi.org/10.7488/ds/295`.

[177] E. C. Titchmarsh. *The Theory of Functions*. Oxford University Press, Oxford, 2nd edition, 1939.

[178] S. I. Vainshtein and Y. B. Zeldovich. Origin of magnetic fields in astrophysics. *Sov. Phys. Usp.*, 15:159–172, 1972.

[179] M. van Dyke. *An album of fluid motion*. Parabolic Press, Stanford, CA, 1981.

[180] L. van Veen, S. Kida, and G. Kawahara. Periodic motion representing isotropic turbulence. *Fluid Dyn. Res.*, 38:19–46, 2006.

[181] F. Waleffe. The nature of triad interactions in homogeneous turbulence. *Phys. Fluids A*, 4:350–363, 1992.

[182] M. Wan, S. Oughton, S. Servidio, and W. H. Matthaeus. von Kármán self-preservation hypothesis for magnetohydrodynamic turbulence and its consequences for universality. *J. Fluid Mech.*, 697:296, 2012.

[183] M. Wan, S. Servidio, S. Oughton, and W. H. Matthaeus. The third-order law for increments in magnetohydrodynamic turbulence with constant shear. *Phys. Plasmas*, 16:090703, 2009.

[184] H. Wedin and R. R. Kerswell. Exact coherent structures in pipe flow: travelling wave solutions. *J. Fluid Mech.*, 508:333–371, 2004.

[185] A. P. Willis and R. R. Kerswell. Turbulent dynamics of pipe flow captured in a reduced model: puff relaminarization and localized 'edge' states. *J. Fluid Mech.*, 619:213–233, 2009.

[186] Y. Yamazaki, T. Ishihara, and Y. Kaneda. Effects of Wavenumber Truncation on High-Resolution Direct Numerical Simulation of Turbulence. *J. Phys. Soc. Jap.*, 71:777–781, 2002.

[187] S. R. Yoffe. *Investigation of the transfer and dissipation of energy in isotropic turbulence.* PhD thesis, University of Edinburgh, 2012. arXiv:1306.3408.

[188] T. Zhou. Bifurcation. In W. Dubitzky, editor, *Enclyclopedia of Systems Biology*, pages 79–86. Springer, 2013.

[189] J.-Z. Zhu, W. Yang, and G.-Y. Zhu. Purely helical absolute equilibria and chirality of (magneto)fluid turbulence. *J. Fluid Mech.*, 739:479–501, 2014.

[190] J. Zrake. Inverse cascade of nonhelical magnetic turbulence in a relativistic fluid. *Astrophys. J.*, 794:L26, 2014.